DOCTOR OF PHILOSOPHY

Study of Steady and Pulsating Impinging Jets

Medina Medina, Humberto Jesus

Award date:
2008

Awarding institution:
Queen's University Belfast

Thesis submitted for the degree of PhD in Aeronautical Engineering

Study of Steady and Pulsating Impinging Jets

The Queen's University of Belfast

School of Mechanical and Aerospace Engineering

Submitted by

Humberto Jesús Medina Medina

M.Eng Aeronautical Engineering

Business Education Initiative

Supervisors:

Dr. E. Benard

Prof. S. Raghunathan

April 15, 2008

Acknowledgements

First and foremost, I would like to thank my supervisors; Dr. E. Benard and Prof. S. Raghunathan. It is true that in the course of preparing a Ph.D, many things can and will go wrong. When things get dark and you cannot see the light, certain things help: a tap in the shoulder, a smile, words of encouragements, but most important of all, a solution. For all these reasons, I would like to especially thank Emmanuel, who seems to possess a special ability to solve the most awkward experimental difficulties whilst always keeping a smile.

I would also like to thank Norman (my second problem solver). This work could have never been completed if it wasn't for his personal dedication to making the pulsator, or as he called it, "that thing again", work. Many thanks also to all the technicians in the workshop, who also made an effort to see this project through. Many thanks to the department secretaries: Susan, Karen, Marie Theresa and Sandra, who always had a smile on their faces.

As far as discussions go, I have to admit to have always enjoyed discussing my work with Glen. He always had an interesting observation or approach to offer. In addition, he is a Matlab guru. Unfortunately for him, Matlab does not offer a "help command" on marriage. I wish him the best on his married life. Also, my thanks for his insight.

I would also like to thank my colleagues in the Department, for all those many well deserved coffee breaks, that sometimes were extended a little longer because of the "must see" episode of Neighbours that I was forced to watch. I also have to thank them for not laughing too hard when I told them when I received my water-soluble paint, for my "water" tank. Especial thanks to Rachel for being my good next door office neighbour and for her words of 'wishdom'. Also, the 'footie' lads, who over the years gave me a lot of bruises, but I'm sure I got some

of them back, accidentally of course. Marty, Sloaner, Alister, Dee. Thank you for being such understanding housemates when I walked around the house at night looking for inspiration.

Now, I would also like to thank my close friends, Emi and Alvaro. Emi thanks for having read this thesis. Your input was greatly appreciated. Alvarito, thanks for taking me out of the house when I needed it most. I don't know how you knew, but you did. Also, thanks for giving me some space the week before submission, I know it was hard.

I have to thank someone special, who always makes me smile, and gives me a little something to smile about each day. Claire, thank you so much for all you have done in the course of the last weeks before submitting this theses. But also, thank you for having me in your house in France for a few days, they were magical. I have to admit that even though, I never got to touch "that" cow, I quite enjoyed the countryside.

Finally, but equally important, my dear family. I would have never ever been able to complete this work without each one of you by my side. My brothers, for giving me reasons to laugh, you silly clowns. My sister for forgiving my many unreturned phone calls. My dad for always being interested in the subject of aviation and introducing me to airplanes as a child. Thanks also to my "other" family, I really enjoyed every single meal we shared. To conclude, a very, very big thank you to my loving mother who has supported me throughout all these years. I simply have no words that could accurately describe my gratitude for such a especial person, who has been not only there for support, but also for advise and care. I would have never got this far without you. To you with all my love and thanks.

Abstract

An experimental investigation on the fluid mechanics of steady and pulsed impinging jets is presented in this thesis. An experimental facility was custom-built in order to generate axisymmetric and incompressible impinging jets (pulsed and steady). In order to ensure that the velocity profiles at the exit were fully developed, the jet was discharged from a round nozzle of 50 diameters in length. The effects of the Reynolds number, the nozzle-to-plate spacing and the Strouhal number were investigated systematically. The range of the Reynolds numbers covered is 4000 to 10000 for the steady jets, and 4200 to 10240 for the pulsed jets. The nozzle-to-plate spacings considered are 2, 3 and 4 nozzle diameters, because at these distances heat transfer enhancement is present for pulsed jets. The Strouhal number ranges from 0 (steady case) to 0.5. It was found that the Reynolds number does not affect the flow field of impinging jets as significantly as the nozzle-to-plate spacing, in particular, for pulsed jets, which exhibit significant changes in the distribution of the Reynolds stresses near the impinging wall for small nozzle-to-plate spacings. In addition, it was also found that the axial convection term of the mean axial momentum balance near the impinging wall is significantly larger for a jet pulsed at $St \approx 0.5$ than its steady counterpart when $H/d = 4$. This work also expands the present knowledgebase of both steady and pulsed jets in three main areas; (1) it presents in-depth velocity measurements and turbulence statistics for pulsed and steady jets, (2) the transitional regime of impinging jets is examined, and finally, (3) it presents data for turbulence model validation of a real incompressible pulsed jet.

Contents

List of Figures

Nomenclature

Latin Letters

$A_N = U_{rms}/U_{avg}$		pulse amplitude
d	m	jet diameter
D_{im}	m^2/s	mass diffusivity
f	Hz	frequency
h	W/mK	heat transfer coefficient
H	m	plate-to-nozzle spacing
k_f	W/mK	thermal conductivity
$Nu = hd/k_f$	-	Nusselt number
p	m	nozzle-to-nozzle spacing
$Pe = Ud/\alpha$	-	Peclet number
$Pr = \nu/\alpha$	-	Prandtl number
$q = h(\Delta T)$	W/m^2	heat flux
r	m	radial distance measured from the jet axis
$r_{1/2}$	m	jet half radius
$Re = U_e d/\nu$	-	jet Reynolds number
$Sc = \nu/D_{im}$	-	Schmidt number
Sh	-	Sherwood number
$St = fd/U_e$	-	Strouhal number
$St_c = d/U_e$	-	Strouhal number for which reduction in entrainment Reynolds stresses is expected
t	s	time
T	$^\circ C$	temperature
T_1	$^\circ C$	initial water temperature

T_2	$^\circ C$	final water temperature
$T_{avg} = (T_1 + T_2)/2$	$^\circ C$	averaged water temperature
T_r	$^\circ C$	room temperature
u	m/s	local streamwise (axial) velocity component
u'	m/s	local streamwise turbulent velocity component
u'_{rms}	m/s	axial turbulent velocity component rms
u'^3	m/s	axial triple correlations
$u'v'$	m/s	turbulent Reynolds stresses
U	m/s	streamwise mean velocity component
U_e	m/s	time-averaged centreline exit velocity
v	m/s	local radial velocity component
v'	m/s	local radial turbulent velocity component
v'_{rms}	m/s	radial turbulent velocity component rms
v'^3	m/s	radial triple correlations
V	m/s	cross-stream (radial) mean velocity component
x	m	vertical distance measured from the nozzle
z	m	vertical distance measured from the plate

Greek Letters

α	m^2/s	thermal diffusivity
δ	m	boundary layer thickness
λ	m	wave length
ν	m^2/s	kinematic viscosity
ρ	kg/m^3	water density
ω	m	jet width

Subscripts and Superscripts

avg	-	averaged value

c	-	related to centreline conditions
e	-	related to jet exit
ex	-	excitation
np	-	non-pulsating flow
p	-	pulsating flow
rms	-	root mean square
s	-	related to surface
$stag$	-	related to stagnation point

Abbreviations

avg	-	time-averaged
BL	-	boundary layer
DC	-	duty cycle (time on/total time of cycle)
HT	-	heat transfer
$Imgs.$	-	images
LIF	-	laser induced fluorescence
MT	-	mass transfer
$No.$	-	number
rms	-	root mean square
PIV	-	particle image velocimetry
TKE	-	turbulent kinetic energy
TLC	-	thermo-chromatic liquid crystals

Coordinate System

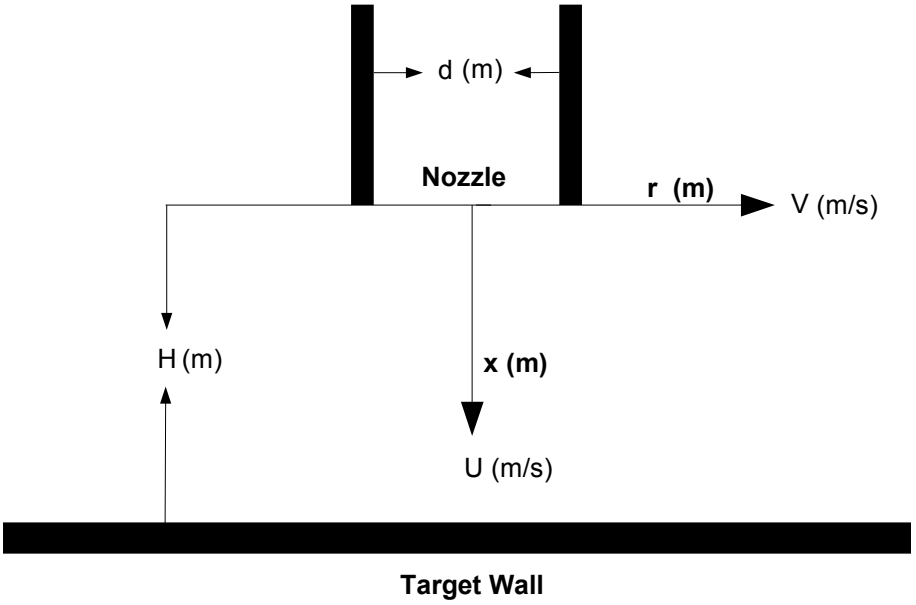

Chapter 1

Introduction

Jets generate a type of flow which consists of a fluid being discharged from a nozzle, whether it is an orifice, a slot, a round nozzle, a contracting nozzle, etc. into an ambient fluid. This type of jet is called a free-jet. However, when a surface is placed in such a way that the development of the jet is interrupted, an impinging jet is created. Impinging jets are characterised by a rapid deceleration of the discharged fluid as it approaches the surface. This deceleration leads to high rates of momentum, heat and mass transfer, consequently, impinging jets have found a place in many industrial applications. For example, cooling of electronics, cooling of the inner surfaces of turbine blades, etc.

Due to the numerous practical applications of impinging jets, their study has been mainly oriented towards understanding their mass, momentum and heat transfer characteristics [17] [18]. However, they are also significant from an academic point of view, since they offer a simple configuration for the study of both, free shear layers and boundary layers. Furthermore, they are also important from a modelling point of view, since turbulence models are mostly tested on flows that are parallel to a wall, therefore, they are not equipped to deal with impinging flows whose streamlines are are not parallel to the wall. Even though efforts to improve computational models have been made, they are being held back by the lack of detailed experimental data [10]. Research on impinging jets is still mainly oriented towards understanding the heat transfer characteristics of impinging jets at high Reynolds numbers, because they offer the highest rates of heat transfer. In addition, due to the many different configurations for jet impingement, there

are often contradictions observed in the literature [6]. Interestingly, when impinging jets are pulsed, there is evidence that suggests that heat transfer can be enhanced in comparison to steady jets [19] [4], but similarly to steady impinging jets. This evidence is also contradictory, given that the literature on the heat transfer characteristics of pulsed jets also show a deterioration of heat transfer in the presence of pulsation [20]. In addition, research on pulsating impinging jets has also concentrated on heat transfer, and the velocity and turbulent fields have been mostly ignored. There are only a few works available that study the velocity field of pulsed jets [21] [5]. However, these studies only consider either laminar or turbulent pulsating jets, but also, are still mainly devoted to the understanding of heat transfer, and therefore, only present limited velocity data. Finally, it is evident that due to the large number of potential experimental configurations, and the contradictions observed throughout the literature for both steady and pulsating jets, there is a need for both, a systematic approach to the study of impinging jets, and also an in-depth study of their flow field and fluid mechanics. This can not only serve as a basis to understanding how the velocity field might affect heat transfer, but also to provide data for turbulence model validation.

1.1 Aims and Objectives

1.1.1 Aims

The aims are:

- To present velocity and turbulence statistics data in a systematic fashion, which will expand the current knowledgebase, serving as a basis for the understanding of the heat transfer characteristics of steady and pulsed jets, but also to aid in the validation of turbulence models.
- To expand the existing knowledgebase of both, steady and pulsed impinging jets, by studying their fluid mechanics within the transitional regime.

1.1.2 Objectives

The objectives are:

- To validate the use of PIV for turbulence statistics measurements.
- To assess the effect of each experimental variable on the fluid mechanics of steady and pulsed jets in isolation, and identify the most influential.
- To provide turbulent statistics data for turbulence model validation of axisymmetric and incompressible impinging jets.
- To identify similarities or differences in the fluid mechanics of steady and pulsed impinging jets.
- To identify which configurations could lead to heat transfer enhancement for pulsed jets.
- To identify, based on the velocity and turbulent fields, any reasons for contradictions in the literature regarding the heat transfer characteristics of pulsed jets.

1.2 Thesis Overview

This section presents the overall organisation of this thesis. Also, it provides the reader with a short description of the content within each chapter. The page number where the information can be found is shown in brackets.

Chapter 1 Introduction: This chapter presents the relevance and motivation behind this work, as well as the aims and objectives of this project.

Chapter 2 Literature Review: Relevant literature on the subject of jets is examined in this section, including free-jets, impinging jets, both steady and pulsed, and also multiple impinging jets (5). The main findings from the available literature are summarised in table 2.1 on page 28.

Chapter 3 Experimental Programme: This chapter describes the experimental rig used to carry out the experiments presented in this thesis (29). It

also describes the instrumentation used for data acquisition (37), as well as an estimation of experimental error and uncertainty (46). Also, it includes a description of the experimental variables considered in this investigation (52) and a summary of the test condition for each experiment (table 3.3 on page 56). Finally, the way in which the experimental data was analysed is also described (55).

Chapter 4 Steady Jets (Base Flow): This chapter presents the results and discussion of the steady jet case (61). In addition, it serves a double purpose: (1) to validate the experimental data by presenting the results from other researchers whenever possible, but also, (2) to serve as a base flow for comparison with the pulsed jet regime. This is achieved by studying the effect of both, the Reynolds number (62) and the nozzle-to-plate spacing (90).

Chapter 5 Pulsed Jets: The results and discussion for pulsed jets are contained in this chapter. Also, the effects of the Strouhal number on transitional (109) and turbulent jets (127) is examined , as well as the effects of the Reynolds number (144) and the nozzle-to-plate spacing (160). These results are compared to the steady case.

Chapter 6 Conclusion: The findings from this work are summarised in this section. Suggestions for future work are highlighted.

Appendices: Useful information is contained within the appendices. Including basic concepts, detailed drawings of the experimental rig and the design process for the pulsator, etc.

Chapter 2

Literature Review

2.1 Introduction

A review of the available literature on the subject of jets is presented in this section, including, free-jets, impinging pulsed and steady jets, and, finally, multiple jets. Emphasis is made on impinging jets since they comprise the subject of this work. A summary of the main findings from the literature survey is shown in table 2.1 on page 28. For general and background information on jet impingement see appendix A on page 196.

2.2 Free Jets (Free-Surface Jets)

Even though free jets are not within the intended framework of this project, a general understanding of the fluid mechanics and generalities of free jets is, nonetheless, an important foundation for the subsequent understanding of the dynamics of impinging jet flows. This section will describe the progress made to date in their study.

The study of jets is not a new area of research. In fact, the general characteristics of jets have been known for many decades now. The study of free jets is of interest because it presents a simple set up for the observation of free shear layers. As early as 1962, Tomich [22] studied the flow and temperature field of free jets. They concentrated on the effect of the Mach number on the jet. There is also a comprehensive textbook in the subject of turbulent jets by Abramovich pub-

lished in 1963[23]. Throughout the 60's [22][23][24], and 70's[25][26][27], research on free jets concentrated on their overall characteristics, including their velocity field, statistics, and heat transport. Research was mainly focused on high Mach number jets. These studies utilised classical experimental methods[1]. In 1979, Lau et al.[28] experimented on free-jets using laser velocimetry. Their work was not intended to expand the knowledgebase for free-jets, instead, it was aimed to demonstrate the viability of using laser-operated instrumentation in order to acquire velocity measurements. It can be regarded as a milestone in proving that laser instrumentation is a reliable means for obtaining velocity measurements. In the early 80's, the work of Hussain became one of the most comprehensive studies on free-surface jets [29] [30] [31] [32]. One of the main contributions from this work is the use of a triple decomposition method in order to analyse the turbulence characteristics of a jet flow when a controlled excitation (cyclic flow) is applied. Following the trend from previous decades, Hussain studied the overall flow field of free jets. By the end of the 80's, subsequent studies on free jets attempted to expand the knowledgebase by examining free jets in more detail. For example, Dorian [33] studied the near-field of round jets in relation to entrainment. Their work is limited to the streamwise component of vorticity, and it is simply descriptive in nature. Fox [34] studied the effect of vortical structures on the thermal field of jets. They observed that viscosity is not a driving factor in the total temperature separation, and that the effect of entrainment is essentially to preserve the inviscid process. Lemoine [35] successfully applied laser-induced fluorescence (LIF) and Laser Doppler-Anemometry (LDA) to measure the temperature field (LIF) and the velocity field (LDA) of free jets. The data provided by LIF and LDA was in agreement with previous data, therefore, validating such techniques for data acquisition. The work of Pietri [36] further validated the use of LDA for velocity measurements. In contrast with Lemoine [35], Pietri [36] validated the use of LDA for turbulence intensity measurements. Lawson [37] used LDA in order to obtain turbulence point-data, due to the high sampling rate (100Hz) provided by LDA systems at the time, whereas, the use of PIV was limited to whole-field measurements of the velocity. In 2004, O'neill [38] successfully used a

[1]Primarily hot-wire anemometry

PIV measuring technique in order to obtain turbulence intensities and Reynolds stresses for low Reynolds number round jets ($Re \leq 1,030$).

From the literature available on free jets, it can be observed that their fluid mechanics and dynamics have been extensively studied. However, the thermal field of free-surface jets has not been studied to such an extent. Anderson [39] concluded that, even though, the effect of the velocity field on the thermal field cannot be denied, the temperature field also affects the velocity field. This was found to be particularly applicable to jet configurations where there is a considerable difference in temperature between the jet and the ambient fluid.

2.3 Impinging Jets

2.3.1 Single Impinging Jets

Due to their highly localised heat and mass transfer rates, impinging jets are widely used in many industrial applications, whether cooling or heating of a surface is required. Examples include, drying of clothes, cooling turbine blades, cooling of electronic equipment, use in aircraft anti-icing systems, etc. The study of impinging jets is also important from a turbulence modelling point of view. Models of momentum and heat transport in turbulent shear flows are developed by reference to flows parallel to walls. Furthermore, turbulence models for separated and recirculating flows are by no means satisfactory [13]. In order to provide data for these models to be improved and/or developed, many researchers have studied impinging jets flows, both numerically [40] [41] [42] and experimentally [43] [44] [9]. Due to the interest on impinging jets, the available literature on the subject is very large. However, the literature covers experimental and numerical studies that focus mainly on the heat transfer[2] characteristics, whereas, the fluid mechanics, to some extent, have been neglected since impinging jets are mostly used for heat transfer applications. Nonetheless, those studies that present significant information on the fluid mechanics of impinging jets will be

[2]Experimental studies on mass transfer are also available. An interesting paper on experimental mass transfer setups is the work by Kataoke [45]. Mass transfer from impinging jets to orthogonally impinged surfaces is examined by Moreno et al.[18]

addressed.

Fist of all, it is important to remember that the velocity field of an impinging jet differs drastically from that of a free jet. The major difference is that impinging jets never reach self-similarity[3]. This is due to the presence of the impinging surface which affects the development of the jet. It is not yet fully understood exactly how the impinging surface affects the developing of the jet, although, Aydore [46] indicated that the effect of the surface can be noticed as early as $x/d = 0.85 - 1.60$, where formation of vortices in impinging jets ($H/d = 4$) becomes noticeable. This value is equal to $x/d = 3.3 - 4.5$ for free jets [46].

Even though, the flow field of impinging jets has not been widely studied, a wide range of methods have been used in order to acquire the velocity data, hot-wire anemometry [46] [44] [47] [13] and Particle Image Velocimetry (PIV) [10] [9] [48] being the most commonly used. In an interesting work by Fairweather [48], results on jet impingement obtained by PIV measurements were compared with previous data obtained using both, LDA (Laser Doppler Anemometry) and hot-wire anemometry. It was found that both LDA and PIV lead to very similar results while hot-wire results were significantly different. These differences were attributed to high turbulence intensity effects on the hot wires due to their intrusive nature, or directional ambiguities encountered when using such probes in highly turbulent flows.

Flow field studies concentrate on observing and/or quantifying the effect of various parameters e.g. Reynolds number, nozzle-to-plate spacing, nozzle diameter, nozzle geometry, confinement, etc. on the overall behaviour of the impinging jet. Ultimately, the intention is to understand the flow and its structure. For instance, coherent structures are responsible for most of the momentum, heat, and mass transfer. Therefore, understanding these structures can be translated into improved heat/mass transfer system design. These structures have been identified in several flow visualisation studies [49] [50] [16]. They are readily observed when laminar flow conditions at low Reynolds numbers are imposed. However, when the Reynolds number is high, most flow visualisation techniques

[3]Self-similarity means that the non-dimensional velocity profile of the jet is unvarying with distance from the nozzle, following a development length.

fail to identify the coherent structures [46]. This highlights the influence on the Reynolds number on the flow field of impinging jets. Fitzgerald [9] studied the flow field of a confined and submerged impinging jet. Reynolds numbers of 8500, 13000 and 23000 were considered, with nozzle to plate spacings (H/d) smaller that 4 diameters. They found that both the Reynolds number and the nozzle to plate spacing have a significant influence on the recirculation pattern of impinging jets. As the Reynolds number increases, the toroid (structure present in submerged and confined jets) moves radial outwards from the stagnation point, also moves closer to the impinging wall. Similarly, as H/d increases, the toroid move radially outwards, although its position relative to the wall remains unchanged (for $H/d = 3$ and 4 at $Re = 8500$). This work is very comprehensive, but it is limited to fully turbulent jet flows ($Re > 8500$). Deshpande [51] carried out a numerical investigation on laminar impinging jets ($Re = 1 - 1000$, $H/d = 3$ and 4). Their results are in agreement with those of Fitzgerald [9] where a similar trend for the position of the toroid is found. In this case the work is limited to laminar jets. Cooper [13] also studied a wide range of nozzle-to-plate spacings ($H/d = 2, 4, 6, 10$ at$Re = 23,000$ and $70,000$). Their work shows a strong influence of H/d on the flow field. In all H/d cases, the wall jet grows linearly with distance away from the immediate vicinity of the stagnation point, but the slope of this linear growth increases with the jet discharge height (H/d). However, the most significant contribution from this paper is the obvious link that is observed between the flow field (fluid mechanics) and the heat transfer incurred by the jet. For example, as H/d is raised from 2 to 6, there is an increase in the stagnation point turbulence intensity of 6%, which is followed by an increase in the Nusselt number. However, this work is limited to high Reynolds numbers.

Other researchers have attempted to explain the relationship between the flow field and the mass/heat transfer characteristics of the jet. Angioletti [16] is among the first to carry out this research. They also attempted to quantify the effect of different variables on heat transfer. They studied an air jet with a PIV system using four different configurations; $h/d = 2.0$ and 4.0, and $Re = 1000$ and 4000. They concluded that there is a clear link between coherent structures and the heat transfer characteristics of the jet on the impinging surface. For

instance, the heat transfer is higher in the region where large structures impinge on the surface, leading to the development of a local maximum, however, for $h/d = 2.0$, there was a noticeable offset of the maximum Nu, coinciding with previous results [52]. Nonetheless, the major insight from this work, is the clear link between these local maxima and large-structure interactions with the surface. Angioletti [16], as well as, Huang [52] noticed a relationship between the location of this Nu maxima and both, Re and H/d. Huang observed that at $h/d = 1$ and $Re > 13000$, the local maximum occurred at $r/d = 1.8 - 2.0$. They also observed that the maximum Nu_{stag} occurs at $h/d = 6$, which is in agreement with previous findings; also as Re decreases and h/d increases, this maximum shifts towards the stagnation point i.e. $Nu_{stag} = Nu_{max}$. Although, the work by Angioletti [16] and Huang [52] agree in the relationship between h/d, Re and Nu, their work does not show a consistency between the location of the local maximum. For example, at $h/d = 2.0$ Angioletti [16], noticed a maximum of Nu located at $r/d = 0.5$, whereas, the work of Huang [52] does not show this maximum offset for similar conditions. This indicates that there is still "grey" areas in the understanding of impinging jets.

At this point, it is interesting to notice that throughout the study of jet impingement, it has been assumed that the non-dimensional heat transfer notation, the Nusselt number, Nu, is effective in predicting the geometry effects of the system. San [53] observed that Nu is dependent on the jet diameter, d, and observed that if Re is kept constant, Nu increases with increasing the diameter (up to 6 mm). In this work, correlations for the Nusselt number are presented. This is a widely used and accepted way to correlate for the Nusselt number:

$$Nu = f(h/d, r/d, Re, Pr) \tag{2.1}$$

In other words, the Nusselt number is a function of the jet-to-plate distance, the radial position, the Reynolds number, as well, as the Prandtl number. Jambunathan [6] presents a detailed review of heat transfer data for impinging jets, most of the references included in this work use correlations in the form of equation 2.1.

The study of impinging jet heat transfer is not only limited to experimen-

tal investigations [54] [17] [55] [56]. Numerical and analytical solutions to the problem are also available in the literature [57] [58] [11] [59]. Computational, analytical and theoretical work help clarify and corroborate the findings obtained experimentally, in the same way that experimental data is used to improve computational solutions. For instance, based on experimental data Kendoush [15] [60]. Kendoush [15], derived the following correlation for the stagnation Nusselt number:

$$Nu = 1.06[Pe(1.04 - 0.034h/d)]^{1/2} \tag{2.2}$$

where $Nu = hd/k$ and $Pe = Ud/\alpha$ is the Peclet number, and α is the thermal diffusivity. Kendoush [60], in a different publication, shows the basics to developing the previous solution, although, limited to laminar flow and low Prandtl number fluids. As more experimental data is available to validate computational models, their corresponding accuracy or ability to mimic real world scenarios is highly improved. Craft [42] developed four different turbulence models for jet impingement, with various levels of success. Their third model is the one capable of reproducing real jet impingement more closely. Nonetheless, its maximum error[4] for the prediction of the mean velocity was in the order of 10%. Song [61] developed a single turbulence model and the maximum error in this case was only 5%. The importance of experimental data availability in developing and improving turbulence models can, therefore, not be underestimated.

2.3.2 Multiple Impinging Jets

Even though there are numerous applications for single jet impingement, the use of multiple jets impinging on a surface is also common in industrial applications; cooling of turbine blades and cooling of electronic equipment, and also in the aircraft industry in the anti-icing systems for a wing or nacelle leading edge. The fluid dynamics of single jet impingement is without a doubt a complex subject. However, the dynamics of multiple jets is more complex due to the mixing and/or interaction between adjacent jets, but also there are fewer publications available. In the modelling and analysis of multiple jets, yet another variable is introduced,

[4]When compared with experimental data

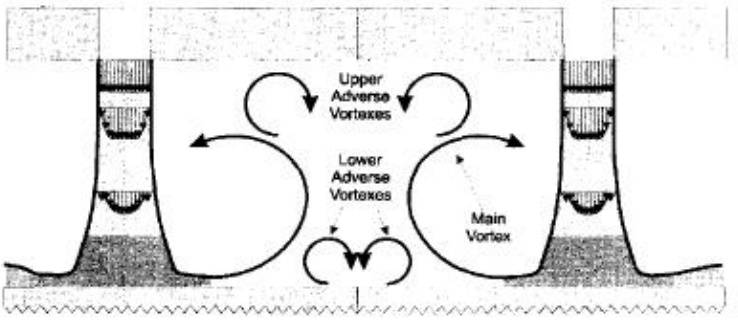

Figure 2.1: Interaction between adjacent jets (Fig. 14 from [1])

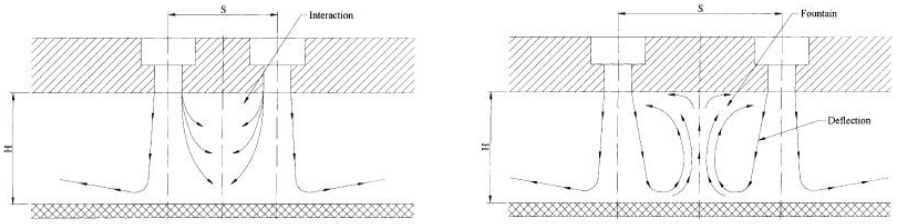

Figure 2.2: Jet interference (left) and jet fountain effect (right)(Figs. 4 and 5 from [2])

namely, the jet pitch, normally in the dimensionless form p/d, where p is the pitch or distance between two jets and d is the nozzle diameter at exit. Fig.2.1, extracted from [1], shows the interaction between adjacent jets (confined). It can be noticed that two regions of adverse vorticity exist. As a consequence, the performance (in terms of averaged Nu) of single impingement jets is higher than that of multiple jets [1].

San [2] further studied the interaction between adjacent jets. Two different types of interaction are described: *interference* and *jet fountain*. Jet interference occurs before impingement, its effect is to reduce the strength of the jets, which consequently deteriorates the overall heat transfer. Jet fountain is originated by the frontal encounter of the two adjacent wall jets, and this results in flow recirculation between the fountain and the centre jet. Due to entrainment effects, the heat transfer of the jet array is also deteriorated. Fig.2.2 shows jet interference and jet fountain respectively.

Unfortunately, there is no evidence, from the literature, of research of multiple impinging jets that focus on the velocity field. The research found on multiple jets is based on heat transfer studies of such jets. This could be in part due

to the lack of measurement techniques that allow measurements of the velocity field of such complicated flows. Nonetheless, due to the recent development of non-intrusive techniques (e.g. PIV), there is now a potential to investigate on the dynamics of such flows.

Brevet [62] studied the jet heat transfer characteristic for different multi-jet configurations (3-row and 1-row) with the intention to find the parametric conditions that will lead to enhanced heat transfer. They considered $Re = 3000 - 20000$, $z/d = 1 - 10$ and $p/d = 2 - 10$. It was found that the heat transfer is a growing function of Re, and can be approximated by the power-law $Re^{0.88}$ (for averaged Nusselt number). They also found $H/d = 3$ to be a good estimate for optimum heat transfer. The optimum pitch (p/d) was identified as $p/d = 4 - 5$. This value leads to the highest heat transfer rates in relation to the amount of fluid (air) used. It should be noticed that this represents the maximum averaged heat transfer, but it does not takes surface temperature uniformity into account. For surface temperature uniformity higher values of p/d are necessary.

San [2] identified the optimum configuration that leads to maximum Nu_{stag}. The results cover a range of $Re = 10000 - 30000$ and $p/d = 4 - 16$. They realised that the optimum p/d for max Nu_{stag} depends on both Re and H/d. Particularly interesting are the findings for $H/d = 4$ and $Re = 20000$, where two values of p/d for maximum Nu_{stag} co-exit; 6 and 12. They indicate that for one configuration the interference effect is greater that the fountain effect and vice versa.

Brown [14] explored different parametric configurations for aligned multiple jets. Their results show that heat transfer increases as H/d increases from 1 to 5. For $H/d > 5$, heat transfer depends on p/d. If $p/d \leq 15$, the heat transfer is a maximum at a value of $H/d \approx 5$ and reduces for higher h/p. For values of $p/d \geq 20$, the heat transfer is constant for $H/d = 5 - 25$. The size of the nozzle diameter was found to influence heat transfer as well. For instance, heat transfer for the larger nozzle diameter ($2.5mm$) was 7-8% less than that of smaller diameter ($1.5mm$). This work also includes correlations for heat transfer that cover the various configurations examined.

Chang [63] developed correlations to predict the averaged Nusselt number for single and multiple impinging liquid jets. The correlation for multiple jet

impingement was based on that for single jet impingement, since the expected heat transfer for multiple jets is lower than that of single jets. The following correlation was obtained:

$$\overline{Nu}(r)_{multi-jet} = 1.667(z/d)^{-0.116}\overline{Nu}(r)_{single-jet} \tag{2.3}$$

And,

$$\overline{Nu}(r)_{single-jet} = 0.7017Re^{0.574}Pr^{0.4}(z/d)^{-0.106}(r/d)^{-0.62} \tag{2.4}$$

It can be observed from equation 2.3 that the pitch of the nozzles does not seem to have an effect on the averaged Nu. This is in agreement with Brown [14], since they only considered nozzle-to-plate spacings between 1.5 and 6.0. For these spacings, H/d is the governing parameter.

2.4 Pulsating Jets

The study of artificially excited jets is not a recent area of interest in fluid mechanics and heat transfer research. When a jet is excited or pulsed higher rates of mixing and turbulence intensities can be achieved. In the case of impinging jets this is beneficial since increased turbulent intensities can result in higher rates of heat transfer [13]. As mention in the previous section the applications of impinging jets are endless (see section 2.3), as a consequence, most researchers have preferred to concentrate their efforts on studying the effect of both excitation and pulsation on impinging jet heat transfer[5]. Therefore, the literature on pulsating or excited jets from a fluid mechanics/dymanics point of view is limited. Nonetheless, there are some studies on free-surface pulsed and excited jets. Hill [64] investigated the effect of excitation on the behaviour of a free-surface jet. Their work was aimed at finding potential applications for excited jets, in particular to be used as part of a vertical and short take off and landing aircraft. They found increases in the centreline turbulence intensity of excited jets of up to 15% in the first 8 diameters from the nozzle exit (St = 0.315). These results are in agreement with the work presented by Zaman [65], however, they go into

[5]studies concentrating on pulsed jet heat transfer will be dealt with later in this section

more detail exploring the effect of the Strouhal number on the centreline velocity intensities. They found that the turbulence intensity is closely related to the non-dimensional frequency (St), in addition, they found that excitation does not always lead to an increase in turbulence intensity, as was the case for their test on a jet excited $St = 1.6$. In a companion paper, Hussain [66] introduced the concept of a triple decomposition of the velocity information in order to fully interpret the data whilst taking into account the effect of the excitation. The velocity data, with the aid of phase averaging techniques, was separated into a mean, a periodic and a turbulent part, as shown in equation 2.5 below.

$$f(x,t) = \overline{f}(x) + \widetilde{f}(x,t) + f'(x,t) \tag{2.5}$$

Where $\overline{f}(x)$ is the global mean over time, $\widetilde{f}(x,t)$ is the phase-locked or periodic component and, finally $f'(x,t)$ is the turbulent component. This is one of the main contributions from their work, since it provides a way to evaluate data from cyclic flows clearly. This decomposition has found many applications, for instance, numerical studies of cyclic flow, including fully pulsed surface-free jets. Graham [67] conducted a numerical study using this triple decomposition, which accounts for both the intrinsic and the periodic components of the flow. They found that, using a modified $\kappa - \epsilon$ turbulence model, the characteristic change in slope of the mean velocity decay curve, the jet growth and the turbulent kinematic energy of the flow could be predicted accurately up to a distance of 50 jet diameters ($x/d = 50$).

More recently, Bremhorst [68] carried out experiments using LDA measurements in a fully pulsed jet with a significant "no-flow" period between pulses. They found that the streamwise component of the aggregate turbulence intensity is significantly different to that of a steady jet due to the strong periodic component, whereas, the radial distribution is almost independent of the distance from the nozzle exit (x/d), but it is higher than that of steady jets. This was the case for the range of x/d studied ($x/d = 50$). This could imply increased heat transfer (if a surface was present) caused by flow pulsations. These results motivated the study of the flow field of impinging pulsed jets. Tsubokura [69] carried out a numerical investigation of the eddy structures of impinging jets excited at

the inlet, for both planar and round jets. Their results indicate increased shear stresses at the stagnation point for excited jets when compared to steady jets. Their work, although thorough when considering the development and behaviour of fluid structures (vortices, eddies, etc), does not analyse these structures from a heat transfer point of view. On the other hand, the PhD thesis of Vrjrazka [5] is a step forward in the study of the flow field and its influence on heat transfer due to excited jets, however, limited to turbulent jets issuing from a contracting nozzle.

Important observations on the flow field of pulsed jets were made by Mladin[6] [3]. They describe the velocity field of a pulsed jet as "a propagation of the pulse as a wave of variable amplitude". This can be observed in Fig.2.3, were the ensemble-averaged profiles of the centreline velocity are presented at four instants in time equally separated over one forcing period $1/f_{ex}$. The distance between two subsequent velocity maxima or minima represent a measure of the local instantaneous wavelengths. An approximation to calculating the wavelength in the near-nozzle region is given by:

$$\frac{\lambda}{\omega} = \frac{1}{2St_d} \tag{2.6}$$

Mladin [4], in a different publication, also presents the effect of the pulsation on the centreline velocity. In Fig.2.4, it can be observed that for the various experimental conditions the averaged centreline velocity is not influenced by either the amplitude (Mladin defines the amplitude as $A_N = U_{rms}/U_{avg}$) or the frequency.

Vejrażka [5] further studied the velocity field of an impinging jet when excited by a given frequency. The excitation frequency was created by means of a speaker. In Fig.2.5, the effect of the excitation frequency on the velocity rms at $r/d = 1$ (position where large scales are most likely to interact with the surface), $z/d = 0.04$ and $h/d = 2$. The results for a natural (excitation-free) jet are also shown.

Vejrażka [5] also studied the dependence of the flow response to the excitation frequency. The velocity rms is plotted against the non-dimensional frequency in

[6]The flow pulsation is generated by two pipes connected in parallel, where one pipe is undisturbed, and the other is intermittently disturbed, therefore, producing the pulse/excitation

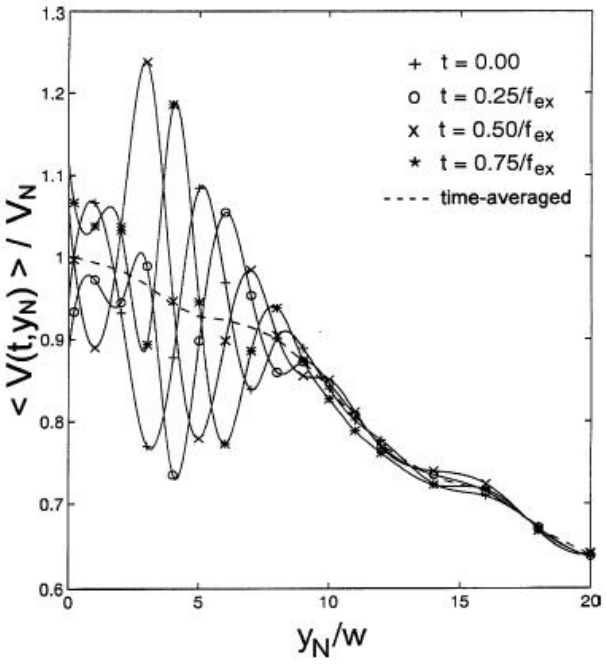

Figure 2.3: Ensemble-averaged profiles of the centreline velocity. $Re = 1000$, $A_N = 5\%$ and $f_{ex} = 82\text{Hz}(St = 0.13)$ (Fig. 3 from [3])

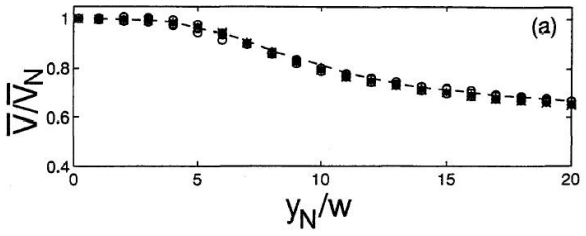

Figure 2.4: Influence of amplitude on centreline velocity (Fig. 5a from [4])

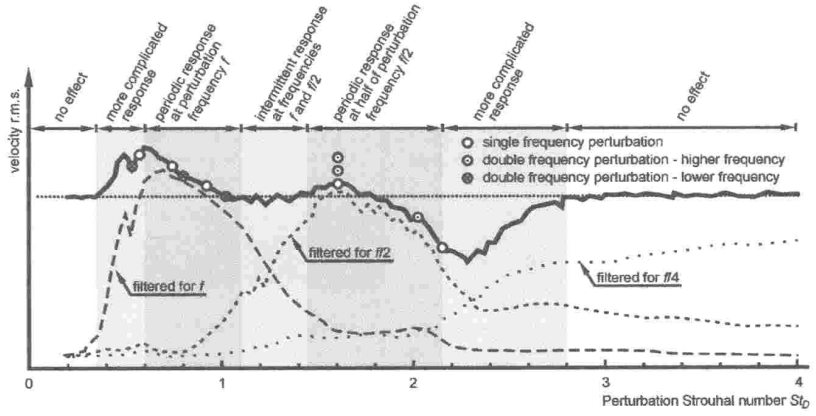

Figure 2.5: Effect of Strouhal number on velocity (Fig. 7 from [5] project overview)

Fig.2.5, showing that excitations in the frequency range, $St_d = 0.35-1.0$, increase the velocity r.m.s. compared to the natural jet, while a decrease is observed for excitation frequencies between $St_d = 1.9$, and 2.8. This figure also shows the velocity r.m.s., which was bandpass filtered to contain only the perturbation frequency (f) or its subharmonics; $f/2$ and $f/4$. When the r.m.s. of the signal filtered to a given frequency, say f or $f/2$, approaches the the non-filtered r.m.s. signal, it suggests that the velocity signal is periodic and its frequency is either f or $f/2$.

It is now clear that by pulsating the jet, the overall velocity field is affected. The next step for most researchers was to study the effect of the pulsations on the heat transfer characteristics of the jet. Mladin [3] also studied the dissipation of heat in a pulsed jet. Fig.2.6 shows that similar to the velocity, heat also propagates as a pulsed wave. Again different instants in time are presented, and the Nusselt number is normalised with respect to the time-averaged Nusselt number to highlight the relative magnitude of instantaneous fluctuations. It can be observed that the fluctuations amplitude reached maximum values between 4 and 6 nozzle widths from the stagnation line. Also, the time-averaged Nusselt number was higher than that of a steady jet, in this particular region.

Mladin[7] [3] concludes that the enhancement of heat transfer by pulsed jets is mainly within the wall jet region of the flow (See Fig.2.7a and 2.7b). It is also indicated that a high value of $St_d A_N$ will lead to enhanced heat transfer, whereas, lower values will lead to lower or similar heat transfer rates compared to steady jets. Mladin's research indicates that a large $St_d A_N$ value is desired, but it fails to indicate a threshold of $St_d A_N$ at which enhancement is expected, where St_d is the Strouhal number based on the jet diameter, and A_N represents the cycle amplitude.

Vejraẑka [5] also observed an enhancement on heat transfer at certain configurations, although, the enhancement achieved on their work is considerably lower than that of Mladin [3][4]. This could be in part due to the difference between their experimental setup and the process used for generating the pulse. Vejraẑka used a loudspeaker to generate the pulse (sinusoidal). He also used two forcing

[7]See footnote 6

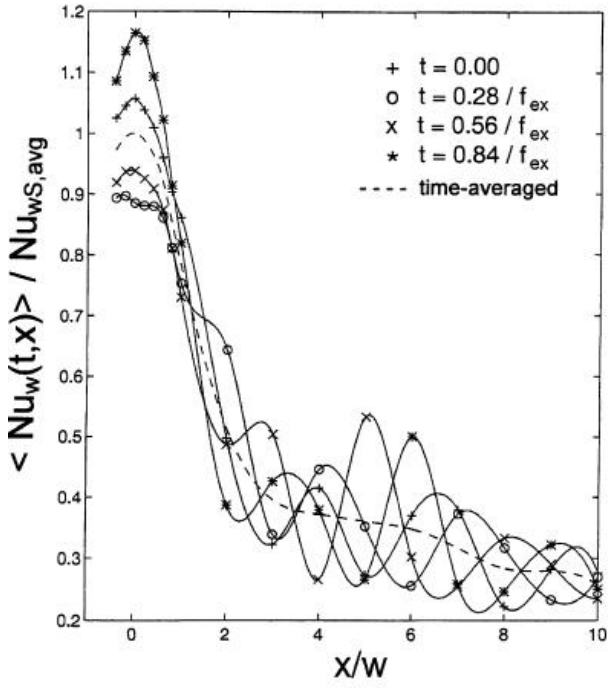

Figure 2.6: Instantaneous Nusselt number distribution. $Re = 1000$, $A_N = 5\%$ and $f_{ex} = 80\text{Hz}(St = 0.106)$, and $H/\omega = 5$ (Fig. 5 from [3])

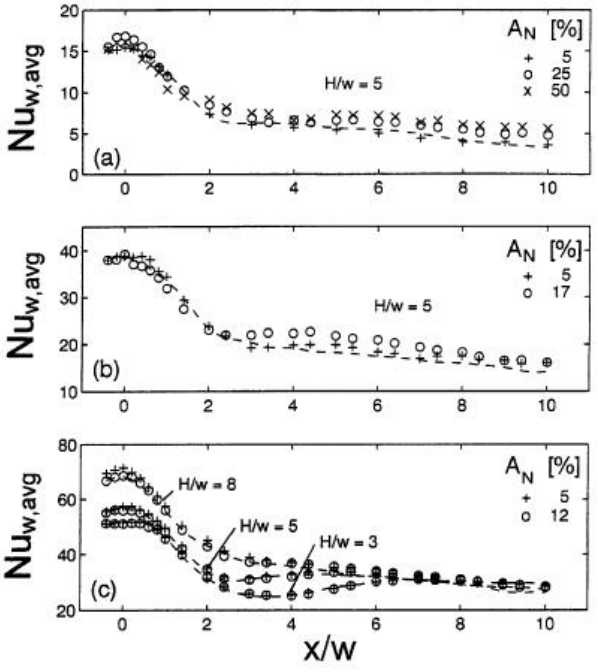

Figure 2.7: Influence of pulse amplitude on time-averaged Nusselt number distribution. — Steady jet a) $Re = 1000$, $f_{ex} = 41\text{Hz}$, $St = 0.054$, b) $Re = 5500$, $f_{ex} = 41\text{Hz}$, $St = 0.011$, c) $Re = 11000$, $f_{ex} = 23\text{Hz}$, $St = 0.003$ (Fig. 9 from [3])

frequencies. Vejražka [5] observed that the enhancement on heat transfer caused by the excitation of the jet was most noticeable in the region, $r/d \approx 1.2 - 2.8$ for $St = 1.75$. This result is in disagreement with that of Mladin [5], where the maximum enhancement effect is noticed in the region $r/d \approx 4 - 6$. The literature available for excited or pulsating jets presents several examples in which different observations are made regarding the benefit of such jets for heat transfer applications. Whereas, Sailor [19] found only a small heat transfer enhancement for pulsating jets for certain configurations, Mladin [4] found heat transfer enhancement in all configurations. Such disagreements in the literature are also evident when examining numerical studies of pulsating jets [70][21]. Observing the contradictions encountered in the literature regarding pulsating jets, it can be concluded that the behaviour of such jets is not fully understood. Most studies have been devoted to assessing the heat transfer characteristics of pulsating jets, leading to a gap in the understanding of their fluid mechanics and dynamics. This implies that the effects of the parameters affecting the flow field and the heat transfer of pulsating jets are not fully understood. These parameters include the diameter of the jet, the Reynolds number, the frequency, etc. Therefore, there is a need to further studying these parameters and their effects.

2.5 Key Parameters

This section will address the parameters that affect the jet flow and heat transfer. They are intended to be grouped in the most logical fashion possible. The main objective of this section is to provide an understanding of the effects of each parameter suggested by the literature, but also to provide the reader with a taste of the complexity involved in fully predicting the behaviour or effects of one isolated parameter, especially, since most of these parameters have "coupled" effects.

2.5.1 Nozzle Type

This refers to the nozzle used in a particular configuration. The main types of axisymmetric nozzles are: smooth contractions, long pipes and orifices. It is

believed that the use of different types of nozzles is one of the reasons behind the existing scatter and differences between the results of the various experimental investigations on jet flow and heat transfer [5] [6].

The characteristics of all these jets are different. For example, the use of smooth contractions leads to a more uniform flow if compared to orifices and pipes [71]. The potential core of orifice flows has been reported to be shorter than other types of nozzle flows, and also exhibit higher turbulence levels [54]. Garimella [54] experimented on the effect of nozzle aspect ratio (length to diameter) on heat transfer. He observed that at very small nozzle aspect ratios ($l/d < 1$)[8], the heat transfer coefficients are the highest. As l/d is increased from 1-4, the heat transfer coefficients drop sharply, but with further increases of l/d of up to 8-12, the heat transfer coefficients gradually increase. The effect of nozzle aspect ratio was found to be less pronounced as H/d is increased. The jet Reynolds number does not influence the role of nozzle aspect ratio on heat transfer. Correlations for Nu_{stag} as a function of Re, Pr, H/d and l/d were proposed. It is worth mentioning that even though, the nozzle effects on heat transfer are evident, not many researchers have chosen to further study its effect. There are no correlations in the literature to attempt to reconcile the results of experimental investigations using, for example, long pipes and smooth contractions. Nonetheless, the effect of the nozzle can not be neglected.

2.5.2 Non-Dimensional Distances

The main non-dimensional distances include: nozzle-plate separation (H/d), plate-to-nozzle distance (z/d), nozzle-to-plate distance (x/d), nozzle-to-nozzle spacing or pitch[9] (p/d) and finally, the radial distance from the stagnation point (r/d). The characteristics of these parameters or distances will be explained in this section, for single steady and pulsed jets, as well as, for multiple jets.

For steady impinging jets, the nozzle-plate separation (H/d) has a pronounced effect on the jet flow and consequently on its heat transfer characteristics. For $h/d < 5$) and small Re, the maximum heat transfer coefficient is located on a ring

[8] l represents the nozzle length

[9] For multiple jet systems

at about $r/d = 0.5$ [16] from the stagnation point. Secondary peaks are noticed at $r/d \approx 1.2-2.0$. The first maximum is believed to originate as the flow is deflected from the impinging surface radially and an increase in acceleration is induced [6]. The second maximum coincides with the location where large coherent structures impinge on the surface [41]. As the Reynolds number increases, and H/d is increased, the maximum Nusselt number is found at the stagnation point [52]. The maximum stagnation Nusselt number occurs at approximately $H/d = 6$ [52], which coincides with the size of the potential core. In can be concluded that the plate-nozzle separation affects heat transfer, although its effect is closely linked to the jet Reynolds number (Re is a parameter which also affects the behaviour of the coherent structures, see section 2.5.6).

In single pulsating jets, the effect of H/d on the average Nusselt number is dependent on the pulse amplitude, the Reynolds number and the pulse frequency (Strouhal number) [3]. Heat transfer enhancement of the pulsed jet over the steady jet is therefore not solely a function of H/d. They concluded that higher Nu can be obtained when the product StA_N is high. Nonetheless, large coherent structures still have a tendency to imping the surface at approximately $r/d = 1-2$ [5], depending on the jet exit conditions, where local maxima are also located. Also, for small enough H/d a ring of Nu_{max} is located at $r/d \approx 0.5$.

For multiple impinging jets, the interaction between parameters becomes even more complex. Nonetheless, the effect of p/d has been observed to some extent by Brevet [62]. They observed that for a configuration of three jets in-line, the optimum hole-spacing (p/d) was $p/d \approx 4-5$, and the optimum H/d was approximately 3. These optimum values for p/d and H/d are based on averaged Nusselt numbers over the impinging surface.

2.5.3 Nozzle Diameter

The use of non-dimensional parameters is based on the assumption that the characteristics of the jet can be universally modelled by scaling the system in terms of a given reference. There is evidence in the literature that indicates that the use of the nozzle diameter (d) as a scaling reference might not entirely be representative of the system. In both [53] and [54] a dependance of Nu on the

jet diameter is observed (when keeping all other parameters constant). They have observed that Nu increases with increasing the diameter. It is possible that this dependance of the Nusselt number on diameter is due to the increase in turbulence intensity as the nozzle diameter is increased.

2.5.4 Impingement Surface

The impingement surface also plays a role in the characteristics of the jet, in particular, the wall jet. The behaviour of the wall jet is determined by the geometry of the surface i.e. flat plate, convex or concave surface. For example, Lai [72], it was observed that for curved wall, the velocity jet front propagates at a faster rate that the velocity front of a comparable radial wall jet that forms when a jet impinges normally on a flat surface. These differences in wall jet propagation rates can be translated on heat and mass transfer differences for the various impingement surfaces.

2.5.5 Confinement and Recirculation

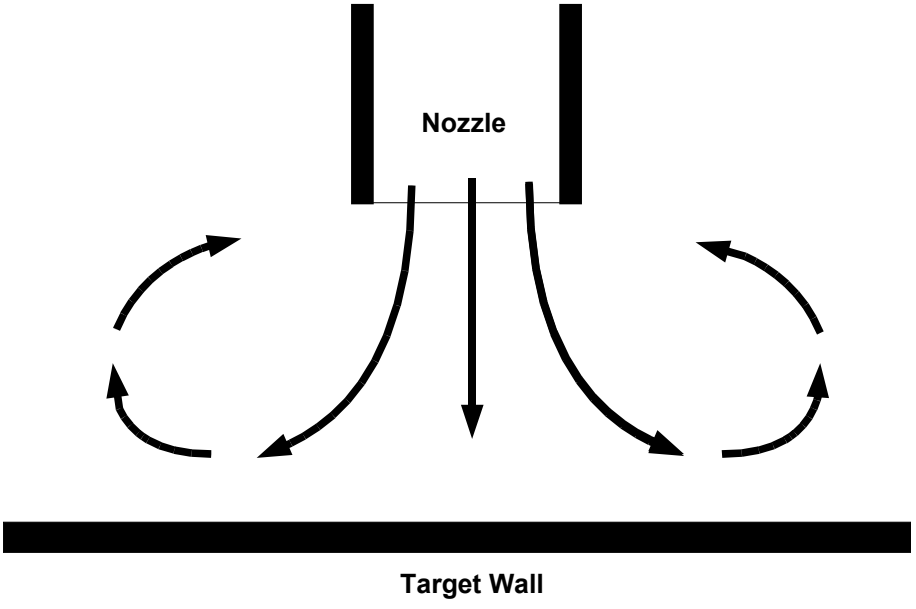

Figure 2.8: Schematic of jet recirculation

Confined and unconfined configurations have been equally considered by numerous researchers. Although, to our knowledge, there is no evidence of any research clearly defining the effect of confinement. The main effect of confinement

comes from examining the available literature. It is a general observation that confinement reduces the heat transfer characteristics of a given jet (also observed by Garimella [54]). Jambunathan [6] in his review of heat transfer for impinging jets, refers to the work of Obot [73], who shows that confinement causes a reduction in heat transfer. This reduction increases with increasing flow rate. This reduction could be credited to the presence of more pronounced flow recirculation, which provides some or all of the air entrained by the jet. Jet confinement is also a factor leading to scatter in experimental data [6]. Fig.2.8 shows a schematic illustrating jet recirculation.

2.5.6 Reynolds Number

The Reynolds number indicates whether the jet is laminar or turbulent, usually for $Re > 4000$. Depending on the Reynolds number, the overall flow characteristics of a jet change drastically. It has been observed that jet flows with high Re show less organised coherent structures compared with lower Re [69], hence, affecting the mass and heat transfer characteristics of the jet.

Jambunathan [6] explains that the heat transfer is a growing function of Re, and can be approximated by the power-law $Nu \propto Re^a$. In Fig.2.9, experimental data of Nu_{stag} for various researchers has been plotted, also the limits $Nu \propto Re^{0.5}$ (laminar) and $Nu \propto Re^{0.8}$ (turbulent). It can be noticed that the data is highly scattered between these two limits. In order to compensate for this scatter in the data. The relationship shown in equation 2.7 is used.

$$Nu = kRe^a \tag{2.7}$$

where k is a constant (obtained experimentally), and a is a function of H/d and r/d. This trend is similar for steady, pulsed and multiple impinging jets.

In pulsed jets, Harkness [74] observed that the main enhancement in heat transfer due to pulsing the jet occurred some distance, approximately $r/d = 3$, from the stagnation point, which is in agreement with the results of Mladin [4]. Harkness [74] also observed that this location was not fixed, but instead, was a function of the Reynolds number. As the Reynolds number was increased, the secondary maximum of Nu moved closer to the stagnation point. This might be

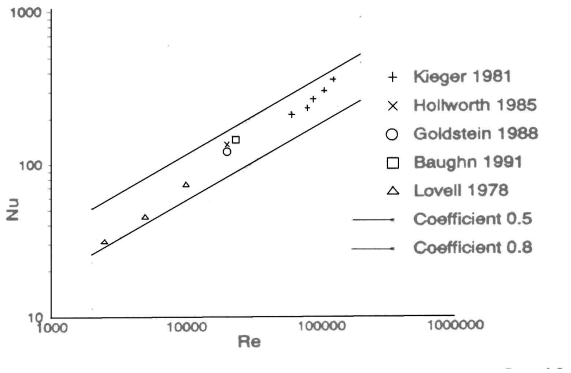

Figure 2.9: Local heat transfer at the stagnation point at $h/d = 10$ (Fig 8. from [6])

due to a change in the location where toroidal structures impinge on the surface, and also to the reduction in size of these structures as the Reynolds number is increased [69]. This trend should be furthered studied in order to validate it. In regards to the stagnation point heat transfer, Harkness [74] observed that stagnation Nusselt number for a pulsed jet is lower than that of a comparable steady jet at low Re, but increases quickly with increasing Re. At a certain Re, the stagnation Nusselt number for a pulsed jet will exceed that of a steady jet, which was termed:"critical Reynolds number". This principle is also noticed for the averaged Nusselt number.

2.5.7 Duty Cycle

The effect of the duty cycle on heat transfer, to the author's knowledge, has only be considered by Sailor [19]. The duty cycle (DC) is the ratio of the 'on' time to the total rotation time of a valve. They observed that although $DC = 0.5$ corresponds to the common square-wave velocity profile used in pulsed flow studies, the lower duty cycle cases consistently produced better heat transfer results. Their results remain unchallenged since no other publications address the effect of the duty cycle. It could also be beneficial to to further study its effect on the velocity field.

2.5.8 Frequency and Strouhal Number

Mladin [3] shows the effect of pulsations on the centreline velocity of a jet. By means of pulsations, the centreline velocity is made to propagate in a wave-like fashion. Pulsations have also been shown to modify and organise the generation of toroidal structures [75]. Mladin [3] also observed that, as opposed to natural vortices, in the presence of an external periodical disturbance, generally, large flow structures have the frequency fixed by forcing. These large structures are formed within the mixing layers at $1/f_{ex}$ time intervals, and travel through the flow as large eddies. Since their frequency equaled f_{ex}, it follows that their associated wavelength and size decreased with increasing forcing frequency.

From all pulsed jet references, it can be observed that the effect of the frequency (or Strouhal number) on the heat transfer characteristics of the jet is dependent on other variables, such as the Reynolds number, which makes it difficult to predict the effects of frequency on heat transfer. Nonetheless, some progress has been made in this respect. For example, Sailor [19] for various plate-to-nozzle spacings (4, 6, 8) and Reynolds numbers (21000, 26000, 31000) observed that for $H/d = 4$, the maximum stagnation Nusselt number is achieved for a frequency of $25 - 35Hz$, independently of the Reynolds number. For $H/d = 6$, the optimum frequency was slightly higher, $30 - 40Hz$ regardless of Re. For $H/d = 8$, the frequency leading to higher heat transfer rates was $30Hz$, but only in the highest Reynolds number case (31000). They also found that medium frequencies tend to perform better. Mladin [4] further studied the effect of the frequency. They concluded that for heat transfer enhancement (compared to steady jets), the product StA_N is a driving parameter. Higher values of StA_N lead to enhanced heat transfer. Although, they fail to provide a threshold of StA_N that will lead to heat transfer enhancement.

2.6 Literature Summary

This section provides a summary of the main characteristics of the various jets. It is intended to serve as a "snap-shot" of the knowledge attained through the literature. The comparison is made in table 2.1 on the following page. This table does not aim to provide an in depth knowledge of jets, but it is useful to get the general picture in the advances made in the subject.

	Velocity Field	Frequency	Heat Transfer	Observations
Free Jets	Velocity field for free jets has been studied in detail. The momentum transfer, the turbulence intensities and other quantities have been studied. Rate of spread, decay rate and half radius have are used to define the behaviour of the jet	In free jets, the breakdown of the shear layer leads to a periodic formation of coherent structures. The frequency at which these structures form is known as the natural roll-up frequency. The formation of these structures is affected by nozzle type	Temperature field is similar to the velocity field (transport of heat). HT occurs only between jet and surrounding medium.	No evidence that cross-stream properties have been studied
Impinging Jets	Velocity field studies limited to average field and velocity fluctuations. Few studies of momentum, turbulence, Reynolds stresses and flow visualisation are available, although, not much have been done on cross-stream properties within shear layer. Emphasis on HT	Similar to free jets, natural roll-up frequencies are also present. The major difference is that the properties at the impinging surface are affected by the periodic collision of these structures against it. This leads to periodic fluctuations of temperature and velocity at the surface where these structure impinge.	Number of HT studies available is large. Scatter of experimental data is noticed. Agreement that at low h/d Nu_{max} occurs at $r/d \approx 0.5$. Maximum Nu_{stag} generally occurs at $h/d = 6$. Some researchers have noticed second maxima at $r/d \approx 1.2 - 2.0$. Due to vortices impinging at this location	Scatter in data has been attributed to type of nozzle used, type of fluid, nozzle diameter, etc. No systematic studies of velocity field encountered. No attempts have been made to introduce effects of nozzle type and diameter in correlations
Pulsed Jets	Basic study of velocity field mainly used to explain heat transfer behaviour. Momentum transfer, turbulence and other parameters describing the velocity field have not been studied. Agreement in ability of pulse to control large coherent structures and shear layer.	Natural frequency of the jet altered by means of an artificial pulse. Therefore, if the forcing frequency is appropriately selected, the formation of coherent structures or vortices can be controlled in order to obtain the desirable surface properties (enhancement of HT). The effect of pulsations is not fully understood	Under certain conditions HT is enhanced compared to steady jets. These conditions are not clearly specified. Agreement that pulse enhances HT at $r/d \approx 1 - 3$. HT is complex function of many parameters that interact with each other. Most influential are: Re, h/d and St	Need to find conditions that will undoubtedly lead to heat transfer enhancement over steady jets. Effect of nozzle and diameter not quantified. Velocity field has not been fully investigated. Effect of frequency not fully understood, but it appears to have a significant effect of HT
Multiple Jets	Very little work on velocity field is available in literature. There is a complex interaction between adjacent jets. Two main types of interaction are noticed: interference and jet fountain	The effects of the frequency are similar to impinging jets if there is no external frequency or pulsation. If a forcing frequency is present, the natural roll-up frequency is also affected	HT is very complex, normally less than that of a single jet, due to jet interacting with adjacent jets. Optimum HT occurs at $H/d \approx 3$, for $p/d \approx 4 - 5$	No evidence of work on multiple pulsating arrays. The diameter and nozzle type also have an influence on HT. No evidence of studies that consider momentum, turbulence, or other velocity quantities

Table 2.1: Comparison of literature for different jets

Chapter 3

Experimental Programme and Apparatus

3.1 Introduction

The objective of this chapter is to describe the experimental facility used to carry out the various experiments that are included in this project. A description of all the various systems and subsystems will be included in order to ensure repeatability of the data presented by researchers willing to further investigate the flow studied in this project. Especial attention will be given to the description of the data acquisition system (Particle Image Velocimetry System) so that the functionality of this system is clearly understood. This chapter will also show the general flow characteristics that the apparatus is capable of producing. Finally, both the experimental programme and the methodology on which this project is based will be presented.

3.2 Apparatus and Components

3.2.1 Apparatus Overview and Operation

The water tank used to carry out the experiments will be described in this section, listing its major components, as well as, its operation. The operating principle of the water tank is quite simple. It relies on a gravity fed mechanism to generate

the jet. For this to be achieved, an overhead tank is used, in order to provide the head needed to drive the water. The water passes through the pulsator (the valve is fully open for the steady jet experiments), then directed to the nozzle, to finally exit at the test section into the main water tank. The excess water from the main tank is collected into a reservoir tank, from there, the water is then pumped back up to the overhead head tank. A constant water level in the head tank is necessary in order to keep a steady supply of water to the test section, therefore an overflow was put in place, the water from this overflow is sent to the reservoir tank. For an overview of the experimental apparatus see Fig.3.1. For detailed drawings of the components that form the water tank see appendix B on page 206. For more detailed information on the design process of the experimental rig, and for a description of design considerations for the manufacture of a water pulsator see appendix C.2

3.2.2 Major Components

Water Tank

The main tank in the experimental rig, is a rectangular glass tank. Glass was a convenient material because it allows visual access to the test section. The inner dimensions of the tank are 605.6mm long, 302.8mm tall and 300.8mm wide. The glass thickness is 2mm. It is capable of holding approximately 55 litres of water.

Nozzle

One of the requirements for this project was for the exit velocity profile to be fully developed. This was achieved by using a PVC nozzle with a length of 50 diameters. The nozzle consists of a straight PVC tube of 1,220mm (40 diameters) in length, and an additional sleeve, which was used to ensure that the inner section of the tube remained circular to produce an axisymmetric jet. The length of the sleeve was 305mm (10 diameters). The inner diameter of the nozzle was 30.5mm. Since water was used as the working fluid, the material of the nozzle chosen was PVC in order to prevent rusting of the nozzle and keep the inner wall of the nozzle smooth.

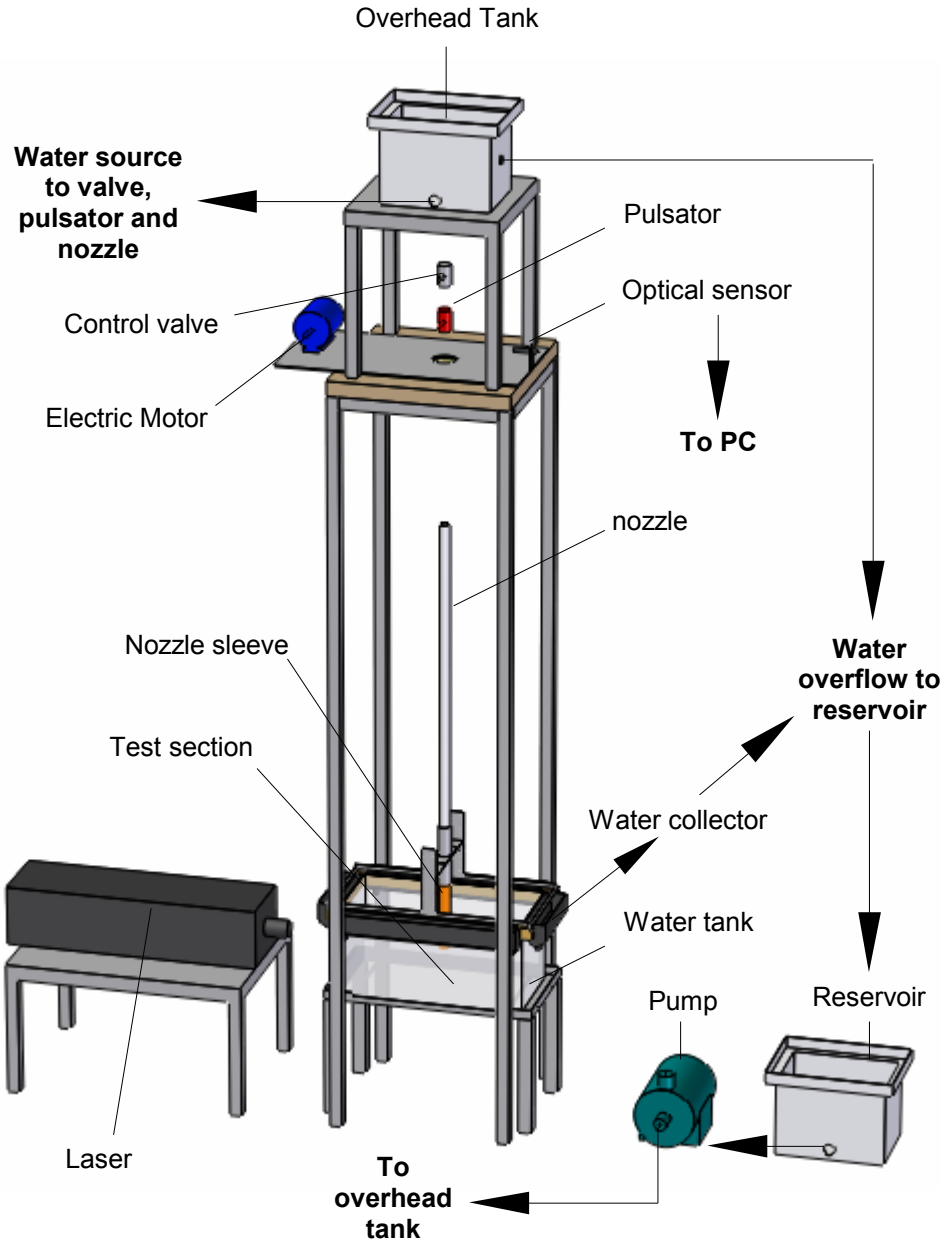

Figure 3.1: Experimental setup overview

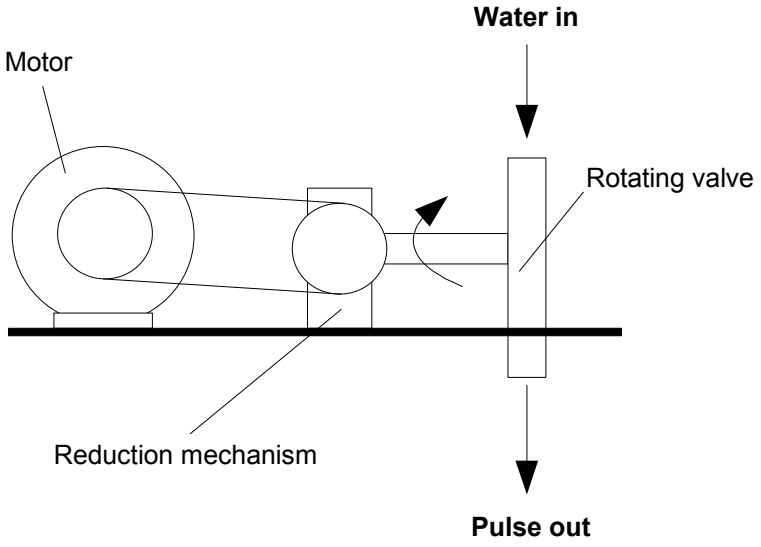

Figure 3.2: Schematic of pulsator assembly

Pulsator

This section describes the components of the pulsator used to carry out the experiments. Fig.3.2 shows a schematic of its components and their assembly. These components are; the driving motor, the rotating valve, and a reduction mechanism. The following sections provide more information about these components. They include:

Rotating valve: In order to generate a pulsing jet a rotating valve mechanism was devised. A ball valve was modified so that it could be attached to a driving motor and rotated at a constant speed (see next section for speed stability details). The working principle of the pulsator is simple. As the valve is rotated, the flow is interrupted when the valve is fully closed, when the valve is fully opened, the water is free to flow. This simple process leads to a pulsation of the flow. The valve used for the pulsator was a one inch PB100 (PN25) chromium plated brass full bore valve (manufactured by Pegler). This valve has a bore of 25mm (for manufacturer's specifications refer to appendix B on page 206). This valve was chosen for two important reasons that must not be underestimated when designing a water pulsator, these are; (1) the valve is water tight, and, (2) it is also air tight. It is a fundamental requirement for the valve to be air tight, as this prevents air from entering the water flow, therefore, preventing the formation of

bubbles.

Motor: A fundamental component of the pulsator is the driving motor. It turns the valve, therefore, producing a pulse. The requirement for this motor is to be able to keep a constant RPM in order to ensure that the pulses, i.e. the rotation of the valve are regular. The motor used was manufactured by ABB (model M2VA71B-2). This 3 phase motor was control using a control unit also manufactured by ABB. It can rotate to speeds of up to 2,850 RPM (47,5 Hz). Once a frequency was selected, it could be kept constant within 0.1 Hz. The motor power was rated at 0.55 Kw.

Pump

A centrifugal pump was used to supply the overhead tank with water. The pump used was manufactured by Grundfos® (model G552103). It has a one inch diameter (both inlet and outlet). It provides a flow rate of 2 m^3/Hr, up to a head of 21m of water (maximum head 28m). The maximum operating temperature of this pump is 90°C which is well above the working temperature of the water used for the experiments in this work.

3.2.3 Setup Capability

The experimental rig was capable of producing impinging jets that go beyond the scope of this project. Nonetheless, the overall capability of the rig will be described. First of all, the rig is capable of generating a fully developed exit velocity profile. It could reach Reynolds numbers from 1500 (steady jets), or 4000 for pulsed jets, up to 20000 (23000 for pulsed jets). For the diameter size used in this project (30.5mm), the nozzle to plate spacing could be set from 1 to 5 nozzle diameters (H/d). In this project nozzle-to-plate spacings higher than 4 nozzle diameters were not considered. This is because is was not the original scope of this project in the first place, and secondly, because of limitations with the PIV system (available field of action of the laser sheet). In addition, there is a concern of possible confinement caused at the top surface of the water tank. In relation to the range of diameters, this experimental rig could operate with nozzle diameters from as little as 8mm to a maximum of 45mm, although operation with

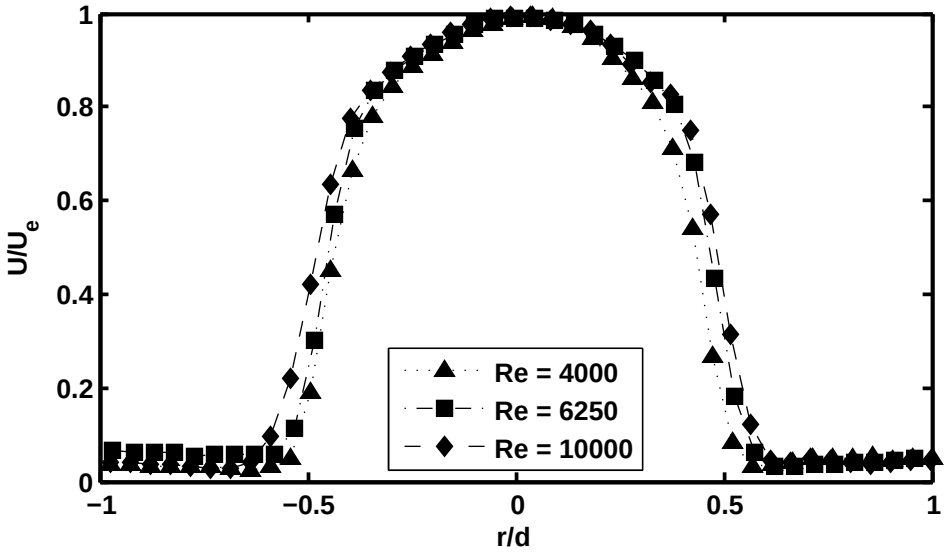

Figure 3.3: Exit velocity profiles at various Reynolds numbers ($x/d = 0.5$)

different diameters would require certain redesigning of the rig.

3.2.4 Flow Characterisation

Exit Conditions

For this project, a fully developed exit profile was desired. This is because, among other reasons, this type of profile has many industrial applications, also, there are numerous previous studies on impinging jets that use fully developed exit profiles. In Fig.3.3, it can be observed that the exit velocity profiles correspond to fully developed turbulent flow. In order to cover the laminar region of the jet flow, for steady jets, jets with Reynolds numbers below 3,500 were looked at, however, they did not exhibit a parabolic exit velocity profile and, consequently, will not be included in this work. On the other hand, for pulsed jets, experiments were carried out only for $Re > 4000$, and also exhibit fully developed velocity profiles.

Axisymmetry

Another design requirement for the experimental setup was for it to generate axisymmetric jets. This is an important feature of the flow, especially, when computational models of the flow are being generated, as a consequence, and in order to provide reliable data, the jet flow must be as axisymmetric as possible.

Even though, it is somewhat difficult to achieve perfect symmetry in the flow, it can be observed in Fig.3.4 that the experimental rig used to carry out the experiment exhibits symmetry, with the largest deviation from symmetry for $Re = 6250$. The main drawback in the test for axisymmetry in this setup is, that it was only possible to check for symmetry in the plane where the laser sheet was originally designed to be located, by folding over the radial profile of the mean radial velocity component near the impinging wall. In addition, attempts were made to test for axisymmetry by observing the flow from underneath the water tank, in other words, parallel to the impinging plate. These attempts failed due to drawbacks inherent to the PIV system and the spatial resolution of the camera. Nonetheless, plane symmetry is still present.

Fig.3.5 shows that there is also symmetry when $H/d = 2$ and 3. For a nozzle to plate spacing of $H/d = 4$ there is a slight break in the symmetry on the negative side of the jet, denoted by "(-)". This deviation from symmetry is attributed to unwanted reflections, as well as, low particle illumination present in this region[1] which could be responsible for the lower values of the recorded radial velocity component.

Confinement

A jet without significant confinement was chosen as the desired configuration for the experiments presented in this thesis as the aim of this work is to provide a data set for a generic jet flow with limited effects from boundary conditions. Therefore, it is necessary to check that there are no confinement effects present. A very straight forward way to check for confinement is to examine the vorticity plot of the mean velocity for the various experiments as the presence of toroid structures is a unique indication of confinement [9]. Fig.3.6 shows the contour plot of a representative vorticity field. It can be noticed that there are no toroidal structures present. This is an indication that there are no confinement effects on the test section. In all of the steady jets tested, there was no sign of toroidal structures, and therefore, it can be assumed that there are no significant effects

[1]For those experiments which were carried out with lower illumination, a small reflection was present in the bottom left-hand side of the test section.

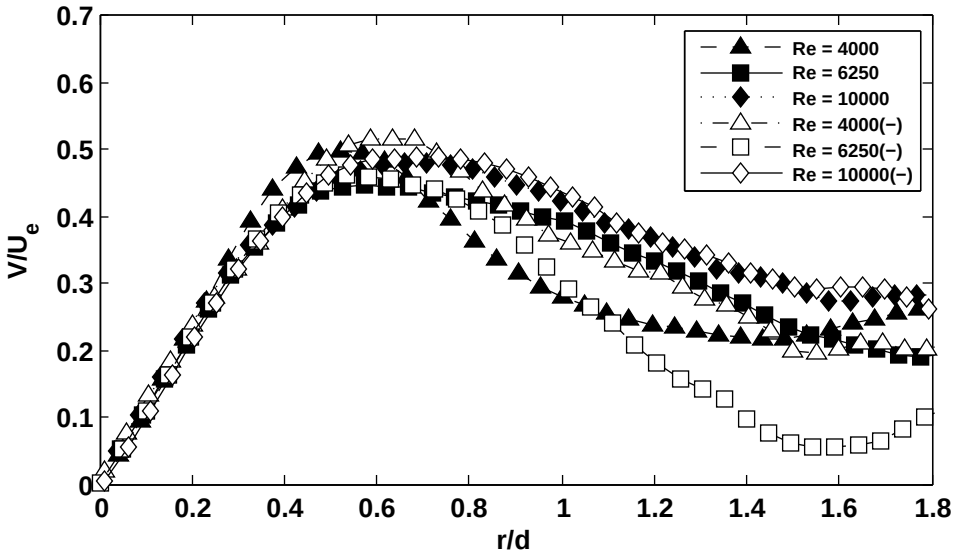

Figure 3.4: Mean radial velocity component near the impinging wall for different Reynolds numbers; (-) represents negative part of the profile which has been folded ($x/d = 2.85$, $H/d = 3$)

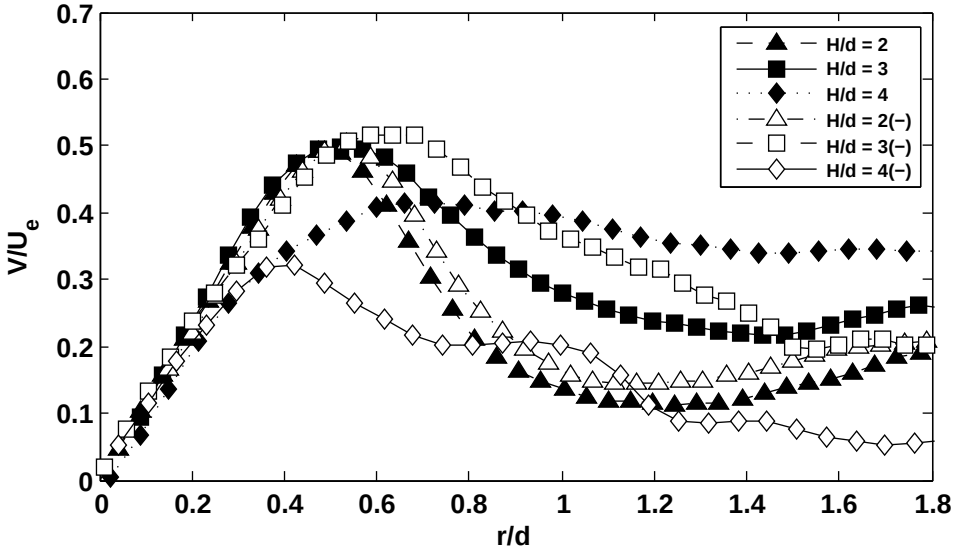

Figure 3.5: Mean radial velocity component near the impinging wall for different nozzle-to-plate spacings; (-) represents negative part of the profile which has been folded ($L/d = 0.95$, $Re \approx 4,200$)

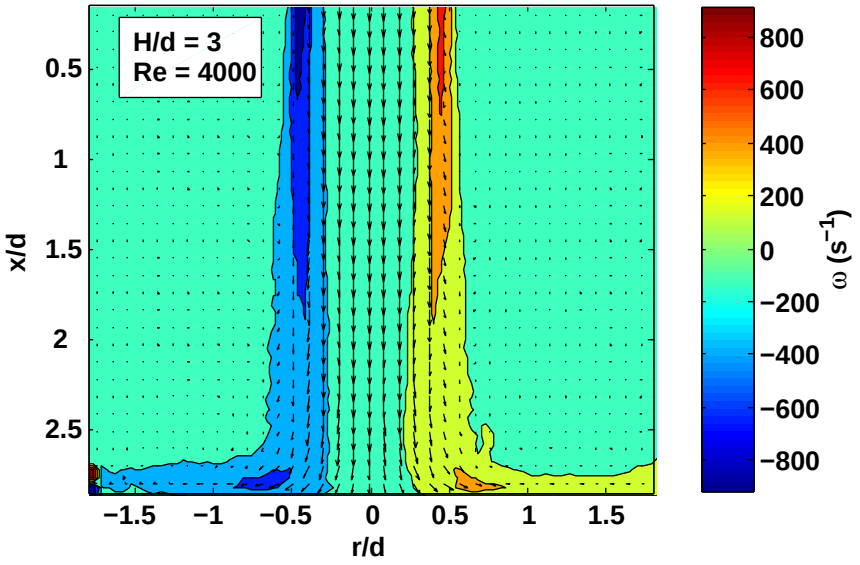

Figure 3.6: Vorticity plot of time-averaged velocity field ($H/d = 3$, $Re \approx 4000$)

due to confinement.

3.3 Instrumentation

3.3.1 Experimental Methods for Turbulence Data Acquisition

Hot Wire Anemometry (HWA)

Hot wire anemometry is probably the most common and well known experimental technique used to measure fluid velocity. It relies on measuring the heat convected away by the fluid. The most important element of in hot wire anemometry is the hot wire probe which is either heated up by a constant current or maintained at constant temperature, whichever method is employed, the heat lost to fluid convection is a function of the fluid velocity. By measuring the change in wire temperature under constant current or the current required to maintain a constant wire temperature, the heat lost can be obtained. The heat lost can then be converted into a fluid velocity in accordance with convective theory. Due to the widespread use of hot wire anemometry, this technique has been greatly developed. In addition, to its relative economy there are a wide range of probes

that are readily available, in fact, there are even probes that can resolve two or three components of the velocity vector, however, for this to be achieved, there is usually a cost in terms of the accuracy of the measurement due to interference effects caused by the presence of the wire. Nonetheless, practice has proven hot wire anemometry to be a very efficient and reliable method for turbulence data acquisition.

Particle Tracking Velocimetry (PTV)

Particle tracking velocimetry is one of the oldest laser measuring techniques in fluids mechanics, in fact, PIV is simply a variation on the philosophy behind particle tracking velocimetry. In addition, it has only been in the last two decades that technology has developed to a level to enable velocity vectors to be measure in sufficient numbers with a significant degree of accuracy. Even though the working principle of PIV and PTV are rather similar, PTV offers advantages over PIV in certain situations, for instance, PIV is not suited to follow the motion of the particles in time. PTV overcomes this difficulty at the proce of the secrifice of some degree of spatial resolution. This is achieved by the use of a single, double or triple camera arrangements which allow particle co-ordinates to be determined photogrammetrically in two or three dimensions, and velocity vectors within an observation plane or volume can be determine accordingly. In any case, PTV is considered the most direct predecessor of PIV.

Laser Doppler Anemometry (LDA)

Laser doppler anemometry (LDA) is an optical technique for the measurement of velocity which is based on the determination of the Doppler shift of light scatters from moving particles which are normally added to the fluid. Lasers are usually used as a light source because they produce a very intensive monochromatic light which is ideal for this type of measurement. This technique relies on frequencies changes of the initial wave generated by the laser. These changes can occur due to movement of the light source, the receiver or the propagating medium. A typical experimental setup, where both the light source and the receiver are kept stationary, the frequency shift is produced by the movement of the particles

which reflect or scatters light from the source to the receiver. Finally, in order to successfully setup a LDA system, the following components are required; a light source, optical arrangements to transmit and collect light, a photodetector and a signal processing arrangement. LDA has found its use in many application where velocity data is to be collected at a point in the flow field, especially when high acquisition frequencies are required and where there is not sufficient space for the use of hot wire anemometry. The major disadvantage of using LDA is that the fluid must be seeded so that light can be scatter back to the receiver, which can be sometime difficult to achieve and/or undesirable.

3.3.2 High-Speed PIV system

The high-speed PIV system used to carry out the experimental programme consists of a power unit, a laser head, a water chiller (to cool the power head), and a high-speed digital camera. This section will provide a general description and technical specifications for all of these components. For a short guide on the principles behind particle image velocimetry (PIV) see appendix D.

Laser Head

Parameter	Specification
Manufacturer	Lightwave Electronics
Model	Q201-HD
Type	Nd:YAG
Wavelength	532nm and 1064nm
Frequency range	Continuous wave -100kHz
Pulse width	20-50ns
Max pulsed power	16.3W@10kHz < 100mW
Typical cw power	500mW < 100mW
Beam diameter	2mm
Beam divergence	2.4mrad
Beam pointing drift	$< 50\ \mu$ rad

Table 3.1: Lightwave Electronics Q210-HD laser head specifications

The laser head used is manufactured by Lightwave Electronics®. For device specifications refer to table 3.1. This laser head generated the light source used to carry out the experiments. It was located between $0.5m$ and $0.8m$ from the test section (depending on experiment).

Power Supply Unit

The power supply unit is also manufactured by Lightwave Electronics®(model QA-PS/M210P-D). This is the unit that controls the laser head for PIV applications. It can be triggered internally and externally. When triggered internally, the laser can be operated to frequencies of up to 100 KHz, when triggered externally, it can be operated up to 16 kHz. It was operated in the range of 60 Hz to 500 Hz during the experimental programme, and it was triggered externally using a PC and software package (see section 3.3.3 for more details on package). The power output of the laser head is also controlled using this device.

Camera

The HSS-2 HighSpeedStar Video Camera System has been provided by LaVision. This is a single frame CCD digital camera with a storage capacity of 1.28 GB. It has a spatial resolution of 1280x1024 pixels. Its operating frequency ranges from 60 Hz to 16Khz. The images taken are stored sequentially to the camera's memory until it is full, then, they are transferred over to the PC for storage and later evaluation. The spatial resolution of this camera is directly related to the operating frequency. There is a resolution reduction as the operating frequency is increased. It can be operated at full resolution up to a frequency of 500 Hz. The camera is connected to the PC through a grabber board on the PCI board. In the setup used in the project, this camera controls the PIV recording by providing the TTL signal that triggers the start of the recording and activates the laser head, in other words, it synchronises the recording. For experiments that require an external trigger, the camera can receive this signal and synchronise the whole process. This was the case for the experiments involving pulsating jets.

Personal Computer (PC)

An important part of the PIV system is the PC and the software that controls the PIV recording. The PC controls the recording by providing timing rules, synchronisation, storage, calibration, etc. This computer operates under Windows®2000 and has a Pentium®IV processor. The PC serves as a centralising unit by monitoring all the other PIV components.

Chiller

The chiller (R-SERIES) of the PIV system was manufactured by Affinity®. The function of this chiller is to cool and maintain the temperature of the laser head. It is important to keep the laser head at optimum temperature so that the quality of the laser sheet is not affected by overheating, or due to sudden changes of the laser head temperature.

3.3.3 Software (Davis 7.0)

The high-speed system used for data acquisition was provided by LaVision, as well as, the software used to control the PIV recording and to post-process the images (Davis 7.0). It also calibrates the camera for Particle Image Velocimetry use. Its various functions will be highlighted in this section. This section is intended to give a general idea of the capabilities and functionalities of the software that were used to obtained the data presented in this project. Those functions that were not used will not be covered here.

PIV Recording Control

The PC provides an interface for all the components in a PIV system. In order for these components to "understand" each other, software is needed to make them "speak the same language". This is precisely what the Davis 7.0 software does. It oversees the PIV recording process and provides an interface for user input. It controls the PIV recording process by synchronising the various devices (power supply, camera and external trigger) and allocating timing rules for their activation. Fig.3.7 shows the connection diagram for the integration of the various

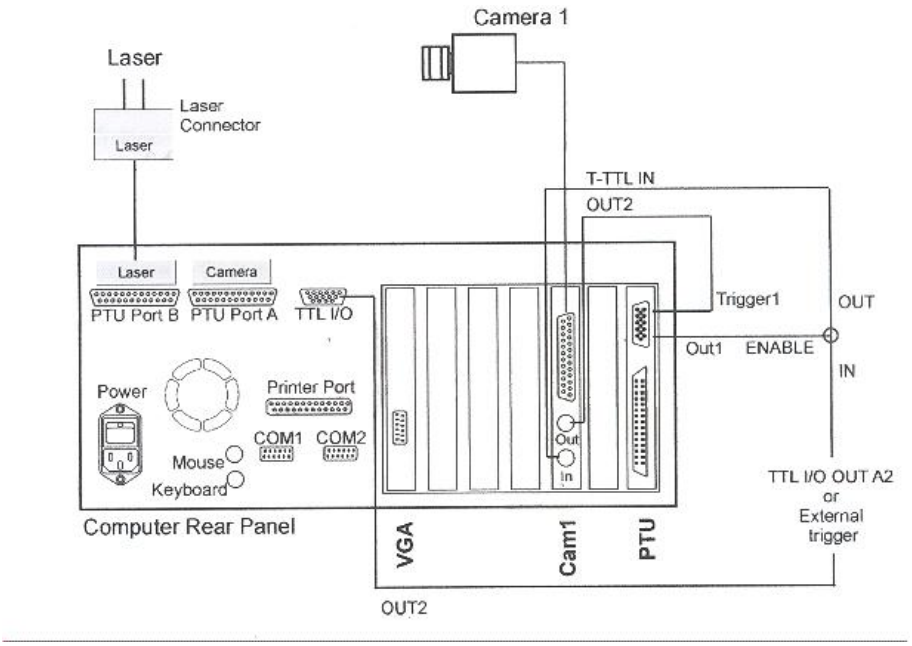

Figure 3.7: PIV system connection diagram (from [7])

devices to the PC.

Image calibration

Image calibration is an essential part of PIV. The purpose of image calibration is, firstly, to allocate the image a reference length (scaling), and secondly, to eliminate image distortions. The camera reads the image information in pixels, then through calibration the software allocates their corresponding length in millimeters. In most PIV setups, the camera is located perpendicular to the plane of view (2-D test section). This minimises potential distortions in the image. Nonetheless, distortions of the image are frequently present, especially, towards the outer edge of the picture frame (caused by the camera lens). Using a calibration plate like the one shown in Fig.3.8, where the distance of the crosses is known, the software generates a mapping function between the image captured by the camera and the corrected image calculated by eliminating the distortion present in the calibration plate, and allocating length units to each pixel. Fig.3.9 shows how the distortions are eliminated. The calibration plate used to calibrate the PIV system was a $80x80mm$ laminated card. It had a white background with 225 black crosses. The distance between the crosses was 5 millimeters.

There are two potential sources of error that must be avoided in the calibration

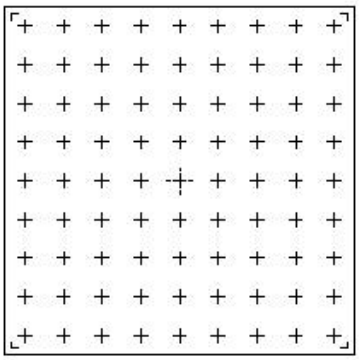

Figure 3.8: Flat calibration plate (from [8])

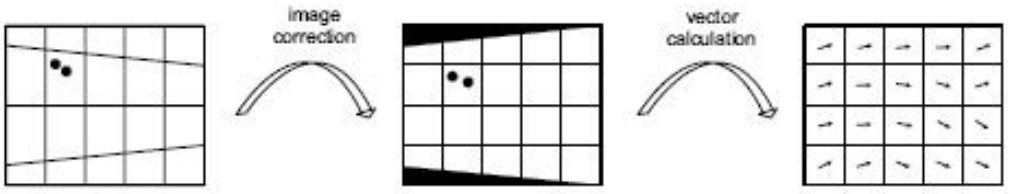

Figure 3.9: Image calibration (from [8])

process. The first source of error arises when the marks are measured with some associated error. This can be reflected on the mapping function calculated by the software. This can be avoided by having as many marks as possible within the calibration plate, also by ensuring that the size of the crosses is not smaller than 1 pixel (roughly $2-3$ pixels). The second source of error can result from the fact that the true mapping function is approximated by a 2D-polynomial of third order, which may not reflect the true distortion sufficiently. The third-order polynomial is usually sufficient for experimental conditions with deviations up to 45° from the perpendicular view

Image Post-Processing

Once the image is calibrated and the PIV recording completed, the images are ready for post-processing. This is the point when the velocity information is extracted from the various exposures by cross-correlation of all the interrogation windows. Once again, Davis 7.0 was used to carry out this process. Sometimes before extracting the velocity information, the image must be pre-processed. There was only one type of pre-processing used (not for all experiments). A sliding

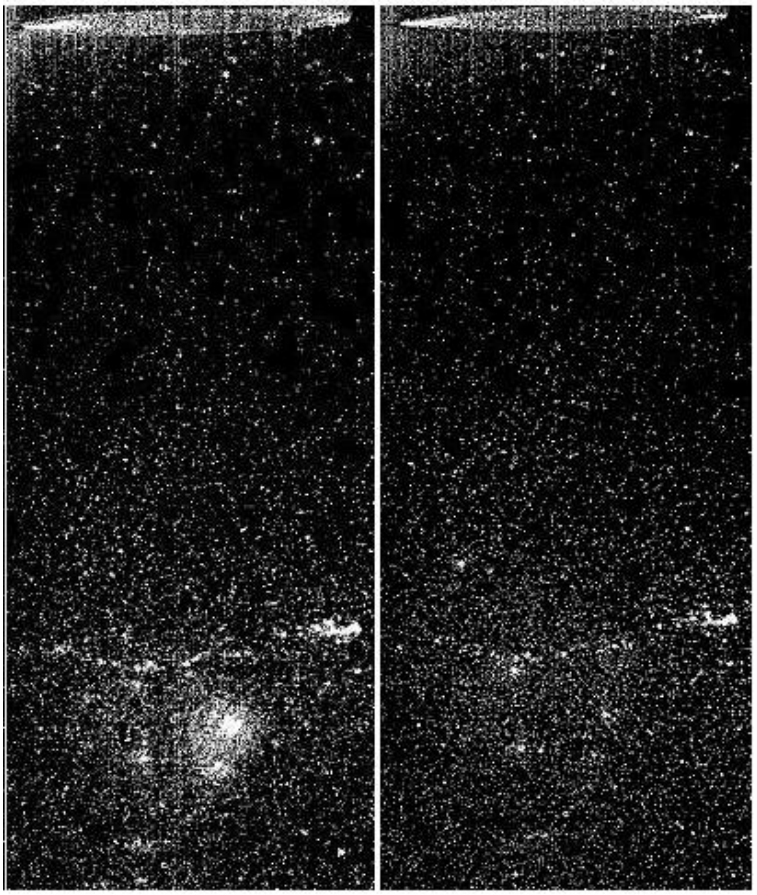

Figure 3.10: Image pre-processing

background subtraction with a length of 3-5 pixels was used. This is used to eliminate intensity fluctuations in the background due to reflections that could not be removed. It acts like a high pass filter, the large intensity fluctuations in the background may be filtered out while the small intensity fluctuations of the particle signal will pass through. Fig.3.10 gives an example of how this filter works.

The velocity data is now extracted from the images. They were all computed using a sequential cross-correlation of the images. They were also all calculated using window multi-pass. This is a process in which the size of the interrogation window is decreased once the vectors are calculated for a given pass, then they are used as a reference vector field for the next pass. This process is continued until the specified final window size is reached. The advantage of this method is that it allows better following of the motion of the particles within the interrogation window, leading to increased spatial resolution and a reduction of erroneous

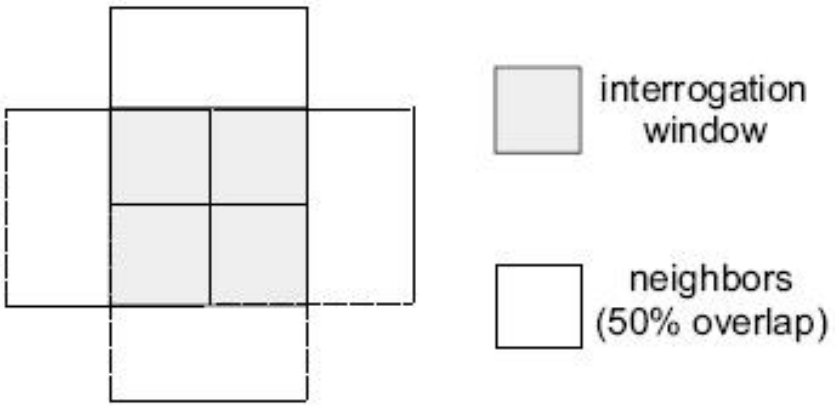

Figure 3.11: Interrogation window overlap 50% (from [8])

vector. In this project the largest initial window size used was 128 pixels, and the final window size was 32 pixels (with 50 percent overlap). Overlapping is a process where the interrogation window is shifted by a given percentage of its length. Fig. 3.11 shows an example of window overlap at 50% of the window. Table 3.3 on page 56 provides a summary of the post-processing applied to each experiment.

3.3.4 Tachometer and Sensor

Tachometer

A digital tachometer manufactured by Monarch Instrument (model ACT-1B) was used for both, measuring the RPM of the rotating valve, and providing the TTL signal to trigger the pulsating jet experiments. The tachometer was customised, by the manufacturer to provide this feature (TTL signal out). The tachometer has a range from 5 to 99,999 RPM with an accuracy of $\pm$ 1 RPM or 0.005 % of the reading and a resolution of 1 RPM. The digital display is updated twice per second for RPM readings above 120 RPM. For reading below 120 RPM the display update is not specified on the manufacturer's user guide, but it was found to update once every second. The tachometer was operated in conjunction with a remote optical sensor.

Experimental Quantity	Associated Error
instantaneous velocities (u, v)	$\pm 1.25\%$
mean velocities (U, V)	$\pm 1.25\%$
turbulent components (u', v')	$\pm 2.00\%$
velocity fluctuations (u'_{rms}/U_e, v'_{rms}/U_e)	$\pm 3.00\%$
Reynolds stresses ($u'v'/U_e^2$)	$\pm 4.50\%$
TKE (k/U_e^2)	$\pm 5.50\%$
triple correlations (u'^3/U_e^3, v'^3/U_e^3)	$\pm 5.50\%$

Table 3.2: Error summary

Sensor

A remote optical sensor, also manufactured by Monarch Instrument (model ROS-5W), was used to provide the signal to the tachometer. The sensor can measure a speed range from 1 to 250,000 RPM. It operates using a simple principle; it requires a reflective tape attached to the shaft on which speed is to be measured. It then generates a pulse per revolution. Its operating range is 0.9 meters from the target surface and up to a 45° degree angle from the reflective tape. The output from the sensor is also a TTL signal (square wave from 0 to 5 volts).

3.4 Experimental Error and Uncertainty

3.4.1 Error and Accuracy Summary

Table 3.2 presents a summary of the estimated error for the various turbulent statistics presented in this work. The accuracy of the velocity measurements was based on the most limiting experiment carried out. corresponding to experiment H3/10000 (see table 3.3 on page 56). This leads to a conservative estimate of the PIV system accuracy of $0.001m/s$.

3.4.2 PIV System Accuracy

The High-Speed PIV system used to take the velocity measurements was provided by LaVision, as well as, the software used to carry out both the recording

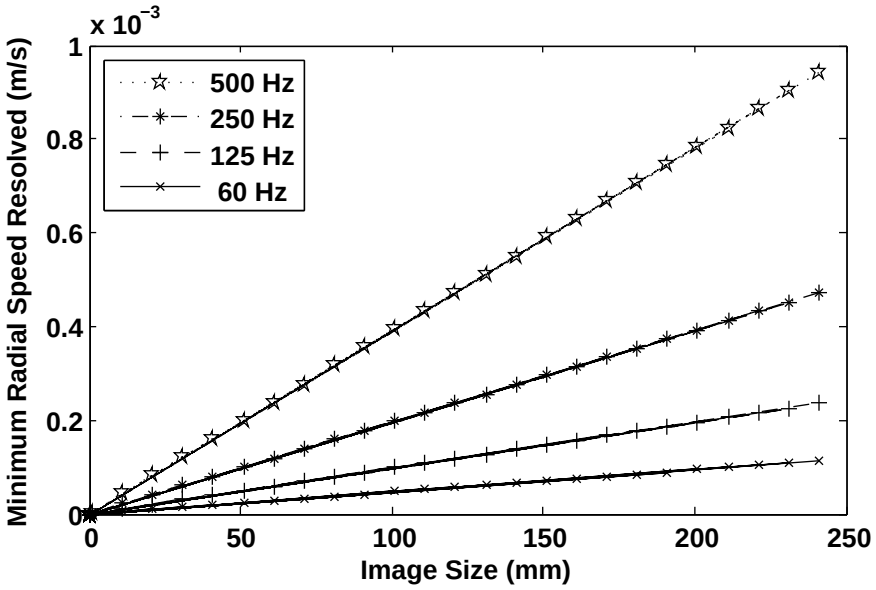

Figure 3.12: System accuracy for radial velocity component (1280 Pixels)

of the images and their post-processing. This system is capable of identifying displacements to an accuracy of 0.1 pixels. The accuracy of the system was checked by carrying out an experiment with a known velocity field and comparing the results with the calculated field using the system. This is a relatively simple check to perform since the only requirement is for the velocity field to be known. A quiescent field can be used to perform the test. This test was carried out and the system accuracy is, as expected, 0.099 pixel. This result implies that for a given acquisition frequency, there is a restriction for the minimum speed that can be resolved, i.e. the equivalent speed for a displacement of 0.1 pixel. This minimum speed is directly related to the camera resolution, the acquisition frequency, and the field size. This relationship is shown in Fig.3.12 and Fig.3.13 for the radial and streamwise components respectively.

It can be observed that, as both the frequency and the image size increase, the minimum resolvable speed also increases. For the different experiments carried out using the High-Speed system, the experiment at $Re = 10000$ was the least accurate.

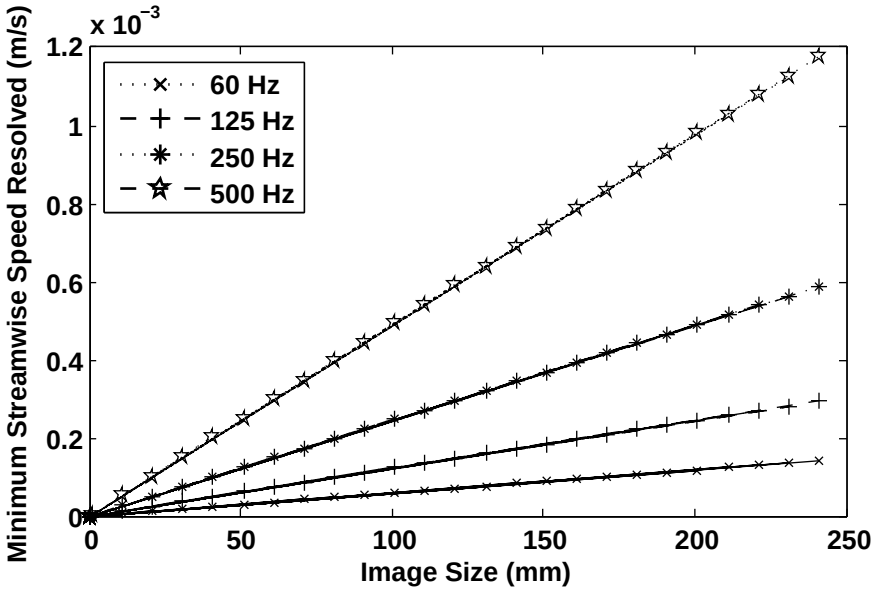

Figure 3.13: System accuracy for streamwise velocity component (1028 Pixels)

3.4.3 PIV System Error

There are many factors that have to be considered in order to achieve reliable and precise PIV measurements. This section addresses these factors and gives an estimate of the expected error associated with the experiments. PIV errors can be divided into two types, namely, systematic and residual. Systematic errors are those which arise due to the inadequacy of the statistical method of cross-correlation in the evaluation of PIV images. This can be reflected on the application of the post-processing algorithm to regions of high velocity gradients, or the use of an inappropriate sub-pixel estimator. By simply selecting a different analysis method or modifying it to suit a given PIV recording, systematic errors can be reduced or even removed. Systematic errors in the system are implicit in the definition of the system accuracy in the previous section since it is assumed that the only effect on the velocity estimation due to the analysis by the software is 0.1 pixel accuracy.

Residual errors are those that remain in the form of measurement uncertainty even when all systematic errors have been removed. The factors leading to the presence of such error are discussed below:

Tracer Particle Choice

One of the primary sources of error in PIV measurements is the influence of gravitational forces on the tracer particles. An equation can be derived from the Stokes drag law to decude the behaviour of the particle under acceleration. Therefore, if the fluid acceleration is not constant or Stokes drag law does not apply (high velocities), the solution is not a simple exponential velocity decay. Nonetheless, the relaxation time is still a convenient measure for the tendency of the particles to attain velocity equilibrium with the fluid flow:

$$\tau_s = d_p^2 \frac{\rho_p}{18\mu} \tag{3.1}$$

where τ_s is the relaxation time for a given particle, d_p is the particle diameter, ρ_p is the particle density and μ is the dynamic viscosity of the fluid. The particles used for the experiments have the following properties: $d_p = 9 - 13\mu m$ and $\rho_p = 1100 Kg/m^3$. The dynamic viscosity for water at $18°C$ (μ) is $0.001053 Ns/m^2$. This gives a maximum relaxation time of $9.8\mu s$, which is much smaller than any significant time scales of the flow. In addition, the working fluid for the experiments was water and the density of the particles is similar (within 10%). Carrying out PIV measurement in water is advantageous since the density of the water and the particles can be readily matched. This makes the effect of gravitational forces on the particles negligible.

Particle Diameter

When the diameter of the particle is smaller than 1 pixel, the velocities obtained from the correlation of the images tend to integer values (pixel). This is known as the peak-locking effect. This effect is usually eliminated when the particle diameter ranges from 2 - 3 pixels. However, anti-peak-locking logarithms have also been successfully used to eliminate peak-locking effects arising due to small particle diameters. The particle diameter for the various experiments carried out as part of this work ranged between 0.12 to 0.16 pixels. The software used to calculate the velocity vectors has an in-built anti-locking logarithm. Furthermore, in order to check whether peak-locking was present in the experiments, a histogram of the displacements was constructed (Fig.3.14). This histogram shows no evi-

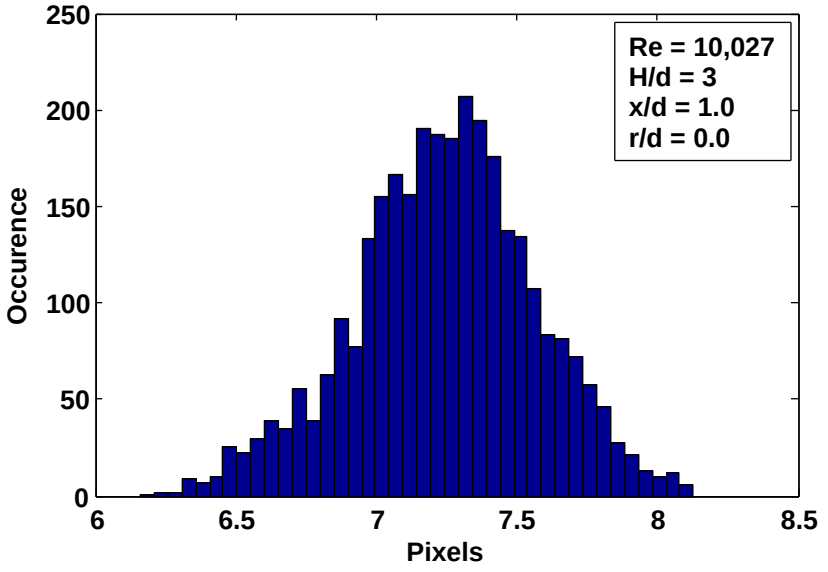

Figure 3.14: Displacement histogram for H3/10000 at $x/d = 1$ and $r/d = 0$

dence of peak-locking in the data. This was the case for all the experiments. It can therefore be assumed that there is no peak-locking errors in the presented data.

Optimisation of Particle Shift

For typical PIV systems, the uncertainty in the displacement measurements is nearly constant for particle displacements greater than 0.5 pixels [76]. Improvements are made on the uncertainty for particle displacement smaller than 0.5 pixel by offsetting the interrogation windows according to the mean displacement vector within the interrogation window, increasing the detectability of the correlation peak because of the increase in the number of particle matches and the ability to use sub-pixel estimators. The accuracy of the system is 0.1 pixel.

Displacements Gradients

Due to the fact that PIV is based on a statistical analysis of the displacement of particles using the correlation between two interrogation windows, the presence of a displacement gradient across a window is likely to result in biased data since not all of the particles present in the first interrogation window will be present in the second. This bias tends to lower displacement values since particles with smaller

displacements will be present in the interrogation window more frequently. This error can be accounted for by the use of decreasing interrogation window size, as well as, window overlapping. This way the bias to lower particle displacements is reduced. This is a feature present in Davis 7.0 and was used in order to correlate images in all experiments.

Out of Plane Motion

If the flow studied is not completely two-dimensional, as the first and second images are being recorded, some particles escape the viewing plane leading to errors in the velocity measurement. This effect is evident in PIV systems that operate two separate lasers, in particular, when the laser sheets generated by each laser do not overlap perfectly. The high-speed system used operates with only one laser head, therefore, there is no need to perform a laser sheet alignment. However, the disadvantage of operating only one laser head is that the pulses generated are less powerful. Finally, the results presented in this thesis were obtained by placing the laser sheet on a plane that intersects the main axis of the jet, therefore, the sheet is placed on a nominal plane of symmetry where the flow will be regarded as two dimensional. As a result, the number of particles that may shift away from the laser sheet between any two consecutive images is minimal.

Laser Accuracy

Another source of error could be the timing accuracy of the laser pulses. For the system used, the maximum laser pulse width is $50ns$. Considering that the shortest image interval used for the experiments was $0.002s$ ($500Hz$), the maximum laser pulse width represents only a 0.0025% of this time interval. Therefore, the laser timing fluctuations during the two exposures can be neglected.

Calibration (Mapping Function)

The camera was calibrated using Davis 7.0, consequently, a mapping function for the camera is generated using a third order polynomial that links x and y pixel coordinates to corrected x' and y' positions. The quality of the mapping

function is expressed by the standard deviation of the location of crosses on a target calibration plate, for a good calibration the system manufacturer suggests that the value for the standard deviation of the crosses should be below 0.4 pixels. The least accurate mapping function for the experiments carried out in this investigation gave a standard deviation of 0.2 pixels. This could be interpreted, assuming a normal distribution of the crosses, and a 95% confidence level, that a given interrogation window will be located within 0.4 pixels of its measured position. If the final interrogation window is 32 pixels, its location will have an error of $\pm 1.25\%$. Since all the other possible sources of error have been considered and their potential effects eliminated or neglected, the overall system error can be considered to be $\pm 1.25\%$, for interrogation windows of 32 pixels.

3.5 Experimental Programme

This project will study the behaviour of both steady and pulsed impinging jets. Also, the jets being studied will be both orthogonally impinging and symmetric. From a detailed study of the available literature it was determined that there is a gap in the knowledgebase for impinging pulsed jets in the transitional regime. A Particle Image Velocimetry (PIV) method will be used for data acquisition. The experiments were carried out in a purpose-built water tank using a high-speed PIV system, which is available at the Queen's University of Belfast. The overall experimental programme includes:

1. Experiments on steady impinging jets; these serve to determine the validity of PIV as a measuring technique by comparing the results obtained with results published by other researchers whenever possible

2. Experiments on pulsed impinging jets

3. Comparison between results obtained for both pulsed and steady jets.

3.5.1 Experimental Variables

This section highlights the different experimental variables concerning the scope of the various experiments that were carried out. They are the nozzle-to-plate

spacing, the Reynolds number and the Strouhal number. These parameters or variables were selected because they are the main factors affecting the behaviour of the flow. Even though, other parameters, such as, the nozzle diameter, the flow temperature, nozzle type, etc., also affect the behaviour of the flow, they are not within the scope of this work, however, they still require further investigation. Furthermore, this project also serves as a starting point from which further research on impinging jets can be undertaken. The experimental variables considered in this project are:

Nozzle to Plate Spacing/Distance This is the distance from the nozzle exit to the target plate. It is normally non-dimensionalised using the nozzle diameter as a reference. This distance plays a fundamental role on the behaviour of the jet.

Reynolds Number This is a non-dimensional number which indicates the influence of velocity effects in relation to viscous effects. It is also used to classify jets as laminar or turbulent. For a typical application (jet) the system is said to be in the transitional/turbulent regime when the Re is approximately 4000. For jets, it is defined as:

$$Re = \frac{U_e d}{\nu} \tag{3.2}$$

Where U_e is the mean centreline velocity at the nozzle exit, d is the nozzle exit diameter and ν is the kinematic viscosity of the fluid.

Strouhal Number The Strouhal number is a dimensionless frequency. It describes the frequency at which a given event occurs e.g. the generation of vortices in a system, or the systematically drop or rise of a particular parameter, It is written as:

$$St = \frac{f d}{U_e} \tag{3.3}$$

Where f is the frequency, d is the nozzle exit diameter and U_e is the mean velocity at the nozzle exit.

3.5.2 Field of View and Measurement Length Scale

The camera for the PIV recording was positioned perpendicular to the laser sheet. It was carefully oriented to capture the free-jet and impinging regions of the jet in order to observe the development of the jet shear layer, and also to examine the effects of the various experimental variables on the initial development of the wall jet. The largest field of view corresponds to the experiment situated at $H/d = 4$. This leads to a rectangular window which was $122mm$ axially and $152.5mm$ radially. The smallest window corresponds to $H/d = 2$ and it was $61x76.25mm$. The choice of field of view determines the physical length scale of the velocity measurements. The measurement length scales for the experiments presented in this work are $0.95mm$, $1.43mm$, and $1.90mm$ for $H/d = 2$, 3 and 4 respectably. This measurement length scale is appropriate for the overall statistical analysis of the velocity signal within the shear layer and the developing wall jet. However, it is not sufficiently accurate for the study of the vortex dynamics.

3.5.3 Test Conditions

A summary of the experimental conditions is shown in table 3.3. This table presents the values of the experimental variables for each experiment, as well as, some other relevant information, including: (1) temperature readings; at the start (T_1) and end (T_2) of each experiment, as well as, the average between the two $(T_{avg})^2$, (2) acquisition information; such as, the acquisition frequency, as well as, the number of images taken[3] and the number of cycles, (3) image post processing; including whether a sliding filter was applied in order to reduce unwanted background intensities, and the selection of window sizes for vector calculation, finally, (4) the exit conditions; the minimum cycle exit velocity (U_{min}), the maximum cycle exit velocity (U_{max}), the exit velocity[4] (U_e), and the exit velocity signal amplitude ($A_N = U_{rms}/U_{avg}$), shown as a percentage. In addition, for a list of the steps followed for the completion of each individual experiment see appendix

[2] T_{avg} was used to calculate the Reynolds number

[3] Since the images were evaluated sequentially, the number of vector fields obtained correspond to No. imgs. - 1

[4] For pulsed jets, U_e represents the average cycle exit velocity

E.

3.6 Data Analysis

This section presents the analysis of the experimental data in order to obtain the results presented in the result chapters. In order to obtain the velocity statistics presented in this work, two different approaches were used, namely, the well known Reynolds decomposition of the velocity signal (steady jets) and a triple decomposition of the velocity data[5] (pulsed jets). These two methods are described in this section separately in order to avoid confusion.

3.6.1 Reynolds Decomposition

The velocity statistics for steady jets were obtained using the Reynolds decomposition of the velocity signal shown in equation 3.4, where $u_{(x,r)}$ represents the "real" or measured velocity, at axial location x, and radial location r, $U_{(x,r)}$ is the local mean of the velocity signal, finally, $u'_{(x,r)}$ is the fluctuating part of the velocity component. In order to make it easier to understand the physical meaning of the Reynolds decomposition, a typical velocity signal is shown in Fig.3.15. This figure shows the velocity signal for a steady jet situated at $H/d = 3$ with $Re = 10000$, also, this signal was extracted at $x/d = 1$ and $r/d = 0$. Furthermore, the turbulent part of the velocity signal can be extracted rearranging equation 3.4, to obtain equation 3.5. Using this relation, the turbulent statics can be computed at each position (x, r), over the entire data range, N, using the equations shown in table 3.6.1, where N, is the number of vector fields. Finally, the time between vector fields corresponds to $1/f$, where f, is the acquisition frequency.

$$u_{(x,r)} = U_{(x,r)} + u'_{(x,r)} \tag{3.4}$$

$$u'_{(x,r)} = u_{(x,r)} - U_{(x,r)} \tag{3.5}$$

[5]The triple decomposition is used in order to remove the cyclic part of the velocity signal

Experiment Code	**Variables**			**Temperatures (°C)**				**Acquisition Information**			**Image Post-Processing**		**Exit Conditions (m/s)**			
	Re	H/d	St	T_r	T_1	T_2	T_{avg}	Freq. (Hz)	No. Imgs.	No. Cycles	Filtering	Evaluation	U_{min}	U_{max}	U_e	A_N
H2/4000	3840	2	-	18.00	18.20	18.90	18.55	125	3066	-	✓	128(2) x 32(2) (50%)	-	-	0.131	-
H2/18000	17000	2	-	18.90	20.80	20.90	20.85	500	3066	-	x	64(2) x 32(2) (50%)	-	-	0.551	-
H3/1500	1410	3	-	18.80	18.20	18.80	18.50	60	3066	-	✓	128(2) x 32(2) (50%)	-	-	0.048	-
H3/2500	2600	3	-	19.00	18.90	19.10	19.00	125	3066	-	✓	128(2) x 32(2) (50%)	-	-	0.088	-
H3/4000	4000	3	-	19.00	20.00	20.20	20.10	250	3066	-	x	64(2) x 32(2) (50%)	-	-	0.129	-
H3/7000	6250	3	-	19.00	20.10	20.40	20.25	250	3066	-	✓	64(2) x 32(2) (50%)	-	-	0.204	-
H3/10000	10000	3	-	19.00	20.50	20.60	20.55	500	3066	-	x	64(2) x 32(2) (50%)	-	-	0.330	-
H4/4000	4020	4	-	18.30	17.80	18.30	18.05	125	3066	-	✓	128(2) x 32(2) (50%)	-	-	0.139	-
H4/8000	8870	4	-	18.50	18.30	18.70	18.50	125	3066	-	✓	128(2) x 32(2) (50%)	-	-	0.303	-
H2/4000/05	4420	2	0.45	19.00	20.50	20.80	20.65	250	11235	105	x	64(2) x 32(2) (50%)	0.093	0.263	0.143	45%
H3/4000/01	3800	3	0.11	17.50	16.50	17.40	16.95	60	6840	60	✓	128(2) x 32(2) (50%)	0.079	0.170	0.135	20%
H3/4000/05	4315	3	0.47	19.90	20.20	20.70	20.45	250	10710	102	x	64(2) x 32(2) (50%)	0.083	0.241	0.140	40%
H3/4000/025	4800	3	0.21	18.10	19.90	20.30	20.10	125	6825	65	✓	128(2) x 32(2) (50%)	0.120	0.204	0.157	20%
H3/7000/025	7990	3	0.22	17.10	16.10	16.90	16.50	250	8520	71	x	64(2) x 32(2) (50%)	0.190	0.397	0.2872	25%
H3/10000/01	10560	3	0.10	18.00	19.90	20.50	19.75	250	16380	78	x	64(2) x 32(2) (50%)	0.121	0.497	0.350	35%
H3/10000/025	10240	3	0.25	17.90	18.60	19.30	18.95	500	13284	81	x	64(2) x 32(2) (50%)	0.223	0.502	0.345	30%
H4/4000/05	5250	4	0.40	20.50	19.30	20.50	19.90	250	7800	78	x	64(2) x 32(2) (50%)	0.061	0.351	0.173	50%

Table 3.3: Test conditions summary

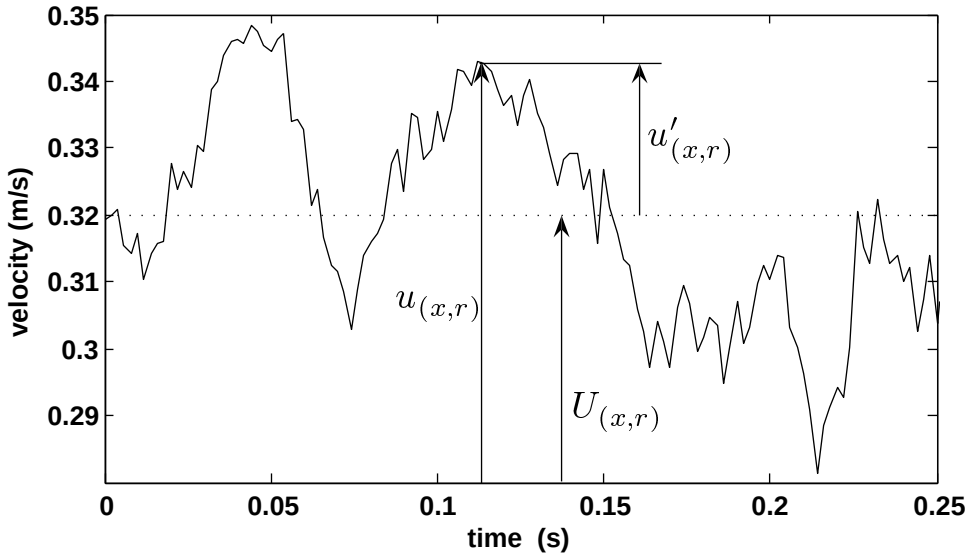

Figure 3.15: Reynolds decomposition of the velocity signal ($r/d = 0$, $x/d = 1$ for H3/10000)

Statistic Type	**Equations**
Velocity Fluctuations	$u'_{rms(x,r)} = \sqrt{\frac{1}{N}\sum_{i=1}^{N}(u_{i(x,r)} - U_{(x,r)})^2}$
Skewness Factor	$u'^3_{(x,r)} = \frac{1}{N}\sum_{i=1}^{N}(u_{i(x,r)} - U_{(x,r)})^3$
Mean TKE	$k_{(x,r)} = \frac{1}{2N}\sum_{i=1}^{N}(u_{i(x,r)} - U_{(x,r)})^2 + (v_{i(x,r)} - V_{(x,r)})^2$
Reynolds Stress	$u'v'_{(x,r)} = \frac{1}{N}\sum_{i=1}^{N}(u_{i(x,r)} - U_{(x,r)})(v_{i(x,r)} - V_{(x,r)})$

Table 3.4: Turbulent quantities equations used for steady jets

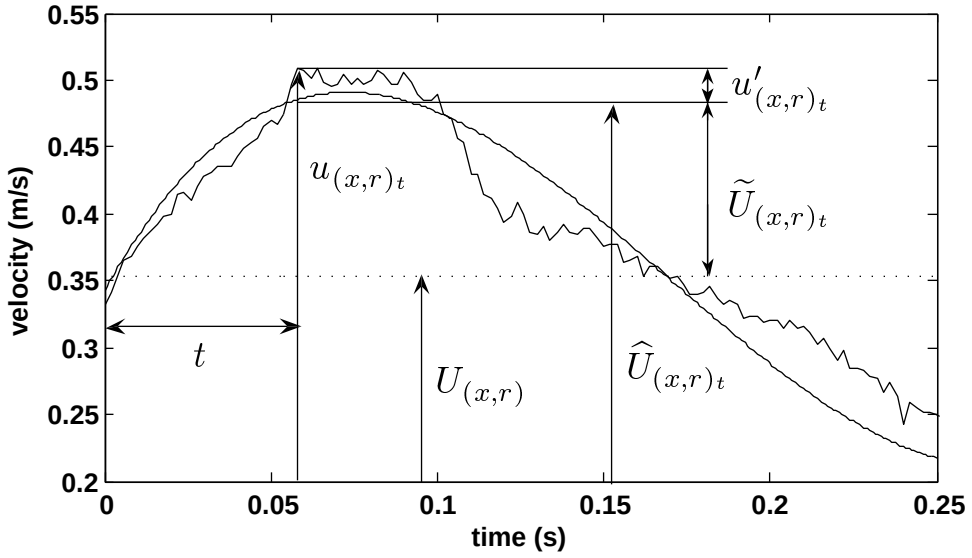

Figure 3.16: Triple decomposition of the velocity signal ($r/d = 0$, $x/d = 1$ for H3/10000/025)

3.6.2 Triple Decomposition

The velocity signal of the pulsed jets was decomposed using a triple decomposition [66] [77], shown in equation 3.6, where $u_{(x,r)_t}$ is the total velocity or "true" velocity, $U_{(x,r)}$ is the time-averaged velocity over all the cycles, $\widetilde{U}_{(x,r)_t}$ is the phase-locked average velocity, measured from $U_{(x,r)}$, and finally, $u'_{(x,r)_t}$ is the turbulent or fluctuating component. In addition, x and r, represent the axial and radial locations where the velocity signal is extracted, at time t. This triple decomposition is represented graphically in Fig.3.16. In order to reduce computing time, the time-averaged velocity $U_{(x,r)}$, which has a fixed value over time, was combined with the phase-locked average velocity $\widetilde{U}_{(x,r)_t}$ resulting in $\widehat{U}_{(x,r)_t}$, therefore, equation 3.6, can be rewritten as shown in equation 3.7, which represents a dual decomposition of the velocity signal. Finally, the turbulent component of the velocity signal can be extracted using equation 3.8. This process is shown in Fig.3.17. Therefore, $u'_{(x,r)_t}$, represents the "pure" turbulent part of the velocity signal at time t of the cycle, but with the cyclic component removed. The relations used in order to calculate the turbulent quantities for pulsed jets is shown in table 3.5, where N is the total number of velocity fields and t_i represents the time in the cycle that corresponds to a given value of N.

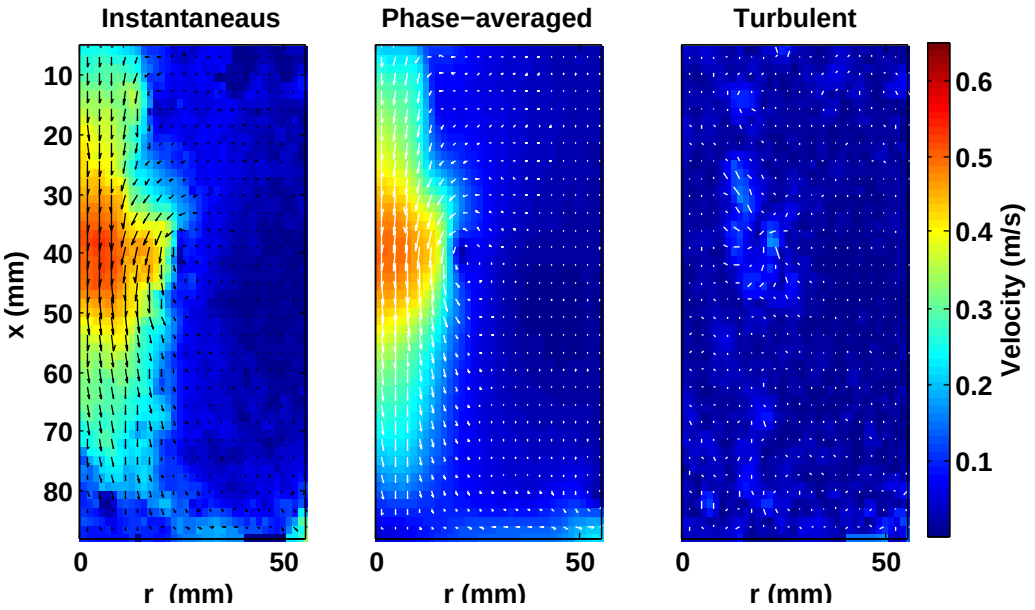

Figure 3.17: Dual decomposition of the velocity signal (H3/10000/025)

Statistic Type	**Equations**
Velocity Fluctuations	$u'_{rms(x,r)} = \sqrt{\frac{1}{N}\sum_{i=1}^{N}(u_{i(x,r)_{t_i}} - \widehat{U}_{(x,r)_{t_i}})^2}$
Skewness Factor	$u'^3_{(x,r)} = \frac{1}{N}\sum_{i=1}^{N}(u_{i(x,r)_{t_i}} - \widehat{U}_{(x,r)_{t_i}})^3$
Mean TKE	$k_{(x,r)} = \frac{1}{2N}\sum_{i=1}^{N}(u_{i(x,r)_{t_i}} - \widehat{U}_{(x,r)_{t_i}})^2 + (v_{i(x,r)_{t_i}} - \widehat{V}_{(x,r)_{t_i}})^2$
Reynolds Stress	$u'v'_{(x,r)} = \frac{1}{N}\sum_{i=1}^{N}(u_{i(x,r)_{t_i}} - \widehat{U}_{(x,r)_{t_i}})(v_{i(x,r)_{t_i}} - \widehat{V}_{(x,r)_{t_i}})$

Table 3.5: Turbulent quantities equations used for pulsed jets

$$u_{(x,r)_t} = U_{(x,r)} + \widetilde{U}_{(x,r)_t} + u'_{(x,r)_t} \tag{3.6}$$

$$u_{(x,r)_t} = \widehat{U}_{(x,r)_t} + u'_{(x,r)_t} \tag{3.7}$$

$$u'_{(x,r)_t} = \widehat{U}_{(x,r)_t} - u_{(x,r)_t} \tag{3.8}$$

Chapter 4

Steady Jets (Base flow)

4.1 Introduction

This chapter presents the results and discussion of the steady jet case. It also serves two purposes: (1) it serves as a validation of the experimental apparatus and measurements by providing comparisons to the work of other researchers whenever possible, and, (2) it examines the effect of the Reynolds number and the Strouhal number on steady jets, which will then serve as a basis for the comparison between the steady and the pulsed jet regimes.

4.2 Data Characterisation

For all the different experiments, the velocity data at the centreline ($r/d = 0$), and at one diameter from the nozzle exit ($x/d = 1$) was gathered and normal probability plots were constructed in order to assess the normality of the data at the centreline, where it is less likely to be influenced by any external factors that might change the distribution of the data. Fig.4.1 shows the normal probability plot for the data of the jet at $H/d = 3$ and $Re = 10,000$. It can be observed that the axial velocity data at this location follows a normal distribution since the observed values are close to the straight line. All normal probability plots are included in appendix F.

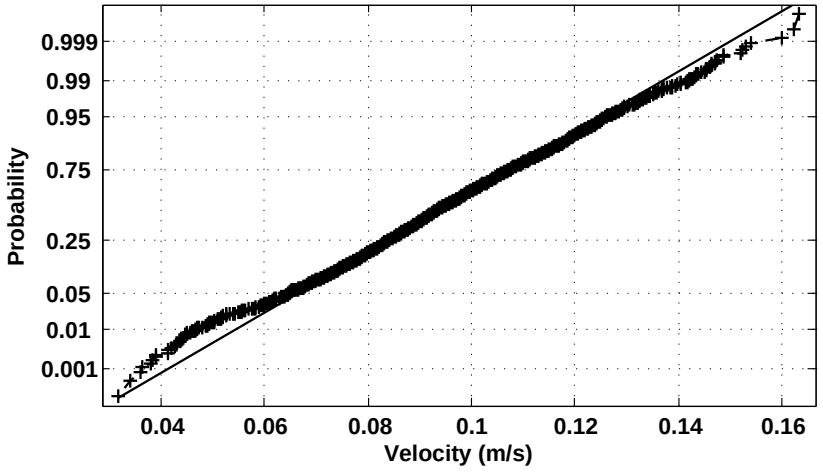

Figure 4.1: Normal plot of velocity data ($Re = 10000$, $x/d = 1$, $r/d = 0$)

4.3 Effect of the Reynolds Number

4.3.1 Introduction

In the following section the effect of the Reynolds number is examined while keeping all other parameters constant. Three different Reynolds numbers are considered; 4000, 6250 and 10000, which correspond to transition, the onset of turbulence, and a turbulent jet respectively. The jet diameter and the nozzle-to-plate spacing have both been kept constant ($d = 30.5mm$, $H/d = 3$). In many practical applications, nozzle-to-plate spacings in the range of 2 to 5 nozzle diameters are used, therefore, the selected value for this distance ($H/d = 3$) became a reasonable choice since it also corresponds to the start of heat transfer enhancement for jet impingement heat transfer. The highest rates of average heat transfer correspond to distances of $3 - 4.5$ nozzle diameters. It is known that as the Reynolds number is increased, the heat transfer at the stagnation point increases [78][52] following the relationship $Nu \propto Re^a$ [6]. However, there is disagreement in regards to the value of the exponent a, in particular for lower Reynolds numbers (2500 to 10000). Therefore, the study of the fluid mechanics for the selected values of the Reynolds number could provide an insight on the understanding of the relationship between the flow field of the jet and its heat transfer characteristics.

4.3.2 Time-Averaged Flow Field

The effect of the Reynolds number on the whole field time-averaged velocity magnitude is shown in Fig.4.2. This figure shows that the Reynolds number does not have a strong influence on the jet mean characteristics within the jet core. This is clearly observed in Fig.4.3. This figure shows centreline velocity decay of the axial component. As is can be observed, there is not a significant decline of the jet velocity up to 2 diameters away from the nozzle exit. However, from 1 diameter away from the target plate, the effects of the impinging wall on the velocity of the jet are significant, leading to a rapid decrease of the jet axial velocity. This region is known as the impingement zone. Due to the presence of the impingement surface, it is characterised by a rapid decrease in axial velocity and a corresponding increase in static pressure and an acceleration in all directions perpendicular to the original flow. Fig.4.2 also shows that as the Reynolds number is increased, the jet becomes wider and the wall jet becomes stronger. This effect is more clearly observed in Fig.4.4, where radial profiles of the axial and radial velocity components at different axial locations are shown.

Near the impinging wall (Fig.4.4a) the mean axial component shows no significant variations, only a moderate increase in magnitude as the Reynolds number is increased. However, the Reynolds number has a strong influence on the development of the mean radial velocity (Fig.4.4a (right)). It shows that as the Reynolds number is increased, the location of the radial velocity maximum shifts away from the stagnation point ($r/d = 0.5, 0.6$ and 0.75). Also, it shows that the mean radial velocity magnitude increases. However, the jet with the lowest Reynolds number ($Re = 4000$) exhibits the highest local radial component maximum. This maximum is followed by a rapid decrease of the radial velocity component, which indicates that the initial exit velocity is not capable of forcing the fluid in the radial direction as efficiently as jets with higher Reynolds numbers. Finally, the results of Fitzgerald [9] are also shown. They correspond to a $Re = 23000$ and $H/d = 3$ for a squared-edged nozzle (confined jet). Fitzgerald's results help illustrate that as the Reynolds number is furthered increased, the magnitude of the local maximum increases rapidly and its location shifts also away from the stagnation point.

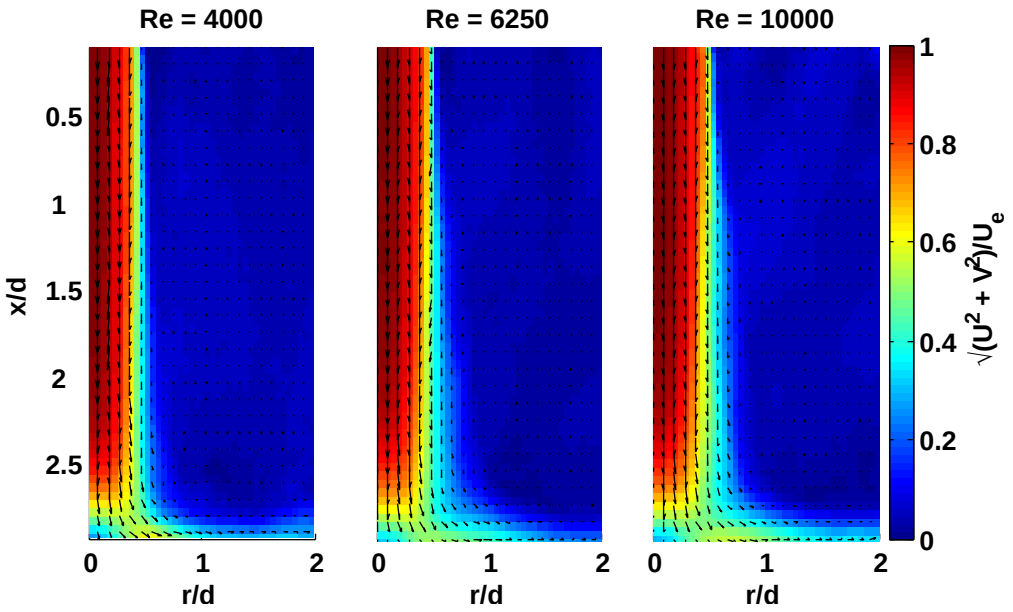

Figure 4.2: Effect of Re on the time-averaged velocity field

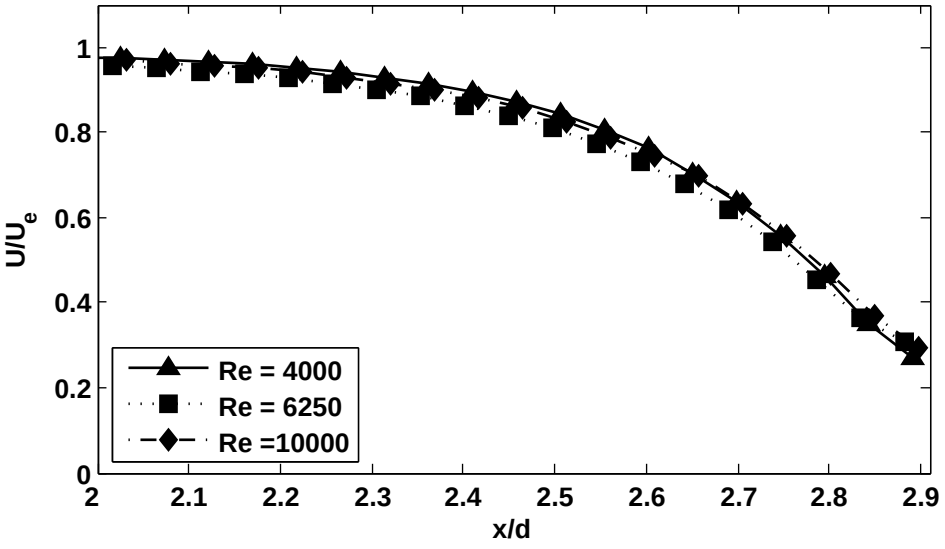

Figure 4.3: Centreline axial velocity decay

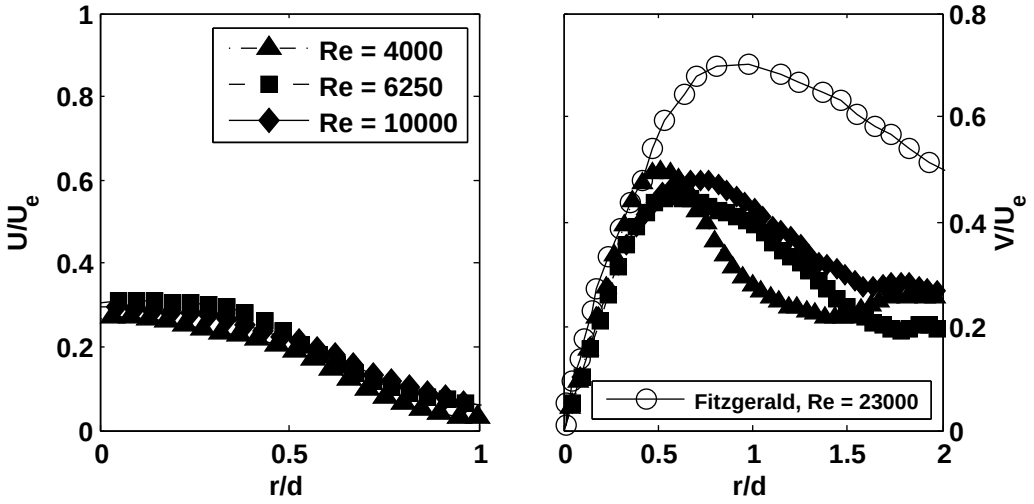

(a) x/d = 2.85

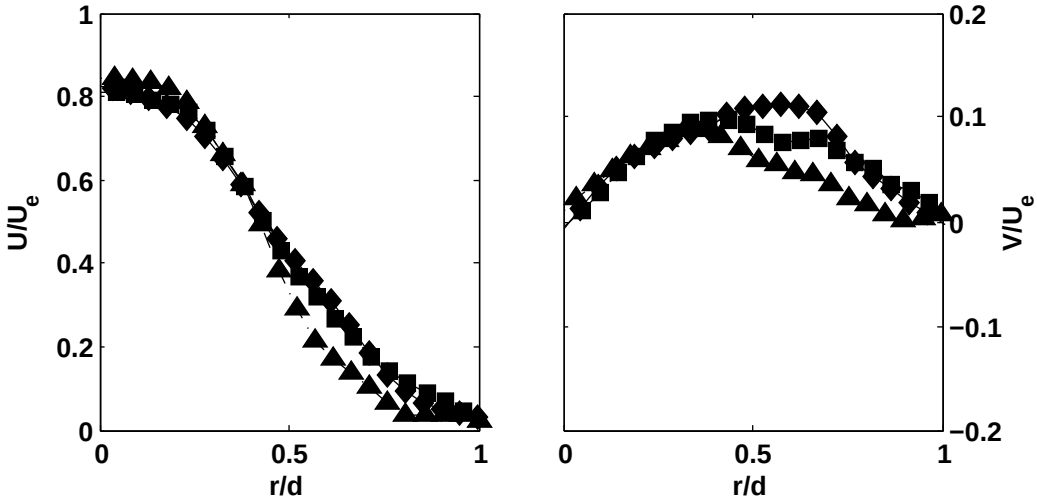

(b) x/d = 2.5

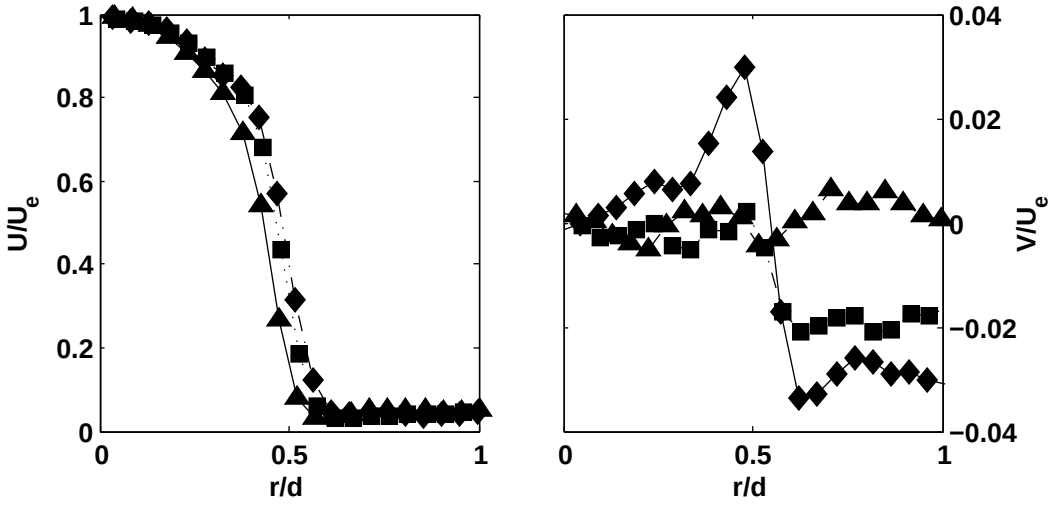

(c) x/d = 0.5

Figure 4.4: Radial profiles of mean axial (left) and radial (right) velocity components - Fitzgerald [9] ($Re = 23000$, $H/d = 3$)

Fig.4.4b shows profiles of the mean axial and radial velocity components at $x/d = 2.5$. At this location, the presence of the impinging wall has already affected the development of the jet (see Fig. 4.3 on page 64). The axial component profiles show that the jet spreads more rapidly as the Reynolds number is increased. This observation is confirmed by the profiles of the radial velocity. They show that as the Reynolds number increases, the magnitude of the radial component increases, and the location of the local maximum shifts away from the jet axis, from 0.085 at $r/d = 0.33$ ($Re = 4000$), to 0.096 at $r/d = 0.43$ ($Re = 6250$), to 0.112 at $r/d = 0.57$ ($Re = 10000$). The increase in the spread of the jet as the Reynolds number is increased could explain the shift of the local maximum of the radial component away from the stagnation point near the wall.

The radial profiles of the radial velocity component show that there is recirculation (negative values of V) present near the nozzle exit (Fig.4.4c), which becomes stronger as the Reynolds number is increased.

4.3.3 Velocity Fluctuations

In the study of jets it is customary to use the jet exit velocity (U_e) or the centreline velocity (U_c) to non-dimensionalise the velocity fluctuations root mean square. This give rise to two distinct non-dimensional quantities u'_{rms}/U_e and u'_{rms}/U_c. Although, commonly referred to as the turbulence intensity of the jet, these two non-dimensional quantities are not a good representation of the jet turbulent characteristics [79] [5]. Therefore, in order to avoid confusion, it is suggested in those studies to regard these quantities as either a measure of mixing or, alternatively, as a measure of the influence of the exit velocity[1] on the flow field. This implies that low values of these quantities indicate a stronger influence of the jet exit or centreline velocity. In the current study it was found that such interpretation only holds for locations within the jet but not at the far-field. At locations away from the jet, these quantities assume their traditional meaning, that is, the higher they are, the more turbulence is present. This is because, the jet exit velocity becomes analogous to the free stream velocity in turbulence studies of wall flows.

[1] When the exit velocity is used

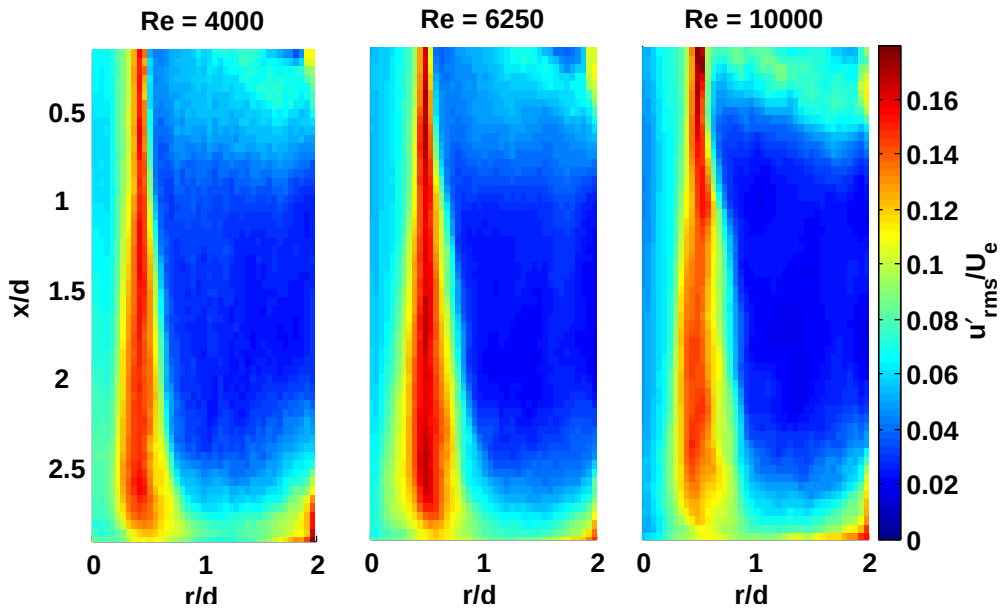

Figure 4.5: Effect of Reynolds number on the axial velocity fluctuations

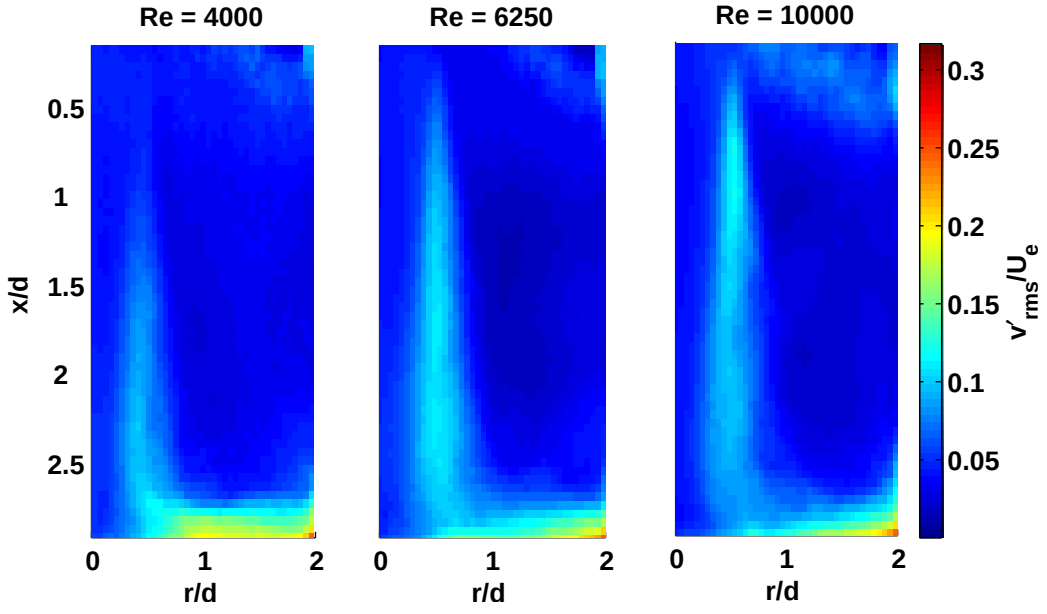

Figure 4.6: Effect of Reynolds number on the radial velocity fluctuations

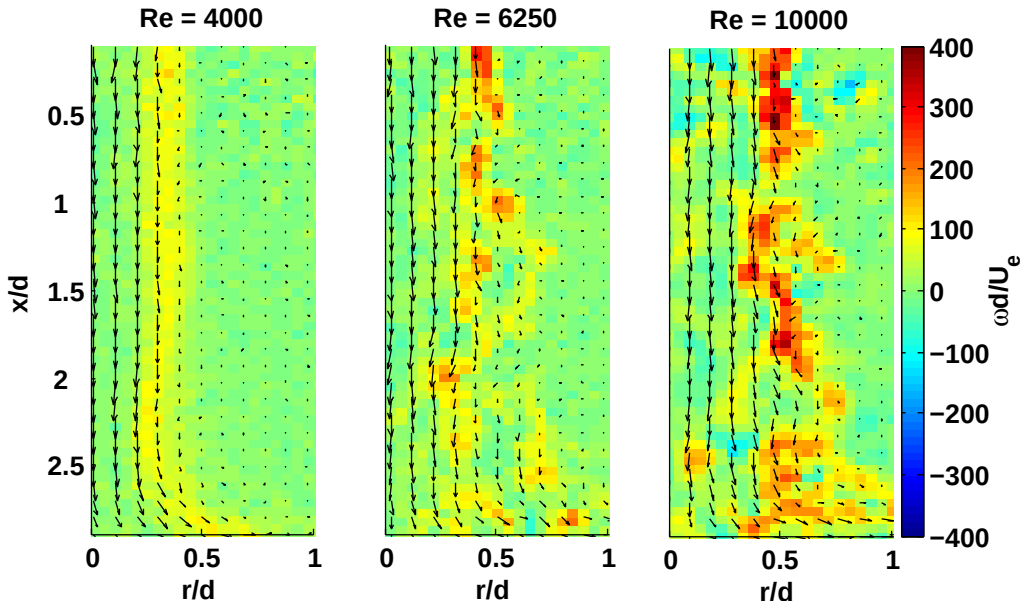

Figure 4.7: Instantaneous vorticity field for different Reynolds numbers ($H/d = 3$)

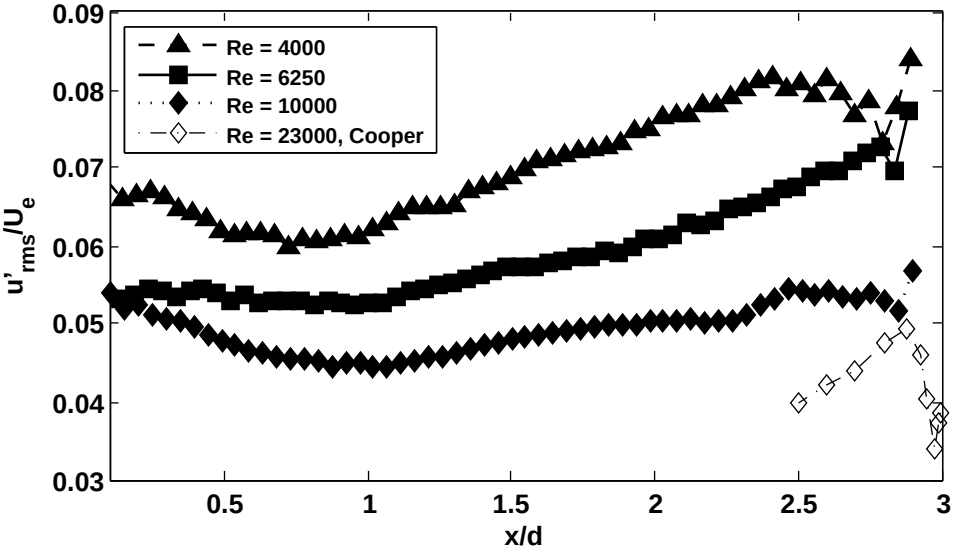

Figure 4.8: Effect of Reynolds number on centreline axial velocity fluctuations non-dimensionalised with nozzle exit velocity

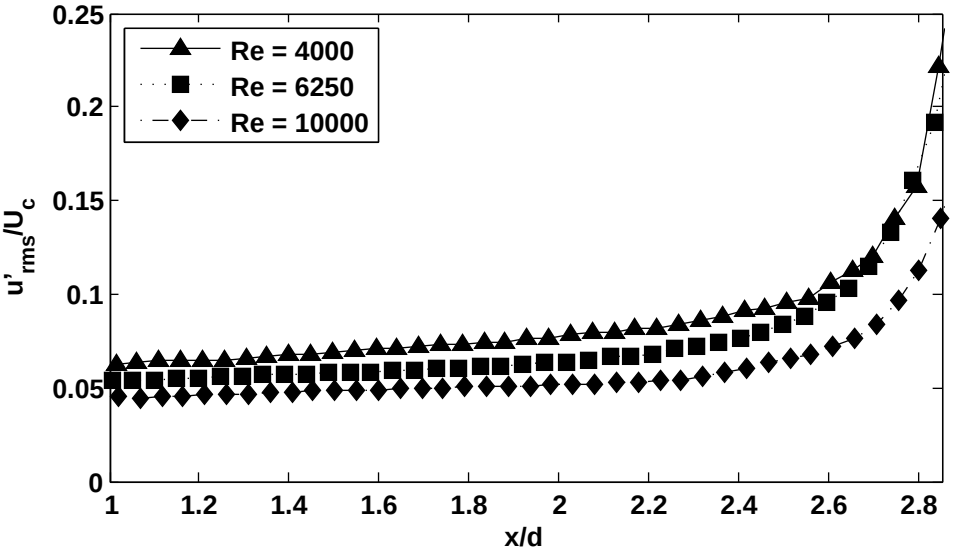

Figure 4.9: Effect of Reynolds number on centreline axial velocity fluctuations non-dimensionalised with nozzle centreline velocity

The whole-field axial velocity fluctuations are shown in Fig.4.5. It can be observed that as the Reynolds number is increased, the velocity fluctuations show an overall increase, with the exception of the jet with $Re = 6250$ which shows higher axial velocity fluctuations within the shear layer than the jet at $Re = 10000$. The increase of the axial velocity fluctuations, when the Reynolds number is increased from $Re = 4000$ to $Re = 6250$, can be attributed to the break up of the shear layer into turbulent eddies. Interestingly, the velocity fluctuations also show decreasing levels when the Reynolds number is further increased to $Re = 10000$. This decrease could be linked to the merging of individual eddies as the Reynolds number is increased to $Re = 10000$, as shown in Fig.4.7, which shows the vorticity field of the instantaneous velocity fields for the various Reynolds numbers. Finally, Fig.4.5 also shows that increasing the Reynolds number leads to an overall reduction in the axial velocity fluctuations towards the impinging wall ($2.5 < x/d < 2.8$). However, close to the target wall, the axial velocity fluctuations increase with the Reynolds number.

The radial velocity fluctuations are shown in Fig.4.6. This figure shows that as the Reynolds number is increased, there is a decrease in the radial velocity fluctuations near the impinging wall. It also shows a reverse effect of the Reynolds

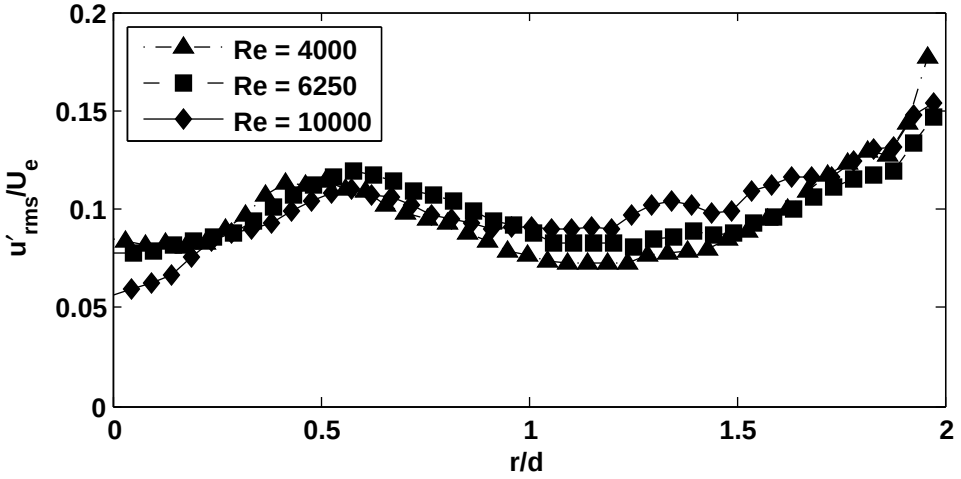

(a) x/d = 2.9

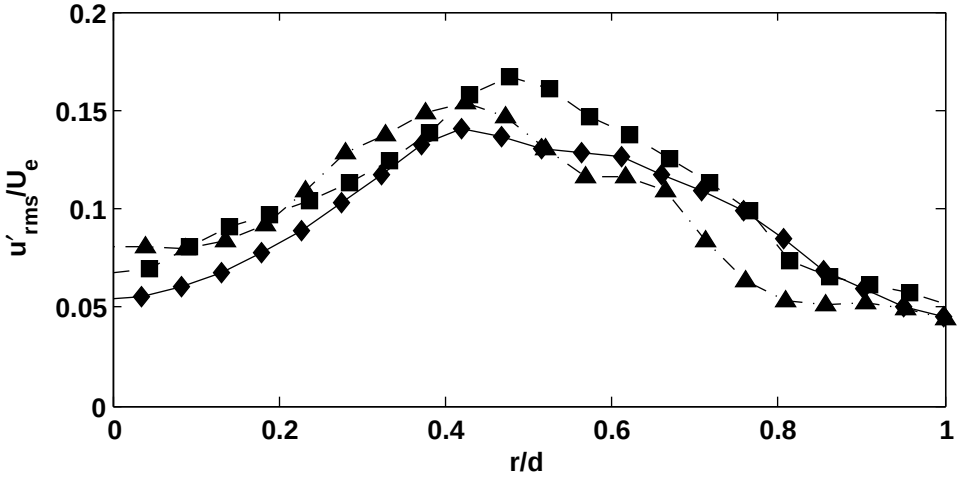

(b) x/d = 2.5

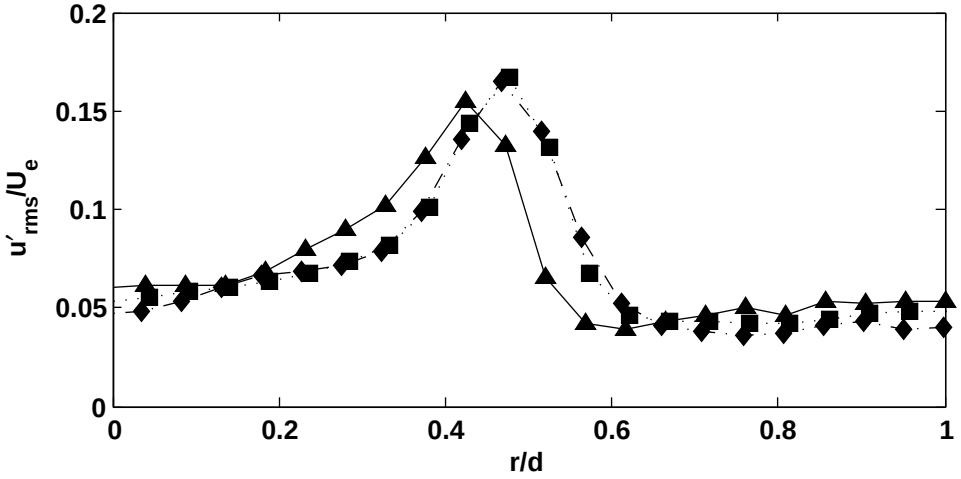

(c) x/d = 0.5

Figure 4.10: Radial profiles of axial velocity fluctuations

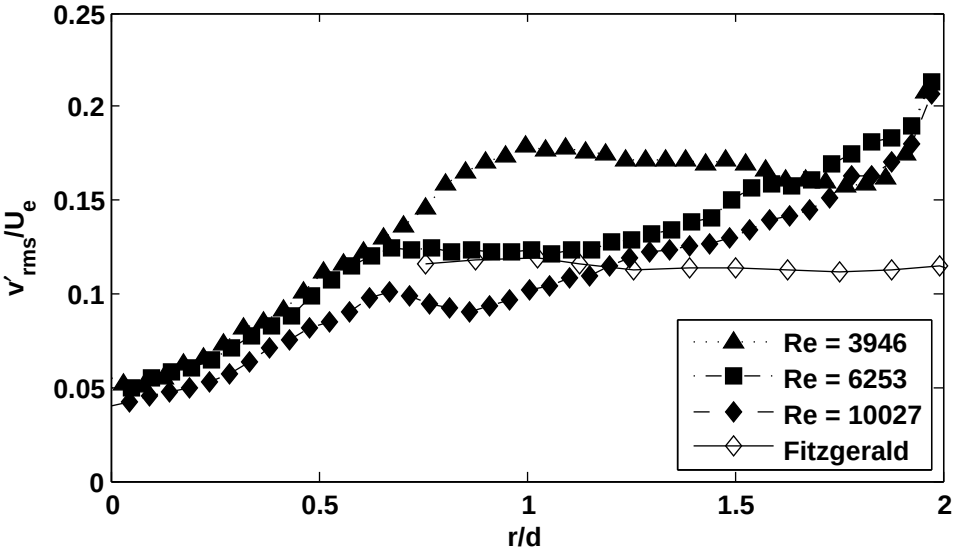

Figure 4.11: Effect of the Reynolds number on the radial velocity fluctuations near the impinging wall; Fitzgerald [9] ($H/d = 3$, $Re = 23000$)

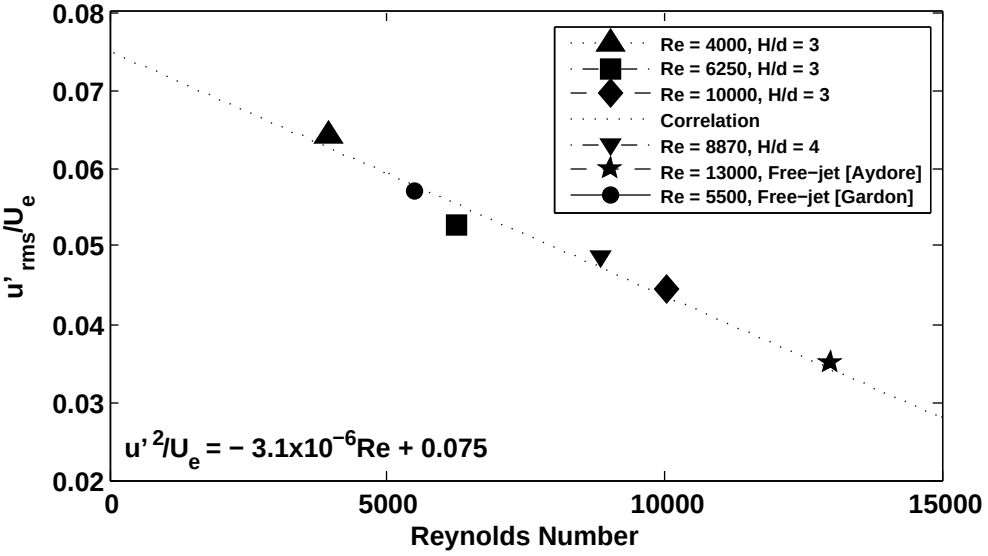

Figure 4.12: Correlation showing the effect of the Reynolds number at $r/d = 0$ and $x/d = 1$

number on the axial velocity fluctuations within the shear layer. However, for $Re = 6250$ the radial velocity fluctuations are larger than the jet with $Re = 10000$ for $1.5 < x/d < 2.75$.

The effect of the Reynolds number on u'_{rms}/U_e at the jet centreline is shown in Fig.4.8. It can be observed that the jet with the highest Reynolds number has lower values of the velocity fluctuations, this implies that as the Reynolds number is increased, there is less mixing at the jet centreline. If a jet is used in cooling or heating applications less mixing is desirable. If the jet exhibits mixing, then the temperature transfer is affected by entrainment of ambient fluid. Lower mixing at higher Reynolds numbers agrees with the observed increased rates of heat transfer at the stagnation point as the Reynolds number is increased [6]. Fig.4.8 also shows that there is a clear reduction in the u'_{rms}/U_e at the nozzle exit when the jet becomes turbulent. A similar trend is observed in Fig.4.9, which shows the centreline velocity fluctuations, this time non-dimensionalised using local mean centreline velocity, U_c. This figure does not provide additional information, due to the fact that non-dimensionalising with respect to the jet exit velocity is widely practised and frequently observed in the literature because it provides a measure of the effect of the exit velocity[2], the velocity fluctuations will be non-dimensionalised with respect to U_e in subsequent sections.

The radial profiles of the axial velocity fluctuations are shown in Fig.4.10. It shows that there is an increase in the velocity fluctuations at approximately $r/d = 0.5$ for all the different Reynolds numbers. This is representative of the presence of the jet shear layer. Near the jet exit (Fig.4.10c), at $x/d = 0.5$, the transitional jet ($Re = 4000$) shows lower mixing (lower value compared to the other jets). The profiles for the higher Reynolds numbers jets tend to collapse, with the exception of radial distances between $0.4 < r/d < 0.6$, which corresponds to the development of the shear layer. This indicates that once transition is no longer affecting the behaviour of the jet, the Reynolds number has little effect on the mixing characteristics of the jet.

Fig.4.11 shows the radial velocity fluctuations of the radial velocity component

[2]Impinging jets are mostly used for heat transfer applications, therefore, the main interest is to assess how the exit conditions reflect on heat transfer (fluid mechanics in this study)

near the impinging wall. It shows that the Reynolds number does not have a significant influence on the mean radial velocity fluctuations in the impinging region ($0 < r/d < 0.5$). However, in the region where the wall jet develops ($0.5 < r/d < 1.5$), the effect of the Reynolds number on the radial velocity fluctuations is similar to its effect on the axial velocity fluctuations, that is, the velocity fluctuations become smaller in comparison to the exit velocity as the Reynolds number is increased. This indicates a stronger influence of the exit velocity on the flow field as the Reynolds number is increased. Fig.4.11 also shows that for the transitional jet there is an increase in v'_{rms}/U_e for $0.6 < r/d < 1.6$. This increase in v'_{rms}/U_e could be a consequence of the rapid decrease in radial velocity present for such jet (see Fig.4.4a). This could be representative of a transitional wall jet or the presence of adverse pressure gradients. The results of Fitzgerald [9] for $Re = 23000$ and $H/d = 3$, show that for $r/d > 1.25$, further increases in the Reynolds number lead to even lower values of v'_{rms}/U_e. The presence of higher values of v'_{rms}/U_e for $0.75 < r/d < 1.25$ can be attributed to the smaller nozzle diameter used ($d = 6.35mm$). Fitzgerald [9] showed that larger diameters led to lower values of v'_{rms}/U_e.

The values of the axial velocity fluctuations at the centreline ($r/d = 0$) and at 1 diameter away from the nozzle exit are shown in Fig.4.12 for different Reynolds numbers, along with results from Aydore [46] and Gardon [79]. The correlation holds for Reynolds numbers ranging from 3500 (transitional) to 15000, as long as $H/d > 3$ (for fully developed exit profiles). The correlation to include higher Reynolds numbers would not be a simple straight line because for $Re > 20000$ the value of u'_{rms}/U_e tends to an asymptotic value of 0.01 [56][11]. The correlation is given by:

$$u'_{rms}/U_e = -1.3x10^{-6}Re + 0.075 \tag{4.1}$$

Fig.4.12 shows that impinging jets, near the nozzle exit, have similar velocity fluctuations to that of free jets. It also serves to validate the velocity fluctuation data presented in this work within the free jet region of the impinging jet. Finally, this figure also shows that as the Reynolds number is increased, the velocity fluctuations near the nozzle exit decrease which indicate less mixing in the axial

direction. This is typically the case within the core of the jet, which indicates an increasing influence of the jet exit velocity.

4.3.4 Turbulent Kinetic Energy

The mean turbulent kinetic energy is a quantity that measures the tendency of the flow to become more or less turbulent. The definition of the mean turbulent kinetic energy used in this work only includes the axial velocity fluctuations (u'), and the radial velocity fluctuations (v') because it was not possible to obtain measurements of the out-of-plane velocity fluctuations (w'). This was mentioned in section 3.2.4 on page 34.

The mean turbulent kinetic energy can be considered as measure of turbulence in the plane of symmetry of the jet. However, as already mentioned in section 4.3.3, in the context of jet impingement, it is more appropriate for it to be regarded as a measure of mixing which accounts for both u' and v'. The effect of the Reynolds number on the mean turbulent kinetic energy is shown in Fig.4.13. This figure, once again, confirms that the mixing on the shear layer of the jet with $Re = 6250$ is higher, even when compared to the jet with $Re = 10000$. It also shows that as the Reynolds number is increased, the wall jet exhibits lower levels of turbulent kinetic energy, i.e. there is less mixing near the impinging plate relative to the exit velocity. This is linked to higher rates of heat transfer as the Reynolds number is increased since less of the initial thermal conditions are lost to the surrounding fluid. The increase of heat transfer as the jet Reynolds number increases is well documented in the literature [6].

Fig.4.14 shows radial profiles of the mean turbulent kinetic energy near the impinging wall. It shows that for all the different Reynolds numbers there is a steady increase in the mean TKE for $0 < r/d < 0.6$. However, for $r/d > 0.6$, the mean TKE of the transitional jet continues to rise until $r/d \approx 1.7$, where all profiles coincide. The most significant differences on the mean TKE profiles are in the range, $0.6 < r/d < 1.7$, where the wall jet is developing. For this range of r/d, the effect of the Reynolds number is to reduce the mean TKE as it increases.

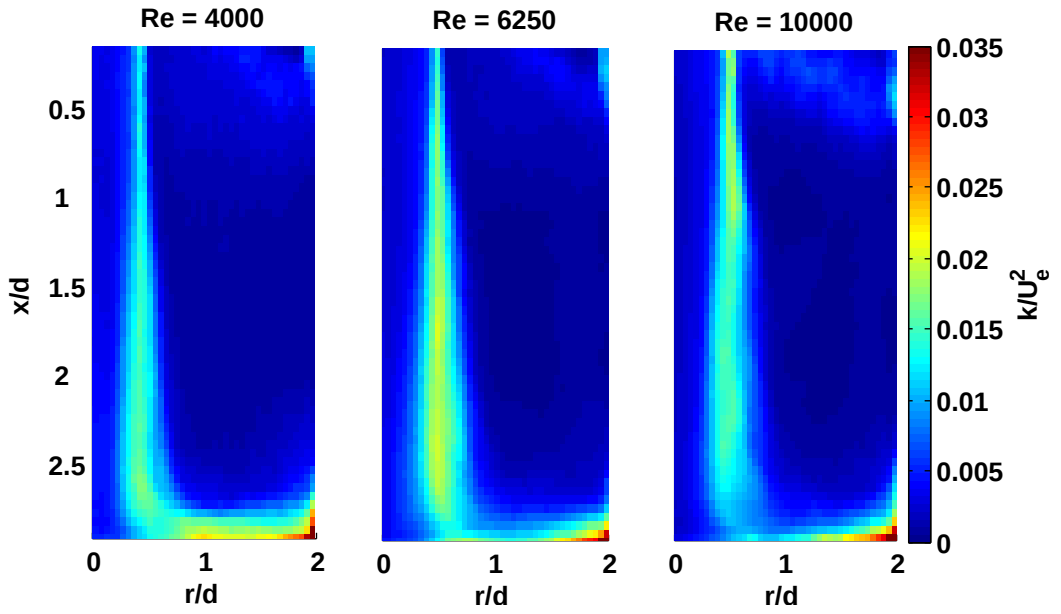

Figure 4.13: Effect of the Reynolds number of the mean turbulent kinetic energy

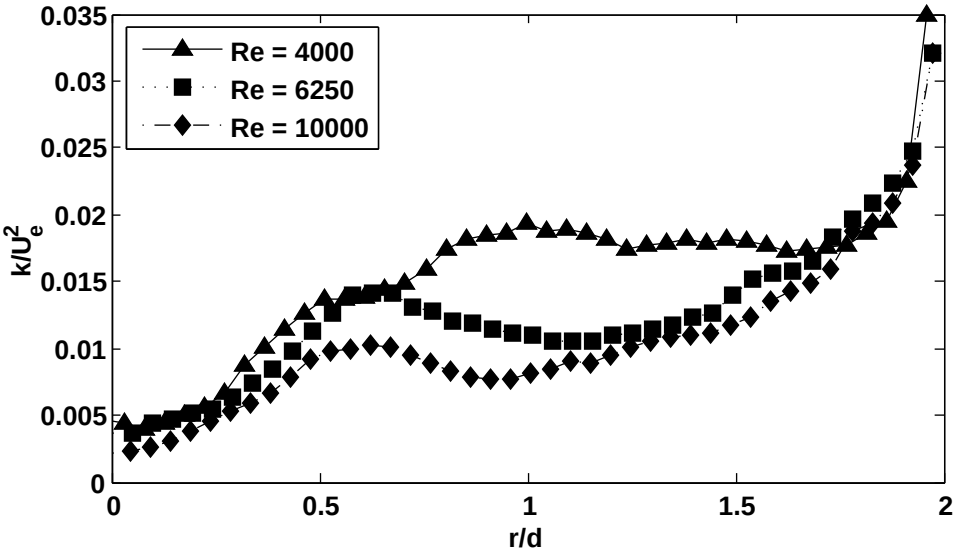

Figure 4.14: Effect of the Reynolds number of the mean turbulent kinetic energy near the impinging wall ($x/d = 2.85$)

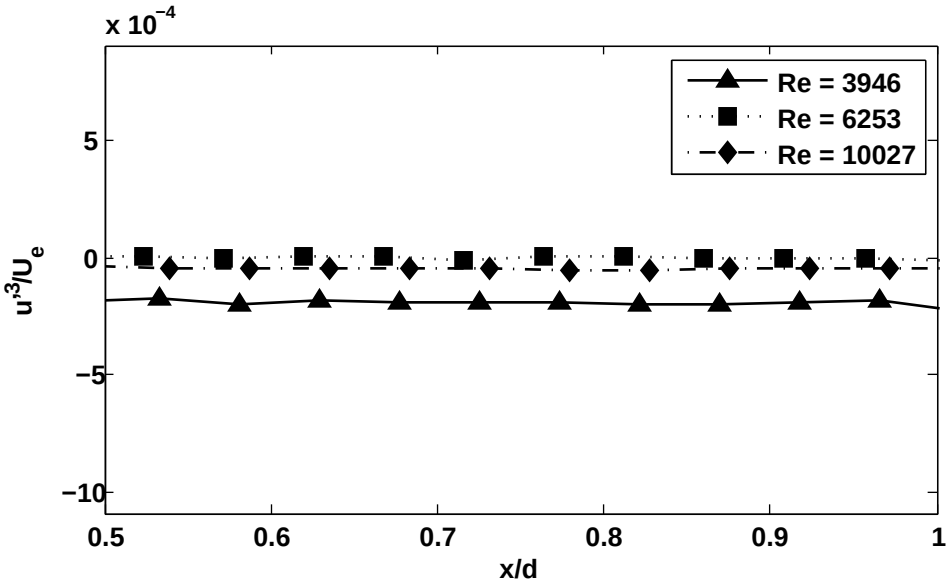

Figure 4.15: Effect of the Reynolds number on the centreline skewness factor in the axial direction

4.3.5 Skewness Factor

This section will present the skewness factor of the jet at different Reynolds numbers in an attempt to further investigate its effects on the flow field. In section 4.2, it was shown that the velocity data near the nozzle exit follows a normal distribution. The skewness factor is related to the concept of skewness, in the sense that they represent a measure of how the data is distributed (tails of the normal distribution). Positive values of the skewness factor indicate that the velocity data collected at a given location falls in the upper bound of the local mean, and viceversa. In the present study, the skewness factor is non-dimensionalised with respect to the exit velocity in order to assess the deviation of the local velocity distribution relative to the exit velocity. Considering that the velocity distribution near the exit can be assumed to be normally distributed, the skewness factor can be regarded as an indication of local turbulent acceleration or deceleration[3] due to fluidic interactions. Fig.4.15 demonstrates that the jet centreline values of

[3]Skewness factor is not a measure of acceleration or deceleration, rather, an indication of the presence of fluidic interactions that lead to a deviation from a normal distribution. The terms turbulent acceleration and deceleration are used to indicate positive and negative values of the skewness factor respectively, which indicates whether the time-averaged turbulent component falls above or below the local mean

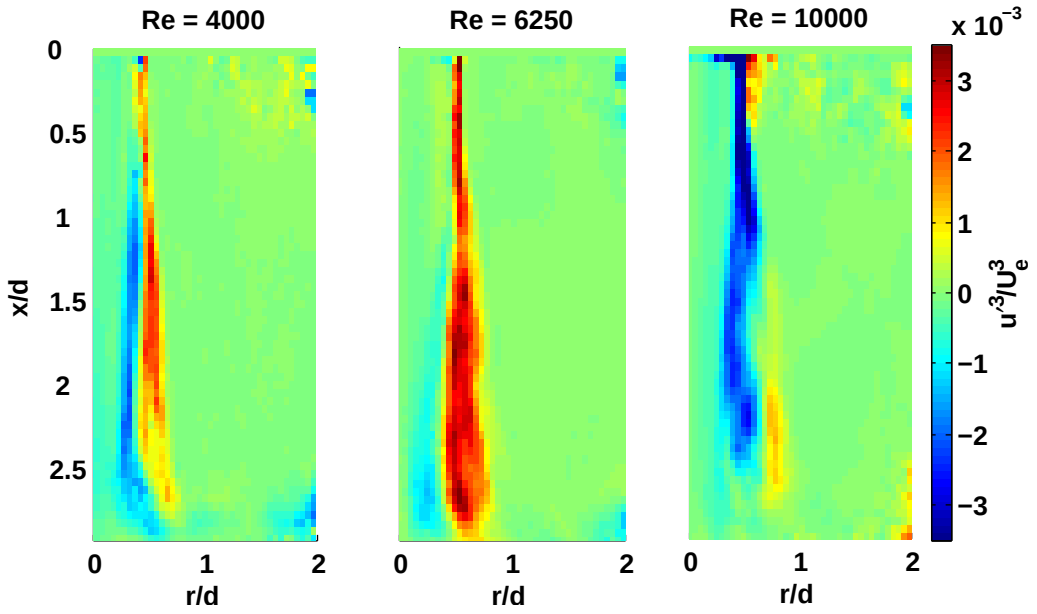

Figure 4.16: Effect of the Reynolds number on the skewness factor in the axial direction

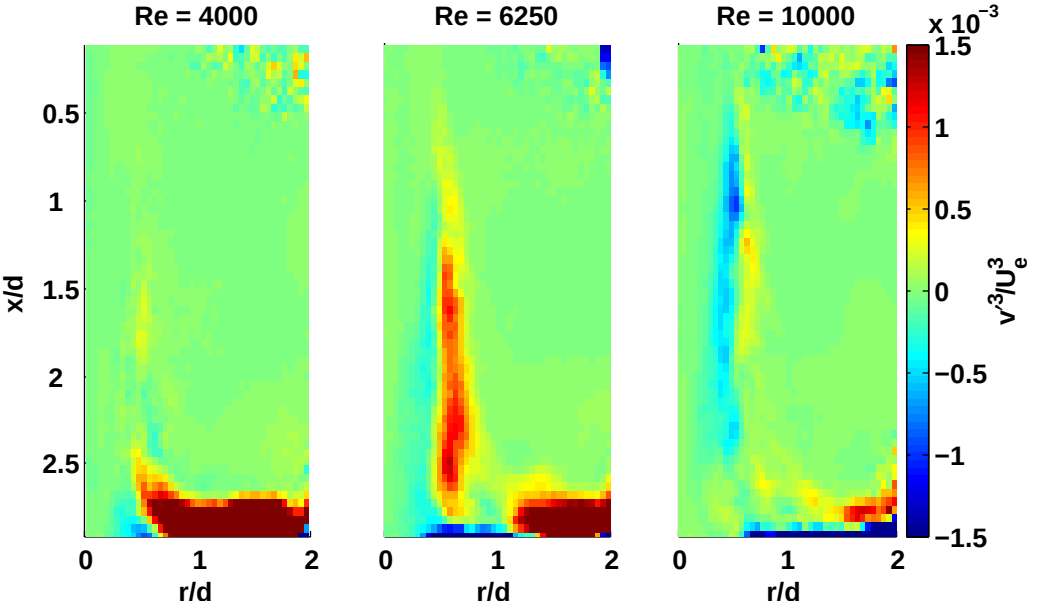

Figure 4.17: Effect of the Reynolds number on the skewness factor in the radial direction

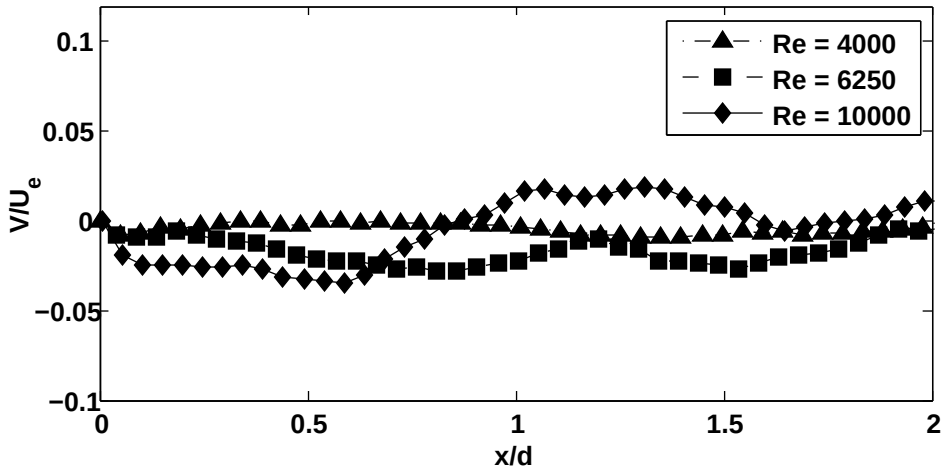

Figure 4.18: Axial development of the time-averaged radial velocity component ($r/d = 0.6$)

the skewness factor near the nozzle exit is negligible, this validates the assumption of a normal distribution at the nozzle exit. Additionally, normal plots of the velocity data are shown in appendix F on page 232. Furthermore, the information obtained from the skewness factor provides an insight for the analysis of the Reynolds stress in subsequent sections since they indicate the direction of the axial and radial turbulent velocity components.

The whole-field axial and radial skewness factor is shown in Fig.4.16 and Fig.4.17 respectively. Fig.4.16 shows that for the low Reynolds number case ($Re = 4000$), the shear layer is balanced, the blue side represents turbulent deceleration on the inside of the jet, which is balanced by turbulent acceleration in the axial direction in the outer region of the shear layer ($r/d > 0.5$). In contrast, as the Reynolds number is increased, this balance is disturbed. For $Re = 6250$, the inner region of the shear layer shows lower values of u'^3/U_e^3 than expected. This suggests that, at the outer region of the shear layer, the flow in the axial direction experiences velocity bursts towards the wall. As the Reynolds number is further increased to 10000, there is a sudden reduction in the values of u'^3/U_e^3 within the shear layer which indicate an increase in turbulent deceleration within the shear layer. In addition, in the outer region of the shear layer, there is virtually no sign of turbulent acceleration which was exhibited by lower Reynolds number jets. Even though the jet is transitional at $Re = 3946$, the skewness factor

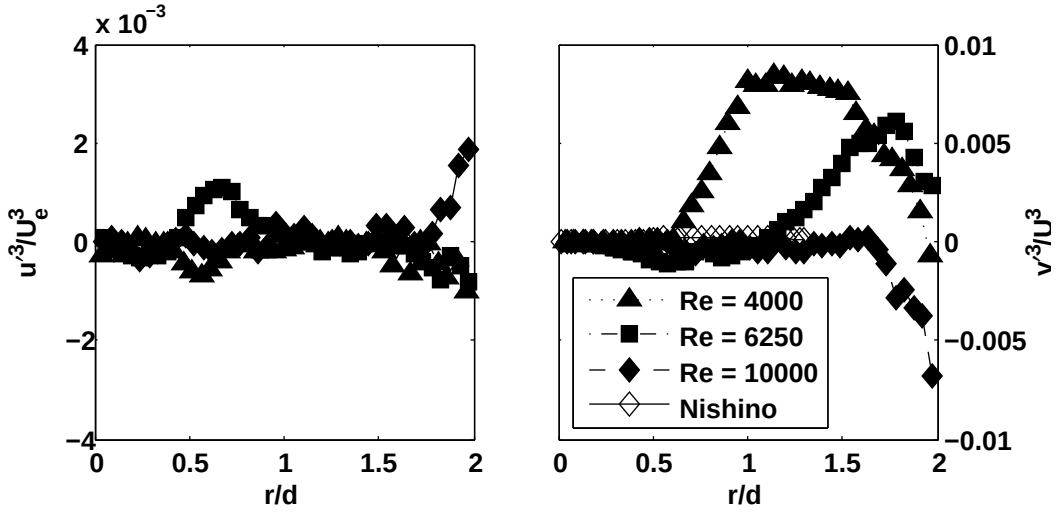

(a) x/d = 2.9

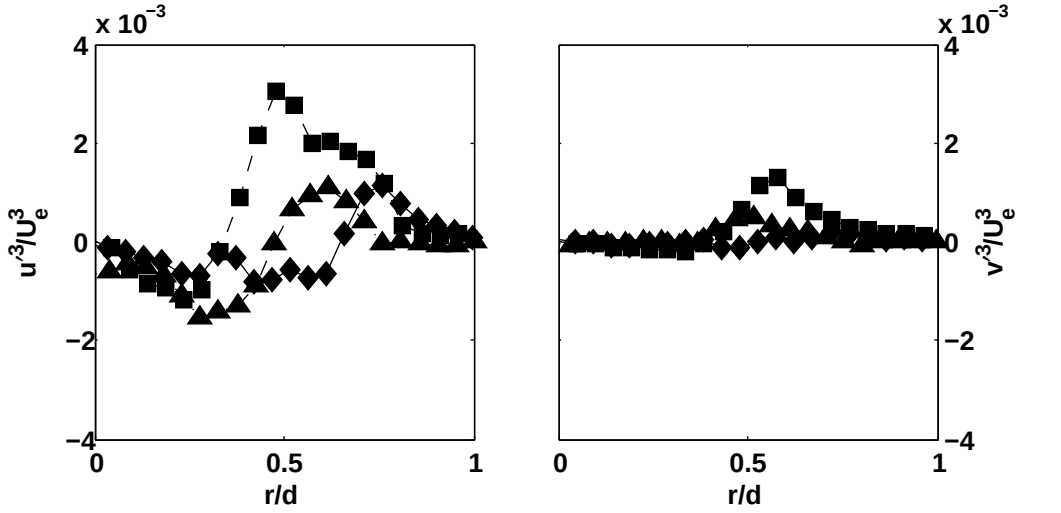

(b) x/d = 2.5

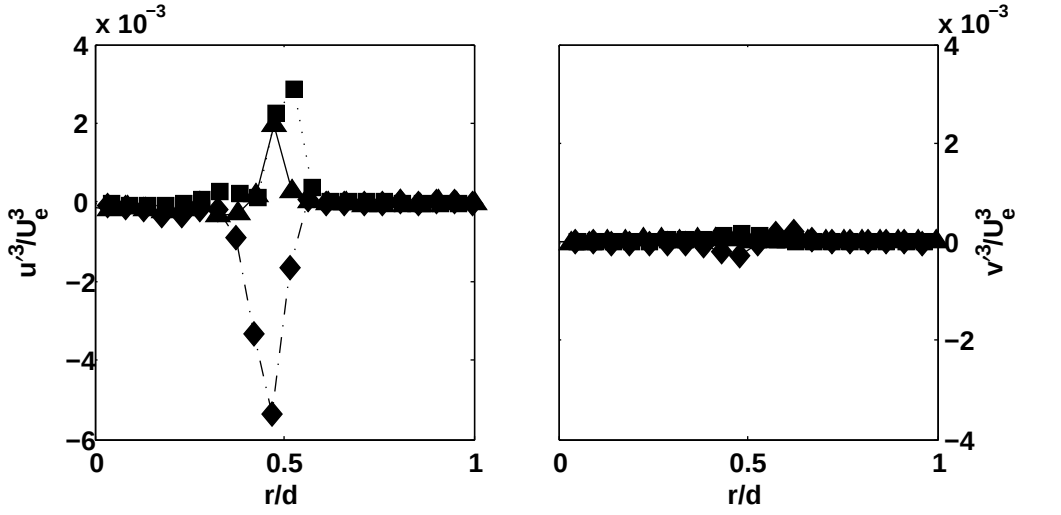

(c) x/d = 0.5

Figure 4.19: Radial profiles of the axial (left) and radial (right) skewness factor at different axial locations; Nishino [10] ($Re = 13000$,$H/d = 6$)

indicates that the shear layer is balanced. However, for $Re = 6250$ this balance is only disturbed moderately. In addition, within the shear layer, the values of u'^3/U_e^3 show a distinct unbalance when the Reynolds number is further increased to $Re = 10000$. Observing the plot for $Re = 10000$, it can also be noticed that there is a positive region of $u'^3/{U_e}^3$ near the nozzle exit, probably caused by recirculation effects. The presence of recirculation is shown in Fig.4.18, which illustrates the axial development of the time-averaged radial velocity component at $r/d = 0.6$. The positive values of u'^3/U_e^3 present near the nozzle exit, suggest that flow recirculation could be responsible for disturbing the jet exit conditions, leading to the formation of turbulent eddies (Fig. 4.7 on page 68). The presence of turbulent eddies would explain the negative values of u'^3/U_e^3 for $Re = 10000$. Furthermore, Fig.4.17 shows that as the Reynolds number is increased, there is a decrease in magnitude of the positive values of v'^3/U_e^3 near the impinging wall and an increase in the magnitude of the negative values. It also shows that for $Re = 4000$ the values of v'^3/U_e^3 in the shear layer are negligible. As the Reynolds number is further increased to $Re = 6250$, there is a sharp increase of v'^3/U_e^3 at the outer region of the shear layer for $1.25 < x/d < 2.7$. In contrast, for $Re = 10000$ there is a decrease in the values of v'^3/U_e^3 in the inner region of the shear layer for $0.6 < x/d < 2.2$. Interestingly, the locations where v'^3/U_e^3 begin to exhibit changes in the shear layer ($x/d \approx 1.25$ and $x/d \approx 0.6$) also correspond to changes in the development of the mean radial velocity component at $r/d = 0.6$. Fig.4.18 shows that for $Re = 6250$, the mean radial velocity component experiences a second reduction in magnitude at $x/d \approx 1.25$. However, for $Re = 10000$, the radial velocity experiences increases at $x/d \approx 0.6$. This suggests that a local increase in velocity leads to negative values of the skewness factor, whereas a reduction in velocity leads to positive values. Therefore, negative values of v'^3/U_e^3 can be regarded as an indication of a local resistance to flow, whereas, positive values indicate positive turbulent bursts in the direction of the flow.[4].

Fig.4.4a showed that for the jet with the lowest Reynolds number, there was rapid decrease in the mean radial velocity component once it reached its maximum

[4]This interpretation of the skewness factor is only valid for the coordinate system used in this study

value. Fig.4.19a shows that this rapid decrease in velocity is translated into turbulent acceleration in the radial direction. It also shows that v'^3/U_e^3 decreases as the Reynolds number is increased. Furthermore, as the Reynolds number is increased to 10240, Fig.4.19a suggests that, as the wall jet develops, there is a local resistance to flow in the radial direction for $r/d > 1.5$. Fig.4.19a also shows the skewness factor obtained by Nishino [10] for a jet located at $H/d = 6$ with $Re = 13000$. It shows that the values of the skewness factor, for their jet and the jet with $Re = 10000$, are in agreement despite the difference in Re and H/d. Fig.4.19c shows that the jet with $Re = 6250$ exhibits a positive peak of u'^3/U_e^3. However, for $Re = 10000$, a negative peak is present. Furthermore, the transitional jet ($Re = 4000$) exhibits a double peak, one negative and one positive, again, indicating the unbalancing effect of the Reynolds number on the distribution of the axial skewness factor within the jet shear layer as it is increased. Fig.4.19a shows that near the impinging wall, the magnitude of u'^3/U_e^3 is lower than v'^3/U_e^3 by a factor of 10. This indicates that near the wall, the contribution to the Reynolds stress is mainly influenced by the radial velocity fluctuations, in contrast, from the nozzle exit to up to $x/d = 2.5$ (Fig.4.19b), the contribution to the Reynolds stress is dominated by the axial velocity fluctuations. Finally, at $x/d = 0.5$, Fig.4.19a shows that, near the nozzle exit, the jet with lower Reynolds numbers exhibit positive values of u'^3/U_e^3. However, for $Re = 10000$, there is only a negative peak present. Therefore, there must be value for the Reynolds number at which u'^3/U_e^3 becomes negative and must be located in the range $6253 < Re_r < 10027$.

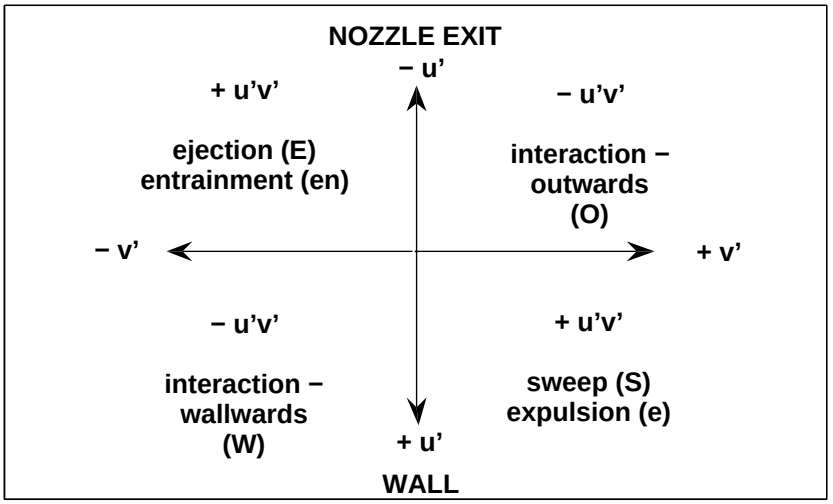

Figure 4.20: Sign convention for the Reynolds stress

4.3.6 Reynolds Stress

The effect of the Reynolds number on the Reynolds stress ($u'v'$) will be presented in this section. The Reynolds stress are a measure of the net transfer of momentum across a surface due to fluctuations in fluid velocity. They are also referred to as eddy stresses. The analysis of the Reynolds stress presented in this study is based on the work of Wallace [80]. The results obtained for the skewness factor (previous section) will be utilised in order to assess the contribution of the velocity fluctuations to the Reynolds stress. Also, their sign will be used in order to classify the Reynolds stress according to their physical significance. The classification of the Reynolds stress used in this study is shown in Fig.4.20. The notation shown makes a distinction of the Reynolds stress by the use of lower case letters and capital letters to indicate shear layer stresses and wall jet stresses respectively. This distinction is necessary due to the fact that the flow changes direction, from the initial streamwise direction, to the wall jet region developed upon impingement. The border for the wall jet region chosen was 0.5 diameters from the wall (use of capital letters). In addition, within the shear layer, two types of Reynolds stress were observed which are both positive. Firstly, both u' and v' being negative which is representative of entrainment (en). Secondly, both being positive which indicates turbulent expulsion (e). Within the wall jet, four

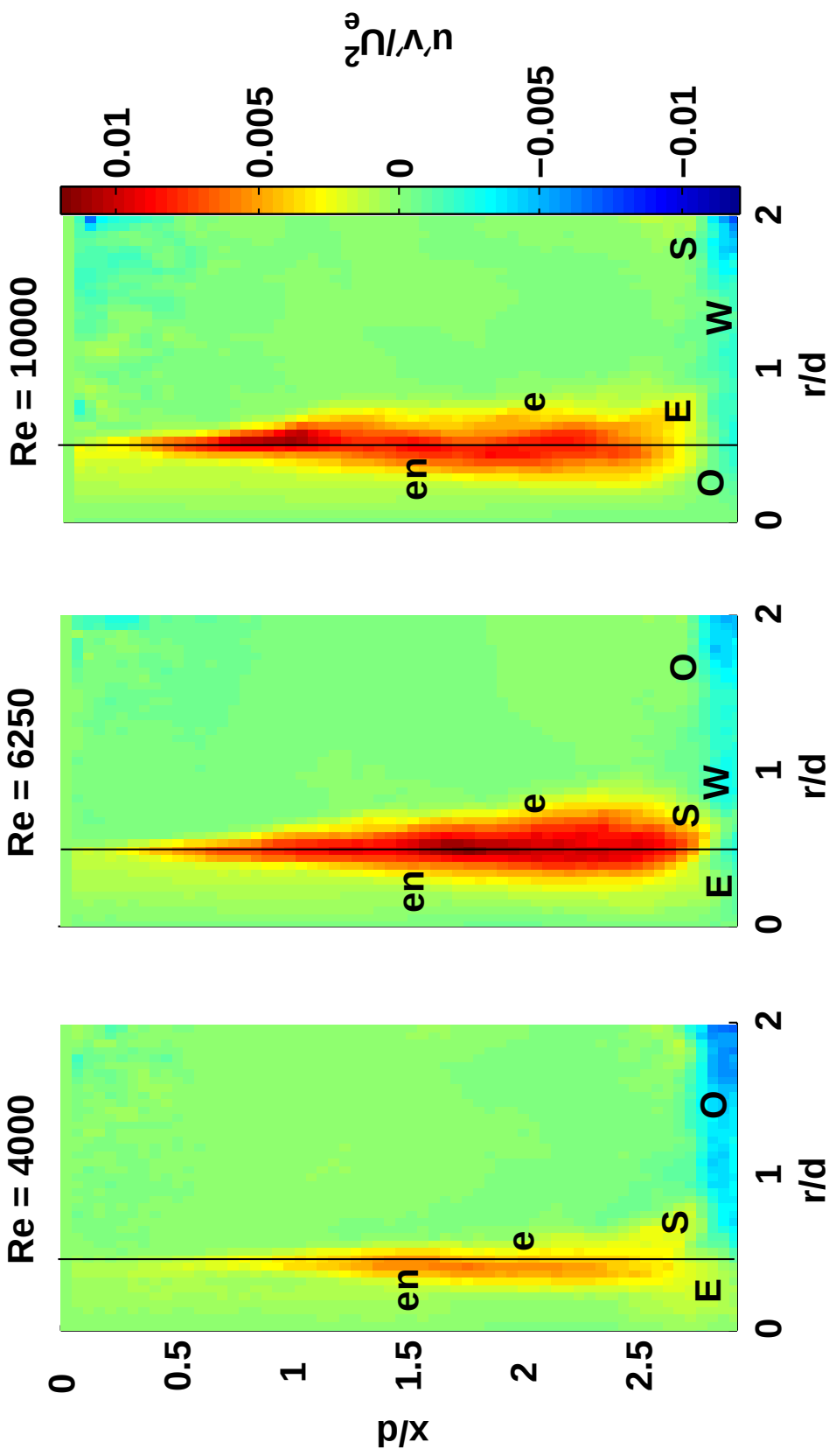

Figure 4.21: Effect of the Reynolds number on the Reynolds stress; entrainment (en), expulsion (e), ejection (E), sweep (S), wallward interaction (W), outward interaction (O)

distinct patterns for the Reynolds stress are observed, two of which lead to positive values of $u'v'$, whereas, the remaining two lead to negative values. Positive values of $u'v'$ are generated when both u' and v' are either positive of negative. If u' and v' are positive they produce a sweep-type motion (S), however, if they are both negative they produce an ejecting effect (E). The two remaining types of Reynolds stresses are negative. The first is generated when u' is positive and v' negative, which are linked to low-speed fluidic interactions reflected towards the wall (W). In contrast, when u' is negative and v' positive their corresponding Renolds stresses are linked to high-speed fluidic interaction outwards from the wall (O).

The effect of the Reynolds number on the Reynolds stress is shown in Fig.4.21. This figure shows that as the Reynolds number is increased, there is also an increase in the entrainment product of the Reynolds stress along the shear layer of the jet. However, for $Re = 6250$ the expulsion (e) maximum occurs at $1.25 < x/d < 2$, whereas, for $Re = 10000$ this maximum is located in the region $0.6 < x/d < 1$. This increase in the Reynolds stress at such locations is linked to the effects of recirculation observed in the previous section, suggesting a significant effect of recirculation on behaviour of the shear layer. Its influence is such that, the expulsion Reynolds stress (e) are larger for $Re = 6250$ than $Re = 10000$ at $x/d > 1.5$. This is in line with the observation that the recirculation affected the shear layer of the jet with $Re = 6250$ at axial locations father away from the nozzle exit, which led to higher values of the skewness factor as shown in Fig.4.19b. Fig.4.21 also shows that the distribution of the Reynolds stress is drastically affected by the Reynolds number near the wall. For the lower Reynolds numbers the Reynolds stress exhibit turbulent ejection (E) in regards to the wall or entrainment (en) in regards to the shear layer notation. However, for $Re = 10000$ the Reynolds stress exhibit high-speed outward interactions. This indicates that as the Reynolds number is increased the shear layer penetrates the wall further, leading to the elimination of entrainment Reynolds stress (en) from stagnation point to $r/d \approx 0.5$. The development of the wall jet is also affected by the Reynolds number. For instance, for both $Re = 4000$ and $Re = 6250$, there are sweeping Reynolds stress present in the outer region of the shear layer as it

approaches the wall, however, for $Re = 10000$ there is ejection (E) present instead, probably due to the fact that the wall jet becomes stronger as the Reynolds number is increased (Fig. 4.2 on page 64), therefore, the flow experiences increased "resistance", which in turn leads to turbulent deceleration in both u' and v'. In the wall jet region, for $Re = 4000$, the Reynolds stress are mainly due to high-speed outward fluidic interactions. As the Reynolds number is increased, there are low-speed Reynolds stress directed towards the wall instead. However, for $Re = 6250$ there are outwards interactions present for $r/d > 1.5$, whereas, for $Re = 10000$ sweeping Reynolds stress are present instead, which have a wallwards direction. This indicates momentum transfer towards the wall, which implies that the fluid within the wall jet for $Re = 10000$ has a tendency to stay closer to the wall.

4.3.7 Mean Axial Momentum Balance Near the Wall

The mean axial momentum balance near the impinging wall was calculated using equation 4.2 as suggested by Nishino [10]. Their work also suggests that when pressure readings are not available, the pressure term can be calculated as residual, in addition, they found the viscous term to be negligible and was therefore omitted.

$$\underbrace{V\frac{\partial U}{\partial r}}_{\text{radial diffusion}} + \underbrace{U\frac{\partial U}{\partial x}}_{\text{axial convection}} + \underbrace{\frac{\partial(r\overline{u'v'})}{r\partial r}}_{\text{Reynolds stresses}} + \underbrace{\frac{\partial\overline{u'^2}}{\partial x}}_{\text{normal stresses}} + \underbrace{\frac{\partial P}{\rho\partial x}}_{\text{pressure}} = 0 \tag{4.2}$$

The momentum balance near the impinging wall for the different Reynolds numbers tested is shown in Fig.4.22. It shows that regardless of the Reynolds number, the main source terms are the axial convection and the radial diffusion, and their momentum is converted to static pressure. The contribution of the axial convection is a consequence of the deceleration of the axial mean velocity component towards the impinging wall. Overall, it can be observed, that the Reynolds number does not have a significant influence on the distribution of the momentum balance near the wall. However, as the Reynolds number is increased, the profile of the static pressure momentum becomes flatter, as a consequence of

a prolonged contribution from the radial diffusion, which is caused by the development of a stronger wall jet as the Reynolds number is increased, as seen previously. Finally, the results obtained from Nishino [10] are also shown. They correspond to a jet being discharged from a nozzle with a smooth contraction, which has a flat velocity profile at the exit. The Reynolds number for this jet is $Re = 13000$, and $H/d = 5.86$. It can be observed that the profile of the static pressure term is even flatter for this jet, confirming the previous observation on the effect of the Reynolds number. However, for this jet, the turbulent normal stresses are a significant source term, which was attributed to the fact that the jet is still developing at larger axial distances from the nozzle as a result of a flat exit velocity profile [10]. The main implication is that there is a substantial momentum transport from the turbulent field to the mean field, which is not present for jets with a fully developed exit profile. This could could be an indication that jets with fully developed exit profiles maintain their momentum transport within the mean field more efficiently.

4.3.8 Power Spectrum Analysis

The frequency content embedded within the vorticity signal at the shear layer ($r/d = 0.5$) and relatively close to the nozzle exit ($x/d = 0.5$) for the various Reynolds numbers has been determined. The power spectral density of the vorticity signal will help identify the presence of any periodical events occurring at this location, as well as, the effect of the Reynolds number on the formation of such structures. The Power Spectral Density (PSD) was obtained using the Matlab® PWELCH function on the time-resolved vorticity signal computed from the PIV vector field. The PWELCH function computes the Power Spectral Density (PSD) estimate of a discrete-time signal vector X using Welch's averaged periodogram method, and the resulting PSD is the distribution of power per unit frequency. The averaging process is carried out by dividing the signal into 8 equal segments of 512 elements and using a Hamming window with a 50% overlap between windows.

The PSD for the various Reynolds numbers is shown in Fig. 4.23. In this figure, the y-axis, as already mentioned, represents the Power Spectral Density

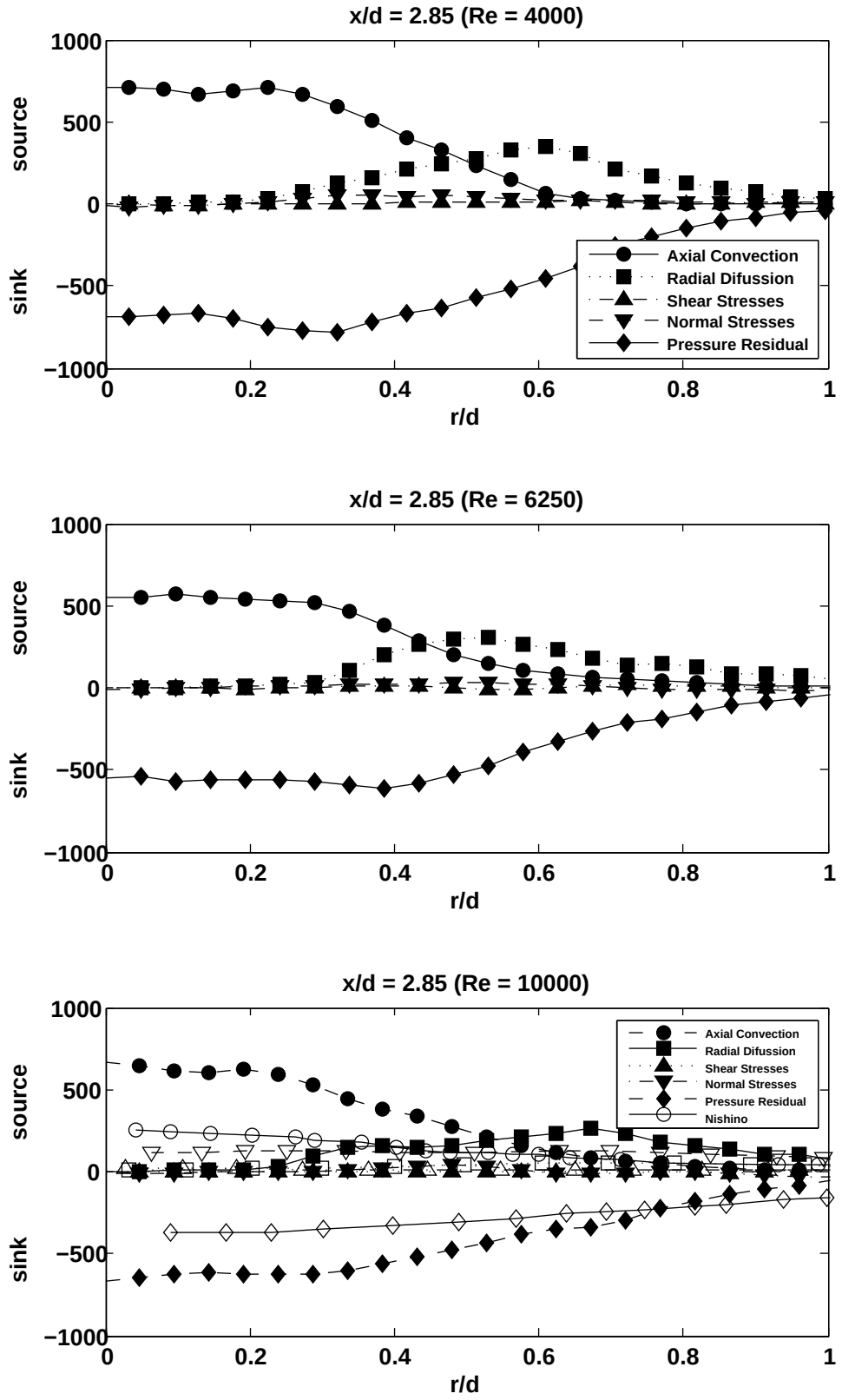

Figure 4.22: Effect of the Reynolds number on the mean axial momentum balance ($x/d = 2.85$) non-dimensionalised by d/U^2; open symbols - Nishino [10] ($Re = 13000$, $H/d = 5.86$)

(PSD) in terms of power per unit density, on the other hand, the x-axis represents the non-dimensional frequency given by $\hat{f} = fd/U_e$. As it can be observed from Fig. 4.23, for the lower Reynolds numbers, the dominating frequencies are $\hat{f} \approx 0.25$ and $\hat{f} \approx 0.175$ for $Re = 4000$ and $Re = 6250$ respectively. However, as the jet Reynolds number is further increased, and the jet becomes fully turbulent, the dominating frequency increases to approximately $\hat{f} = 0.75$. Furthermore, from a direct observation of the vorticity field of the jets, the presence of Kelvin-Helmholtz-like instabilities can be easily identified, suggesting that the shedding of small-scale vortices occurs at $St = 0.25$, $St = 0.175$ and $St = 0.75$ for $Re = 4000$, $Re = 6250$ and $Re = 10000$ respectively. Finally, in the next chapter the presence of a critical pulsating Strouhal number is observed (see chapter 5). The critical Strouhal number for the transitional pulsed jet was $St_c = 0.25$, whereas, for the turbulent pulsed jet it was $St_c = 0.1$. Whenever the jet is pulsed below and/or above these Strouhal numbers, the fluid mechanics of the jet change considerable, in addition, when the jet is pulsed at frequencies close to St_c, the jet exhibits a behaviour similar to its steady jet counterpart. Interestingly, Fig. 4.23 shows that in the case of the transitional pulsed jet, St_c corresponds to the peak of the fundamental non-dimensional frequency, however, for the turbulent pulsed jet, St_c corresponds to the 8^{th} subharmonic of the fundamental frequency which is approximately $\hat{f}_{\frac{1}{8}} = 0.09$. This finding suggests that when the pulsing frequency of a jet is locked to the equivalent fundamental (transitional jet) and 8^{th} subharmonic (turbulent) such pulsed jet will exhibit similar turbulence statistics compared to its steady counterpart. Unfortunately, the amount of data obtained in this work does not allow to compute the PSD of the vorticity signal with better resolution. Finally, in order to fully understand the relationship between the natural shedding frequency of Kelvin-Helmholtz instabilities of the steady jet and the forced frequency of pulsed jets, further studies are necessary and larger data sets are required.

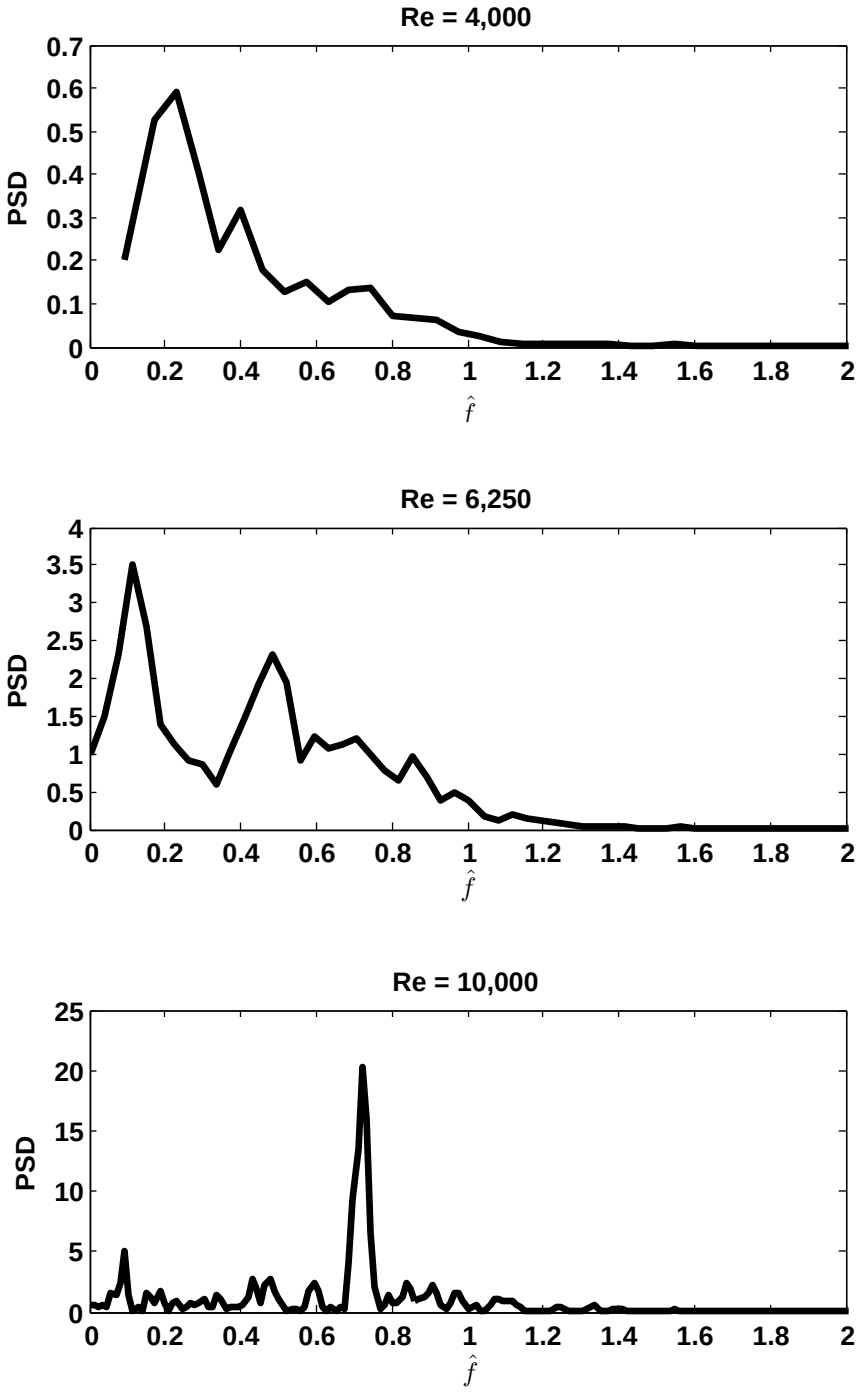

Figure 4.23: Power spectrum of vorticity signal within the shear layer ($r/d = 0.5$) and near the nozzle exit ($x/d = 0.5$)

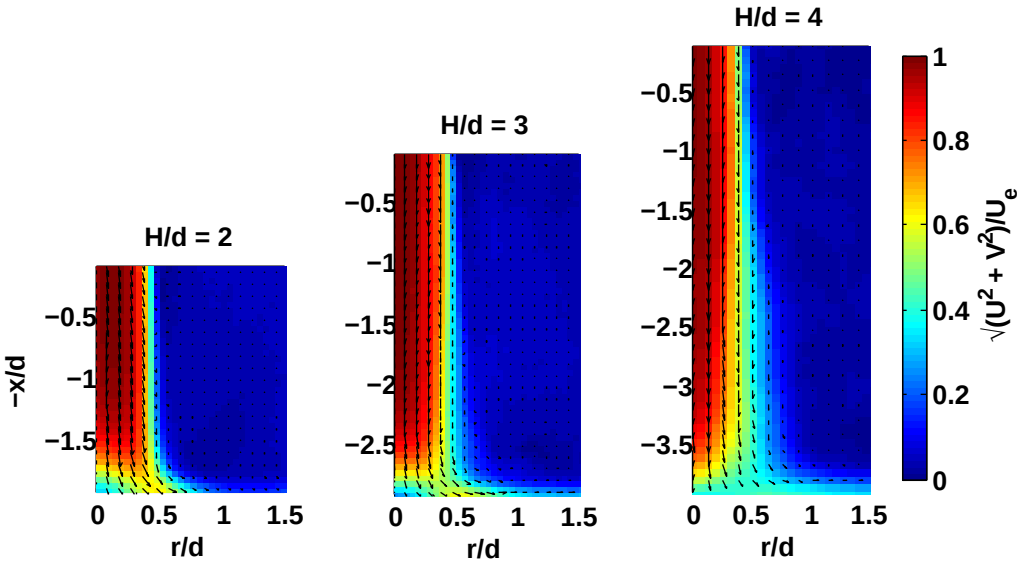

Figure 4.24: Effect of H/d on the time-averaged velocity field ($Re \approx 4000$)

4.4 Effect of the Nozzle-to-Plate Spacing

4.4.1 Introduction

The distance from the jet to the target surface (H/d) also has an effect on both the flow field and the heat transfer characteristics of impinging jets. This section will look at the effect of such distance on transitional ($Re \approx 4000$) jets with nozzle-to-plate spacings of 1, 2 and 3 nozzle diameters, while keeping all other parameters constant. The nozzle diameter was also $30.5mm$. It is important to notice that the axial coordinate has been non-dimensionalised with respect to the distance between the nozzle and the plate (H). Therefore, the axial coordinate x/H has a value of zero at the nozzle exit, and one at the plate.

4.4.2 Time-Averaged Flow Field

The time-averaged flow field is shown in Fig.4.24. It shows that H/d has an effect on the core of the jet where deceleration in the axial direction is more pronounced for lower nozzle-to-plate spacings. Also, the wall jet is affected, the jets located at $H/d = 2$ and $H/d = 3$ show higher values of the velocity magnitude at approximately $r/d = 0.5$. However, for $H/d = 4$ the velocity magnitude at $1 < r/d < 2$ and $x/H > 0.9$ is larger. The effect of H/d is further explored in

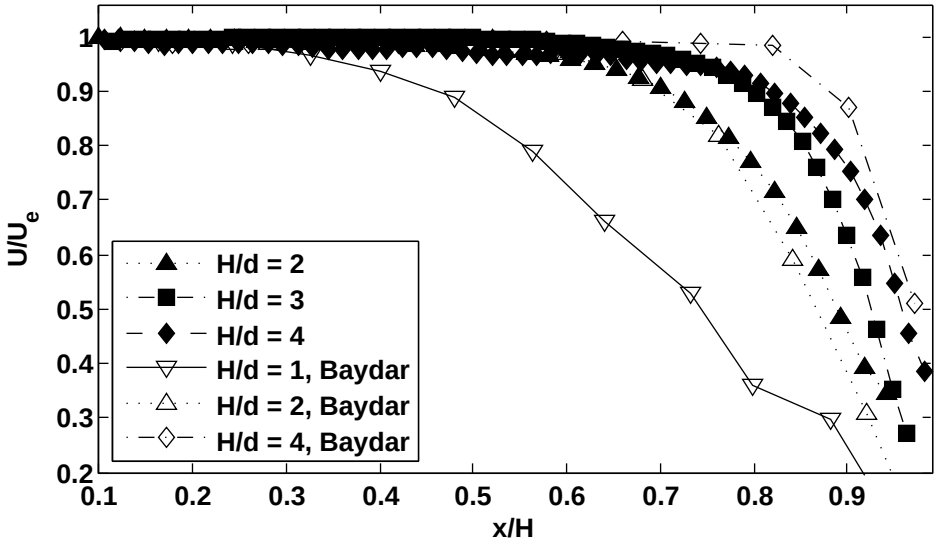

Figure 4.25: Effect of H/d on centreline velocity decay; Baydar [11] ($Re = 30000$)

Fig.4.25 and Fig.4.26.

The jet centreline velocity decay is shown in Fig.4.25. It can be observed that H/d has a strong effect on the velocity decay. As H/d is decreased, the centreline velocity decreases more sharply. Results from Baydar [11] are also shown for $Re = 30000$. They also show a similar trend even though the Reynolds number is much larger. In addition, for $H/d = 2$ the velocity decay profiles for $Re = 4000$ and $Re = 30000$ are similar. However, for $H/d = 4$ the jet with $Re = 30000$ exhibits a velocity reduction closer to the wall. Consequently, it can be argued that for lower nozzle-to-plate spacings the effect of the Reynolds number on the velocity decay is less pronounced. Nonetheless, as H/d is further increased, increases in the Reynolds number lead to a shift of the deceleration region closer to the target wall, implying a stronger effect of the Reynolds number for larger values of H/d.

Radial profiles of the axial and radial mean velocity components are shown in Fig.4.26 at various axial locations. Near nozzle exit (Fig.4.26c), It can be observed that small values of H/d have an effect on axial velocity component at the nozzle exit, since the profile of the jet located at $H/d = 2$ is affected by the presence of the wall. However, the radial velocity component does not exhibit a significant influence due to H/d. Fig.4.26b shows that, further downstream

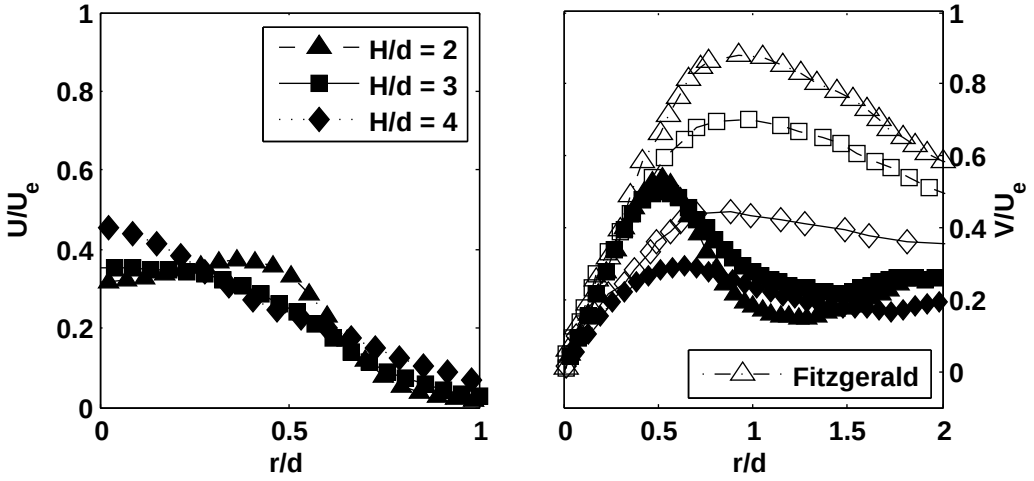

(a) x/H = 0.95

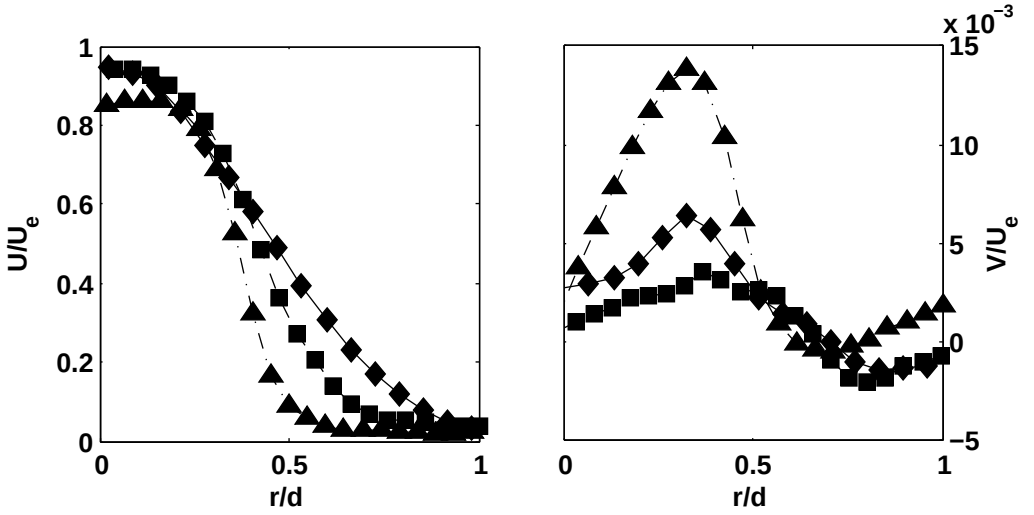

(b) x/H = 0.75

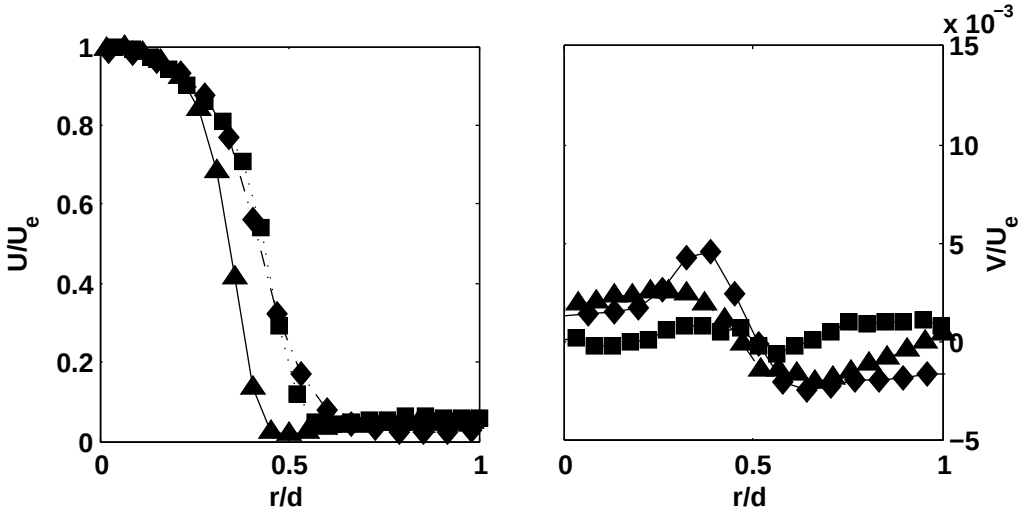

(c) x/H = 0.25

Figure 4.26: Radial profiles of the mean axial (left) and radial (right) velocity components; open symbols - Fitzgerald [9] ($Re = 23000$)

($x/H = 0.75$), the profiles of the axial velocity component become wider, which indicates that as H/d is increased, the jet spreads more rapidly. The profiles of the radial velocity component show that for $0 < r/d < 0.5$, the jet located at $H/d = 2$ begins to experience an increase in radial velocity, probably as a result of the presence of the wall which forces the fluid radially. For $H/d = 3$ and $H/d = 4$ there is only a moderate increase in radial velocity. However, the jet with $H/d = 4$ exhibits slightly higher values of radial velocity, in this case, probably due to a more rapid spread of the jet rather than as a result of the presence of the wall. In addition, it can be seen that for $r/d < 0.5$ all the profiles tend to collapse. The values in this region are only slightly negative, indicating that there is little recirculation present. Near the wall (Fig.4.26a), It can be seen that, for $H/d = 2$, there is a local maximum of U/U_e at $r/d \approx 0.4$, which is not present for the other nozzle-to-plate spacings. This local maximum could be a consequence of the sharp deceleration caused by the wall, which affected the velocity distribution near the jet centreline, leading to a flattening of the velocity profile. Also, Fig.4.26a shows that the profiles of the axial velocity component for $H/d = 2$ and $H/d = 3$ collapse for $r/d > 0.6$, whereas, for $H/d = 4$ there is a slight increase in the values of U/U_e. Fig.4.26a also shows the profiles of the radial velocity component. It shows that for $H/d = 2$ and $H/d = 3$ the profiles are very similar. There is only a significant reduction on V/U_e for $H/d = 4$. The results from Fitzgerald [9] are also shown in Fig.4.26a. They correspond to $Re = 23000$. They show that as H/d is increased, there is a significant reduction in the values of V/U_e. Such an obvious reduction is not present in the profiles of V/U_e for transitional jets. At this point, it is difficult to assess whether these different trends are due to the transitional nature of the jet, or due to the larger diameter used ($d = 6.35$ Fitzgerald). It it is known that larger diameters lead to lower values of V/U_e near the wall [9], but also to higher rates of heat transfer [53] [54].

4.4.3 Velocity Fluctuations

Whole-field surface plots for the axial and radial velocity fluctuations are shown in Fig.4.27 and Fig.4.28 respectively. These plots show that as H/d is increased,

the axial and radial velocity fluctuations within the shear layer also increase. However, the behaviour of the velocity fluctuations is different within both the jet core and the wall jet region. Fig.4.27 shows a decrease in u'_{rms}/U_e within the wall jet as H/d is increased. However, within the jet core there is an increase in u'_{rms}/U_e as H/d decreases. Fig.4.28 shows that, within the wall jet, for $H/d = 2$ and $H/d = 3$, the radial velocity fluctuations are slightly similar, whereas, there is a sharp reduction in v'_{rms}/U_e for the largest nozzle-to-plate spacing.

First, the development of the centreline velocity fluctuations for different nozzle-to-plate spacings is shown in Fig.4.29. This figure shows that the axial velocity fluctuations near the nozzle exit are considerably affected by H/d, they increase as H/d is decreased, remaining unchanged for $H/d = 3$ and $H/d = 4$ up to 40% of their axial length, however, for $H/d = 2$, it remains unchanged up to 60% of its length. Furthermore, the jet situated at $H/d = 4$ shows a rapid increase in the velocity fluctuations as early as 40% of its length. This indicates that for $H/d = 4$ there is considerable mixing in the axial direction. On the other hand, $H/d = 3$ exhibits the lowest values of u'_{rms}/U_e near the wall for $Re \approx 4000$, which suggests that $H/d = 3$ would lead to the highest rates of heat transfer [79] for a transitional jet. This strongly suggests that in order to minimise mixing in the axial direction, both the jet's Reynolds number and H/d must be taken into consideration. The results of Baydar [11] are also shown. These results correspond to $Re = 30000$. Firstly, these results are much lower because they correspond to a much higher Reynolds number. They show that for a turbulent jet, the axial velocity fluctuations increase in the streamwise direction as H/d is increased. They also indicate that H/d has a greater influence on the values of u'_{rms}/U_e for transitional jets near the nozzle exit since the values of u'_{rms}/U_e for $Re = 30000$ near the exit remain unaffected by H/d. Also, in the study of the effect of the Reynolds number, a sudden reduction in u'_{rms}/U_e at the nozzle exit was observed when the jet was no longer transitional. This indicates that transitional jets exhibit larger mixing on exiting the nozzle in general, which is further influenced by the nozzle-to-plate spacing.

The axial development of u'_{rms}/U_e is shown in Fig.4.30. It shows that the magnitude of u'_{rms}/U_e decreases as the jet reaches the wall. This decrease is more

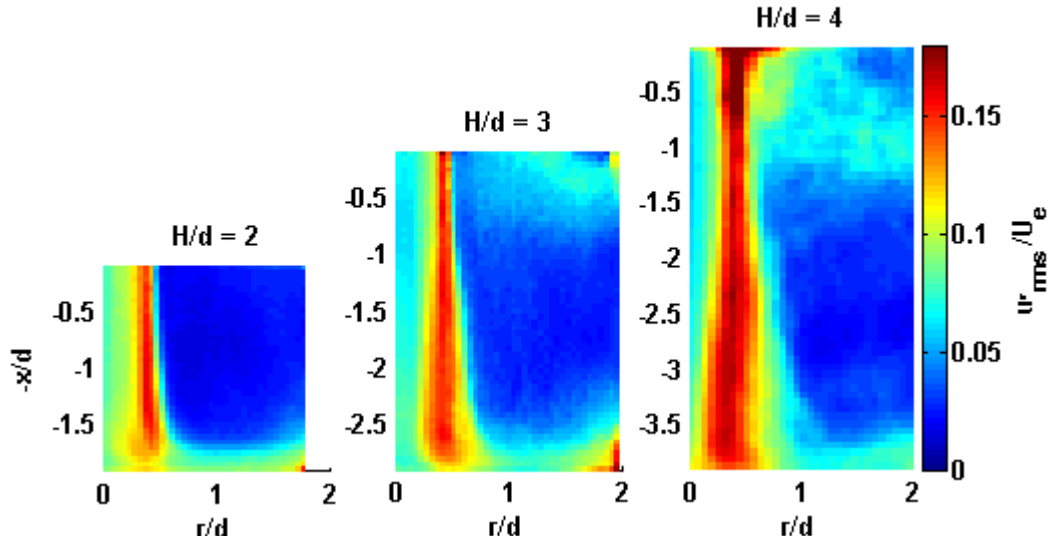

Figure 4.27: Effect of H/d on u'_{rms}/U_e

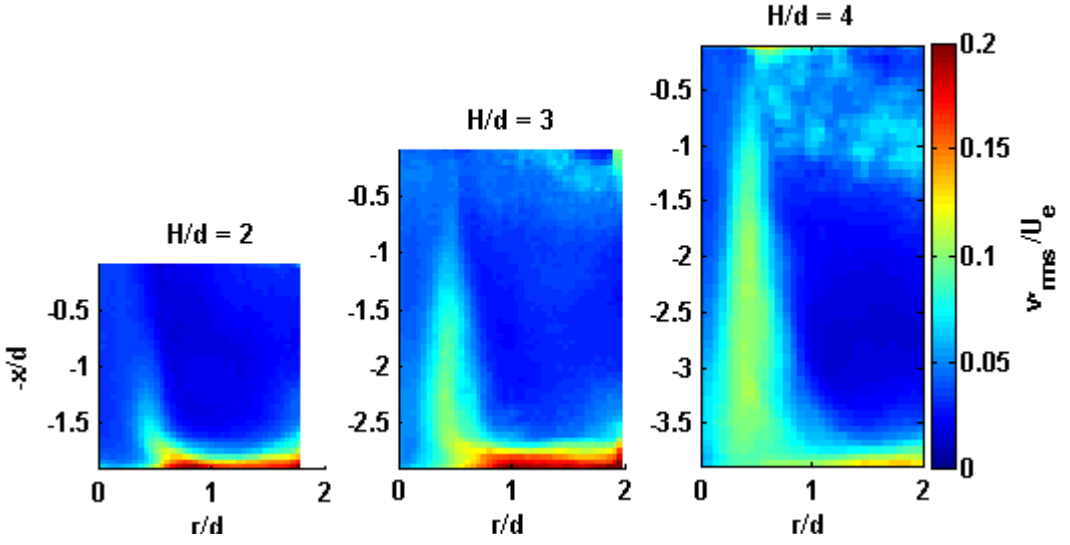

Figure 4.28: Effect of H/d on v'_{rms}/U_e

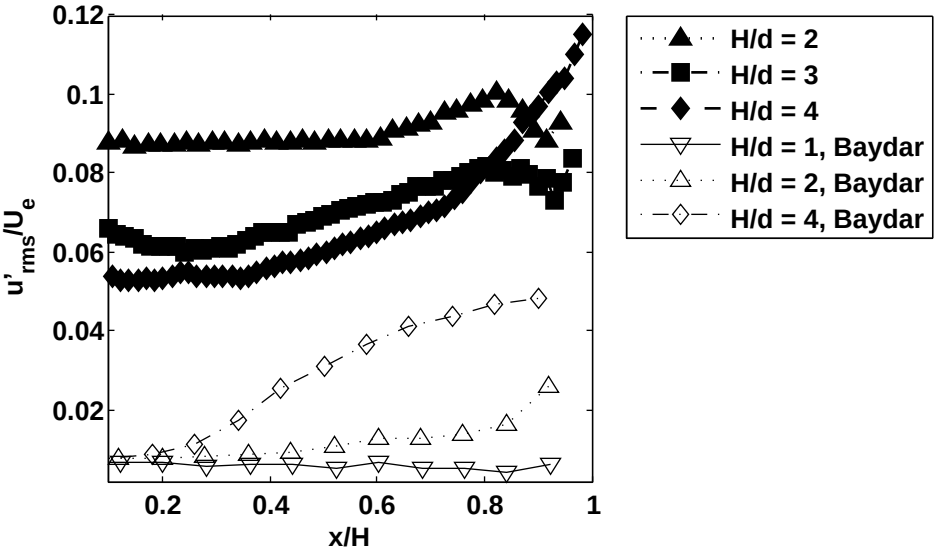

Figure 4.29: Centreline axial velocity fluctuations; Baydar [11] ($Re = 30000$)

pronounced for $x/H > 0.75$. It also shows that as expected, turbulent mixing gradually increases from the centreline to the shear layer and then drops to a single level for $r/d > 1$. It can also be observed that, for up to 75% of the axial length, the profile of u'_{rms}/U_e for $H/d = 2$ exhibits a peak at approximate $r/d = 0.3$. This peak is located at $r/d \approx 0.45$, for $H/d = 3$ and $H/d = 4$, at $x/H = 0.25$. At $x/H = 0.75$, as the jet spreads, their local maximum shifts towards the stagnation point to $r/d \approx 0.4$ and their profiles become flatter, which indicates that turbulent mixing spreads towards the centreline as H/d is increased. Near the impinging wall (Fig.4.30a), the local maximum of u'_{rms}/U_e increases with increasing H/d, interestingly, the profile for $H/d = 3$ exhibits a local minima at $r/d \approx 0.1$. The presence of this local minima could be caused by the shear layers reaching the wall just before they collide keeping the centre of the jet free from their mixing effect. Interestingly, this minima is not present for $H/d = 2$ even though the shear layers have not collided. This is attributed to the influence of the local acceleration present for $0.25 < r/d < 0.5$ (Fig.4.26a) in the axial direction which leads to increases of u'_{rms}/U_e as the axial velocity profile is flattened by the impinging wall. This notion can also explain the similar radial profiles of V/U_e for $H/d = 2$ and $H/d = 3$ shown in Fig.4.26a. In the case of $H/d = 2$, the increase in velocity is caused by local acceleration due to the

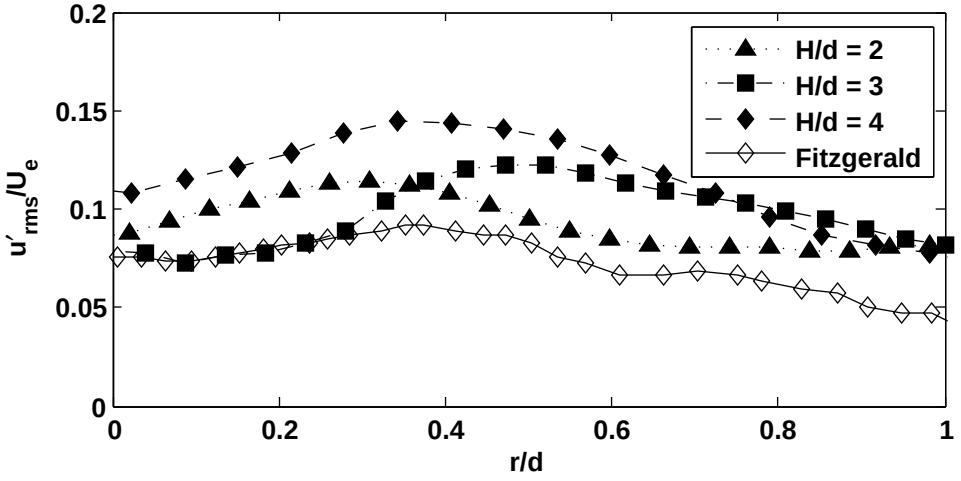

(a) x/H = 0.95

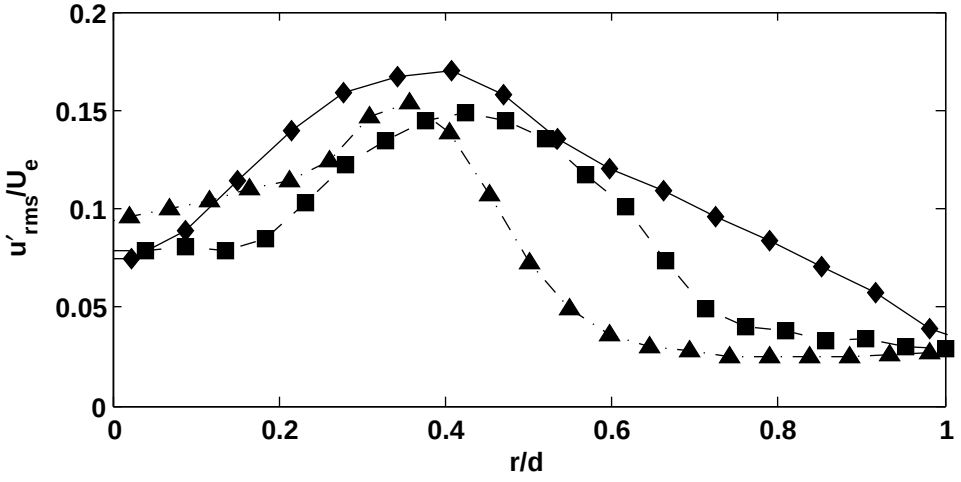

(b) x/H = 0.75

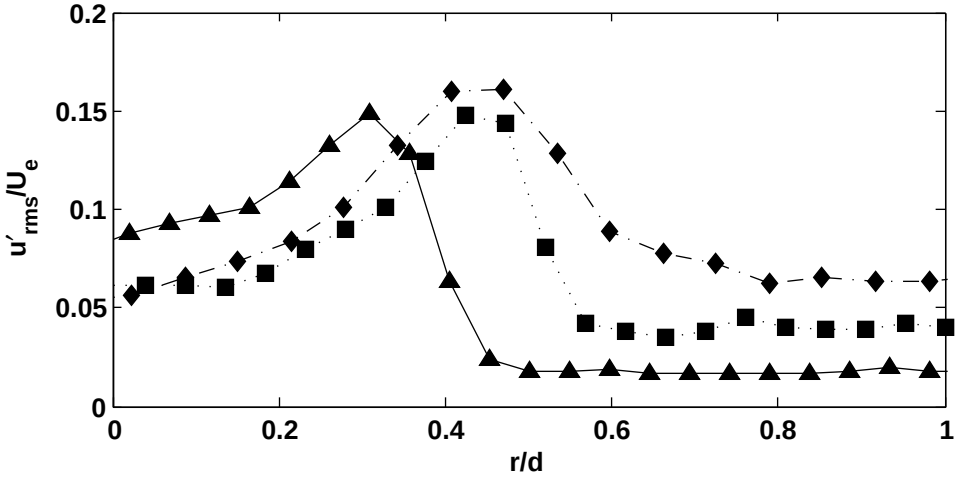

(c) x/H = 0.25

Figure 4.30: Radial profiles of the axial velocity fluctuations; Fitzgerald [9] ($Re = 8500$)

presence of the impinging wall, whereas, for $H/d = 3$, it is a consequence the preservation of the centreline velocity. Finally, Fig.4.30a also shows that the profile of u'_{rms}/U_e, at $H/d = 4$, follows a similar trend to the profile for $H/d = 4$ when $Re = 8500$ [9], which is lower due to the higher Reynolds number.

The effect of the nozzle-to-plate spacing on the radial velocity fluctuations is shown in Fig.4.31. It can be observed that increasing the distance between the jet exit and the impinging wall leads to a decrease in v'_{rms}/U_e. It is interesting to notice that for $H/d = 2$, there is a sudden increase of v'_{rms}/U_e for $0.5 < r/d < 0.75$. This increase in v'_{rms}/U_e could be attributed to the rapid acceleration and deceleration present at $0 < r/d < 0.75$ (Fig. 4.26 on page 92). Also, when H/d is increased from 3 to 4 nozzle diameters, there is a drop in v'_{rms}/U_e of approximately 50% for $r/d > 0.5$, which is linked to the development of lower radial velocities for $H/d = 4$ (Fig. 4.26 on page 92). Fig.4.31 also shows that for turbulent jets (Fitzgerald [9]), increasing H/d also leads to lower values of v'_{rms}/U_e for $r/d > 1.1$, however, the influence of H/d is not as pronounced as for transitional jets. Furthermore, the results of Nishino [10] show that for much larger values of H/d, the radial velocity fluctuations exhibit higher values than the lower Reynolds numbers. This is attributed to the rapid increase of v'_{rms}/U_e as H/d increases, which indicates that radial mixing is influenced by both the nozzle-to-plate spacing and the Reynolds number. However, the influence of H/d is more significant.

The effect of both the Reynolds number and the nozzle-to-plate spacing on the axial velocity fluctuations near the impinging wall is shown in Fig.4.32. It shows that the effect of the Reynolds number is to decrease u'_{rms}/U_e as it increases. In contrast, as the nozzle-to-plate spacing is increased, the axial velocity fluctuations near the stagnation point also increase. Interestingly, there is a reduction in u'_{rms}/U_e present for $H/d = 3$. This reduction could be attributed to the jet impinging on the surface just before its mixing layers collide, which would lead to lower velocity fluctuations near the stagnation point.

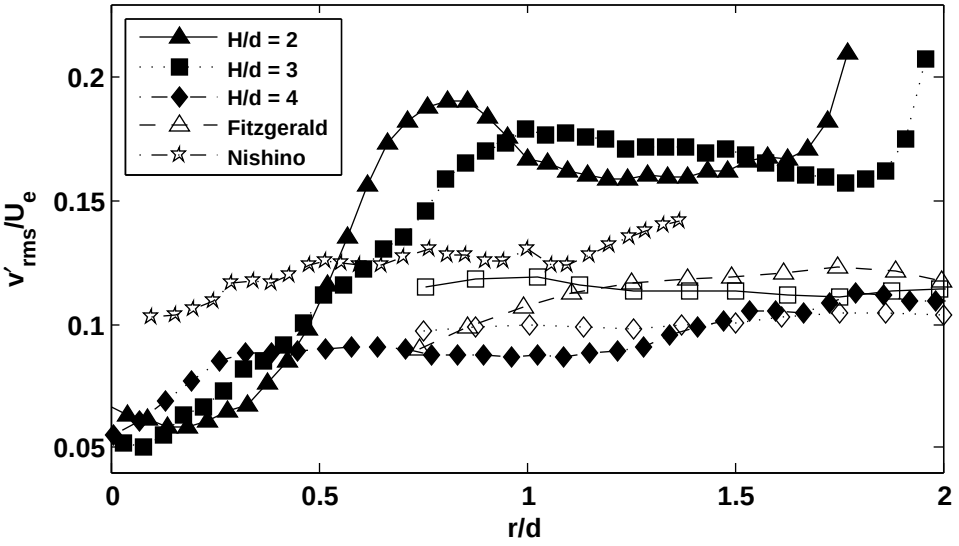

Figure 4.31: Effect of H/d on the radial velocity fluctuations near the impinging wall; open symbols - Fitzgerald [9] (Re = 23000); open star - Nishino [10] ($H/d = 6$, $Re = 13000$)

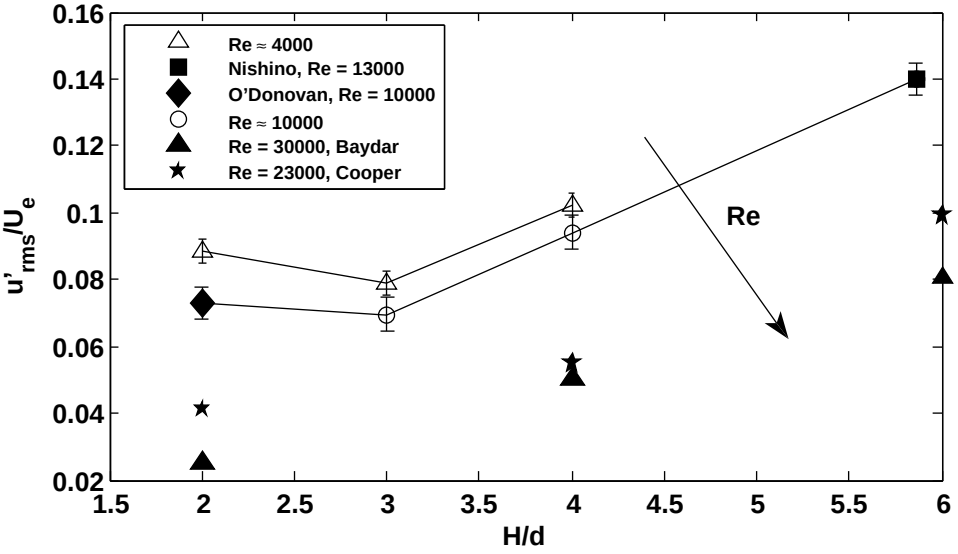

Figure 4.32: Combined effect of Re and H/d on the axial velocity fluctuations near the stagnation point ($x/H \approx 0.95$); Nishino [10]; O'Donovan [12]; Baydar [11]; Cooper [13]

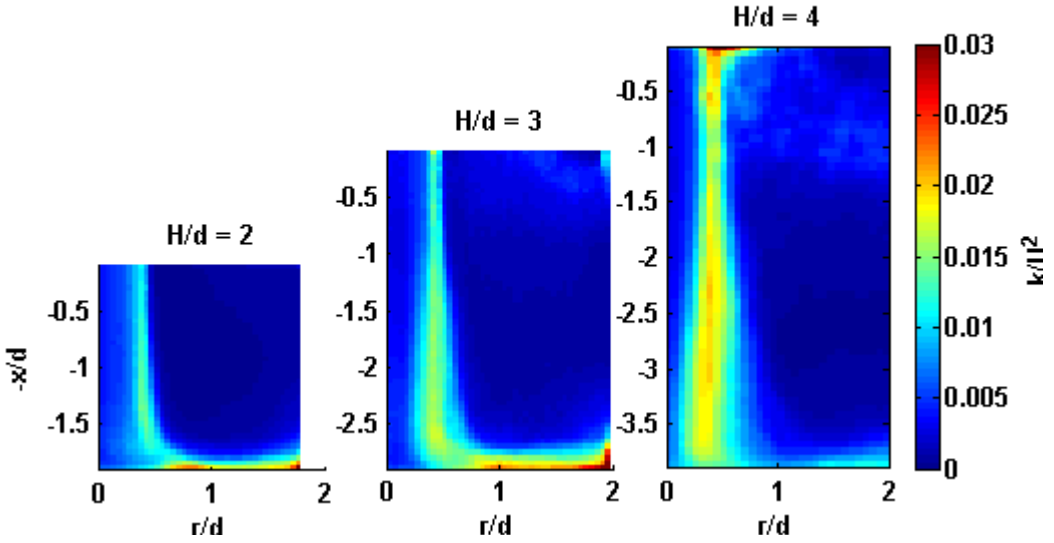

Figure 4.33: Effect of H/d on the mean turbulent kinetic energy

4.4.4 Turbulent Kinetic Energy

Fig.4.33 shows the effect of the nozzle-to-plate spacing on the mean turbulent kinetic energy. It can be observed that as H/d is increased, there is a clear increase in the mean TKE within the shear layer of the jet. As shown in the previous section, this is due to the increasing levels of the velocity fluctuations as H/d increases, since at larger nozzle-to-plate spacings, the shear layer is capable of developing without being influenced by the impinging wall. However, for the wall jet region there is an increase of the mean TKE when the nozzle-to-plate distance is increased from $H/d = 2$ to $H/d = 3$, which is followed by a decrease when $H/d = 4$. The increase in the mean TKE for $H/d = 3$ could be attributed to the shear layer being diverted radially by the fluid within the jet core. Indicating that the wall jet, when $H/d = 3$, is comprised mainly by the shear layer of the jet. However, the fluid within the wall jet for $H/d = 2$ is comprised by the diverted fluid within the core of the jet, whereas, for $H/d = 4$ the wall jet is rather weak and the reduction of the mean turbulent kinetic energy is simply an effect of the deceleration produced by the wall.

Fig.4.34 shows radial profiles of the mean turbulent kinetic energy near the impinging wall. It shows that as H/d is increased, the mean turbulent kinetic energy, on average, decreases. This is particularly evident, for $r/d > 1$ when H/d

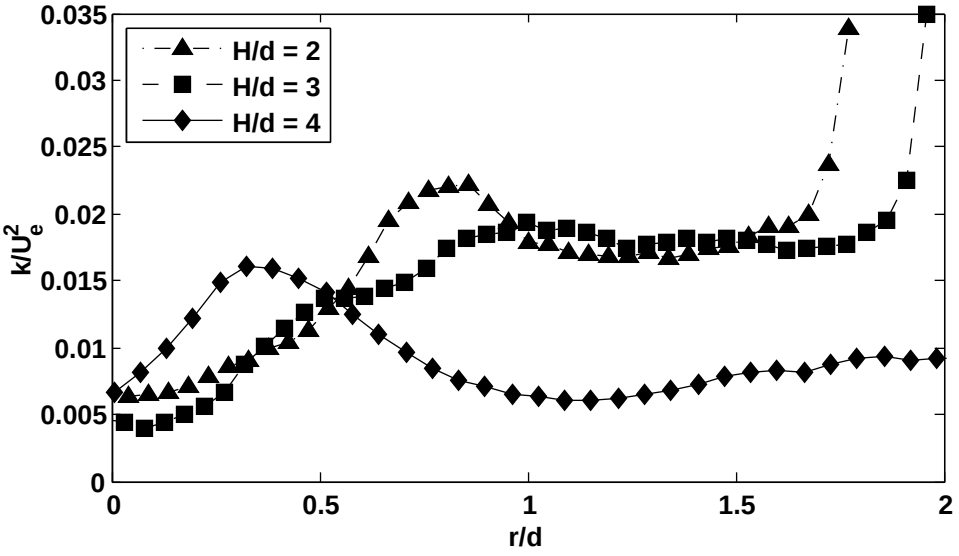

Figure 4.34: Effect of H/d on the mean turbulent kinetic energy near the impinging wall ($x/H = 0.9$)

is increased from 3 to 4 nozzle diameters. Furthermore, the radial profiles of the mean turbulent kinetic energy for $H/d = 2$ and 3 are rather similar. However, for $H/d = 2$, there is a relative increase of the mean turbulent kinetic energy for $0.5 < r/d < 1$ when compared with the jet situated at $H/d = 3$. The radial velocity fluctuations contribute to such an increase as it was shown in Fig.4.31. This could be an indication of the collision between vertical and radial fluid motion. However, for $H/d = 4$ the local maximum of the mean TKE is located closer to the stagnation point at approximately $r/d \approx 0.4$. The presence of this local maximum could be attributed to the interaction between the shear layer and the developing wall jet.

4.4.5 Skewness Factor

Fig.4.35 and Fig.4.36 show the effect of the nozzle-to-plate spacing on the axial and radial skewness factor. Fig.4.35 shows that for $H/d = 2$, the impinging wall has a strong influence on u'^3/U_e^3 within the core of the jet which is translated into negative values of the skewness factor. However, for $H/d = 3$, the distributions of the axial skewness factor is balanced, as H/d is increased to $H/d = 4$ this balance is disturbed and the distributions of u'^3/U_e^3 exhibit a sharp decrease within the

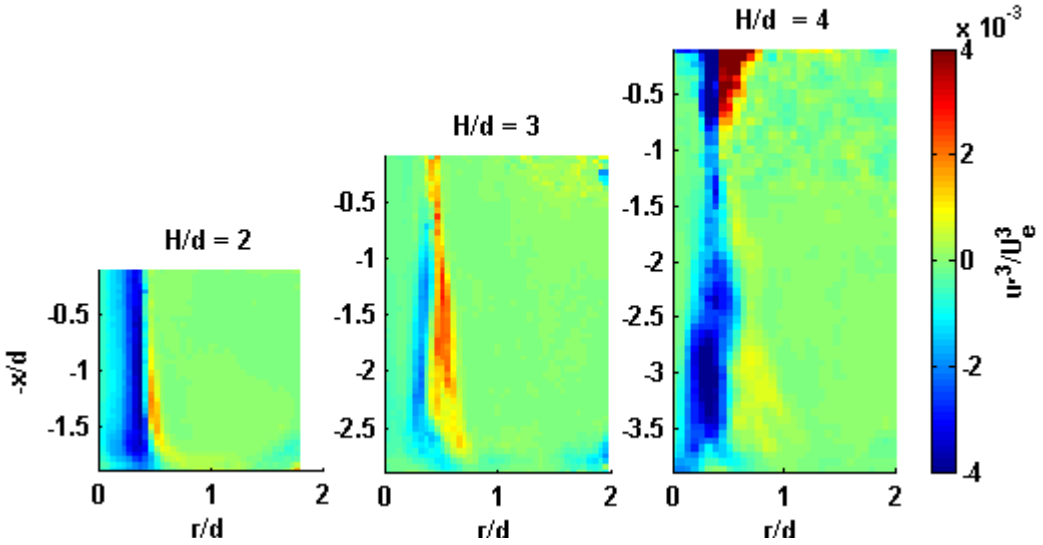

Figure 4.35: Contour Plot of ${u'}^3/{U_e}^3$ for Different H/d

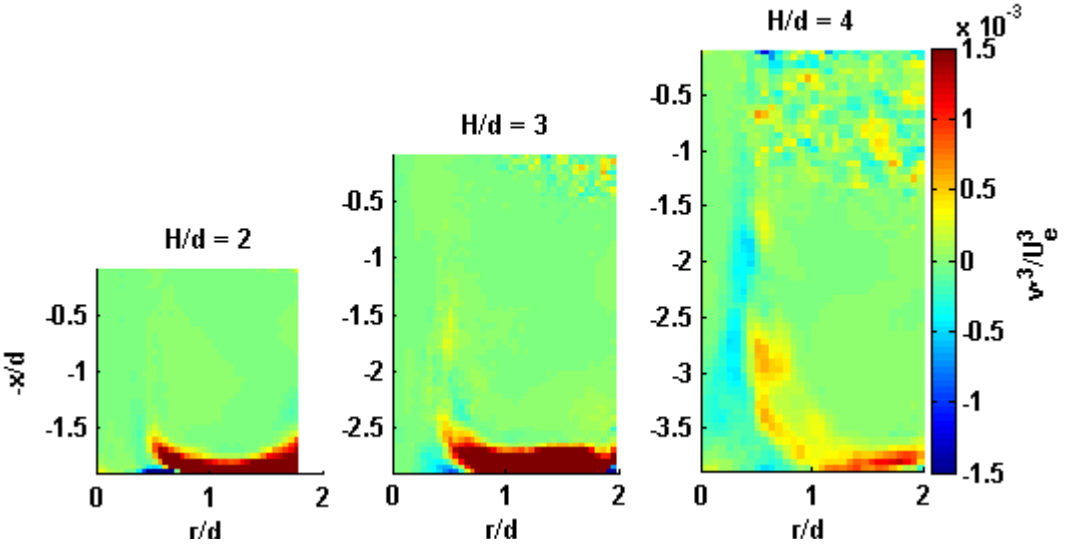

Figure 4.36: Contour Plot of ${v'}^3/{U_e}^3$ for Different H/d

shear layer of the jet. This decrease is most likely due to the faster thickening of the shear layer for larger values of H/d. It seems that the thickening of the shear layer leads to turbulent deceleration, hence, the presence of negative values of u'^3/U_e^3. The influence of the impinging wall on the skewness factor near the nozzle exit is evident from Fig.4.37, which shows a reduction in u'^3/U_e^3 on the jet centreline as H/d is reduced. However, for $H/d = 4$ the values of u'^3/U_e^3 are near zero. This indicates that the probability distribution of the velocity data for low values of H/d has longer negative tails than a gaussian distribution, which implies that the presence of wall leads to turbulent deceleration, since there is a greater probability for a random velocity measurement to be lower than the mean.

Fig.4.36 shows that the nozzle-to-plate spacing does not have a significant influence on v'^3/U_e^3 within the shear layer, exhibiting only small variations for $H/d = 4$, which are probably caused by a more developed shear layer. On the other hand, within the wall jet region, the values of the radial skewness factor tends to decrease as H/d is increased. Finally, it is interesting to observe that near the nozzle exit (Fig.4.35), there is a region of positive $u'^3/{U_e}^3$ at $H/d = 4$, indicating the presence of turbulent acceleration. This region of positive $u'^3/{U_e}^3$ near the nozzle exit could be attributed to recirculation at the top of the water tank, which would lead to fluid being pushed down along the outer side of the nozzle. Unfortunately, whole-field experiments were not possible to be carried out due to limitations of the particle image velocimetry system used.

Fig.4.38 shows that for $H/d = 2$ and 3, the values of v'^3/U_e are positive for $r/d > 0.6$, which is an indication of turbulent accelerations. This could be due to the rapid deceleration of the radial velocity[5] present for $H/d = 2$ and $H/d = 3$. However, for $H/d = 2$, there is a negative peak in the values of v'^3/U_e, for $H/d = 2$ at $r/d \approx 0.5$, which corresponds to the location of the local maximum of the mean radial velocity[6]. Also, the larger values of v'^3/U_e exhibited for $0.8 < r/d < 1.5$ for the jet situated at $H/d = 3$ can be explained by the ability of such jet to sustain larger radial velocities[7] within this region, which generates positive turbulent

[5] see Fig. 4.26 on page 92a

[6] see footnote 5

[7] see footnote 5

velocity bursts in the radial direction i.e. turbulent acceleration. Finally, the results obtained from Nishino [10] for a jet with $Re = 13000$ and situated at 6 nozzle diameters from the impinging wall are also shown. They also show no significant influence on the skewness factor near the wall as the jet located at $H/d = 4$. Indicating that, for $H/d > 4$, the nozzle-to-plate spacing has no evident effect on v'^3/U_e^3

4.4.6 Reynolds Stress

The effect of the nozzle-to-plate spacing on the Reynolds stress is shown in Fig.4.39. The convention used to assess the Reynolds stress was shown in Fig. 4.20 on page 82. First of all, this figure shows that the effect of H/d within the shear layer of the jet is straight forward; as H/d is increased, the contribution of the Reynolds stress related to both entrainment (en) and expulsion (e) also increase. However, near the wall, changes in the nozzle-to-plate spacing affect the distribution of the Reynolds stress significantly. For instance, for the lowest nozzle-to-plate spacing, the contribution to the Reynolds stress, for $0 < r/d < 0.25$, exhibit high-speed interactions outwards (O). This type of Reynolds stress is only observed for $H/d = 2$. In contrast, only ejection (E) is present for the other two nozzle-to-plate spacings, which increases as H/d is increased. This increase is due to fact that the skewness factor in the radial direction also increases as the nozzle-to-plate spacing is increased. Furthermore, the sweeping Reynolds stress (S) present at all nozzle-to-plate spacings shift away from both the stagnation point and the wall as H/d is increased. This is due to the development of weaker wall jets as H/d is increased. In addition, high-speed fluidic interactions in a direction away from the impinging wall (O) are present in all jets. However, their contribution to the Reynolds stress differ significantly depending on H/d. First of all, these contributions are dominated by the radial velocity fluctuations represented by the skewness factor (see Fig. 4.38 on the following page), which explains why $H/d = 4$ exhibits the lowest values, followed by $H/d = 2$ and $H/d = 3$. The higher values of $u'v'/U_e^2$ (O) exhibited for $H/d = 3$ can be attributed to the deflection of the shear layer, which becomes part of the wall jet, leading to larger radial velocity fluctuations.

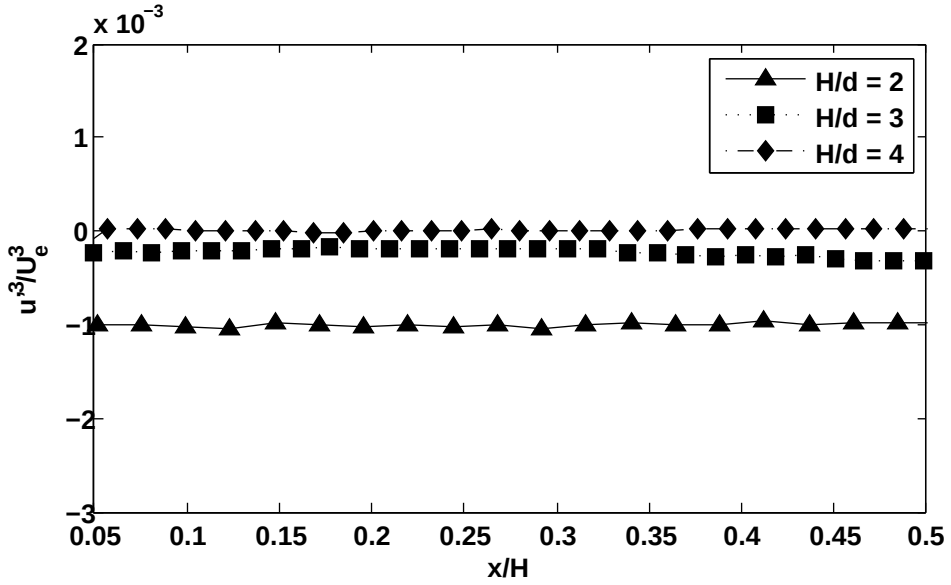

Figure 4.37:

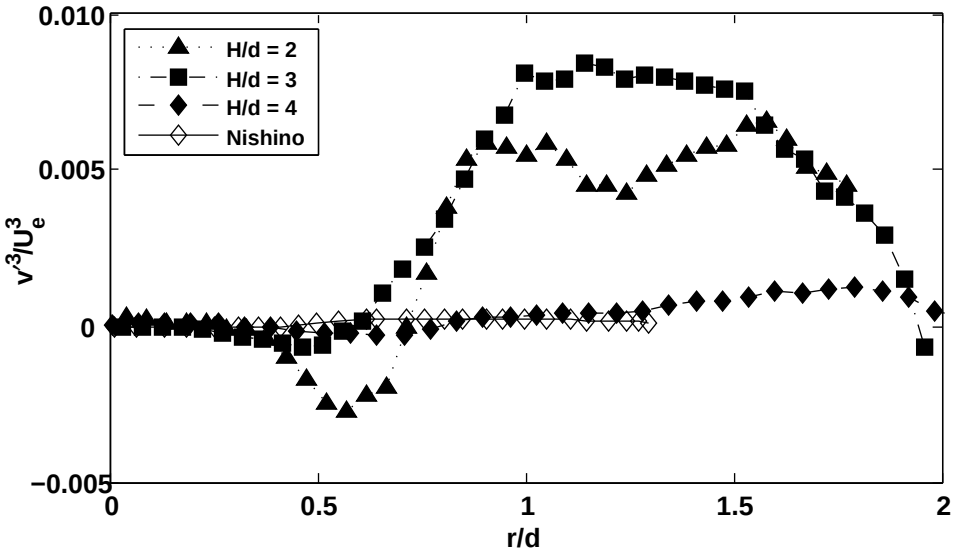

Figure 4.38: Effect of H/d in the radial skewness factor near the impinging wall; Nishino [10] ($Re = 13000$,$H/d = 6$)

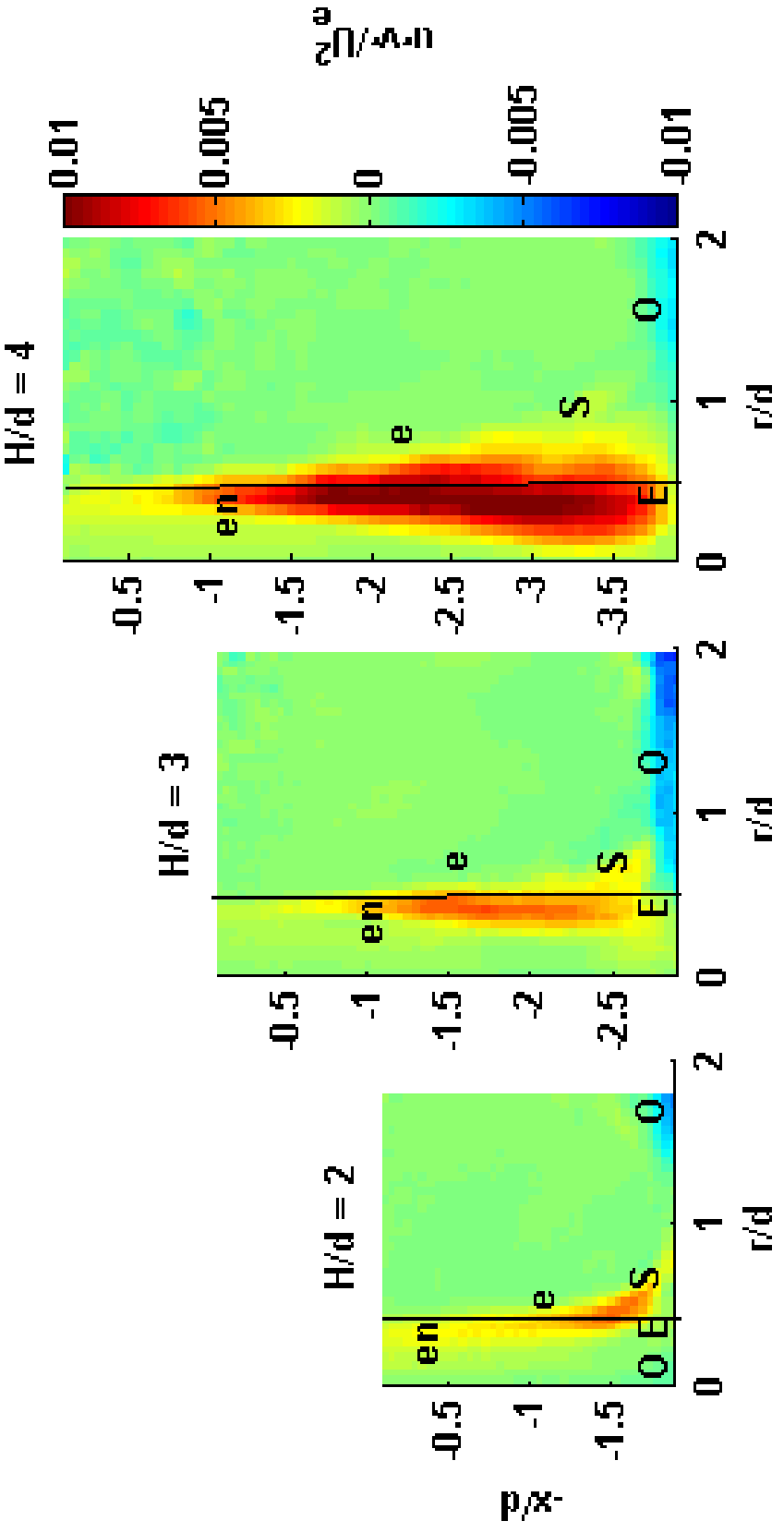

Figure 4.39: Effect of H/d on the Reynolds Stress

4.4.7 Mean Axial Momentum Balance Near the Wall

The effect of the nozzle-to-plate spacing on the mean axial momentum balance is shown in Fig.4.40. This figure shows that the main source terms are the axial convection and the radial diffusion, However, in comparison to the Reynolds number, the effect of the nozzle-to-plate spacing on the distributions of these terms is more pronounced, in particular, on the radial diffusion. For instance, for $H/d = 2$, the radial diffusion exhibits a local maximum similar in magnitude of that of the axial convection, located at approximately $r/d = 0.55$. This is translated into a significant contribution to the static pressure term, exhibiting a local minima at $r/d \approx 0.45$, which is not present for the other nozzle-to-plate spacings. Furthermore, as the nozzle-to-plate is increased, the contribution to momentum from the radial convection reduces. Interestingly, the location of the local maximum of the radial diffusion term for $H/d = 2$ coincides with the change in gradient of the radial profile of U/U_e (Fig.4.26a), which is a consequence of the flattening of the profile due to the presence of the wall. Therefore, the contribution of the radial diffusion to static pressure is the result of the deceleration effect of the wall, combined with the production of significant radial acceleration as a consequence. This explains the reduction in the contribution of the radial diffusion to momentum as H/d is increased.

The results obtained from Nishino [10] are also shown in Fig.4.40. This figure shows that the pressure term is similar in magnitude, compared to the jet at $H/d = 4$, for $0.2 < r/d < 0.6$, although the Reynolds number differ for both jets ($Re \approx 4000$ and $Re = 13000$), this could be the result of the lower nozzle-to-plate spacing ($H/d = 3$ compared to $H/d = 5.86$) for the jet with $Re \approx 4000$. This figure also shows that, even though, the magnitudes are similar for $0.2 < r/d < 0.6$, the profile of the distribution of the pressure term is flatter for the higher Reynolds number jet. Also, as seen earlier, the effect of the Reynolds number was to flatten the profiles of the pressure term, therefore, the dissimilarity between these profiles can be attributed to the difference in the Reynolds number. It can be argued, that the trend exhibited by the pressure term is dominated by the Reynolds number, since it was found that it exhibits a similar trend, even if H/d is significantly different (see section 4.3.7).

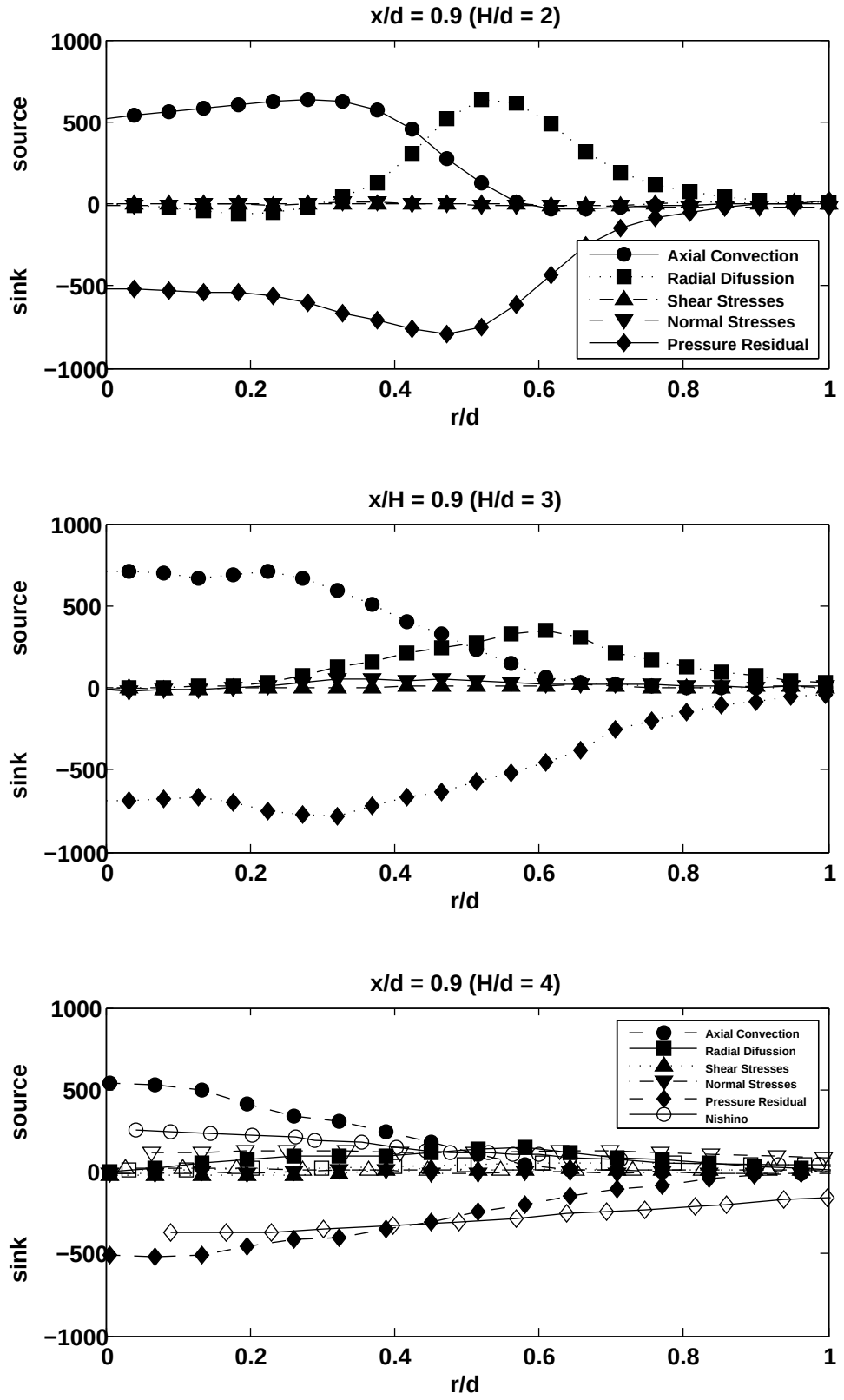

Figure 4.40: Effect of the nozzle-to-plate on the mean axial momentum balance (x/H = 0.9) non-dimensionalised by d/U^2; open symbols - Nishino [10] (Re = 13000, $H/d = 5.86$)

Chapter 5

Pulsed Jets

5.1 Introduction

The results and discussion for pulsating jets are presented in this chapter, using steady impinging jet flows for comparison. First of all, in order to assess the effects of a pulsation on the flow field of impinging jets, the effects of the Strouhal number are examined. Finally, the effects of the Reynolds number and the nozzle-to-plate spacing in the presence of a fixed pulsating frequency are also evaluated and compared with their effects on steady jets.

5.2 Effect of the Frequency (Transitional Jets)

5.2.1 Introduction

The effect of the Frequency, in its non-dimensional form St, on the flow field of transitional ($Re \approx 4200$) and pulsating ($0.10 < St < 0.50$) impinging jets will be presented in this section. The flow field of a steady and transitional impinging jet will be used for comparison. All the other factors that affect the flow field were kept constant ($H/d = 3$, $d = 30.5mm$ and $Re \approx 4200$).

5.2.2 Time-Averaged Flow Field

Firstly, the effect of the Strouhal number on the time-average flow field is shown if Fig.5.1. This figure shows that the core of the jet becomes wider with the

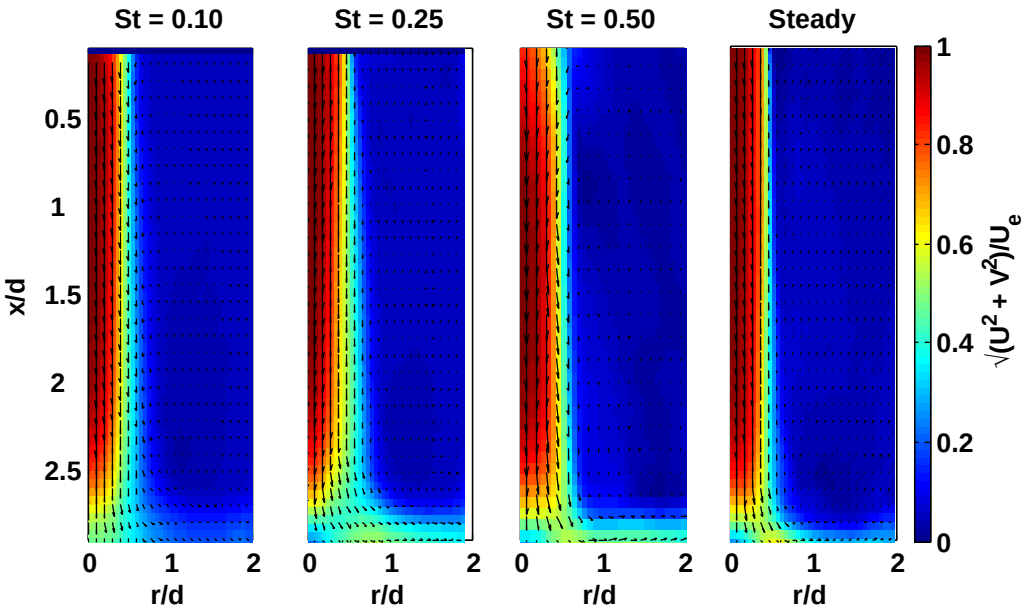

Figure 5.1: Effect of the Strouhal number on the time-average velocity field ($H/d = 3$, $Re \approx 4200$)

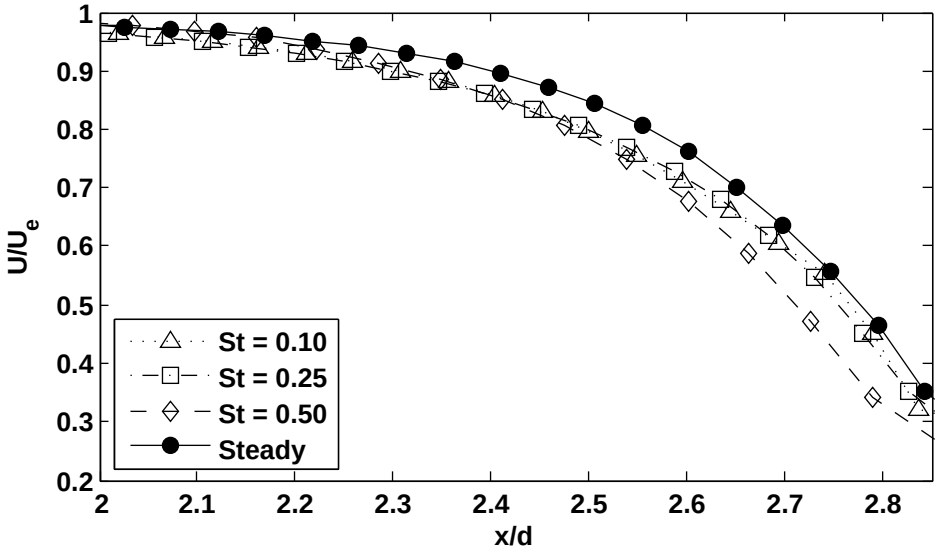

Figure 5.2: Centreline mean axial velocity decay ($H/d = 3$, $Re \approx 4200$)

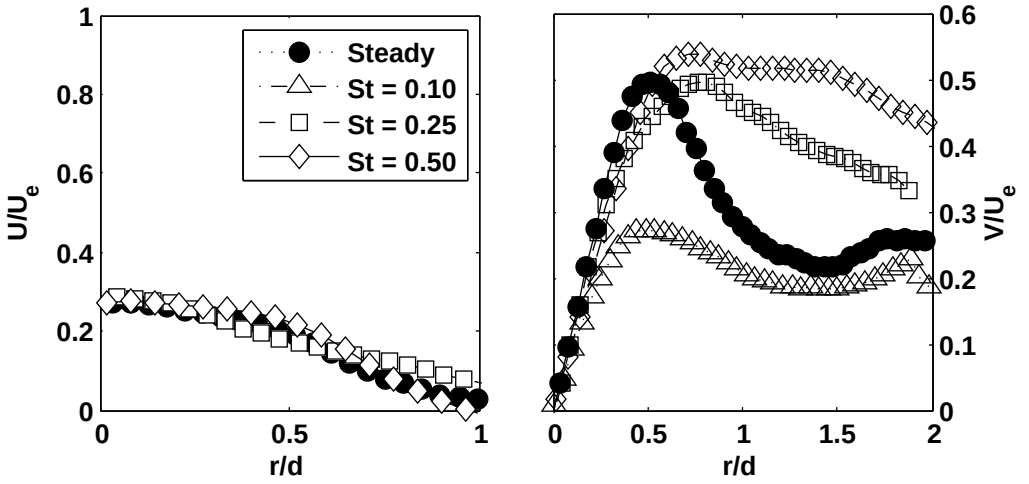

(a) x/d = 2.85

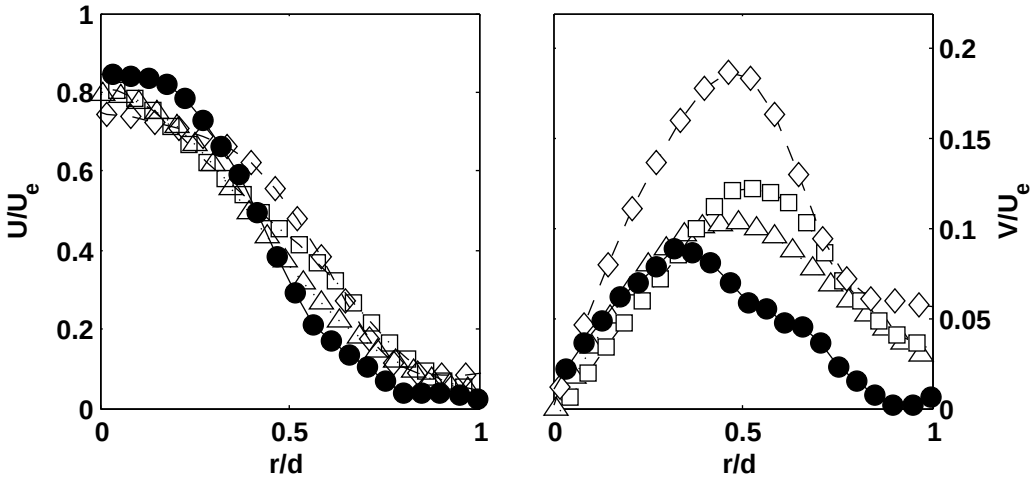

(b) x.d = 2.5

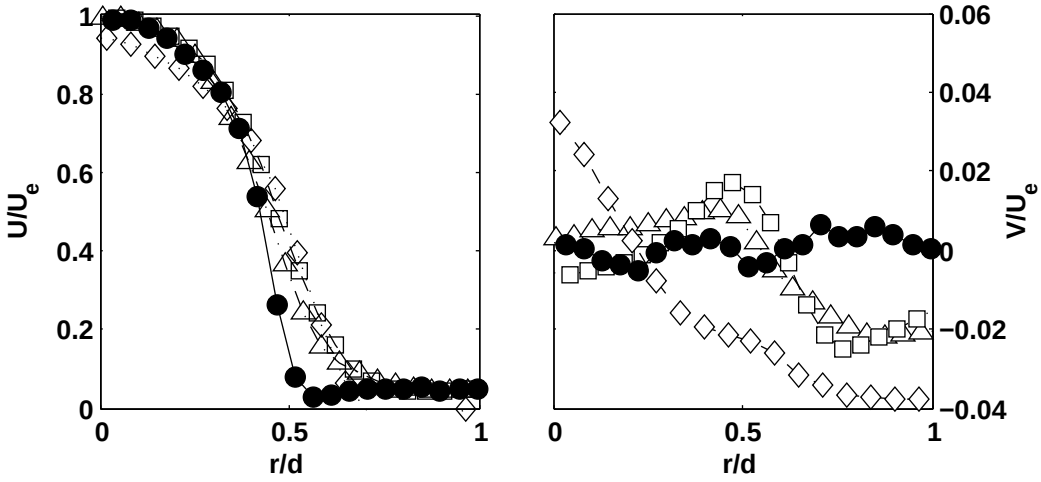

(c) x/d = 0.5

Figure 5.3: Radial profiles of mean axial (left) and radial (right) velocity components ($H/d = 3$, $Re \approx 4200$)

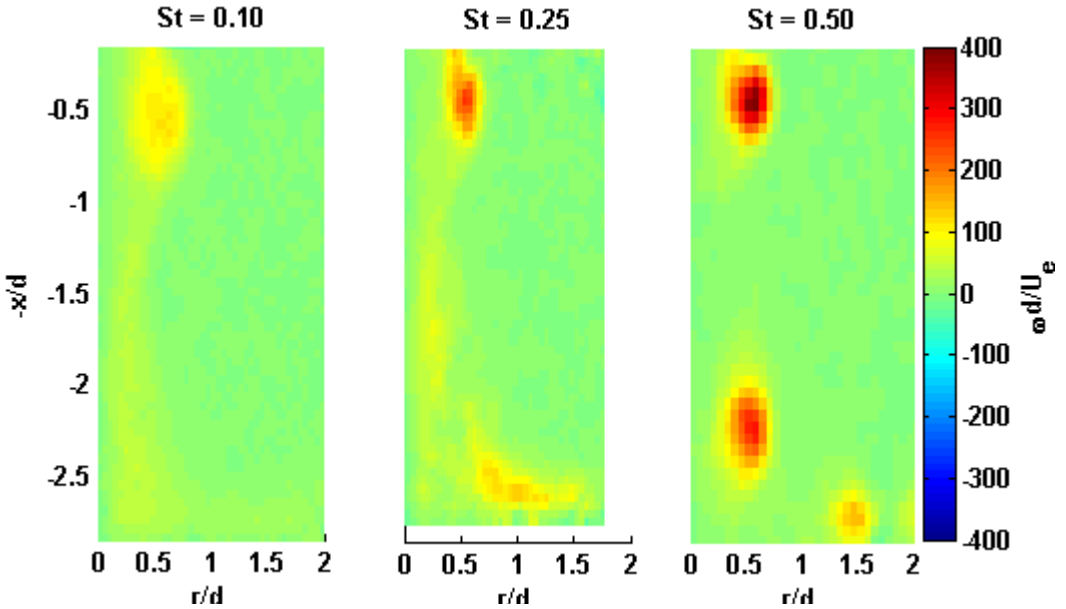

Figure 5.4: Effect of the Strouhal number on the vorticity field ($H/d = 3$, $Re \approx 4200$)

presence of a pulsating frequency for $x/d > 0.5$. Also, the wall jet becomes stronger with increasing the Strouhal number. This indicates that the presence of a pulsation has a considerable effect on the flow field of impinging jets. For instance, the centreline mean axial velocity decay for the various values of St is shown in Fig.5.2. It shows that the centreline velocity decays more rapidly as St is increased, also, it decreases more rapidly than steady jets. For example, up to $x/d \approx 2.5$, pulsed jets exhibit a similar reduction in the centreline axial velocity component (20%), however, for the steady jet, the centreline velocity exhibits a reduction of 20% at $x/d \approx 2.6$.

The presence of a pulsation not only affects the centreline velocity decay, but also the development of the jet in the axial and radial direction, as shown in Fig.5.3. For instance, near the nozzle exit (Fig.5.3c), the radial profiles of the mean axial velocity component (left) for pulsating jets indicate that the presence of a pulsation leads to a more rapid spread of the jet. However, this spread of the jet near the nozzle exit is similar independently of the pulsation frequency (at least for the frequencies tested). Also, the mean radial velocity component is affected by the Strouhal number. Fig.5.3c shows the presence of a local minimum and maximum in the radial profiles of the mean radial component which

increase in magnitude as the Strouhal number is increased. Further downstream, at $x/d = 2.5$, a more rapid spread of the jet as the frequency is increased is evident. Fig.5.3b shows that the radial profiles of the mean axial component become wider as the frequency is increased. Furthermore, the mean radial velocity component also increases as the Strouhal number is increased, once again, indicating that the jet spreads more rapidly as the pulsating frequency is increased. Finally, near the impinging wall (Fig.5.3a), whereas the pulsating frequency does not have a pronounced effect on the mean axial velocity, the mean radial velocity is significantly influenced by the Strouhal number. Fig.5.3a shows that as the pulsating frequency is increased, the mean radial velocity component also increases. This increase is particularly significant for the higher Strouhal numbers tested. The profiles of V/U_e for the higher strouhal numbers exhibit a significant increase when compared to the steady jet. However, for $St = 0.10$, there is a decrease of the radial velocity component when compared to the steady case. The increase of the radial velocity component near the impinging wall as the Strouhal number is increased, could be attributed to the increase in vorticity experienced as the frequency is increased (Fig.5.4). This implies that each individual vortex reaching the target wall carries more angular momentum, in addition, also, as the frequency is increased, such vortices reach the impinging wall more frequently which leads to an increase in the mean radial velocity component, and consequently, a stronger wall jet.

5.2.3 Velocity Fluctuations

Fig.5.5 and Fig.5.6 show the effect of the Strouhal number on the radial and axial velocity fluctuations. These figures show that, overall, there is an increase in the velocity fluctuations, in both the axial and radial directions, as the Strouhal number is increased. This indicates more mixing within the shear layer of the jet as the frequency is increased. Also, both the axial and radial velocity fluctuations are larger for pulsating jets compared to steady jets, even for the lowest frequency tested.

The centreline axial velocity fluctuations are shown in Fig.5.7. It shows that the pulsation frequency also affects the development of the axial velocity fluc-

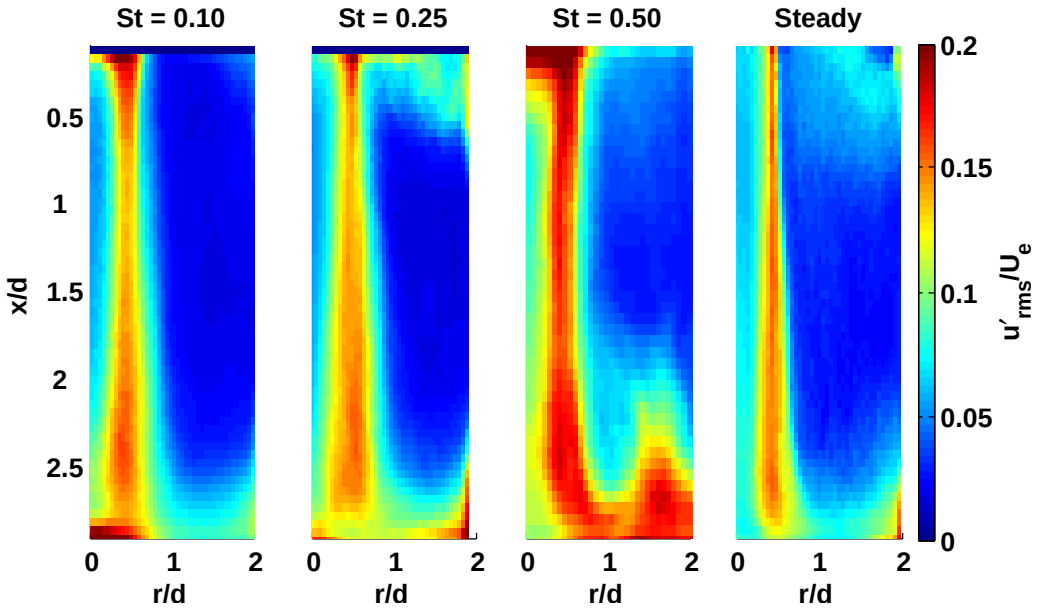

Figure 5.5: Effect of the Strouhal number on the axial velocity fluctuations ($H/d = 3$, $Re \approx 4200$)

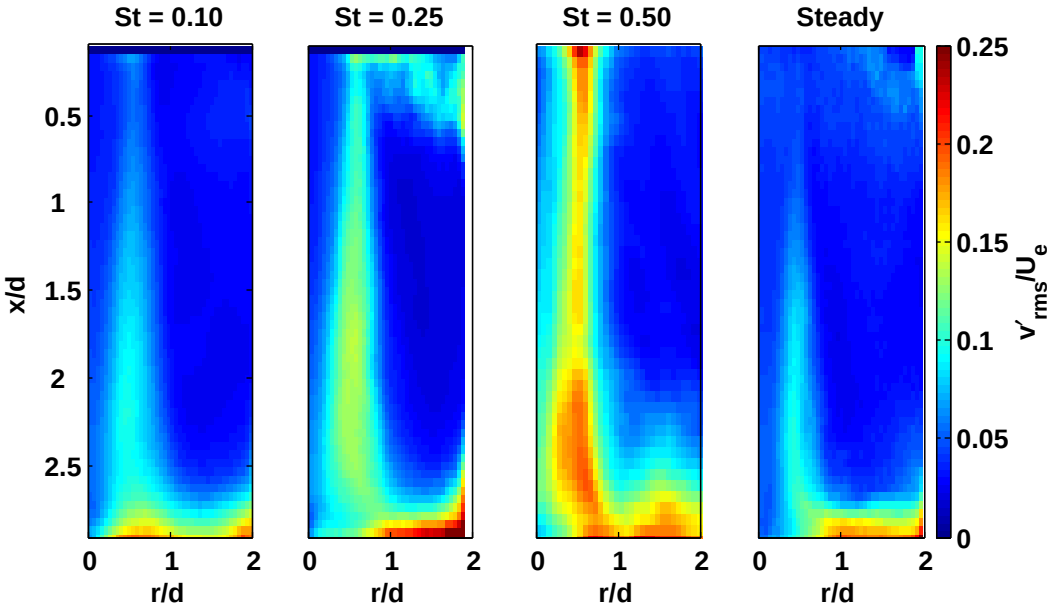

Figure 5.6: Effect of the Strouhal number on the radial velocity fluctuations ($H/d = 3$, $Re \approx 4200$)

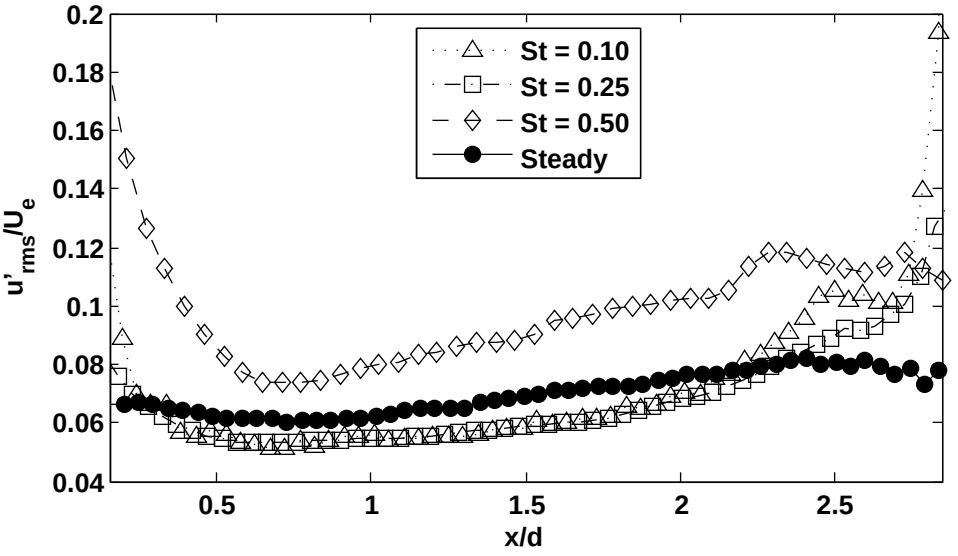

Figure 5.7: Effect of the Strouhal number on the centreline axial velocity fluctuations ($H/d = 3$, $Re \approx 4200$)

tuations. For instance, near the nozzle exit, there is an increase in u'_{rms}/U_e for the pulsating jets when compared to the steady jet, indicating that the presence of a pulsation affects the centreline properties of the jet, thus as St increases, fluid mixing near the nozzle exit is increased. This can be attributed to more frequent fluid acceleration and deceleration cycles as St is increased. Furthermore, Fig.5.7 also shows that for $St = 0.10$ and 0.25, the velocity fluctuations for $0.5 < x/d < 2.2$ are lower than those of the steady jet. This indicates that at these frequencies, the vortex rings are not strong enough to affect the jet centreline. This could also be an indication that mixing is contained within the shear layer of the jet (vortices) more efficiently when the jet is pulsed at $St = 0.10$ and 0.25 than for the steady jet, at least for $0.5 < x/d < 2.2$. However, for $x/d < 2.2$ there is an increase in u'_{rms}/U_e for all pulsed jets. This increase could be a result of the distortion and break up of the vortices, leading to more mixing near the impinging wall for pulsed jets. In addition, the centreline axial velocity fluctuations near the stagnation point decrease with increasing St, probably due to a better preservation of the vortex ring as the frequency is increased, which in turn leads to a stronger influence of the vortices on the jet centreline (see Fig. 5.4 on page 112).

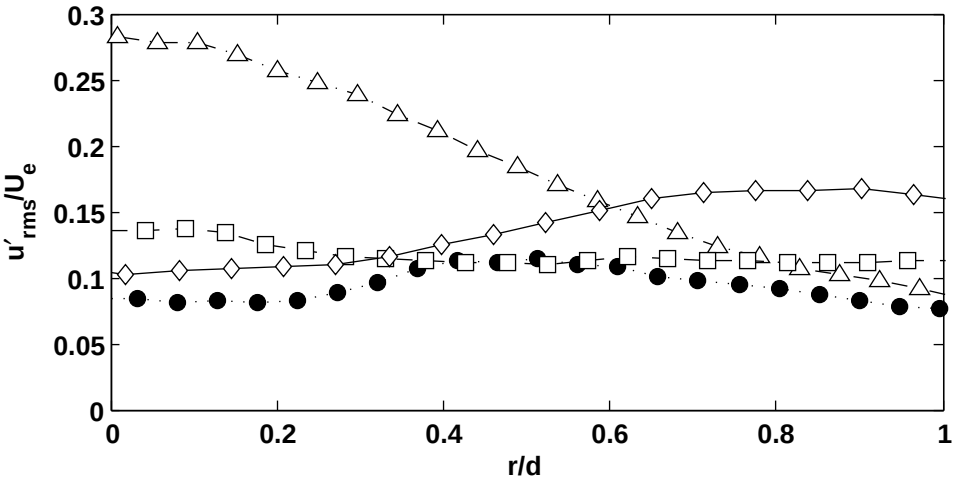

(a) x/d = 2.85

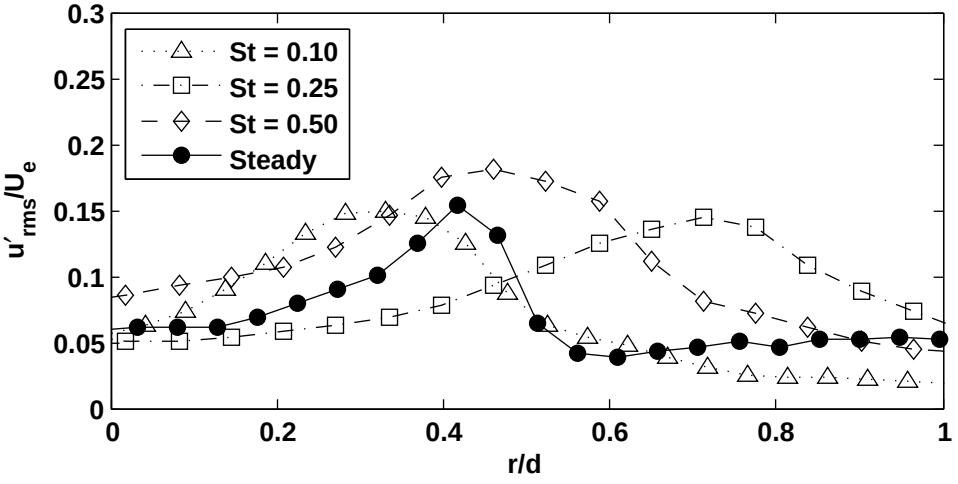

(b) x/d = 0.5

Figure 5.8: Effect of the Strouhal number on the axial velocity fluctuations ($H/d = 3$, $Re \approx 4200$)

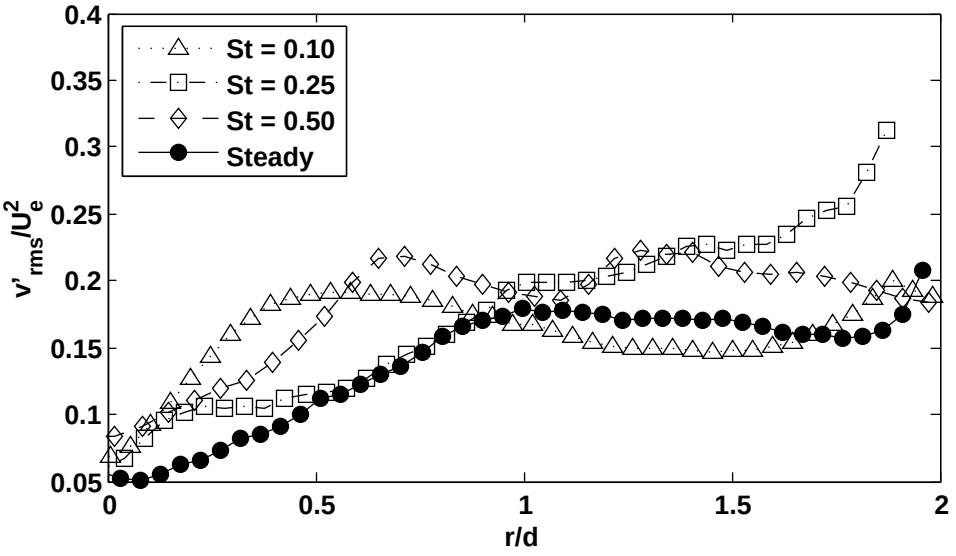

Figure 5.9: Effect of the Strouhal number on the radial velocity fluctuations near the impinging wall ($H/d = 3$, $Re \approx 4200$)

Fig.5.8 shows the axial velocity fluctuations both near the nozzle exit and the impinging wall. At $x/d = 0.5$ (Fig.5.8b), it can be seen that the location of the local maximum is affected by the Strouhal number, however, the location of such maximum does not follow a predictable trend, therefore, requiring further study. However, for the lower frequencies, the local maximum is similar in magnitude to that of the steady jet, only for $St = 0.5$ this maximum becomes larger than that of steady jet. Fig.5.8a, shows that the velocity fluctuations near the impinging wall are larger for pulsed jets. In addition, it shows that for $0 < r/d < 0.3$, there is a reduction of u'_{rms}/U_e as the Strouhal number is increased. It is interesting to notice that the radial profile for $St = 0.1$ shows a reduction of u'_{rms}/U_e for $r/d > 0.3$, whereas, for $St = 0.25$ is almost uniform, however, for $St = 0.5$ there is an increase of u'_{rms}/U_e for $r/d < 0.3$, showing a reversal in the effect of St on the axial velocity fluctuations for the higher pulsating frequency. This increase could be a result of the vortices reaching the impinging surface more frequently, while the influence of the preceding vortex is still present. Nonetheless, this change in the radial profile of u'_{rms}/U_e must occur at a Strouhal number within $0.25 < St < 0.5$ and requires further consideration.

Fig.5.9 shows that the profiles of the radial velocity fluctuations near the

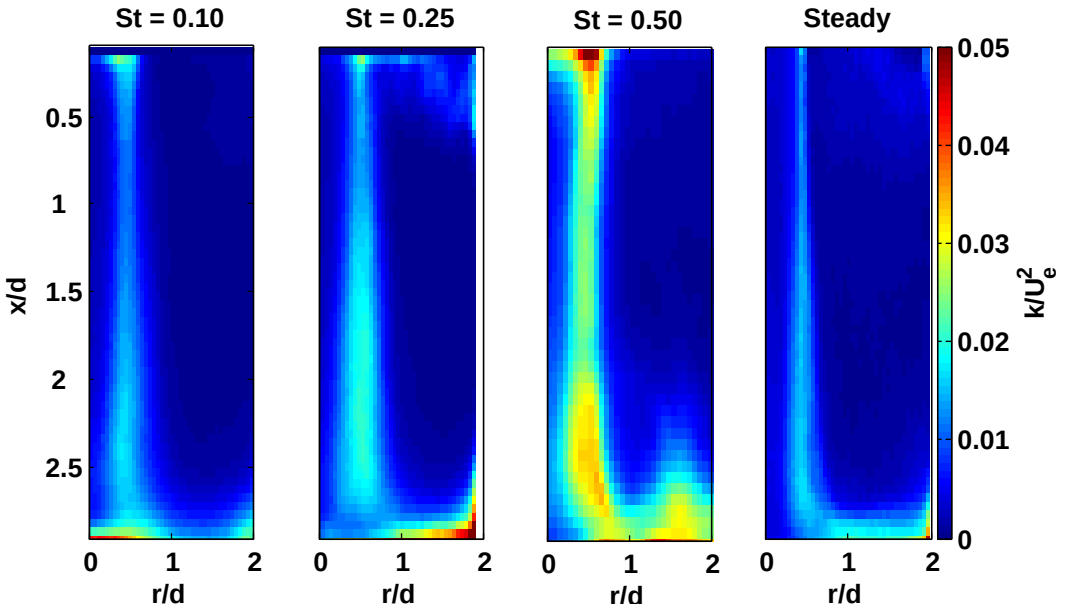

Figure 5.10: Effect of the Strouhal number on the mean turbulent kinetic energy ($H/d = 3$, $Re \approx 4200$)

impinging wall are also affected by the Strouhal number. First of all, it can be observed that the profile for the lower frequency exhibits a trend similar to that of the steady jet since it shows an initial increase of v'_{rms}/U_e followed by a gentle decrease. However, as St is further increased this trend changes, for $St = 0.25$, the radial velocity fluctuations exhibit a steady increase, whereas, for $St = 0.5$, there is an initial increase of v'_{rms}/U_e followed by a gentle decrease and a second local maximum located at approximately $r/d = 1.3$. This second maximum could be a result of the interaction between individual pulses which leads to a local increase of v'_{rms}/U_e (see Fig. 5.4 on page 112).

5.2.4 Turbulent Kinetic Energy

Fig.5.10 shows the effect of St on the mean TKE. It shows that the mean TKE within the shear layer of the jet increases as the Strouhal number is increased. Also, the mean TKE is larger for pulsed jets than steady jets, even for the lowest frequency tested. Interestingly, for the jet pulsed at $St = 0.5$ there is marked increase of the mean TKE within the shear layer at $2 < x/d < 2.8$. This increase could be attributed to the fact that pulses reach the surface more frequently, which are also relative stronger compared to those with lower Strouhal number

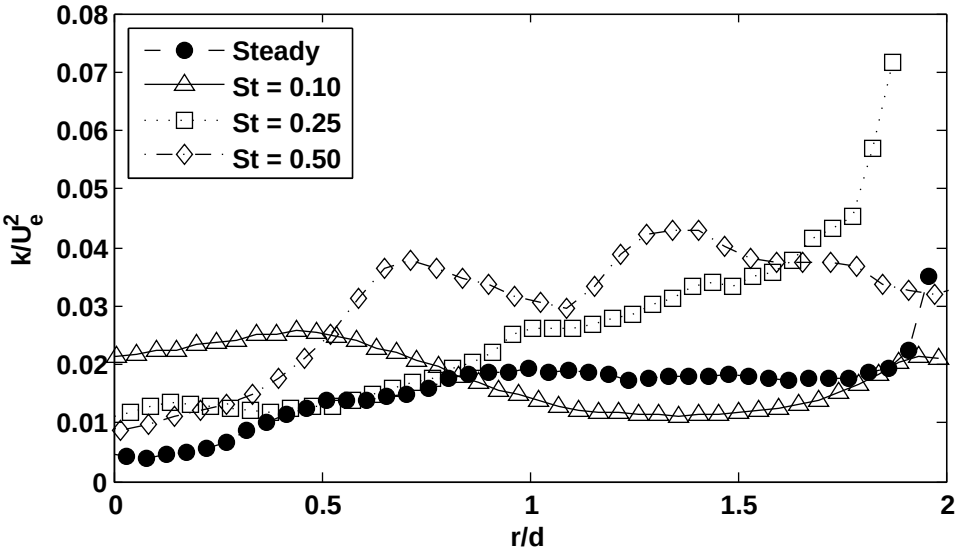

Figure 5.11: Effect of the Strouhal number on the mean turbulent kinetic energy near the impinging wall ($H/d = 3$, $Re \approx 4200$)

(see Fig.5.4), therefore, having interacting effects with each other, while also being distorted by the impinging wall, which in turn leads to increased mixing in this region.

Fig.5.11 shows the effect of the pulsating frequency on the mean TKE near the impinging wall. First of all, it can be observed that the profiles of the mean TKE have different trends depending on the Strouhal number. Firstly, when the jet is pulsed at $St = 0.10$ there is an increase in the mean TKE for $0 < r/d < 0.75$ when compared with the steady case, followed by a decreased for $r/d > 0.75$, where the mean TKE reaches levels lower than that of the steady jet. Secondly, for $St = 0.25$ the mean TKE exhibits a gently increase in the radial direction, following a trend similar to that of the steady jet, however, it exhibits larger values for $r/d > 0.75$. Finally, for $St = 0.5$ the radial profile of the mean TKE exhibits two local maxima, the first located at $r/d \approx 0.6$, and the second located at $r/d \approx 1.4$. These differences in the radial profiles of the mean TKE can be attributed to both the difference in vorticity strength, and the frequency at which vortex rings reach the target wall. For instance, for the lowest Strouhal number, the vortex rings are rather weak and get distorted before reaching the target wall, which explains the larger values of the mean TKE at the stagnation region. In

addition, they reach the target surface less frequently, which can explain the lower values of k/U_e^2 for $r/d > 0.75$. The steady increase in the mean TKE for $St = 0.25$ could be a result of a relative stronger vortex ring reaching the wall in isolation, that is, without being influenced by preceding vortices. This indicates that not only the pulsating frequency would have an effect on the interaction between vortices at the wall, but also the nozzle-to-plate spacing, and must be considered (section 5.5). Finally, the presence of two local maxima in the radial profile of the jet pulsed at $St = 0.5$ could be a result of stronger vortices interacting with each other near the impinging wall, leading to the development of a second maximum, whereas, the first maximum coincides with the location where the inner part[1] of the vortex rings impinge with the wall initially (see Fig. 5.4 on page 112).

5.2.5 Skewness Factor

The effect of the Strouhal number on the axial and radial skewness factor is shown in Fig.5.12 and Fig.5.13 respectively. Fig.5.12 shows that the pulsating frequency has a strong effect on the axial skewness factor. It shows that for the lower pulsating frequency, the distribution of the axial skewness factor within the shear layer is unbalanced, having a more pronounced negative distribution. This indicates that there is a significant presence of turbulent deceleration within the jet core. However, as the Strouhal number is increased, the distribution of u'^3/U_e^3 becomes relatively more balanced. Nonetheless, the values of u'^3/U_e^3 increase in magnitude with increasing the Strouhal number. Interestingly, the distribution of u'^3/U_e^3 within the shear layer for the jet pulsated at $St = 0.25$ is similar to that of the steady jet. This is probably due to individual pulses reaching the impinging wall without being influenced by each other, as opposed to jet pulsed at $St = 0.5$, also, its pulses are strong enough and are not significantly distorted by the ambient fluid, as opposed to the jet pulsed at $St = 0.10$ which experiences strong turbulent diffusion. Finally, for $St = 0.5$, at $2 < x/d < 2.8$ and $1 < r/d < 2$, the axial skewness factor is negative in contrast to the other jets, indicating that the values of the turbulent axial velocity component tend to fall below the local mean. This could be a result of the interaction between

[1]Refers to the peripheral side of the vortex closest to the jet axis

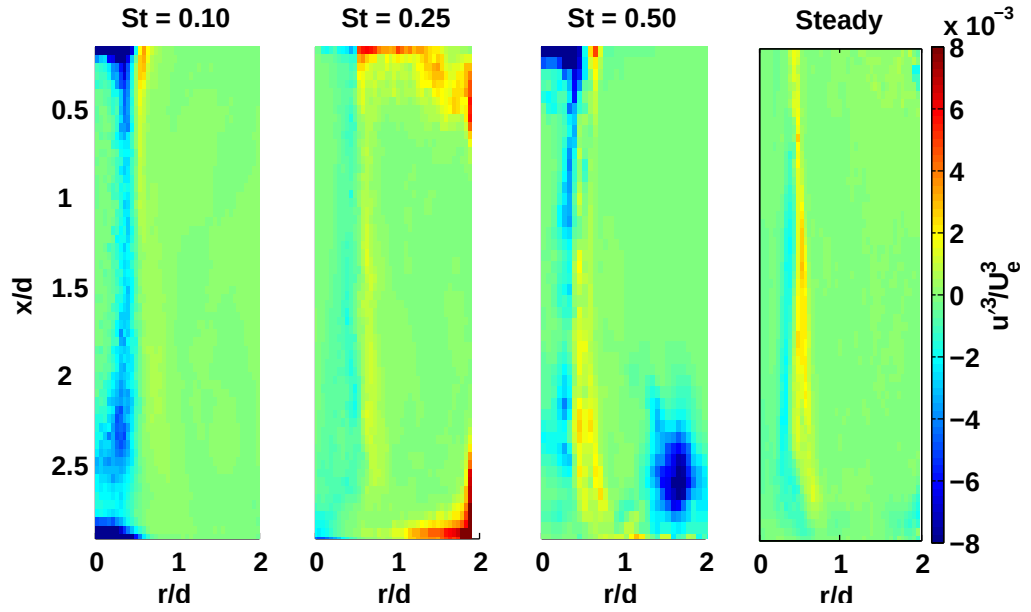

Figure 5.12: Effect of the Strouhal number on the skewness factor in the axial direction ($H/d = 3$, $Re \approx 4200$)

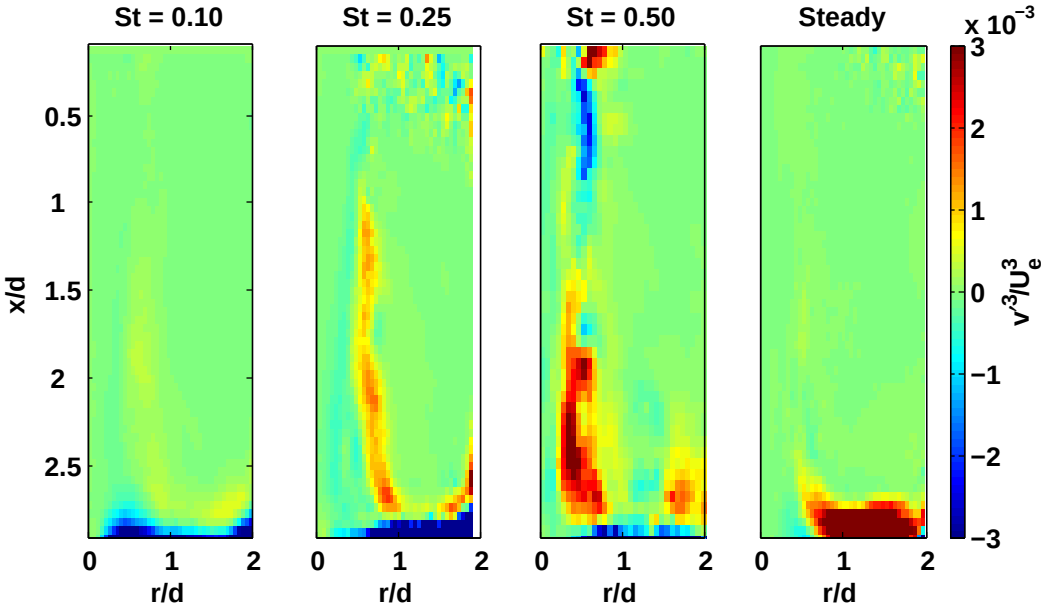

Figure 5.13: Effect of the Strouhal number on the skewness factor in the radial direction ($H/d = 3$, $Re \approx 4200$)

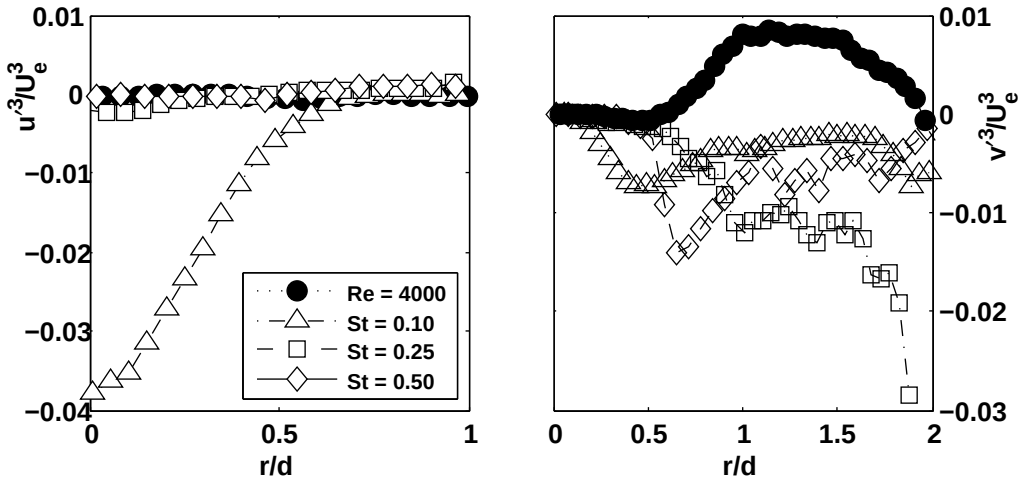

Figure 5.14: Effect of the Strouhal number on the axial (left) and radial (right) skewness factor near the impinging wall ($x/d = 2.85$,$H/d = 3$, $Re \approx 4200$)

vortex rings, or their relative strength, which forces the fluid away from the wall.

Fig.5.13 shows that the radial skewness factor is significantly affected by the presence of a pulsation, indicating that the radial turbulent component within the shear layer of pulsating jets has a stronger influence on the Reynolds stress than for steady jets. It also shows that the distribution of v'^3/U_e^3 near the impinging wall is negative for pulsating jets, whereas, it is positive for steady jets. This could be due to the vortices travelling along the impinging wall leading to a flatter radial velocity profile which does not exhibit sudden deceleration (see Fig.5.3a). In contrast, the rapid deceleration present for the steady jet is thought to be responsible for the positive values of the radial skewness factor, since it seems to generate positive bursts in the turbulent part of the radial velocity component which leads to turbulent acceleration, i.e. positive v'^3/U_e^3. Finally, Fig.5.14 (right) confirms that the radial profiles of v'^3/U_e^3 are negative for pulsed jet, but positive for the steady jet. In addition, Fig.5.14 (left) shows that for the jet pulsed at $St = 0.10$ the profile of u'^3/U_e^3 is negative and significantly lower than the other jets, which exhibit virtually no deviation compared to the steady jet. This strong reduction in the values of u'^3/U_e^3 for $St = 0.10$ could be attributed to its weaker pulse which is damped out by either the wall or the surrounding fluid. Therefore, the distribution of the Reynolds stress for the such jet will most likely exhibit strong entrainment near the stagnation region (see section 5.2.6).

5.2.6 Reynolds Stress

The distribution of the Reynolds stress is also affected by the Strouhal number. Fig.5.15 shows that initially, as the frequency is increased, both entrainment (en) and expulsion (e) within the shear layer increase. However, as the frequency is further increased to $St = 0.5$, there is a significant decrease in the entrainment Reynolds stress (en), in particular for $0 < x/d < 1.5$. This reversal in the effect of the Strouhal number must occur at a pulsating frequency greater than 0.25. Interestingly, taking the steady case as a reference, a critical frequency can be defined as $St_c = d/U_e$ and is equal to $St_c = 0.23$. Therefore, the steady jet case could be use in order to estimate the value of the Strouhal number at which a reduction in the entrainment Reynolds stress (en) is expected.

Fig.5.15 also shows that near the impinging wall the Strouhal number has a strong effect on the type of Reynolds stress and its distribution. For instance, for $St = 0.10$, the Reynolds stresses near the impinging wall are positive and associated with ejection (E). Also, high-speed fluidic interactions in the direction away from the wall are also present (O). However, for $St = 0.25$, Reynolds stress associated with low-speed interaction towards the wall (W) are present, as well, as sweeping Reynolds stress (S) just above. This indicates that as the frequency is increased from $St = 0.10$ to $St = 0.25$, the momentum transport due to the Reynolds stress has a general tendency to act towards the impinging wall. For $St = 0.5$, and similarly to the jet pulsed at $St = 0.25$, sweeping (S) and wallwards Reynolds stress (W) are also present, however, high-speed fluidic interactions away from the impinging wall (O) are also present at $1.5 < r/d < 2$ which indicates that momentum is initially directed towards the impinging wall, then away from it. Finally, the steady case shows that the Reynolds stress is mainly due to high-speed fluidic interactions away from the impinging wall. It is interesting to observe that the distribution of the Reynolds stress for the jet pulsed at $St = 0.5$ resembles that of a jet with a much higher Reynolds number (see Fig. 4.21 on page 83). Therefore, it can be argued that the pulsating frequency would have a significant effect on the heat transfer characteristics of the jet.

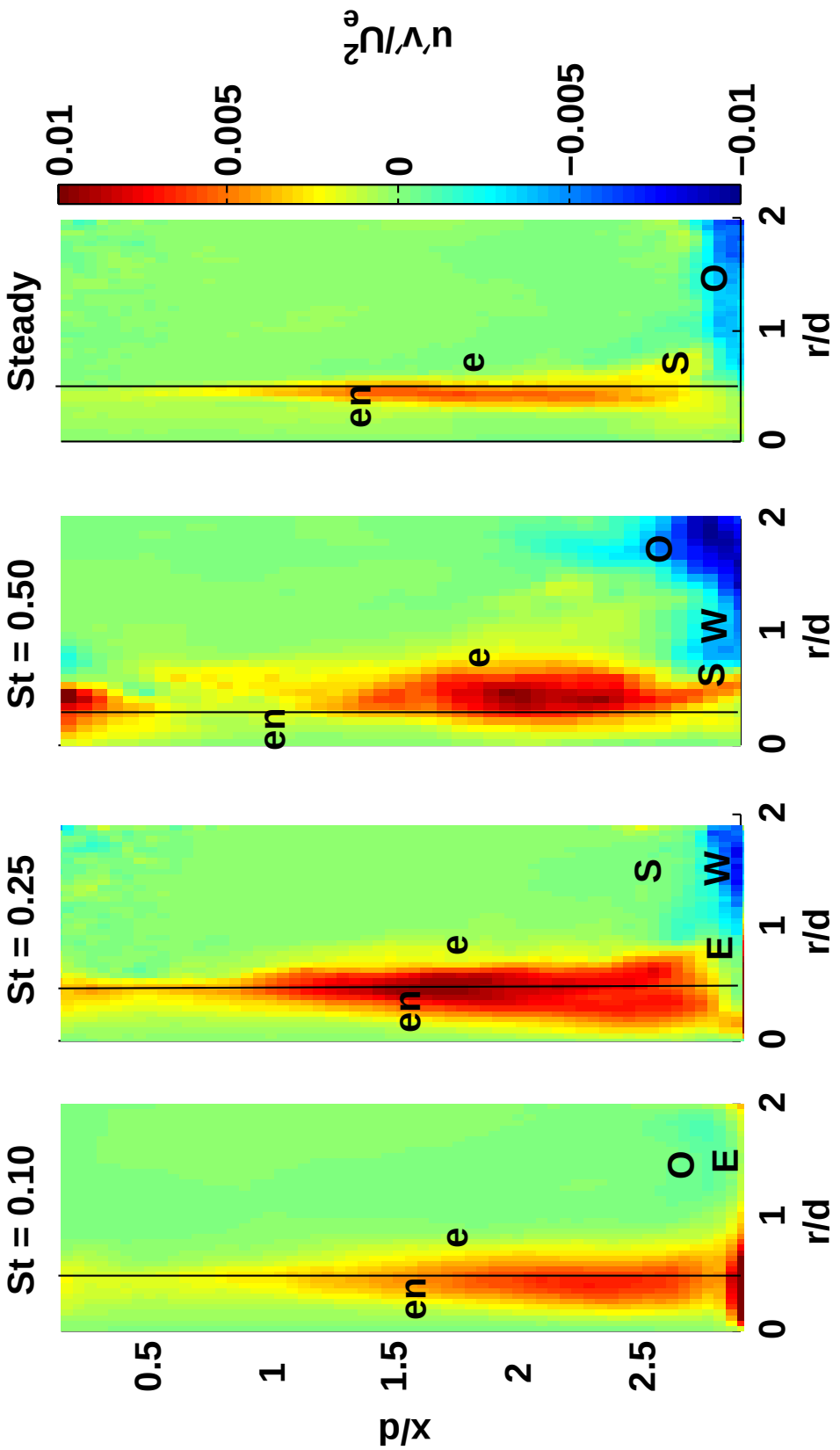

Figure 5.15: Effect of the Strouhal number on the Reynolds stress; entrainment (en), expulsion (e), ejection (E), sweep (S), wallward interaction (W), outward interaction (O) ($H/d = 3$, $Re \approx 4200$)

5.2.7 Mean Axial Momentum Balance Near the Wall

Fig.5.16 shows the momentum balance of a transitional jet pulsated at different Strouhal numbers. First of all, it can be seen, that overall, the axial momentum transfer is reduced by the presence of a pulsating frequency. However, this figure also shows that as the Strouhal number is increased, the contribution to momentum transport due to the radial diffusion also increases. For instance, for $St = 0.5$, the radial diffusion reaches levels similar to that of the steady. This enhancement on the contribution of the radial diffusion is a direct consequence of the increase in the radial velocity component near the impinging wall as St is increased, as shown in Fig.5.3a. Furthermore, the increase in the momentum transfer due to the radial diffusion for $St = 0.5$ is such, that for $r/d > 0.65$, it is converted into static pressure more efficiently than the steady case. This would suggest that further increases in the Strouhal number could lead to an enhancement in the momentum transfer due to radial diffusion.

Fig.5.16 also shows a significant change in the distribution of the mean axial momentum balance for the lower pulsating frequency, since the pressure term has become a source, whereas, the normal stress is a sink term, indicating a momentum transfer from the mean to the turbulent field. This could be attributed to the increased levels of Reynolds stress related to entrainment present near the stagnation point for such jet, as seen in section 5.2.6 (Fig.5.15). Furthermore, the increase of entrainment Reynolds stress is produced by a significant reduction in the axial triple correlations, which is linked to turbulent deceleration, therefore, leading to the normal stress becoming a sink term. Fig.5.16 shows that for the jet pulsed at $St = 0.25$, the normal stresses are also a sink term, however, as St is increased to $St = 0.5$, the distribution of the terms in the momentum balance adopts a pattern similar to that of the steady jet. Interestingly, this change occurs when the strouhal number is larger than St_c[2], which is based on the steady jet, and has a values of $St_c = 0.23$. It also corresponds to the change observed in the behaviour of entrainment and ejection Reynolds stresses when $St \gtrapprox St_c$, shown in Fig. 5.15 on the previous page.

[2] St_c was defined as $St_c = d/U_e$ based on the steady jet

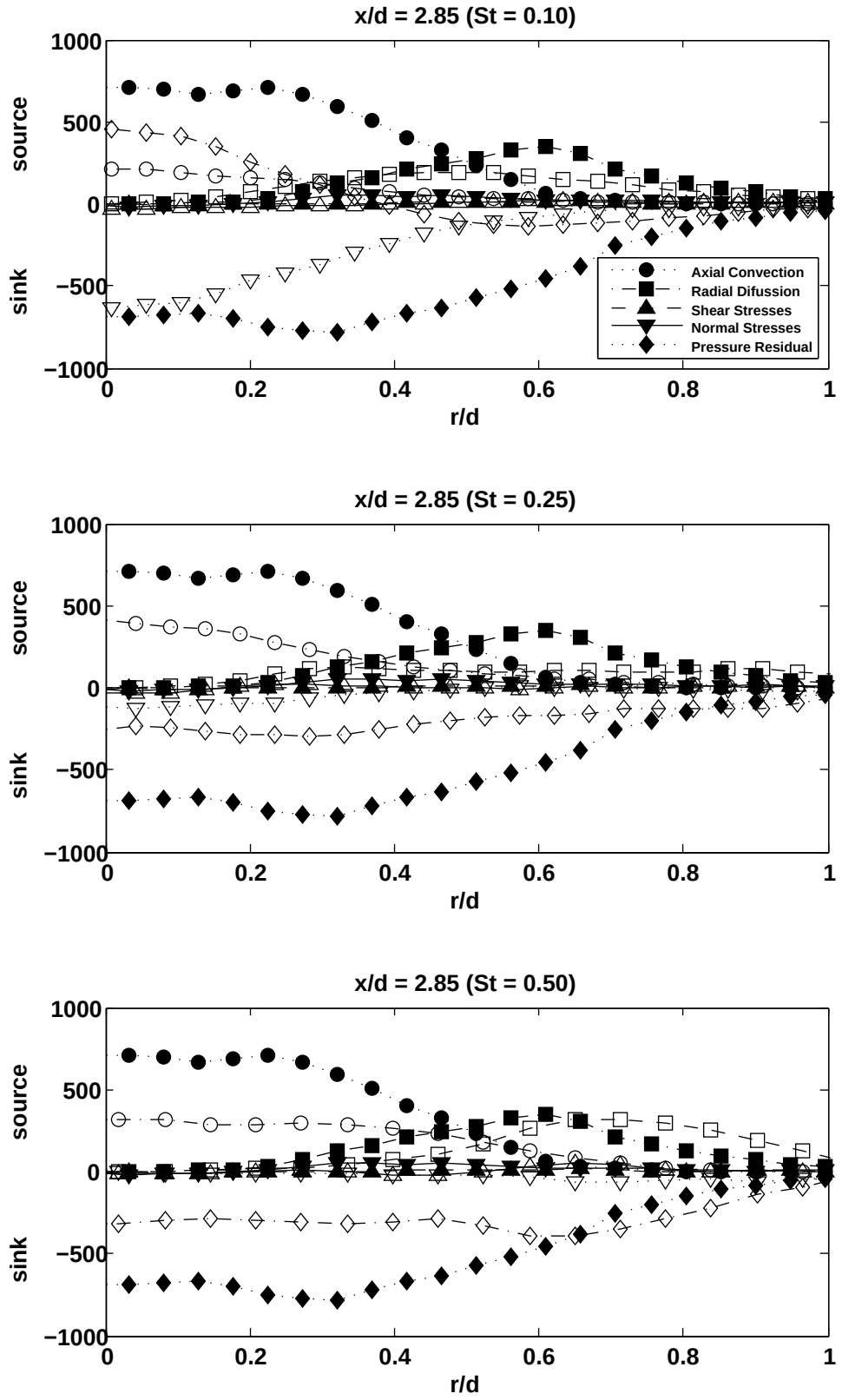

Figure 5.16: Effect of the Strouhal number on the mean axial momentum balance non-dimensionalised by d/U^2; closed symbols - steady jet, open symbols pulsed jet ($x/d = 2.85$)

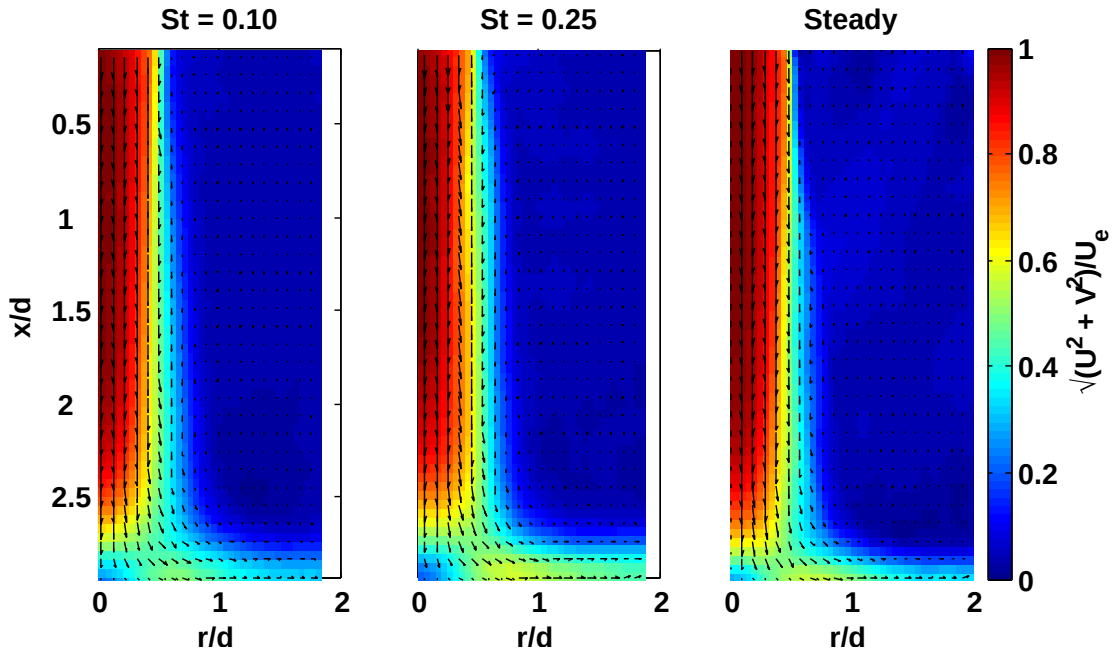

Figure 5.17: Effect of the Strouhal number on the time-averaged velocity field ($Re \approx 10200$, $H/d = 3$)

5.3 Effect of the Frequency (Turbulent Jets)

5.3.1 Introduction

The effect of the non-dimensional frequency, St, on the flow field of turbulent pulsating impinging jets will be explored in this section. All the other parameters that affect the flow field of pulsating jets were kept constant ($Re \approx 10200$, $H/d = 3$, and $d = 30.5mm$). The non-dimensional frequency was set at $St = 0$ (steady jet), 0.10 and 0.25.

5.3.2 Time-Averaged Flow Field

Firstly, the effect of the strouhal number on the time-averaged velocity field of turbulent pulsating impinging jets is shown in Fig.5.17. It shows that as the Strouhal number is increased, the jet core spreads more rapidly, also, the wall jet becomes stronger. This trend is similar for transitional impinging jets as shown in section 5.2. The pulsating frequency also affects the development of the jet centreline axial velocity as shown in Fig.5.18 shows, as expected, that the centre-line velocity decays more rapidly as the Strouhal number is increased. It was also

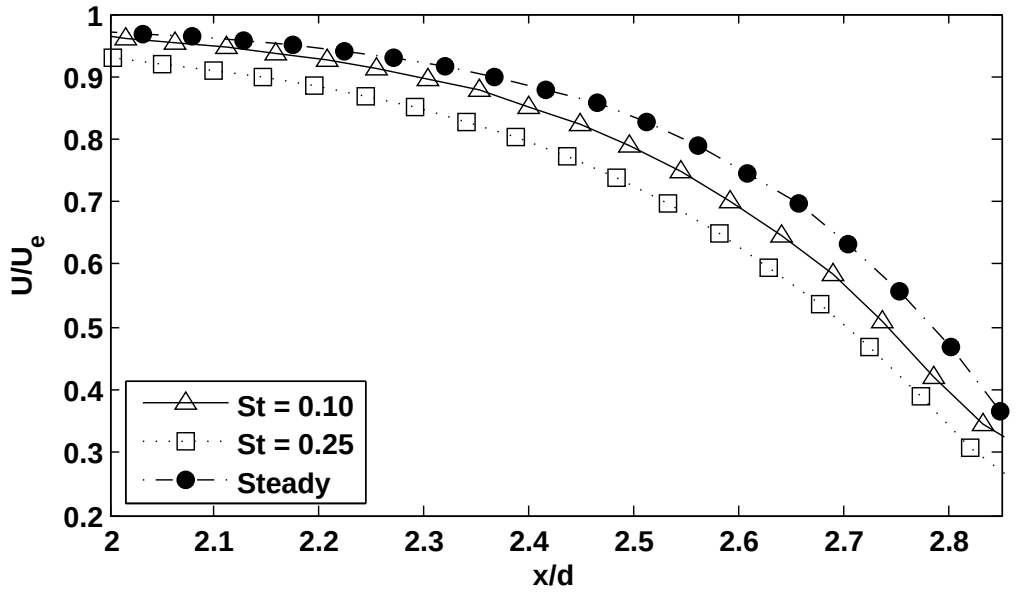

Figure 5.18: Centreline mean axial velocity decay ($Re \approx 10200$, $H/d = 3$)

found that the centreline axial velocity decays more rapidly for turbulent pulsating jets than transitional jets. It begins to decay at $x/d \approx 1.75$ for transitional pulsating jets and at $x/d \approx 1.50$ for turbulent pulsating jets. This indicates that the Reynolds number has a pronounced effect on the centreline velocity decay for pulsating jets, whereas, it has no significant effect on the centreline velocity decay for steady jets (as shown in the previous chapter). Hence, the effect of the Reynolds number in the presence of a pulsating frequency must also be considered and studied (see section 5.4 on page 144).

The development of the mean axial and radial velocity components at various axial locations is shown in Fig.5.19. It shows that near the nozzle exit (Fig.5.19c), the profiles of U/U_e are similar for both pulsating frequencies and they are also similar to the profile of the steady jet. Further downstream, at $x/d = 2.5$ (Fig.5.19b), although the profiles of U/U_e are almost identical, the profiles of V/U_e confirm that as the Strouhal number is increased, the jet spreads more rapidly. However, the Strouhal number has a stronger influence of the spread of transitional jets. Finally, near the impinging wall (Fig.5.19a), whereas the mean axial velocity component is not significantly affected by the pulsating frequency, it plays an important role in the development of the radial velocity component. As the frequency is increased the radial velocity component increases.

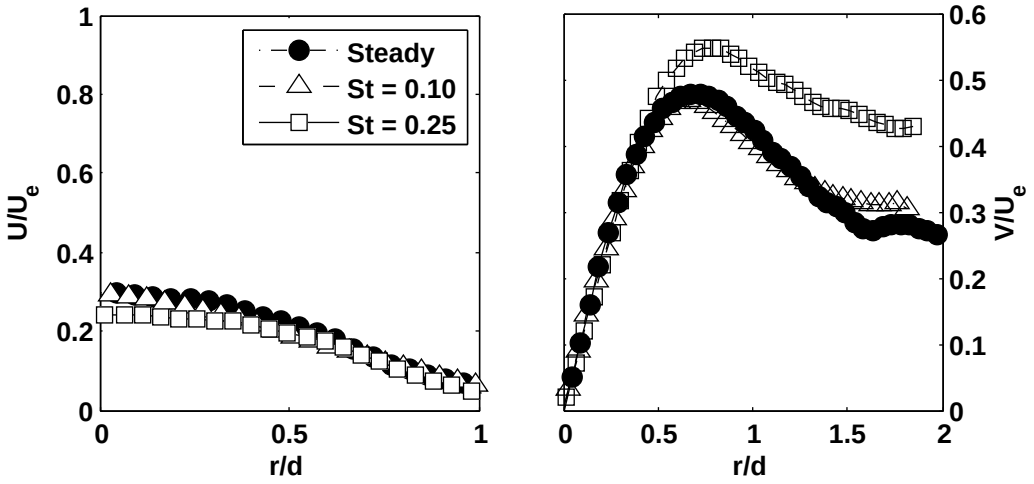

(a) x/d = 2.85

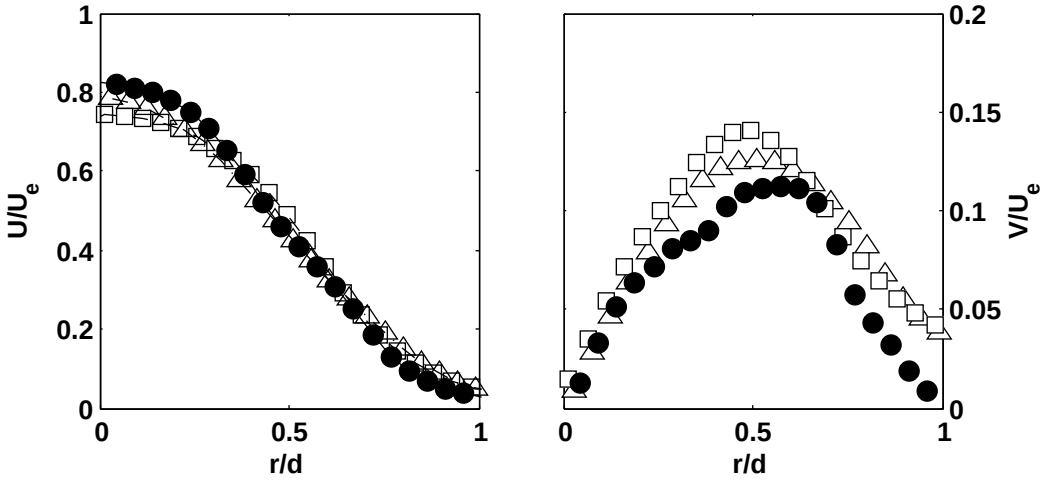

(b) x/d = 2.5

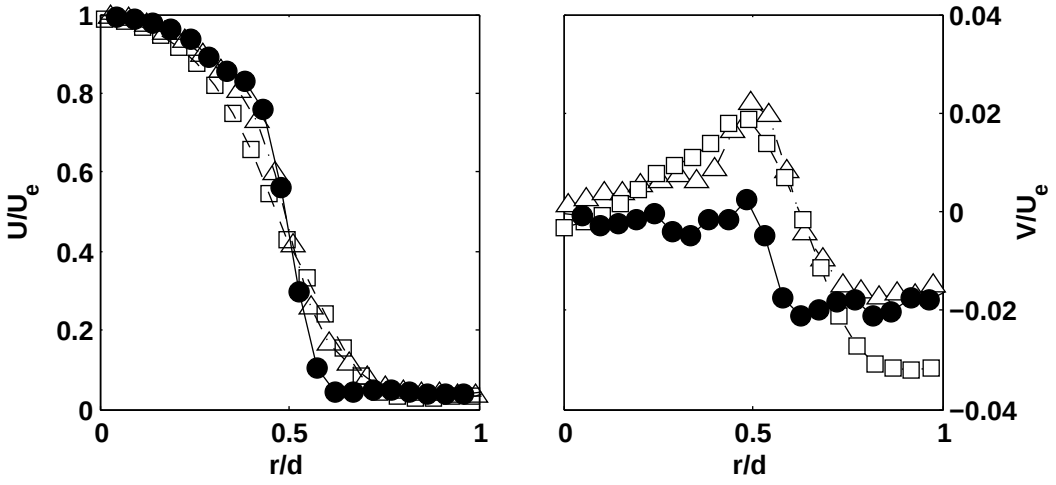

(c) x/d = 0.5

Figure 5.19: Radial profiles of the mean axial (left) and radial (right) velocity components ($Re \approx 10200$, $H/d = 3$)

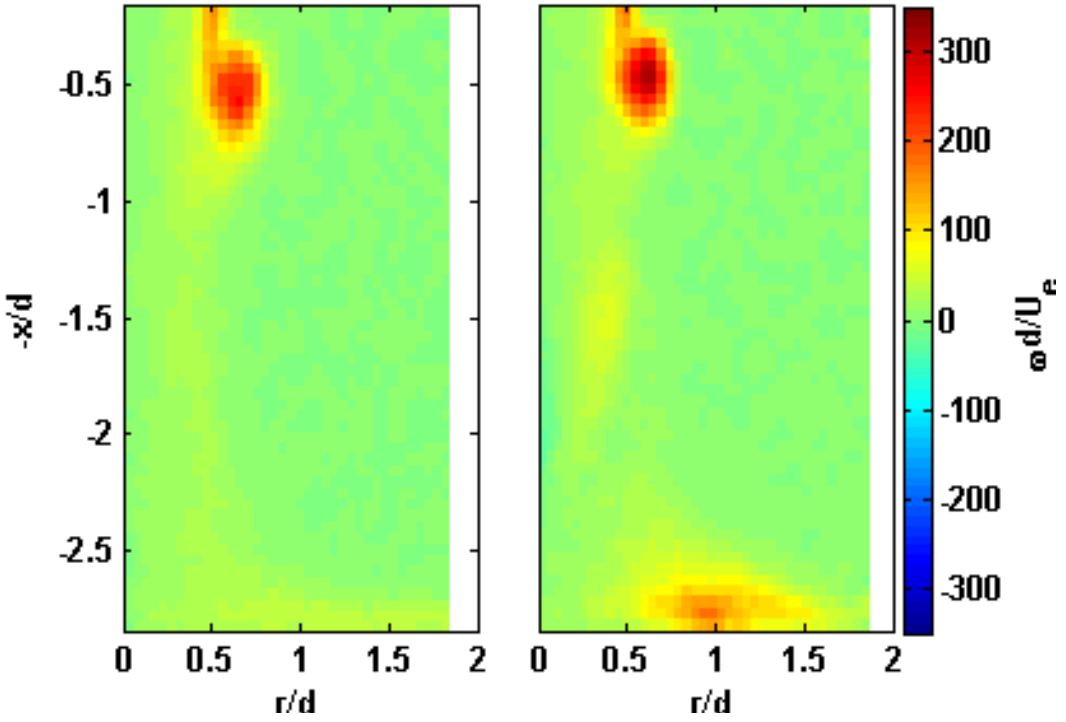

Figure 5.20: Effect of the Strouhal number on the vorticity field ($Re \approx 10200$, $H/d = 3$)

The effect of the frequency is so pronounced, that for $St = 0.25$ the radial velocity is much larger than that of a steady jet. The frequency also affects the location of the local velocity maximum, as St is increased, the local maximum shifts away from the stagnation point. Similarly to transitional jets, the increase of the radial velocity component near the impinging wall can be attributed to vortex rings impinging on the wall more frequently as the Strouhal number is increased, as shown in Fig.5.20. In addition, as the Strouhal number is increased, the vorticity near the surface also increases, which indicates that the tangential velocity at the outskirts of the vortex rings is better preserved as St is increased. As a result, when St is increased, not only the vortex ring reaches the impinging wall more frequently, but it also carries more tangential velocity as it travels across the impinging wall. The movement of the vortex ring away from the centreline, which is caused by the presence of the wall, is then translated into a larger value of the mean radial velocity component near the wall.

5.3.3 Velocity Fluctuations

The effect of the Strouhal number in the axial and radial velocity fluctuations is shown in Fig.5.21 and Fig.5.22 respectively. First of all, it can be observed that as the Strouhal number is increased the axial velocity fluctuations decrease. In contrast, as it was shown in the previous section, the effect of the pulsating frequency on transitional jets is the opposite. This reduction could be attributed to the fact that the vortex rings are much stronger for turbulent pulsating jets (see Fig. 5.20 on the previous page, and Fig. 5.4 on page 112), and therefore, less prone to being distorted, also, to the larger exit velocity of the turbulent jet, making the ratio u'_{rms}/U_e reduce. However, similarly to transitional jets, the radial velocity fluctuations increase as the Strouhal number is increased as shown in Fig.5.22. This increase in the radial direction could be a result of the increase in the spread of the jet with increasing St since the vortex rings, which carry most of the velocity fluctuations, experience a larger radial displacement, however, this increase is more pronounced for transitional pulsating jets, since the spread of the jet is more dependent on the Strouhal number as seen in section 5.2 on page 109.

The axial velocity fluctuations at the jet centreline are also affected by St as shown in Fig.5.23. This figure shows that near the nozzle exit, the axial velocity fluctuations increase as the Strouhal number is increased. This increase could be a result of fluid acceleration and deceleration present in this region, which becomes more pronounced as the frequency is increased, leading to higher values of u'_{rms}/U_e. Furthermore, for $x/d > 0.5$ the velocity fluctuations increase steadily, up to approximately $x/d = 2.5$, where the presence of the wall, and velocity deceleration, leads to a decrease in u'_{rms}/U_e. Overall, increasing the Strouhal number leads to an increase of the centreline axial velocity fluctuations.

Fig.5.24 shows radial profiles of the axial velocity fluctuations at various axial locations. It confirms that throughout the development of the turbulent the jet, for approximately $0.4 < r/d < 0.6$, the effect of the pulsating frequency is to reduce u'_{rms}/U_e, whereas, for transitional jets, increasing the pulsating frequency leads to an overall increase of u'_{rms}/U_e. This indicates that for turbulent impinging jets, the presence of the pulsation helps control the shear layer of the jet and reduces mixing. Nonetheless, outside the shear layer, turbulent pulsating jets, in

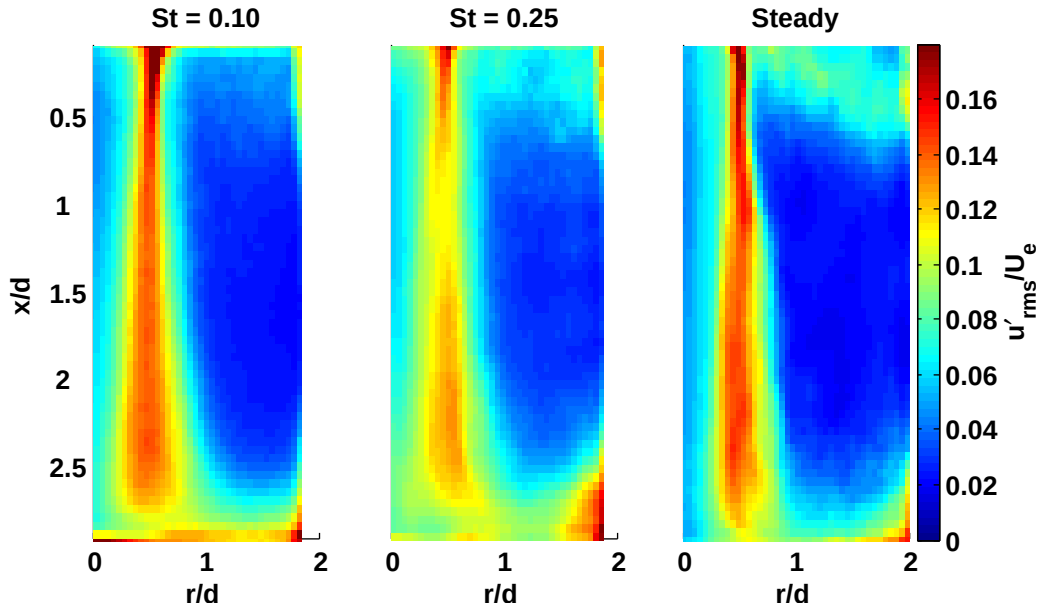

Figure 5.21: Effect of the Strouhal number on the axial velocity fluctuations ($Re \approx 10200$, $H/d = 3$)

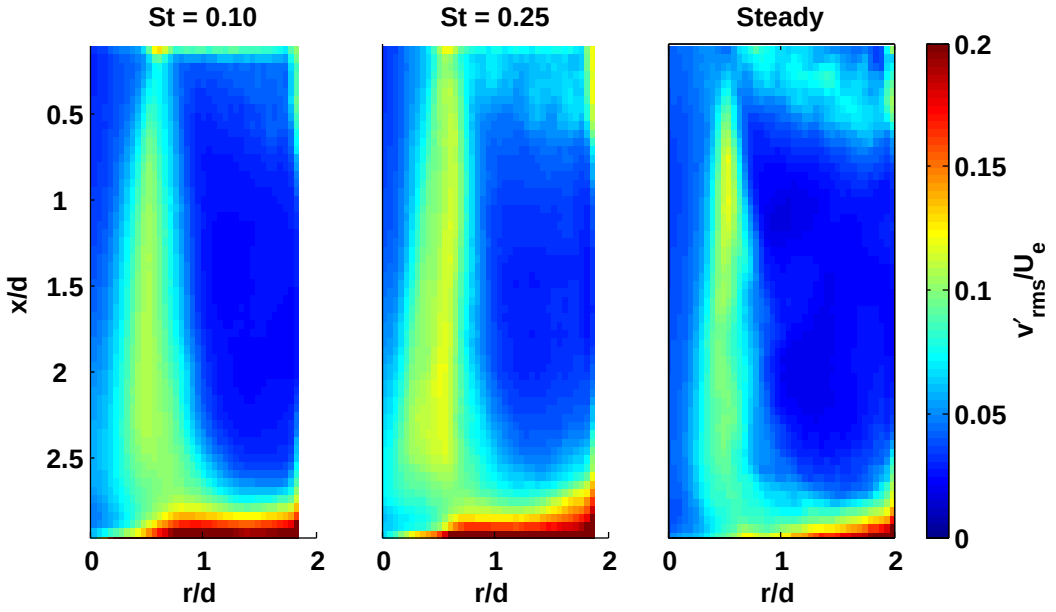

Figure 5.22: Effect of the Strouhal number on the radial velocity fluctuations ($Re \approx 10200$, $H/d = 3$)

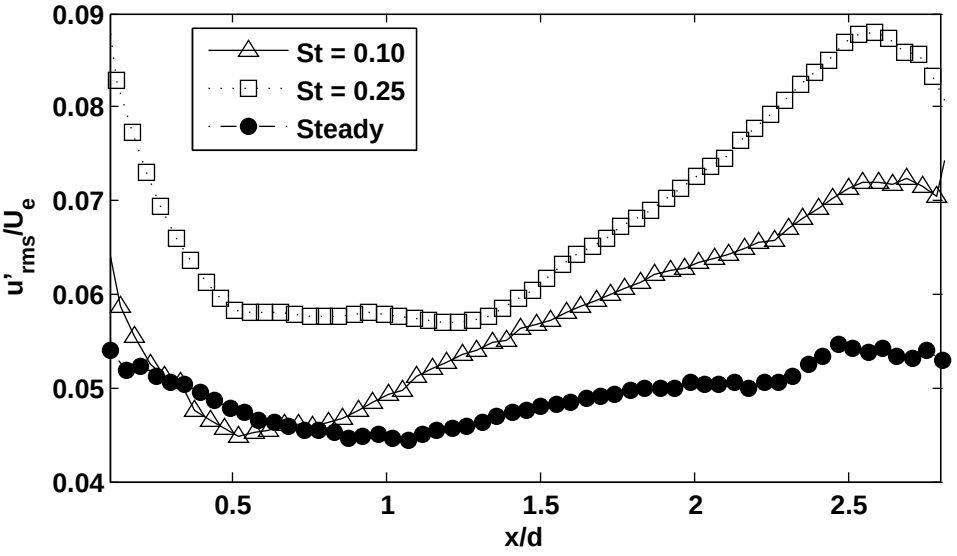

Figure 5.23: Effect of the Strouhal number on the centreline axial velocity fluctuations ($Re \approx 10200$, $H/d = 3$)

comparison to steady jets, exhibit similar or slightly larger velocity fluctuations, which are reduced when the Strouhal number is increased.

Finally, Fig.5.22 showed that, within the shear layer, increasing St leads to increases in v'_{rms}/U_e. However, near the impinging wall this effect is reversed as shown in Fig.5.25. The effect of increasing the Strouhal number is similar to the effect of increasing the Reynolds number for steady jets. Therefore, it could be argued that the development of a stronger wall jet as the Strouhal number is increased (see Fig.5.19a) could be the reason for this reduction of v'_{rms}/U_e. However, the radial velocity fluctuations for the pulsed jet are significantly larger than the steady jet, probably as a result of surface renewal caused by the pulses impinging on the wall. An interesting observation is that the behaviour of the velocity fluctuations is significantly more predictable for turbulent pulsating jets than transitional pulsating jets.

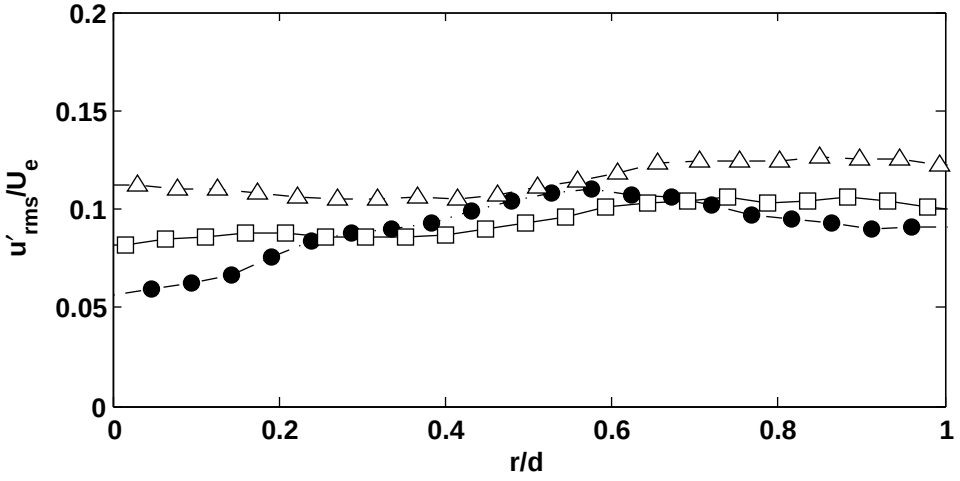

(a) x/d = 2.85

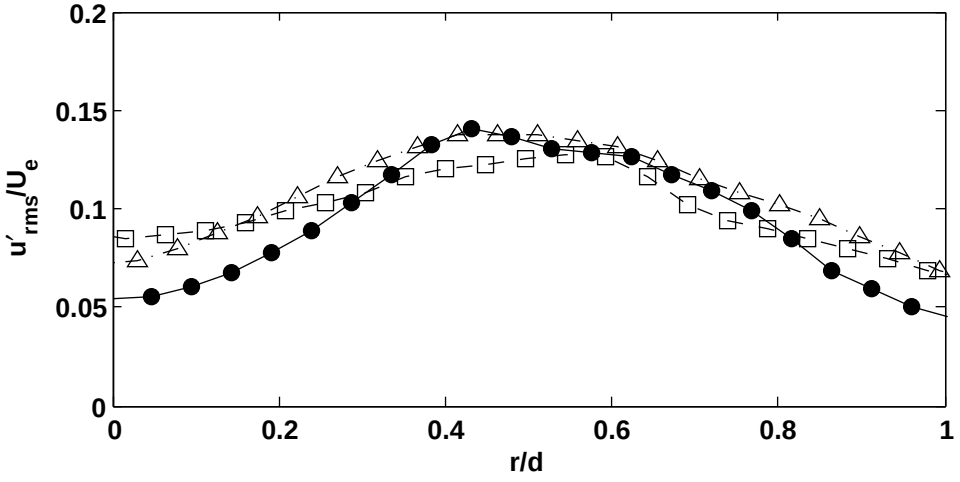

(b) x/d = 2.5

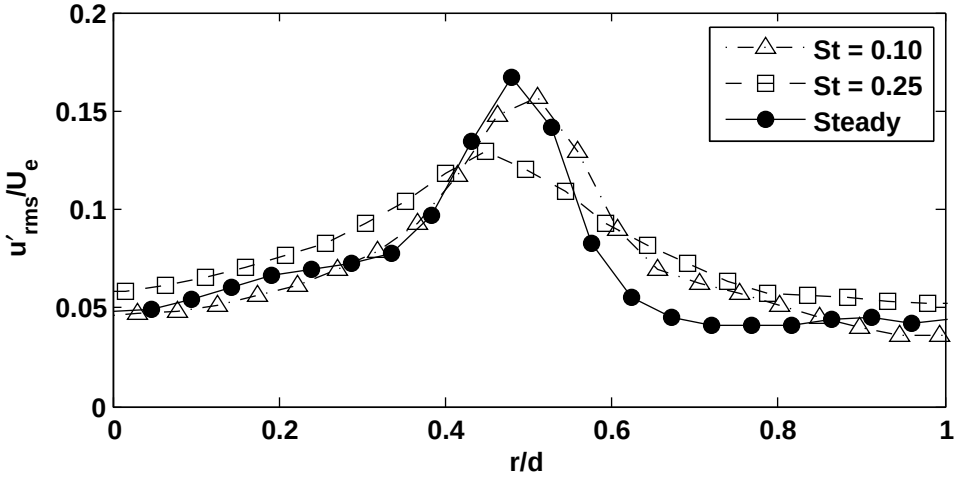

(c) x/d = 0.5

Figure 5.24: Radial profiles of the axial velocity fluctuations ($Re \approx 10200$, $H/d = 3$)

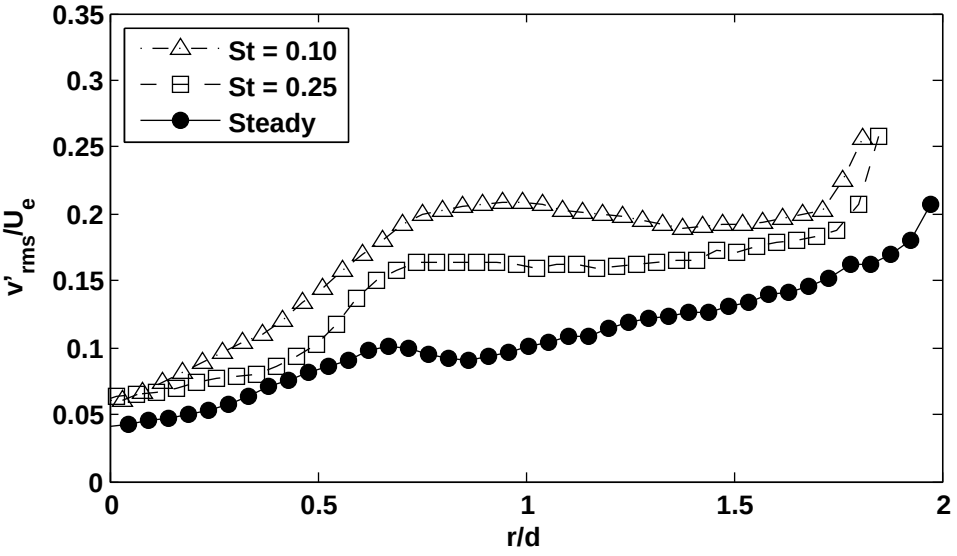

Figure 5.25: Effect of the Strouhal number on the radial velocity fluctuations near the impinging wall ($Re \approx 10200$, $H/d = 3$, $x/d \approx 2.85$)

5.3.4 Turbulent Kinetic Energy

Surface plots of the mean TKE for different values of the Strouhal number are shown in Fig.5.26. This figure shows that when the Strouhal number is increased from 0 (steady) to 0.10, the mean turbulent kinetic energy within the shear layer of the jet increases. However, as St is further increased to 0.25, there is actually a reduction on the mean turbulent kinetic energy of the jet, in particular, for $0.5 < x/d < 1.5$. This reduction is mainly due to the reduction present in the axial velocity fluctuations (see Fig. 5.21 on page 132), which have a significant contribution to the mean TKE. Furthermore, this reduction occurs despite the fact that the radial velocity fluctuations increase with St. This highlights the fact that the axial velocity fluctuations dominate the distribution of the mean TKE within the jet shear layer. Also, this reduction of k/U_e^2 for the jet pulsed at $St = 0.25$ indicates that there is less mixing present within the jet shear layer. Similarly, within the wall jet, the mean turbulent kinetic energy increases as the Strouhal number is increased from $St = 0$ to $St = 0.10$, followed by reduction for $St = 0.25$. This reduction of the mean TKE is linked to the development of a significantly stronger wall jet as the Strouhal number is increased, leading to less mixing in this region. This trend is can be observed in Fig.5.27. This figure shows that the

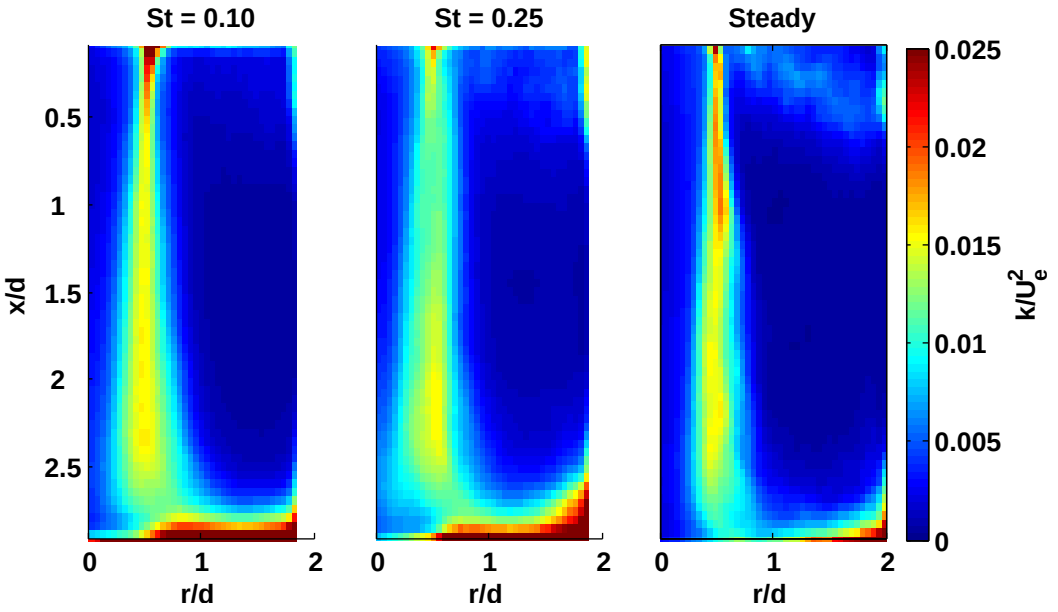

Figure 5.26: Effect of the Strouhal number on the mean turbulent kinetic energy ($Re \approx 10200$, $H/d = 3$)

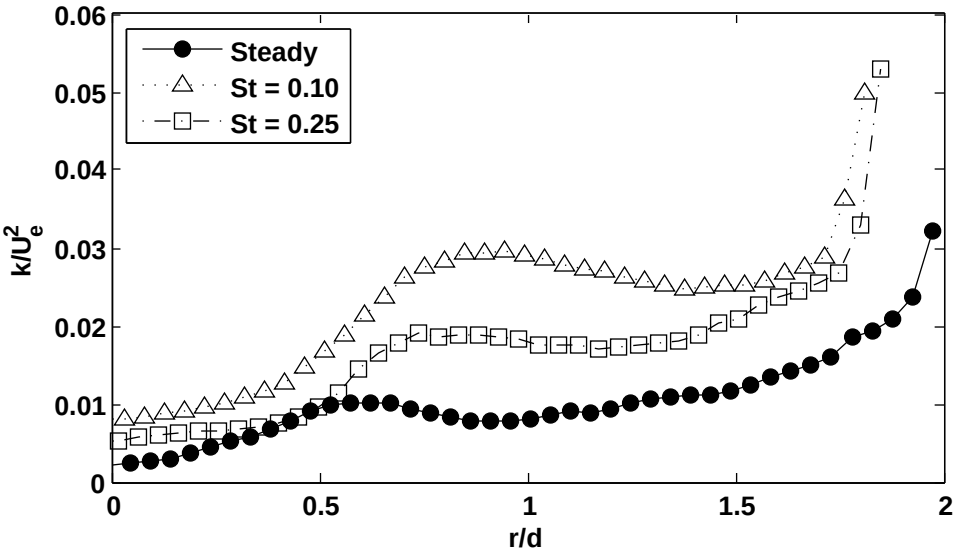

Figure 5.27: Effect of the Strouhal number on the mean turbulent kinetic energy near the impinging wall ($Re \approx 10200$, $H/d = 3$)

radial profiles of the mean TKE near the impinging wall exhibit a steady increase from the stagnation point up to $r/d \approx 0.75$, followed by a plateau region ($0.75 < r/d < 1.5$), then a sharp increase for $r/d > 1.5$. These different trends correspond to the acceleration, deceleration, and establishment of the radial velocity near the impinging wall as shown in Fig.5.19a. Finally, the values of k/U_e^2 near the impinging wall are dominated by the radial velocity fluctuations which becomes evident by observing the similarity between the profiles of v'_{rms}/U_e (Fig. 5.25 on page 135) and k/U_e^2 (Fig.5.27).

5.3.5 Skewness Factor

Surface plots of the skewness factor in the axial and radial direction are shown in Fig.5.28 and Fig.5.29. It can be seen that the magnitude of the axial skewness factor within the jet shear layer is reduced as the Strouhal number is increased. Furthermore, the negative and positive values of u'^3/U_e^3 within the shear layer of the pulsating jets are relatively balanced, exhibiting only a slight tendency towards negative values for the jet pulsated at $St = 0.10$ and a slight tendency towards positive values for $St = 0.25$. However, for the steady jet, negative values of u'^3/U_e^3 significantly dominate the shear layer indicating a strong presence of turbulent deceleration, probably due to the presence of turbulent eddies which lead to the axial turbulent component of the velocity to fall below the local mean more frequently. In contrast, for pulsed jets, the shear layer does not break up into turbulent eddies, instead, well defined vortex rings are present (see Fig. 5.20 on page 130). Finally, near the impinging wall (Fig.5.28), it can be observed that for the jet pulsed at $St = 0.25$, there is a region of negative u'^3/U_e^3 at $2.4 < x/d < 2.7$, which is not present for all the other jets, but is also present in the transitional jet pulsed at $St = 0.5$ (see Fig. 5.12 on page 121). It was not clear in the case of the transitional jet whether the presence of this region was a result of the interaction between vortex rings (as suggested by the vorticity plot shown in Fig. 5.4 on page 112) or due to the fact that the vortex rings are relatively stronger, therefore, forcing the fluid away from the impinging wall. However, from the vorticity plot for $St = 0.25$ of the turbulent jet (Fig. 5.20 on page 130), there is no indication to suggest a strong interaction between vortices,

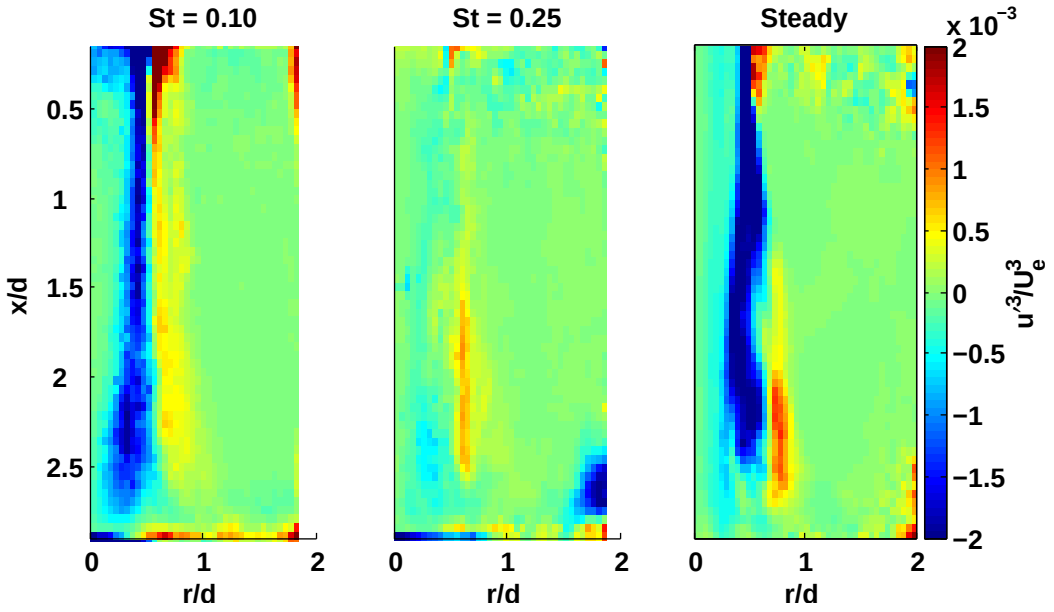

Figure 5.28: Effect of the Strouhal number on the skewness factor in the axial direction ($Re \approx 10200$, $H/d = 3$)

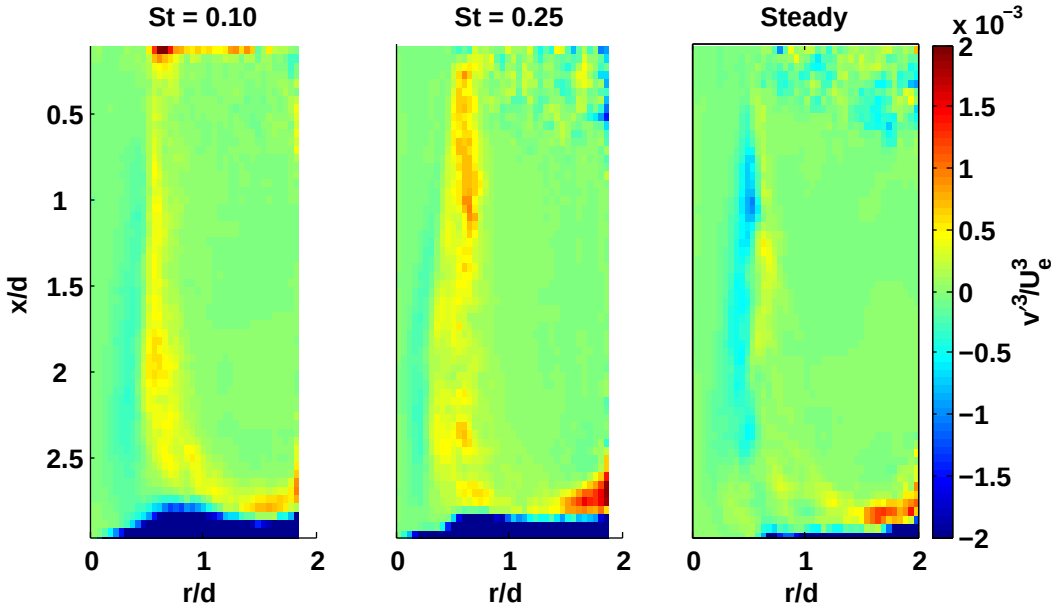

Figure 5.29: Effect of the Strouhal number on the skewness factor in the radial direction ($Re \approx 10200$, $H/d = 3$)

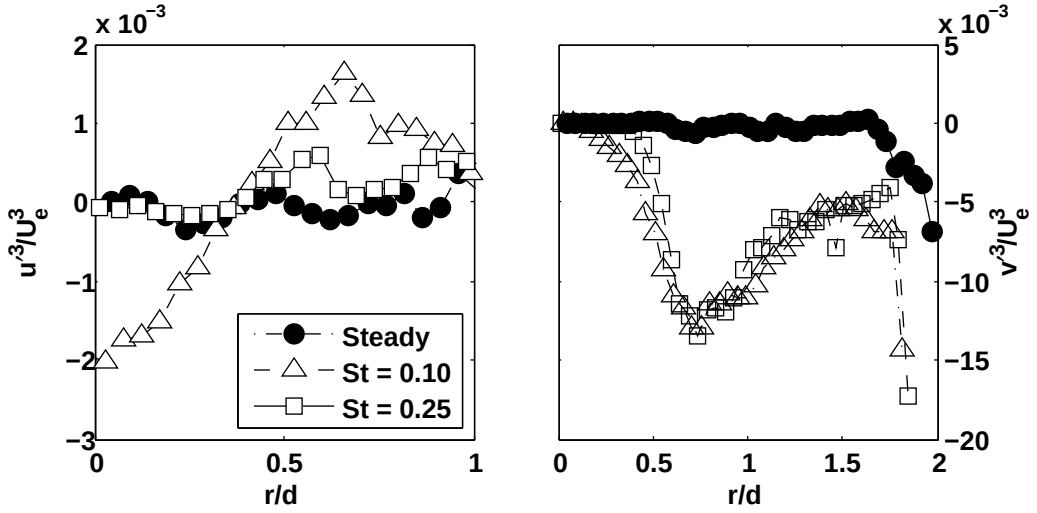

Figure 5.30: Radial profiles of the axial (left) and radial (right) skewness factor near the impinging wall ($Re \approx 10200$, $H/d = 3$)

therefore, this region of negative u'^3/U_e^3 must be caused by the relative strength of the vortices which force the fluid away from the impinging wall, leading to the creation of this region of turbulent deceleration.

Fig.5.29 shows that the negative values of v'^3/U_e^3 within the jet shear layer decrease in magnitude with the presence of a pulsating frequency, however, they are unaffected by the Strouhal number once the pulsation is present. On the other hand, the positive values of v'^3/U_e^3 increase as St is increased. This is probably due to the more rapid spread of the jet core as the frequency is increased, forcing the vortex rings to travel larger radial distances leading to turbulent acceleration in the radial direction.

Finally, near the impinging wall, the radial profile of the jet pulsated at $St = 0.10$ (Fig.5.30) shows both positive and negative values of u'^3/U_e^3, whereas, for both the steady jet and the jet pulsed at $St = 0.25$ the profiles show no significant differences. It suggests that the Reynolds stress for the jet pulsed at $St = 0.10$ would be considerably different. In contrast, the radial skewness factor near the impinging wall (Fig.5.30) shows that the pulsed jets share similar profiles, and are mainly negative, as opposed to the steady jet which shows values of v'^3/U_e^3 which are almost zero up to $r/d \approx 1.5$ where they become negative. This suggest that turbulent pulsating jets experience turbulent deceleration, whereas, the steady jet shows neither turbulent acceleration nor deceleration up to $r/d \approx 1.5$. The

turbulent deceleration present in pulsed jets could be a result of the vortex rings travelling along the impinging surface and being slowed down by the surrounding fluid which could explain why the turbulent component of the velocity fall below the local mean.

5.3.6 Reynolds Stress

The Reynolds stress is affected by the Strouhal number in such as way that entrainment (en) and expulsion (e) Reynolds stress within the jet shear layer reduces sharply as the frequency is increased, as shown in Fig.5.31. This reduction was expected in this set of results since the lowest Strouhal number tested is higher than St_c which has a value of 0.09 based on the steady jet ($St_c = d/U_e$). In the discussion of the Reynolds stress for the transitional jet it was mentioned that for Strouhal numbers higher than St_c the effect of the pulsating frequency was to decrease entrainment and expulsion Reynolds stresses. This assumption has now been confirmed. However, this assumption can not be completely validated since no experiments were carried out for the turbulent jet for $St \lessapprox St_c$. Furthermore, the reduction in such stress is also present in comparison with the steady jet, which was not the case for transitional jets.

Within the wall jet, the Strouhal number also affects the distribution of the Reynolds stress. For instance, for the steady jet, at $x/d \approx 2.75$ and $r/d \approx 0.75$, ejection (E) Reynolds stress is present, whereas, sweeping (S) Reynolds stress is present for the pulsed jets. Furthermore, farther away from the stagnation point ($x/d \approx 2.75$ and $r/d \approx 1.75$), the steady jet exhibits sweeping (S) Reynolds stress, and the pulsating jets exhibit high-speed fluidic interaction away from the impinging wall (O) instead. Closer to the impinging wall, the pulsating jets exhibit ejection (E) at approximate $r/d = 0.75$, whereas, ejection is present farther away from the wall for steady jets. also, Reynolds stress linked to low-speed fluidic interactions towards the wall (W) are present for all jets. However, as St is increased from $St = 0$ to $St = 0.10$ there is an increase in this type of Reynolds stress, followed by a significant reduction for $St = 0.25$.

The presence of ejection (E) Reynolds stress near the wall for pulsed jets could be due to the impingement of individual pulses on the wall (not present for

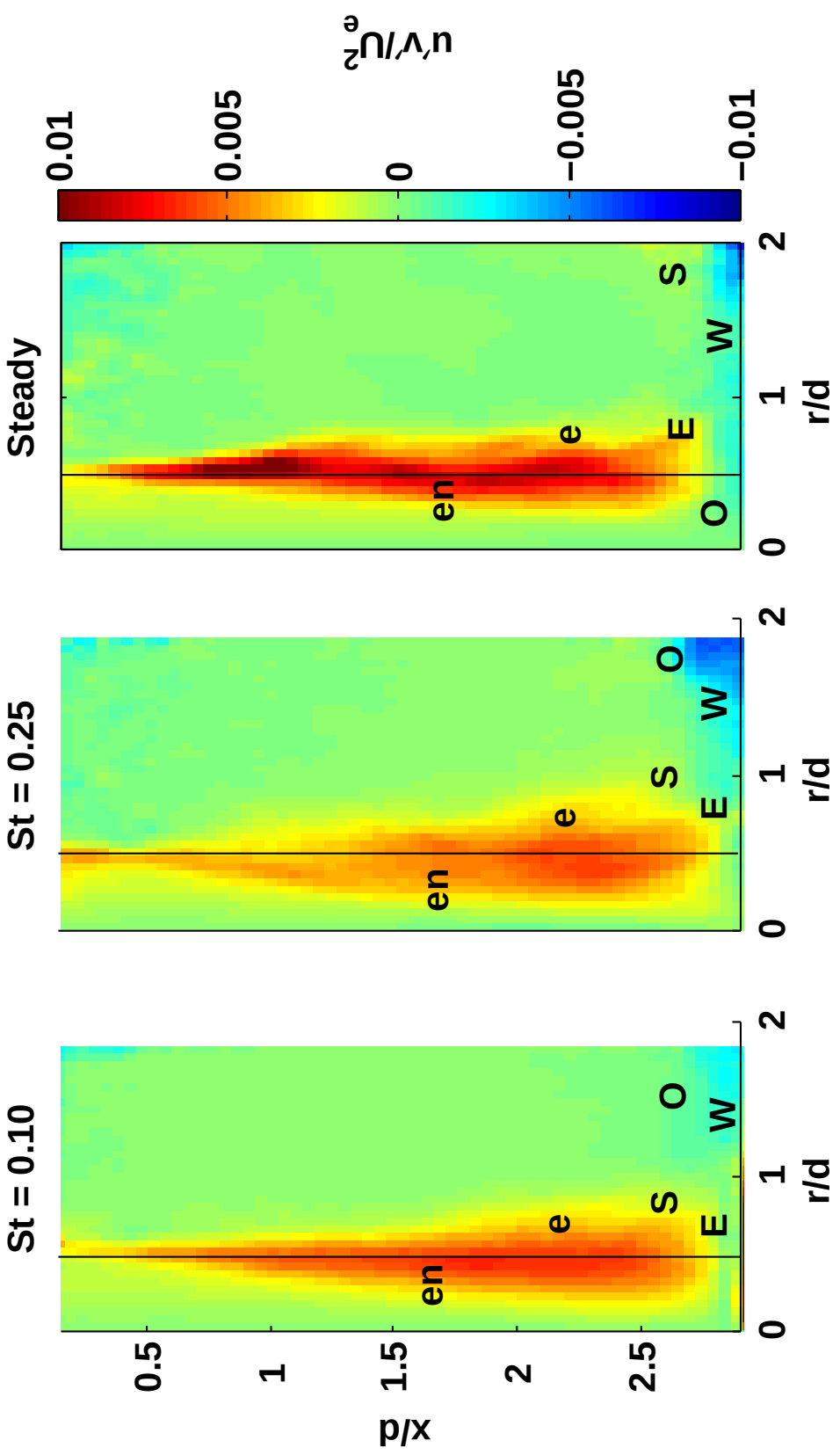

Figure 5.31: Effect of the Strouhal number on the Reynolds stress; entrainment (en), expulsion (e), ejection (E), sweep (S), wallward interaction (W), outward interaction (O) ($Re \approx 10200$, $H/d = 3$)

transitional jets pulsed at $St = 0.5$). Finally, the generation of fluidic interactions away from the impinging wall (O) for the pulsating jets could be a result of the pulses carrying momentum away from the surface as they travel along the wall, as suggested by the presence of negative axial triple correlation values in this region (see Fig.5.28). As it can be observed, the momentum transport due to the Reynolds stress is considerably different between steady and pulsed jets, indicating that the heat transfer characteristics would also differ.

5.3.7 Mean Axial Momentum Balance Near the Wall

The effect of the Strouhal number on the mean axial momentum balance for turbulent pulsating jets is shown in Fig.5.32. This figure shows that the effect of the frequency on the momentum balance is similar for both transitional and turbulent jets, that is, the contribution to momentum transport due to the radial diffusion increases as the Strouhal number is increased. Also, a similar change in the distribution of the momentum terms is present for Strouhal numbers greater than St_c base on the steady jet, which in this case has a value of $St_c = 0.09$. That is, the normal stresses are a sink term for $St \lessapprox St_c$.

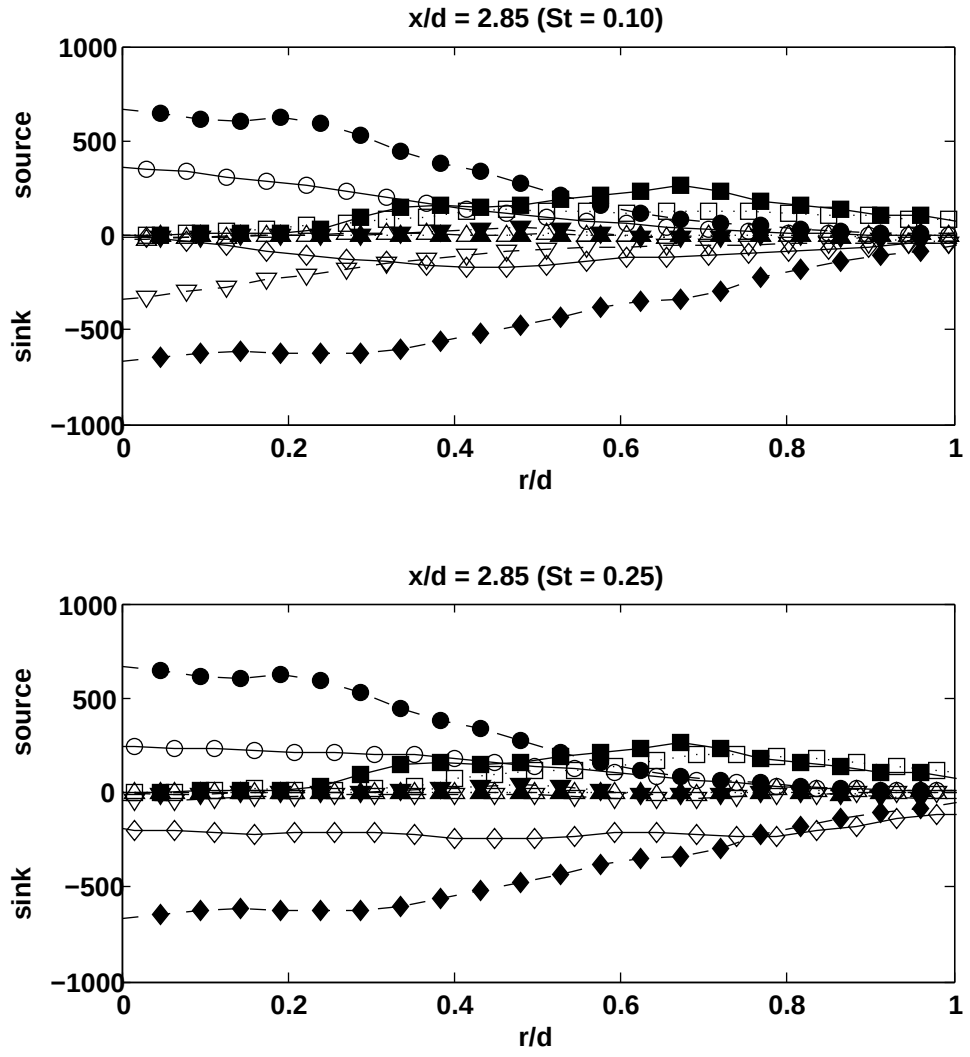

Figure 5.32: Effect of the Strouhal number on the mean axial momentum balance non-dimensionalised by d/U^2; closed symbols - steady jet, open symbols pulsed jet ($x/d = 2.85$)

5.4 Effect of the Reynolds Number

5.4.1 Introduction

In the preceding sections there was evidence suggesting that the Reynolds number might have a different effect on pulsating jets compared to steady jets, therefore, its effect on pulsating jets will be presented in this section. All the other factors that affect the flow field are kept constant; $H/d = 3$, $St = 0.25$. The diameter of the jet (d) is kept at 30.5mm. The Reynolds numbers for comparison are 4800, 7990 and 10240.

5.4.2 Time-Averaged Flow Field

Fig.5.33 shows that as the Reynolds number is increased, the core of the jet shortens which was not the case for steady jets. In addition, for steady jets there is an increase in the radial spread rate of the jet as the Reynolds number is increased. This also holds for pulsed jets but the influence of the Reynolds number on the spread rate is moderate. Finally, Fig.5.33 also shows that as the Reynolds number is increased the wall jet ($r/d > 1$) becomes stronger.

It was found that the centreline axial velocity decay for steady jet does not show a significant reduction up to $x/d = 2$, in contrast, for pulsating jets, it begins to decline at $x/d = 1.5$. In addition, for pulsating jets, the centreline axial velocity component declines more rapidly as the Reynolds number is increased, indicating that the presence of the pulse shortens the core of the jet (Fig.5.34). However, for steady jets, the Reynolds number does not have a significant effect on the centreline velocity decay (previous chapter).

The effect of the Reynolds number on the development of the axial and radial velocity component is shown in Fig.5.35. This figure shows that the Reynolds number does not have a strong influence on the development of the axial velocity component. However, the development of the radial velocity component shows that as the Reynolds number is increased (Fig.5.35c and Fig.5.35b), the spread rate of the jet increases, although this effect of the Reynolds number is more pronounced for steady jets. It can also be noticed that the presence of a pulsation leads to an increase of the jet spread rate in comparison to steady jets (Fig.5.35b).

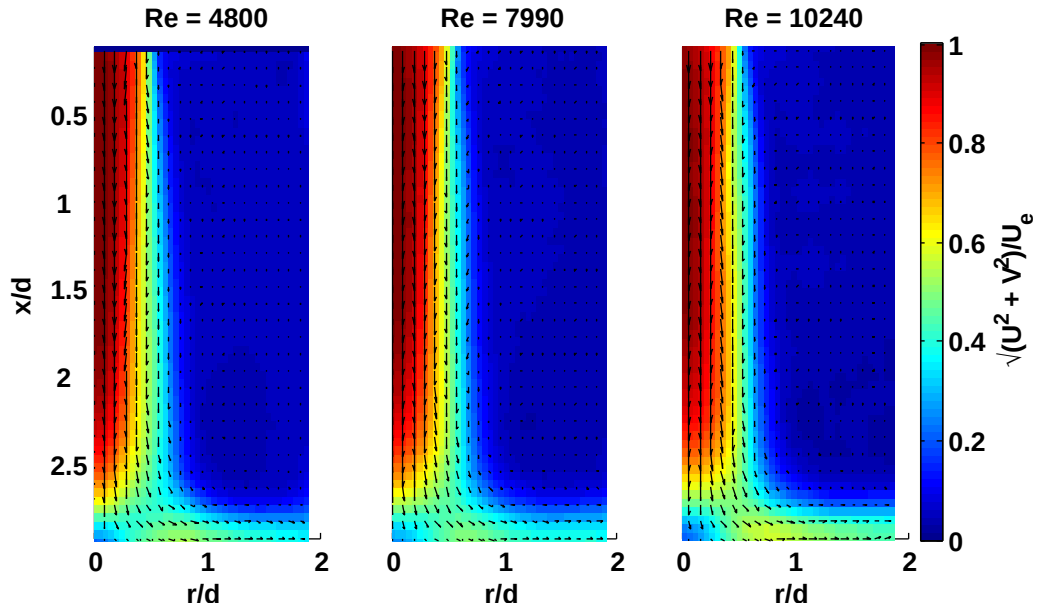

Figure 5.33: Effect on the Reynolds number on the time-averaged velocity field; closed symbols - steady jet, open symbols pulsed jet ($H/d = 3$, $St = 0.25$)

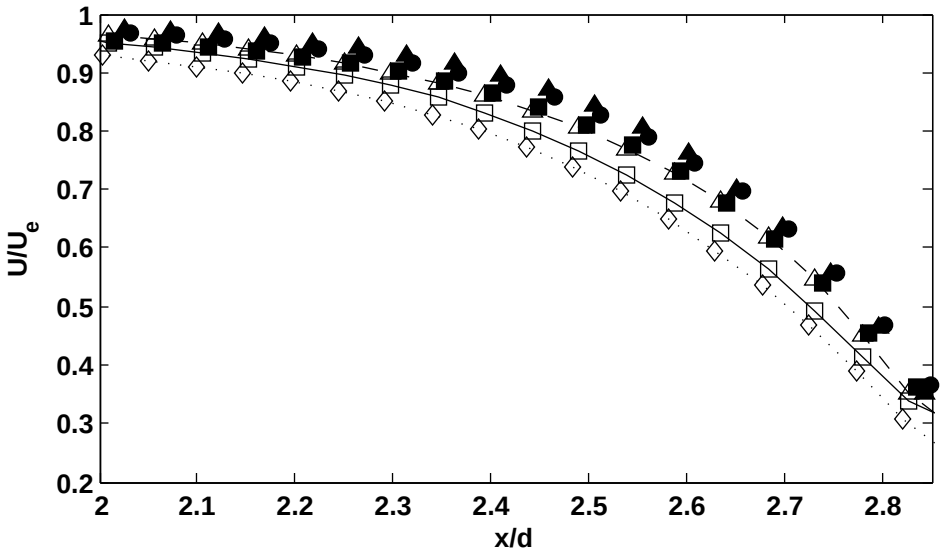

Figure 5.34: Centreline axial velocity decay; closed symbols - steady jet, open symbols pulsed jet ($H/d = 3$, $St = 0.25$)

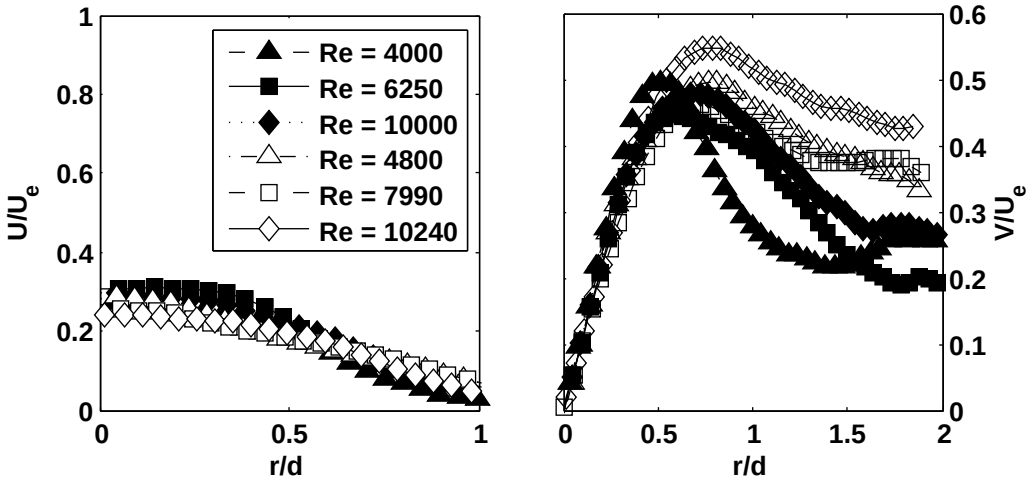

(a) x/d = 2.85

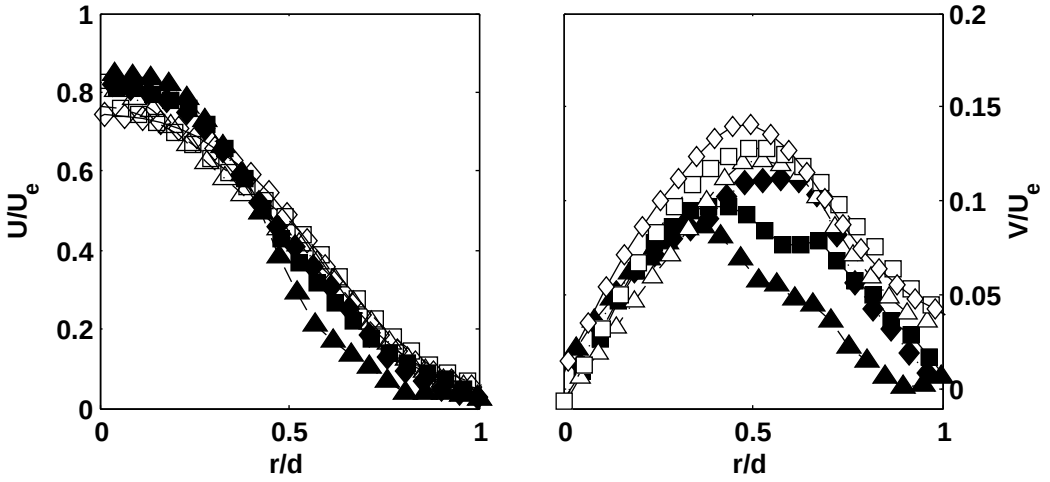

(b) x/d = 2.5

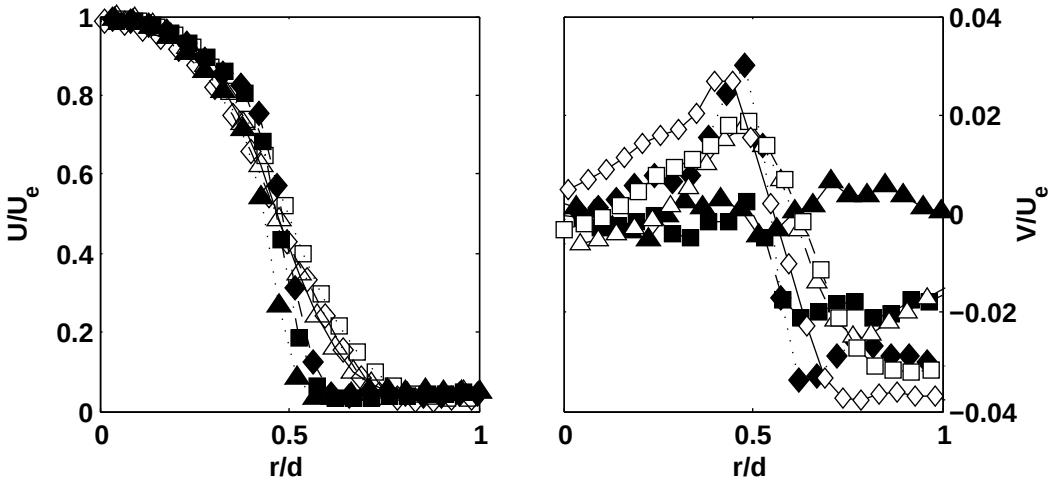

(c) x/d = 0.5

Figure 5.35: Radial profiles of the mean axial (left) and radial (left) velocity components; closed symbols - steady jet, open symbols pulsed jet ($H/d = 3$, $St = 0.25$)

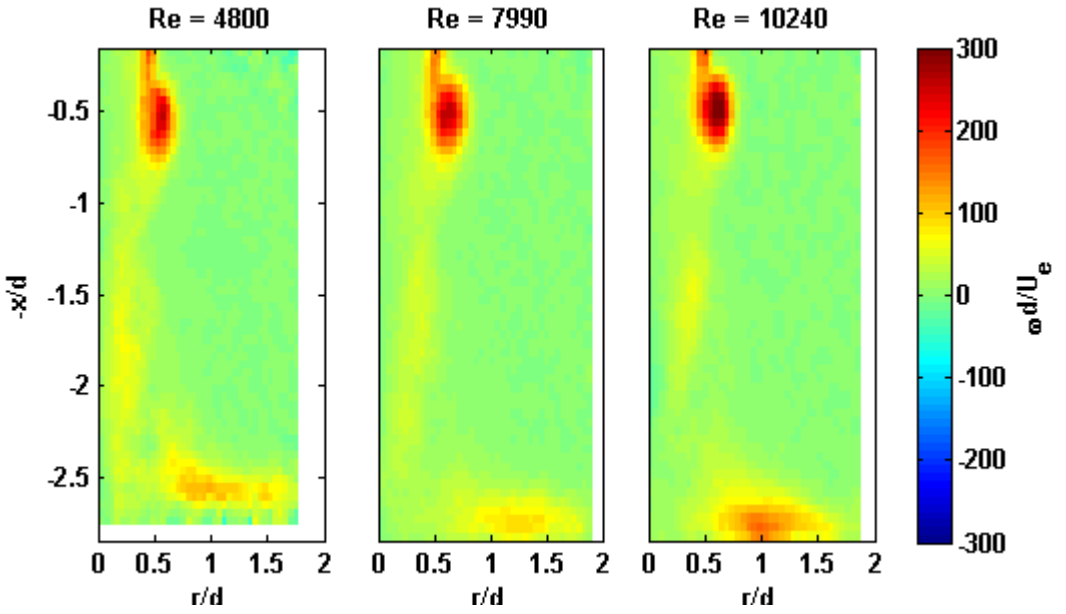

Figure 5.36: Effect of the Reynolds number on the vorticity field ($H/d = 3$, $St = 0.25$)

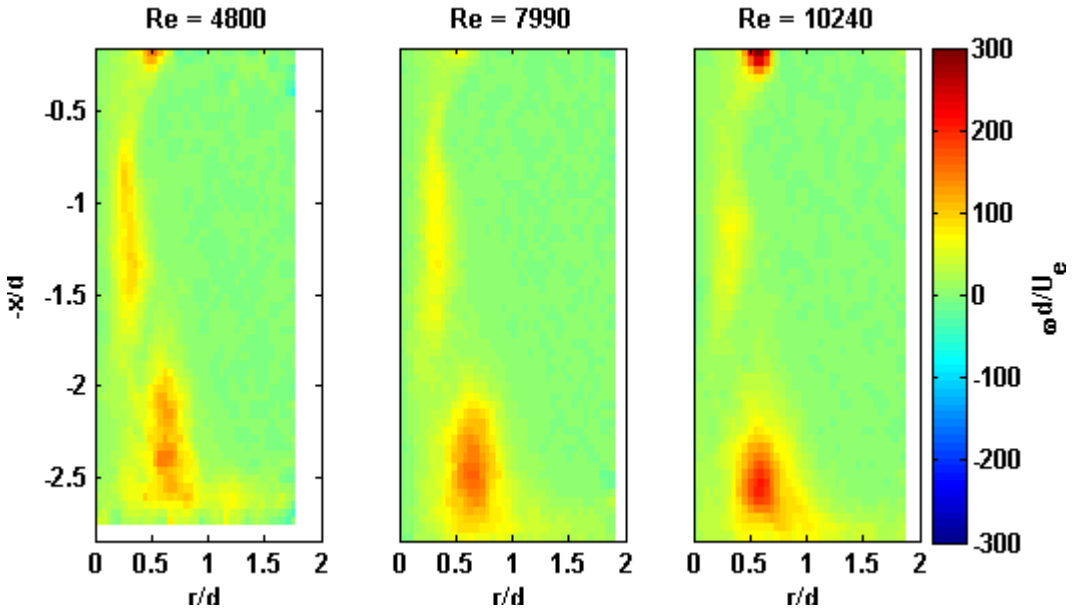

Figure 5.37: Effect of the Reynolds number on the vorticity field ($H/d = 3$, $St = 0.25$)

Interestingly, the most significant influence of the Reynolds number on pulsed jets is found near the impinging wall. Firstly, the presence of a pulsation leads to higher values of the radial velocity component at $r/d > 0.75$ for all jets in comparison to their steady counterpart. Furthermore, the magnitude of the local maximum is not proportional to the Reynolds number, for instance, the jet with $Re = 4200$ exhibits a local maximum larger than the jet with $Re = 7990$, however, it increases for $Re = 10240$, leading to the largest value of V/U_e. This behaviour could be a consequence of significant differences between the vortex rings due to the influence of the Reynolds number. For instance, as the Reynolds number is increased, the vortex rings become stronger, as shown in Fig.5.36. Also, the Reynolds number affects the way the vortices reach and interact with the wall (Fig.5.37). For example, for $Re = 4200$ the vortex is weak and does not penetrate the jet wall jet, however, for $Re = 7990$, the vortex penetrates the wall jet. Interestingly, as the Reynolds number is further increased to $Re = 10240$, its vortex is moved away from the wall, probably forced away from the wall by the fluid within the jet core which begins to move radially sooner and faster (Fig.5.35b), therefore, developing a stronger wall jet which prevents the vortex from penetrating it as deeply as the jet with $Re = 7990$. Finally, the presence of the pulsation fixes the location of the maximum radial velocity component near the wall at approximately $r/d = 0.75$, independently of the Reynolds number, as least for the values of Re tested.

5.4.3 Velocity Fluctuations

First of all, Fig.5.38 shows that, overall, as the Reynolds number is increased, the axial velocity fluctuations decrease. A similar reduction was also encountered for in turbulent pulsating jets as the Strouhal number was increased. In that case, the reduction was due to the strengthening of the vortices which help reduce the turbulent part of the axial velocity component. In this case, not only, the vortices become stronger as the Reynolds number is increased, but also the exit velocity increases, inducing a more pronounced reduction of u'_{rms}/U_e. Similarly, the radial velocity fluctuations (Fig.5.39) also decrease as Re is increased, although, this decrease is moderate.

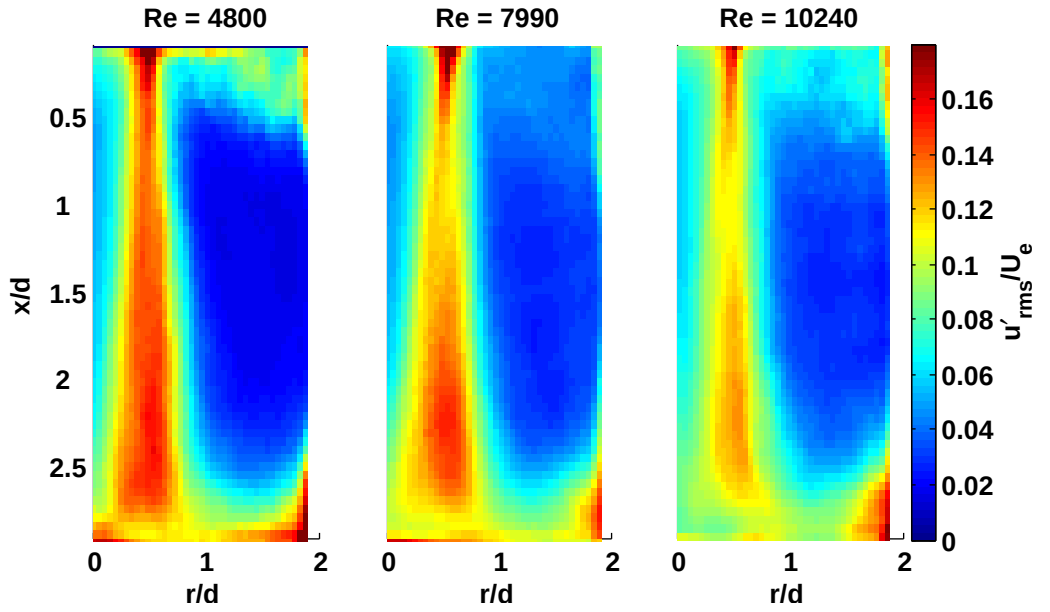

Figure 5.38: Effect of the Reynolds number on the axial velocity fluctuations ($H/d = 3$, $St = 0.25$)

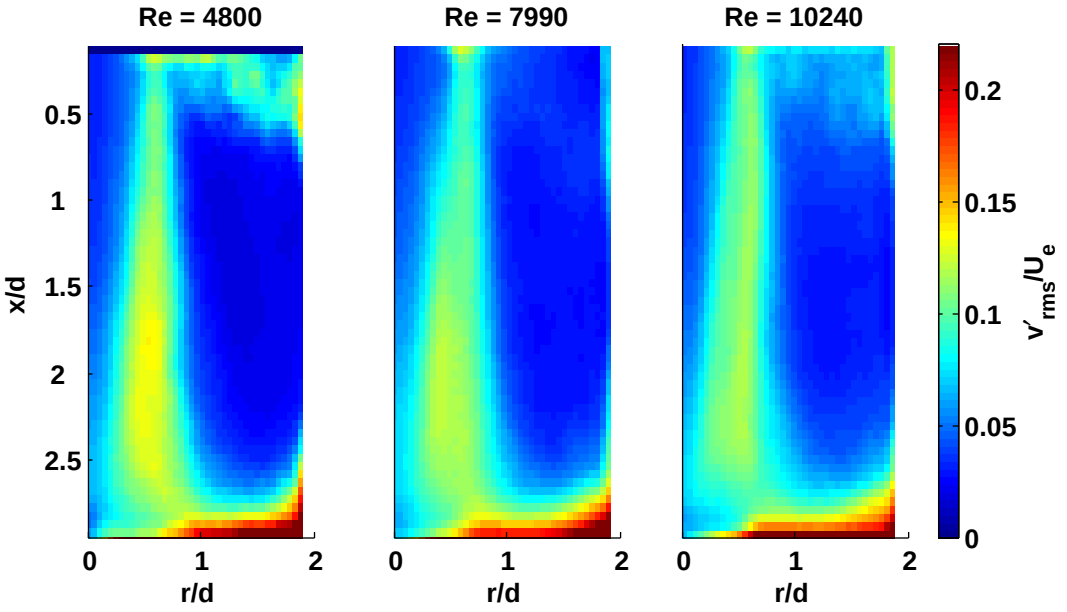

Figure 5.39: Effect of the Reynolds number on the radial velocity fluctuations ($H/d = 3$, $St = 0.25$)

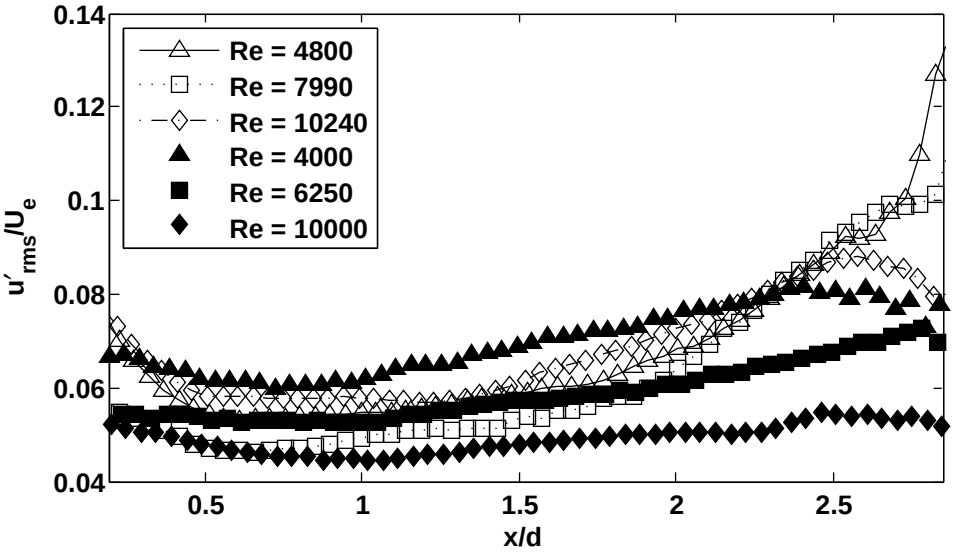

Figure 5.40: Effect of the Reynolds number on the centreline axial velocity fluctuations; closed symbols - steady jet, open symbols pulsed jet ($H/d = 3$, $St = 0.25$)

The effect of the Reynolds number on the centreline axial velocity fluctuations is shown in Fig.5.40. It suggests that the effect of the Reynolds number for pulsating jets is not as straight forward as in steady jets, in particular with the jet at the lowest Reynolds number exhibiting velocity fluctuations that fall between the levels of the other two jets, which could be an indication of the transitional nature of such jet. However, this figure shows that there is a steady increase of the centreline velocity fluctuations at $1.25 < x/d < 2.4$ for pulsed jets, up to $r/d \approx 2.4$, where pulsed jets reach higher values of u'_{rms}/U_e than steady jets. In addition, similarly to steady jets, as the Reynolds number is increased, the centreline axial velocity fluctuations near the stagnation point decrease.

Radial profiles of u'_{rms}/U_e at different axial locations are shown in Fig.5.41. It shows that near the nozzle exit (Fig.5.41c), the Reynolds number does not have a strong influence on the axial velocity fluctuations. However, the profiles of the pulsed jets are flatter than those of their steady equivalent, also, steady jets exhibit slightly higher peak values. Further downstream, at $x/d = 2.5$ (Fig.5.41b), the profiles for the pulsed jets are also wider than the steady profiles, showing an increase of u'_{rms}/U_e for $0 < r/d < 0.25$, but also, the Reynolds number has slightly more influence on u'_{rms}/U_e at $0.2 < r/d < 0.6$, leading to a decrease

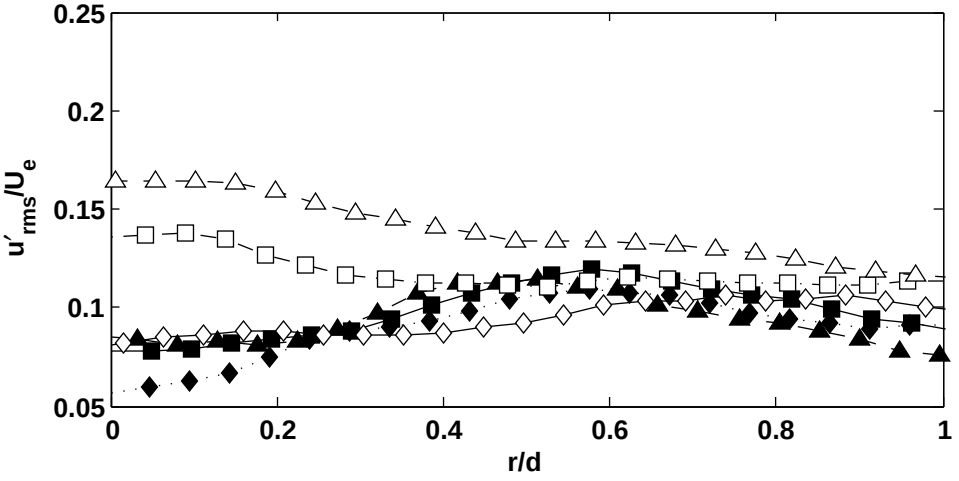

(a) x/d = 2.85

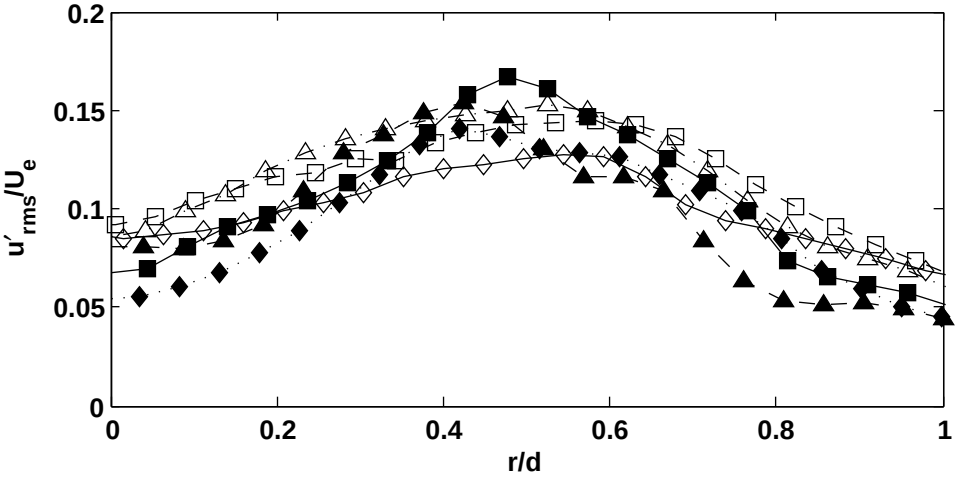

(b) x/d = 2.5

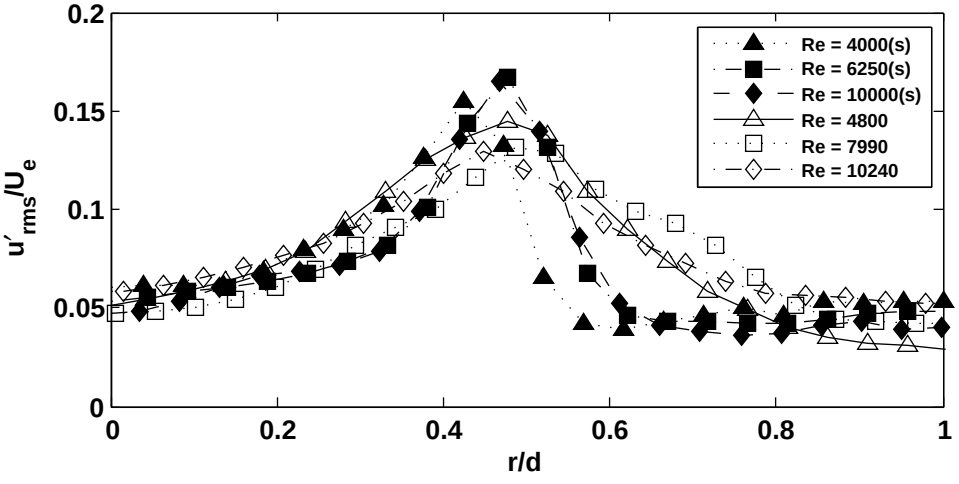

(c) x/d = 0.5

Figure 5.41: Radial profiles of axial velocity fluctuations; closed symbols - steady jet, open symbols pulsed jet ($H/d = 3$, $St = 0.25$)

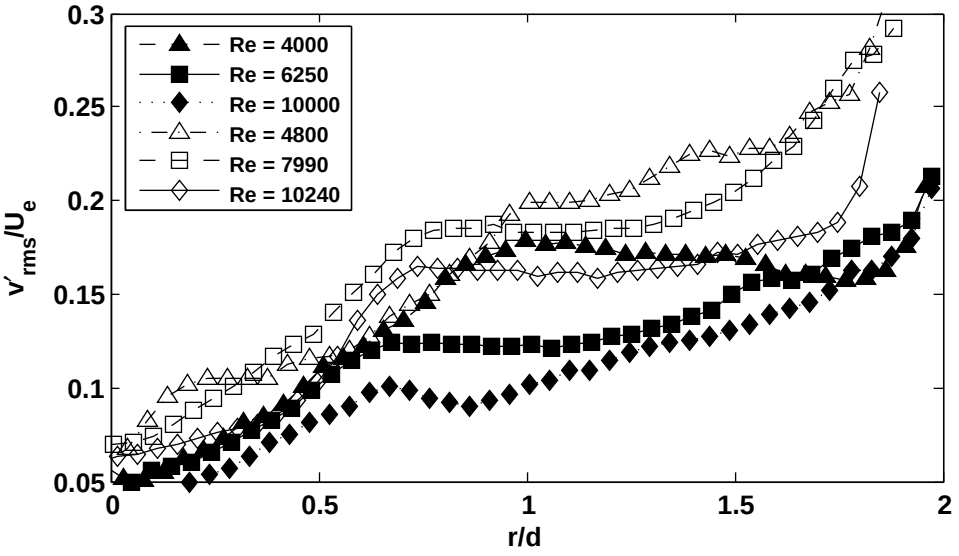

Figure 5.42: Effect of the Reynolds number on the radial velocity fluctuations near the impinging wall; closed symbols - steady jet, open symbols pulsed jet ($H/d = 3$, $St = 0.25$, $x/d = 2.85$)

of the axial velocity fluctuations as it is increased. Furthermore, it is near the impinging wall that the effects of the Reynolds number are most significant as shown in Fig.5.41a. It shows that as the Reynolds number is increased, there is a significant decrease in the values of u'_{rms}/U_e. It also shows an increase of u'_{rms}/U_e in comparison to steady jets within the stagnation region ($0 < r/d < 0.3$).

Fig.5.42 shows radial profiles of the radial velocity fluctuations near the wall. It can be observed that for $r/d > 1$ the effect of the Reynolds number on v'_{rms}/U_e is similar to that of steady jets, that is, it reduces the value of v'_{rms}/U_e. However, for steady jets, this is noticeable from $r/d > 0.5$. This indicates that the presence of the pulse, delays the effect of the Reynolds number on v'_{rms}/U_e to $r/d > 0.75$. Also, it can be seen that the presence of the pulsating frequency leads to higher velocity fluctuations of the radial velocity component at $r/d > 0.5$ for the higher Reynolds numbers, and at $r/d > 1$ for the transitional jet.

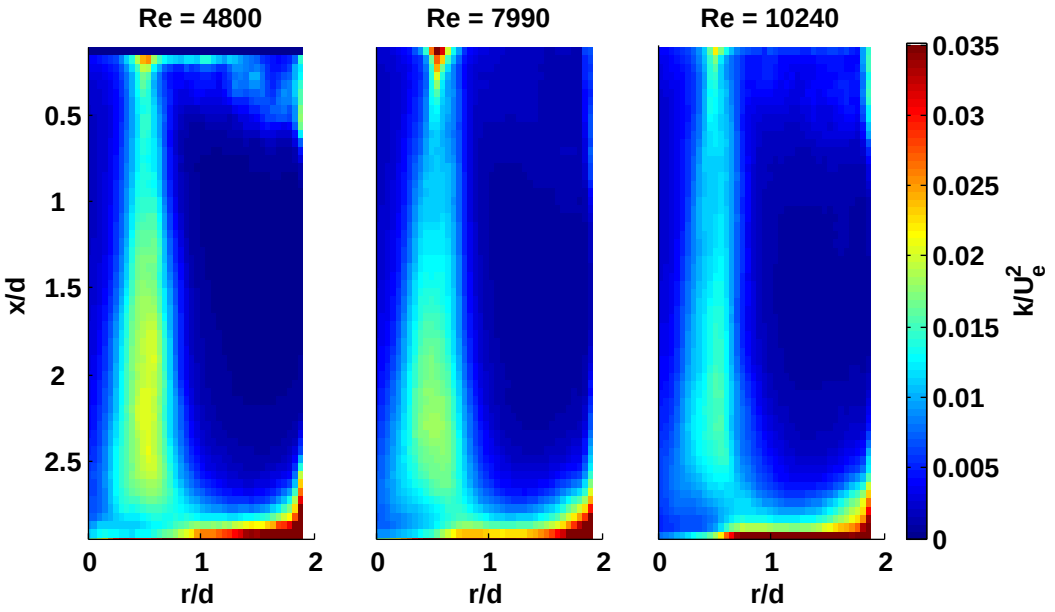

Figure 5.43: Effect of the Reynolds number on the mean turbulent kinetic energy ($H/d = 3$, $St = 0.25$)

5.4.4 Turbulent Kinetic Energy

Fig.5.43 shows that the effect of the Reynolds number is rather straight forward, that is, there is a significant decrease in the mean turbulent kinetic energy as the Reynolds number is increased, especially, within the shear layer of the jet. This decrease is mostly due to the decrease of the axial velocity fluctuations as Re is increased, since they have a stronger influence on the mean TKE within the shear layer than the radial velocity fluctuations.

The effect of Re near the impinging wall is explored in Fig.5.44. It shows, that similarly to steady jets at $0.6 < r/d < 1.5$, the effect of the Reynolds number is to decrease the mean turbulent kinetic energy. Furthermore, for pulsed jets there is a steady increase of the mean TKE for $r/d > 0.9$, whereas, for steady jets, this increase is not evident up to approximately $r/d > 1.5$. Finally, for $Re = 7900$ there is an increase in the values of k/U_e^2 for approximately $0.4 < r/d < 0.9$ when compared to the other jets. This local increase is influenced by the higher values of the radial velocity fluctuations also present at $0.4 < r/d < 0.9$ (Fig. 5.42 on the preceding page). The increase in the values of v'_{rms}/U_e for this region could be a result of the vortices being distorted, combined with the fact that the jet vortex rings penetrate the wall jet (see Fig. 5.37 on page 147).

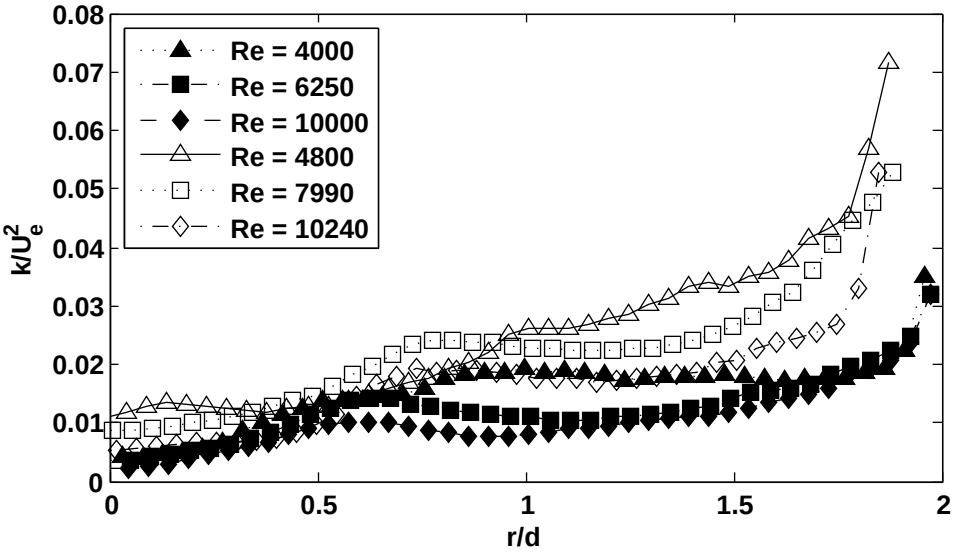

Figure 5.44: Effect of the Reynolds number on the mean turbulent kinetic energy near the impinging wall; closed symbols - steady jet, open symbols pulsed jet ($H/d = 3$, $St = 0.25$, $x/d = 2.85$)

5.4.5 Skewness Factor

The effect of the Reynolds stress on the skewness factor in the axial and radial direction within the shear layer exhibits a behaviour similar to that of the velocity fluctuations, that is, they decrease in magnitude as the Reynolds number is increased. Since the effect of the Reynolds number on the triple correlations is rather straight forward, the discussion in this section will not be as thorough but will concentrate on the major findings.

First of all, it was found that the contribution to the Reynolds stress within the shear layer is mainly dominated by the axial turbulent component, as seen in previous sections. In contrast, within the wall jet, the contribution to the Reynolds stress is mainly dominated by the radial turbulent component.

Significant differences between the profiles of the axial skewness factor is found near the impinging wall, and shown in Fig.5.45 (left). It can be seen that the axial skewness factor, near the impinging wall, increases as the Reynolds number is increased, from negative values ($Re = 4800$) to almost zero ($Re = 10240$), indicating a reduction in turbulent deceleration as the Reynolds number is increased. Finally, the profiles of the radial skewness factor, Fig.5.45 (right), show that for

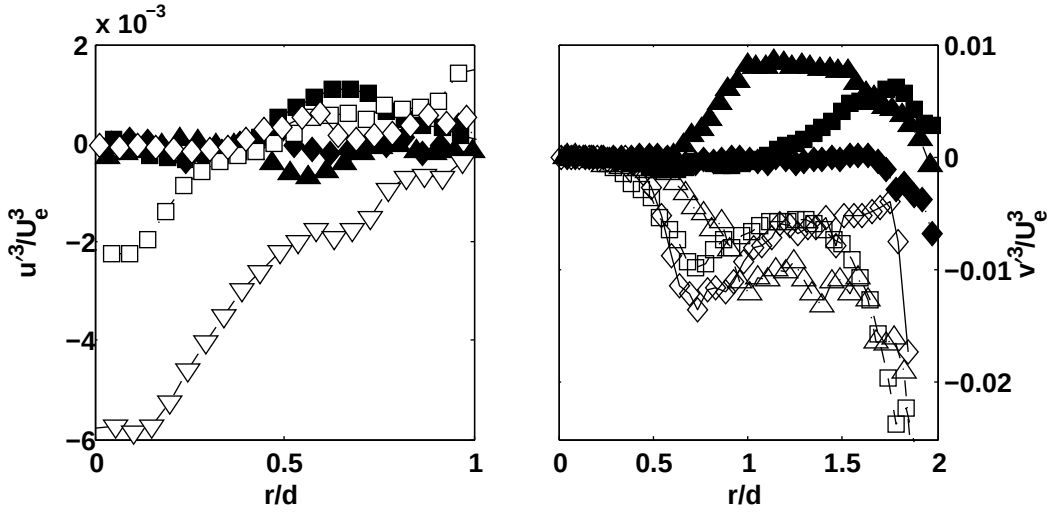

(a) x/d = 2.85

Figure 5.45: Radial Profiles of axial (left) and radial (right) skewness factor; closed symbols - steady jet, open symbols pulsed jet ($H/d = 3$, $St = 0.25$)

approximately $0 < r/d < 0.6$ there is a decrease in v'^3/U_e^3 as the Reynolds number is increased. At $r/d \approx 0.6$, for $Re = 4800$, the radial skewness factor continues with a steady decrease, whereas, for $Re = 7990$ and $Re = 10240$, the values of v'^3/U_e^3 experience a sudden increase, up to $r/d \approx 1.25$, where the radial skewness factor for $Re = 7990$ exhibits a sharp decrease. However, overall, the values of v'^3/U_e^3 for the pulsed jet are negative independently of the Reynolds number, in contrast, v'^3/U_e^3 only become negative for steady jets when $Re = 10000$.

5.4.6 Reynolds Stress

Fig.5.46 shows the effect of the Reynolds number on pulsating jets, including the type of Reynolds stress induced. First of all, it can be noticed that as the Reynolds number is increased, the Reynolds stress linked to entrainment (en) and expulsion (e) decrease for all jets. Near the impinging wall, the type of Reynolds stresses are similar for all jets, apart from high-speed fluidic interactions away from the wall (O), that are not present for the jet with $Re = 4200$. Therefore, these type of Reynolds stresses are generated at $4200 < Re < 7900$, at least within the radial distance covered in these experiments ($0 < r/d < 2$). Interestingly, as the Reynolds number is increased from $Re = 4800$ to $Re = 7990$, there is an increase in the Reynolds stress (w) near the wall at $1.25 < r/d < 1.80$. This increase is linked to the increase of the radial skewness factor at this location (Fig. 5.45 on the preceding page), indicating that the radial turbulent component dominates these low-speed Reynolds stress (W). Finally, it can also be observed that as the Reynolds number is increased from $Re = 7990$ to $Re = 10240$, there is a significant reduction of the Reynolds stress that act away from the wall (O). This decrease is due to a decrease in v'^3/U_e, therefore, this region (O) is dominated by u', which being negative has a direction away from the wall. Consequently, the momentum transport due to this Reynolds stress would have a general directionality away from the impinging wall.

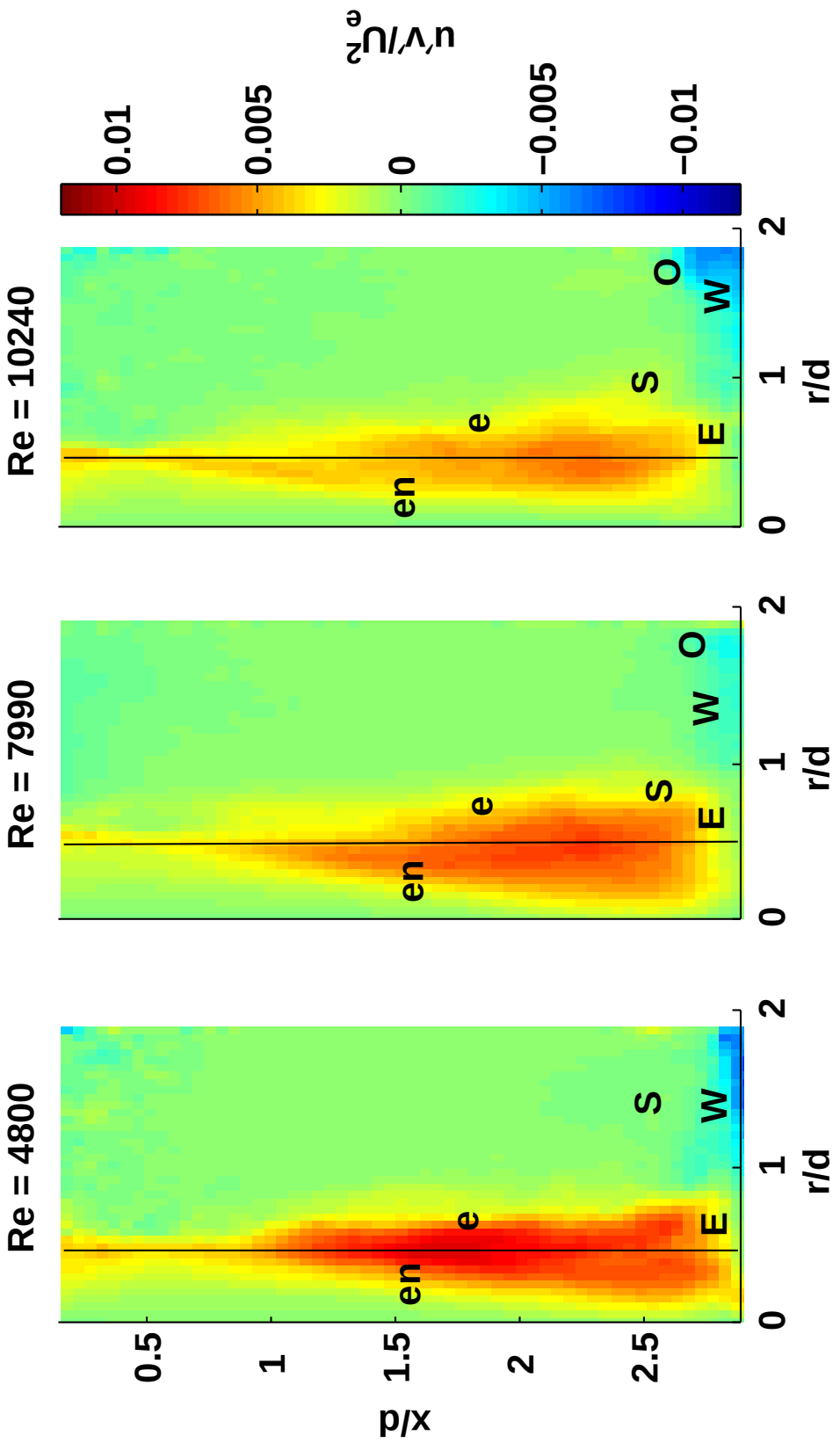

Figure 5.46: Effect of the Reynolds number on the Reynolds stress; entrainment (en), expulsion (e), ejection (E), sweep (S), wallward interaction (W), outward interaction (O) ($H/d = 3$, $St = 0.25$)

5.4.7 Mean Axial Momentum Balance Near the Wall

First of all, Fig.5.47 shows that the mean momentum transfer, near the impinging wall, for steady jets is larger than that of pulsed jets. Also, it can be noticed, that for the lower Reynolds number, the normal stress term is a sink. However, as the Reynolds number is further increased to $Re = 10240$, they show no contribution to the momentum balance near the wall. This change in the behaviour of the normal stresses could be a result of the reduction exhibited by the entrainment Reynolds stress near the impinging wall as the the Reynolds number is increased (Fig.5.46). This indicates that for the lower Reynolds numbers, the effect of increased levels of entrainment is translated into a transfer of momentum from the mean to the turbulent field. Fig.5.47 also shows that as the Reynolds number is increased the contribution to the momentum transport from the radial diffusion increases, this is direct line with the increase in the values of V/U_e seen in the profile of the mean radial velocity component near the impinging wall (Fig.5.35a), which leads to increases in the radial diffusion term for $r/d > 0.8$, particularly for $Re = 10240$. This effect is similar to increasing the pulsating frequency for the same reason. This suggests that, an enhancement in the momentum transfer due to the radial diffusion could be achieved by increasing both, the Reynolds number and the Strouhal number.

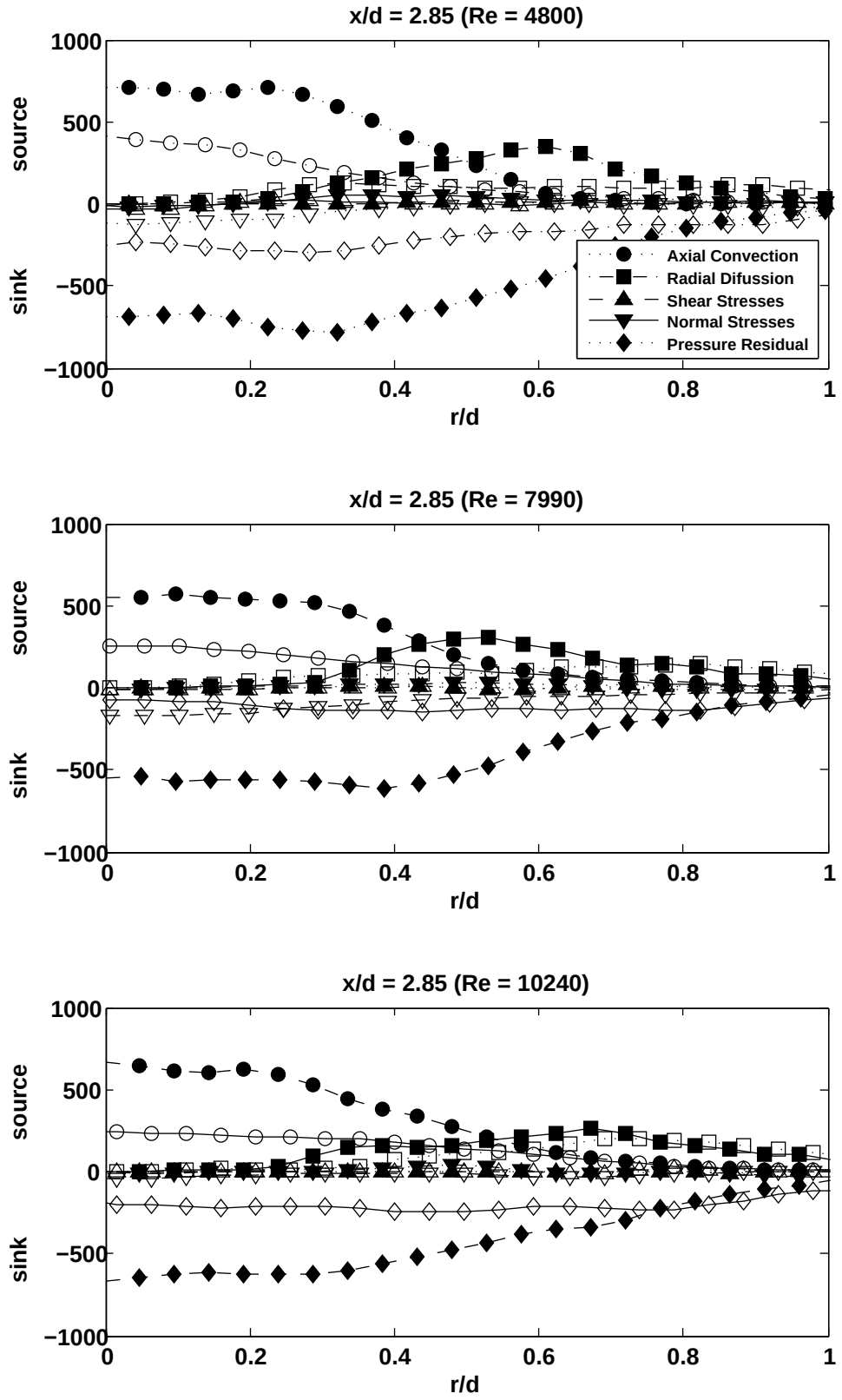

Figure 5.47: Effect of the Reynolds number on the mean axial momentum balance non-dimensionalised by d/U^2; closed symbols - steady jet, open symbols pulsed jet ($x/d = 2.85$, $St \approx 0.25$)

5.5 Effect of the Nozzle-to-plate Spacing

5.5.1 Introduction

This section presents the effect of the nozzle-to-plate spacing on pulsating jets, both the Reynolds number and the frequency are kept constant in order to assess the effect of H/d independently. The Reynolds number was kept at approximately 4,500 and the non-dimensional frequency St was kept at approximately 0.45. Also, the diameter was kept constant and equal to 30.5mm

5.5.2 Time-Averaged Flow Field

The time-averaged flow field for different nozzle-to-plate spacings is shown in Fig.5.48. Firstly, as opposed to steady jets, there is no evidence of the nozzle-to-plate spacing having a significant effect the spread rate of the jet for pulsed jets. It also shows that H/d affects the wall jet differently for steady and pulsed jets. For steady jets, the wall jet ($r/d > 1$) becomes stronger as the nozzle-to-plate spacing is increased (Fig. 4.24 on page 90). However, for pulsed jets, the effect on H/d is not as straight forward, therefore, it deserves further consideration[3]. Finally, Fig.5.48 also shows that as H/d is increased, the core of the jet becomes longer.

The centreline axial velocity decay is shown in Fig.5.49. As expected, and due to the influence of the impinging wall, it shows that the centreline velocity decays more rapidly at smaller nozzle-to-plate spacings. This is also the case for steady jets. For $H/d = 2$, the centreline velocity begins to decay at 65% of the length away from the nozzle exit. Also, the jet situated at $H/d = 2$ exhibits a similar axial velocity decay as its steady counterpart. However, for $H/d = 3$ and $H/d = 4$, the centreline velocity decay is similar between steady and pulsed jets up to $x/d \approx 0.75$, after which, the pulsed jets exhibit lower values of U/U_e.

The development of the axial and radial velocity components is shown in Fig.5.50. It shows that the development of the streamwise velocity component, for pulsed jets, is not significantly affected by the nozzle-to-plate spacing. In contrast, steady jets spread more rapidly as H/d is increased. However, Fig.5.50

[3]Addressed in this section

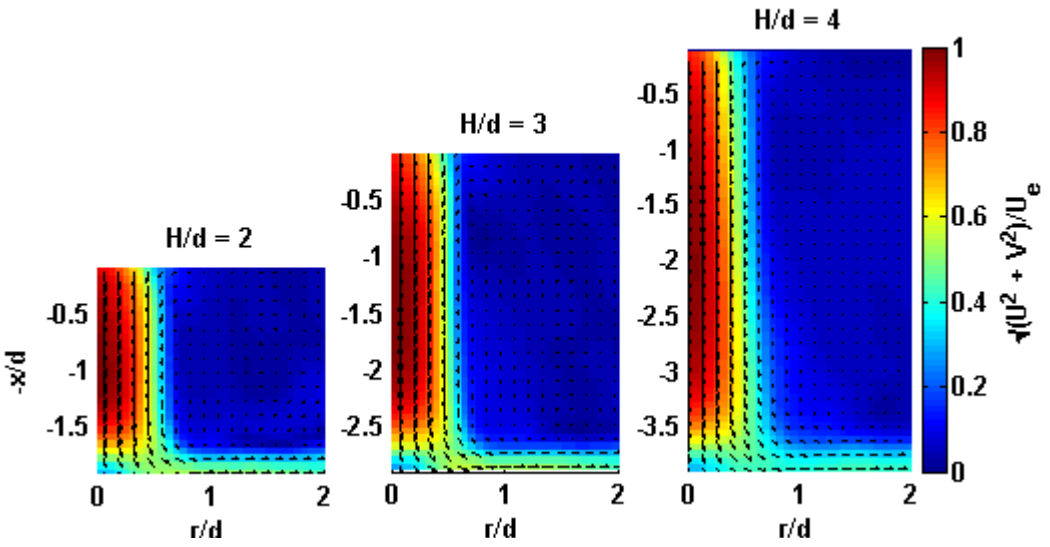

Figure 5.48: Effect of the nozzle-to-plate spacing on the time-average flow field ($Re \approx 4200$, $St = 0.50$)

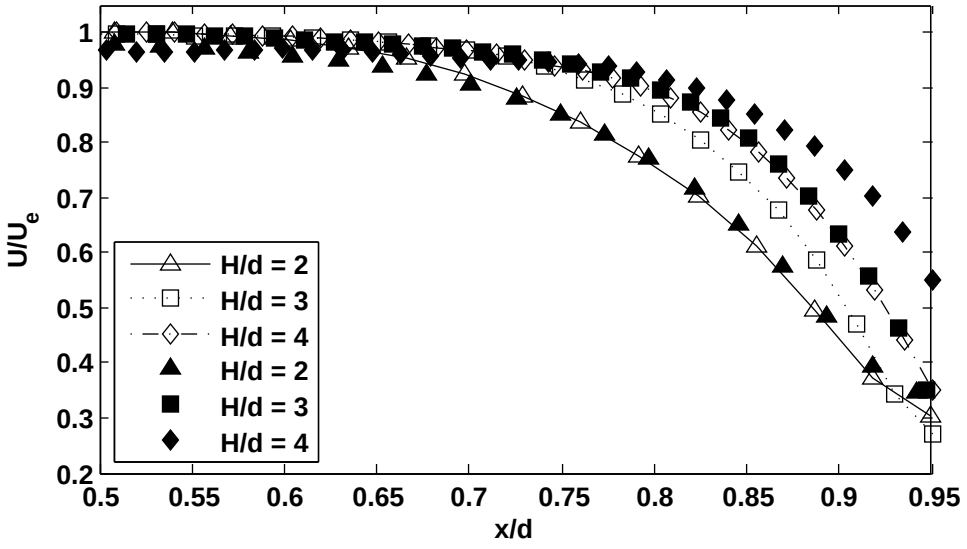

Figure 5.49: Centreline axial velocity decay; closed symbols - steady jet, open symbols pulsed jet ($Re \approx 4200$, $St \approx 0.50$)

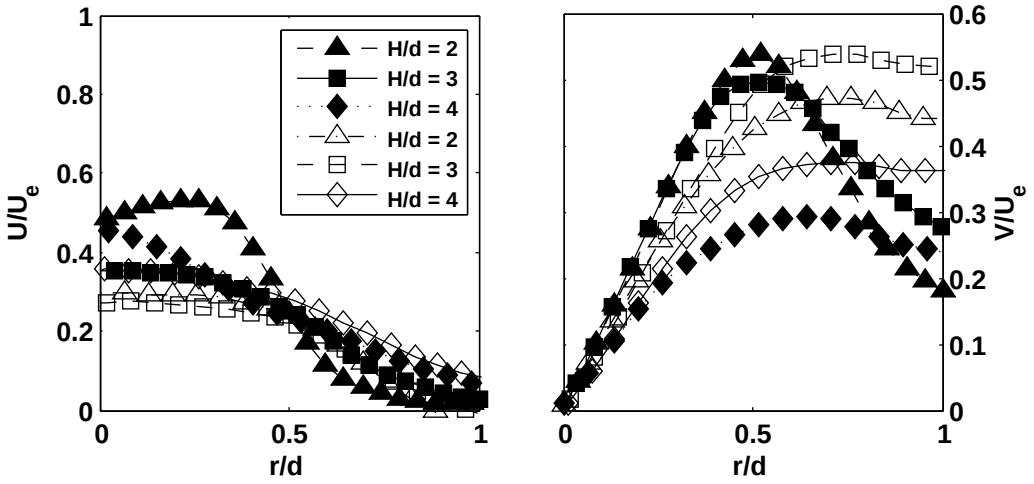

(a) x/H = 0.95

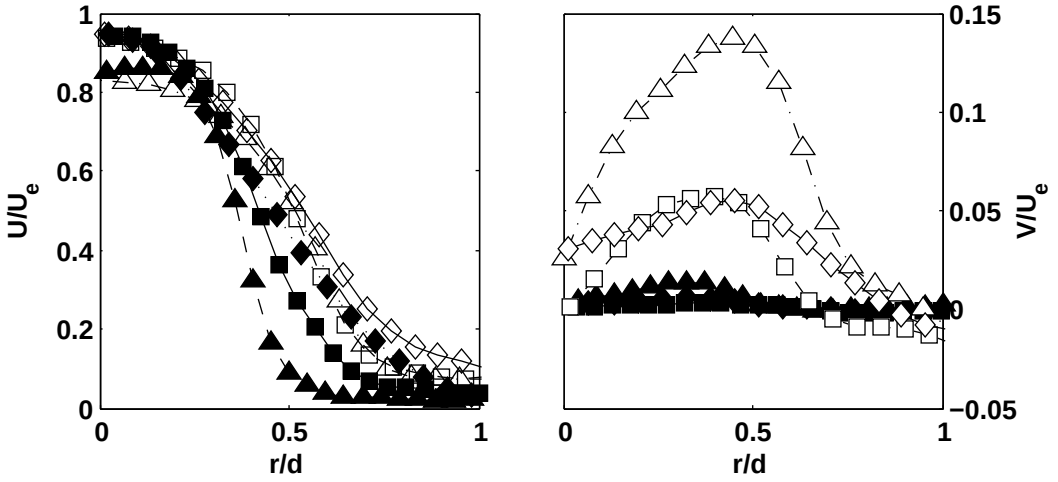

(b) x/H = 0.75

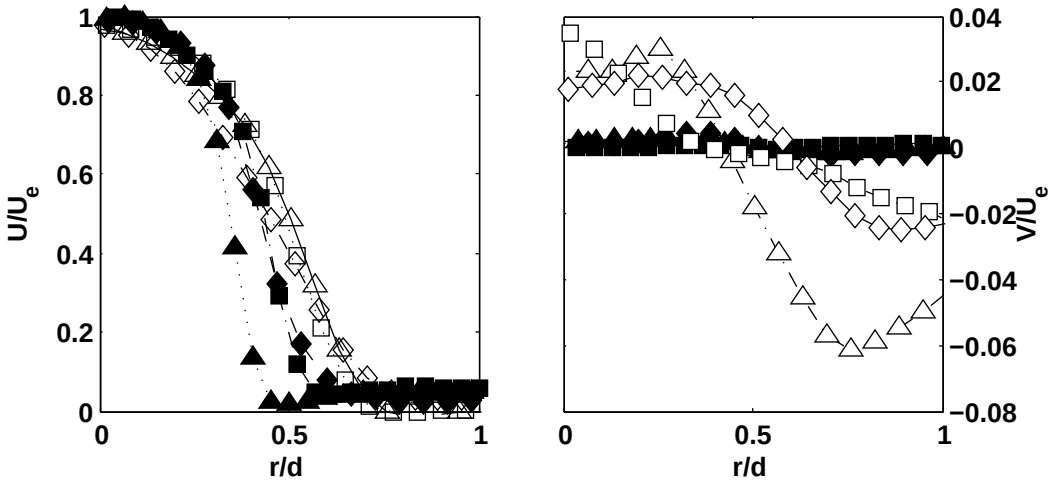

(c) x/H = 0.25

Figure 5.50: Radial profiles of the mean axial (left) and radial (right) velocity components; closed symbols - steady jet, open symbols pulsed jet ($Re \approx 4200$, $St = 0.50$)

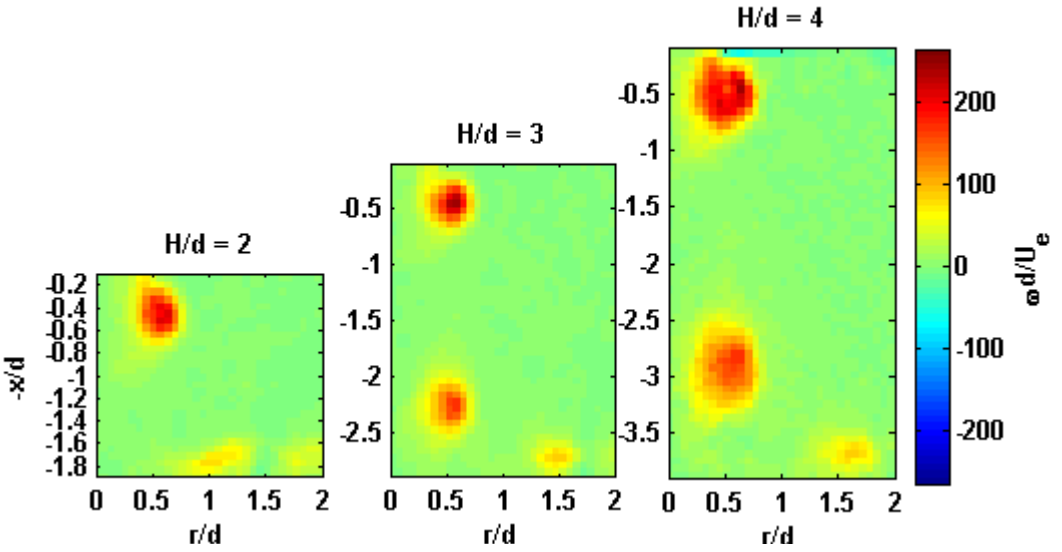

Figure 5.51: Effect of the nozzle-to-plate spacing on the vorticity field ($Re \approx 4200$, $St = 0.50$)

shows that H/d affects the development of V/U_e. Near the nozzle exit (Fig.5.50c), it can be observed that the presence of a pulsation leads to larger values of the mean radial velocity component, also, the profiles for $H/d = 3$ and $H/d = 4$ are relatively similar, however, for $H/d = 2$ at $r/d > 0.5$, the values of V/U_e are significantly lower. Further downstream (Fig.5.50b), shows that the mean radial velocity component follows a similar trend (similar profiles for $H/d = 3$ and $H/d = 4$). However,the jet situated at $H/d = 2$ exhibit larger values of V/U_e, probably as a consequence of the impinging wall forcing the fluid within the jet core radially and away from the jet axis at this location due to earlier fluid deceleration in the axial direction (Fig.5.49). Finally, near the impinging wall (Fig.5.50a), the peak values of V/U_e for pulsed jets do not exhibit a proportional response to H/d. For instance, the largest peak value of V/U_e corresponds to $H/d = 3$, which is contrary to what intuition would suggest. The peak value of V/U_e exhibits a further decrease for $H/d = 2$ and $H/d = 4$. This counter intuitive effect of H/d on V/U_e near the wall could be attributed to differences on how vortex rings impinge and interact with the wall when H/d is changed.

The effect of H/d on the vorticity field is shown in Fig.5.51. It shows the vorticity field when the main vortex is located at $x/d \approx 0.5$. Fig.5.51 indicates

that H/d does not affect the strength of the vortices, but It also suggest that as H/d is increased, vortices impinge on the wall less frequently. This explains the decrease in the mean radial velocity when H/d is increased from $H/d = 3$ to $H/d = 4$, in a similar fashion to the effect of the frequency already explored in section 5.2 on page 109, and section 5.3 on page 127. In addition, the lower values of V/U_e for $H/d = 2$ in comparison to $H/d = 3$ could be as a result of the vortices penetrating the wall jet leading to a reduction of V/U_e, in this respect, H/d has an effect similar to the Reynolds number (section 5.4 on page 144). Consequently, it can be argued that to fully predict the behaviour of pulsating jets all factors must be considered, in particular, their potential cross-effects. Finally, although the behaviour of pulsed jets is a result of the complex interaction between many factors, there are advantages to using pulsed jets. For instance, Fig.5.50a shows that independently of the nozzle-to-plate spacing, the location of the local maximum of V/U_e is fixed as a consequence of the pulsation at $r/d \approx 0.75$.

5.5.3 Velocity Fluctuations

The nozzle-to-plate spacing has a significant effect on both the axial and radial velocity fluctuations, as seen in Fig.5.52 and Fig.5.53. Fig.5.52 shows that as the nozzle-to-plate spacing is increased from $H/d = 2$ to $H/d = 3$, there is a reduction in the fluctuating levels within the shear layer, probably due to a less pronounced influence of the impinging wall. However, u'_{rms}/U_e increases as H/d is further increased, as a result of the vortex being distorted since it travels a longer distance to reach the wall (see Fig. 5.51 on the previous page). Also, for $H/d = 4$, the mixing layer of the jet has significantly penetrated the jet axis. Finally, Fig.5.52 shows that for $1 < r/d < 2$ at $x/H > 0.7$, the axial velocity fluctuations decrease as the nozzle-to-plate spacing is increased.

Fig.5.53 shows that the radial velocity fluctuations within the shear layer, decrease as H/d is increased from $H/d = 2$ to $H/d = 3$, then remain at similar levels for $H/d = 4$, however, the shear layer widens. Also, for $H/d = 3$ and $H/d = 4$, there is a slight increase in v'_{rms}/U_e for $x/H > 0.6$, which coincides with the deceleration of the centreline axial velocity. Therefore, this increase in

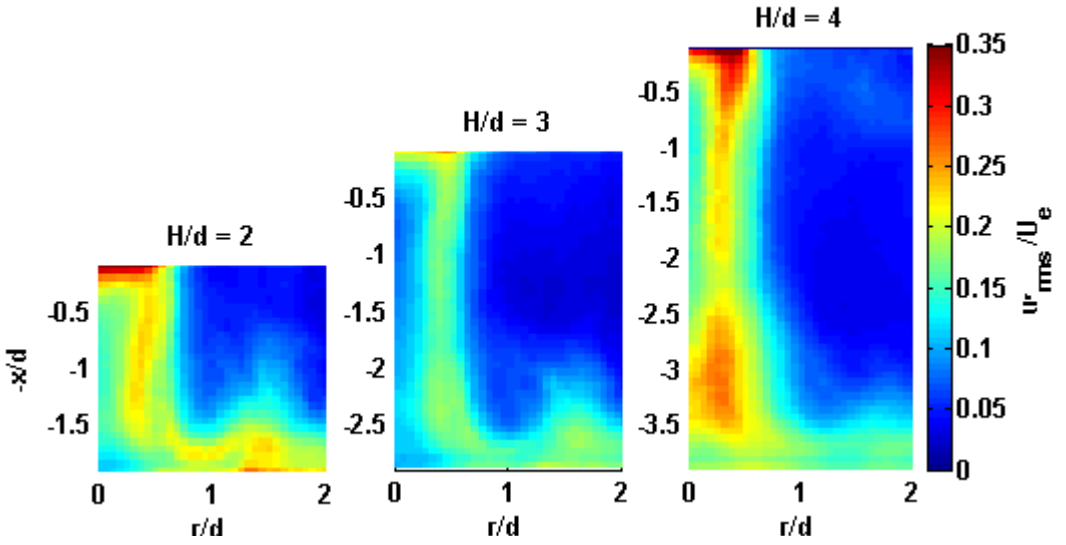

Figure 5.52: Effect of the nozzle-to-plate spacing in the axial velocity fluctuations ($Re \approx 4200$, $St = 0.50$)

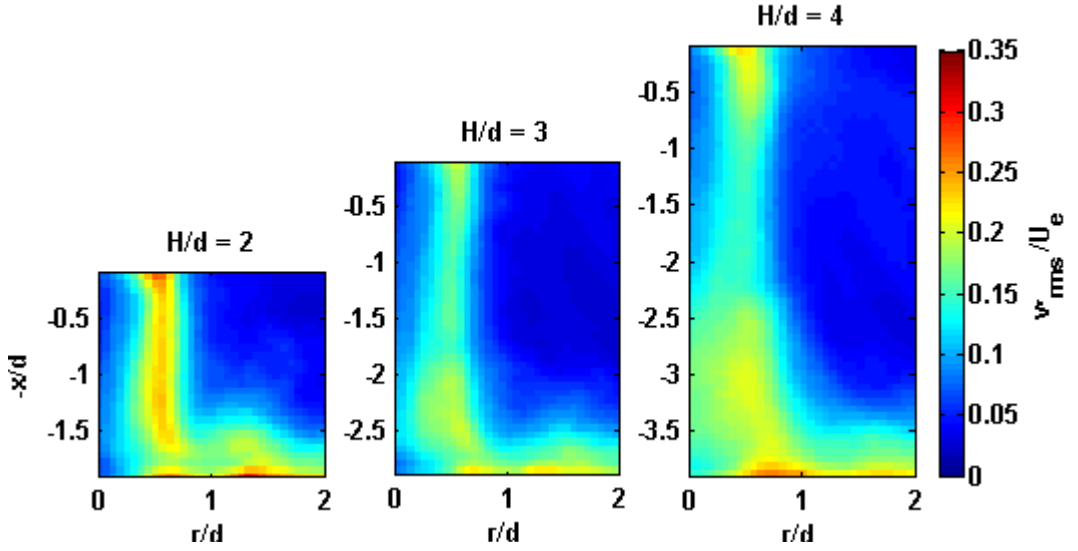

Figure 5.53: Effect of the nozzle-to-plate spacing on the radial velocity fluctuations ($Re \approx 4200$, $St = 0.50$)

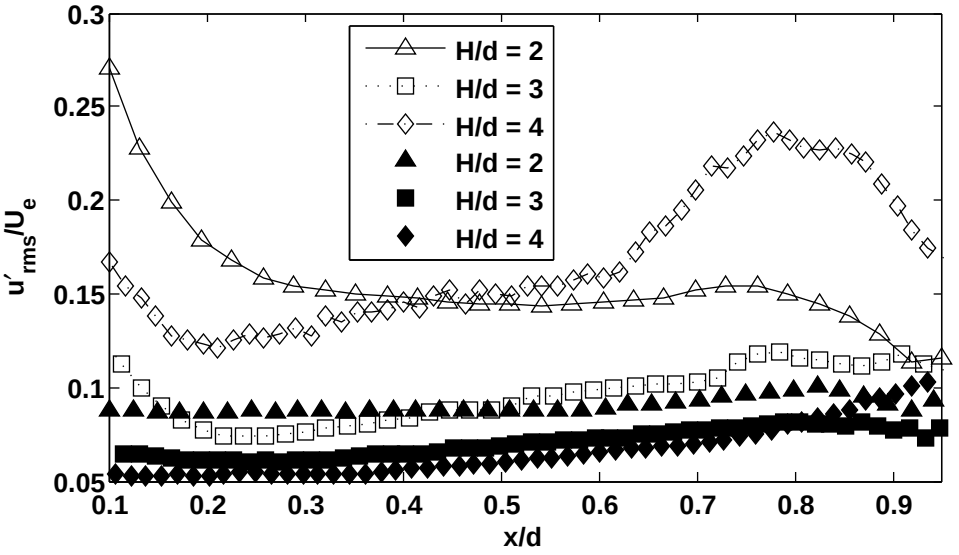

Figure 5.54: Effect of the nozzle-to-plate spacing on the centreline axial velocity fluctuations; closed symbols - steady jet, open symbols pulsed jet ($Re \approx 4200$, $St = 0.50$)

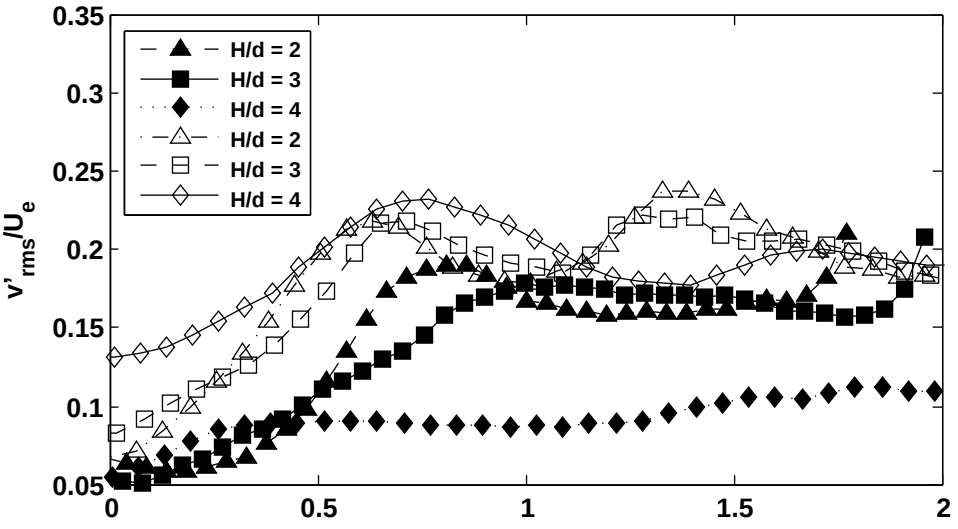

Figure 5.55: Effect of the nozzle-to-plate spacing on the radial velocity fluctuations near the impinging wall; closed symbols - steady jet, open symbols pulsed jet ($Re \approx 4200$, $St = 0.50$)

v'_{rms}/U_e could be the result of the vortices being forced away from the jet axis, combined with their relative distortion. Finally, similarly to the axial velocity fluctuations, there is also a decrease in v'_{rms}/U_e for $1 < r/d < 2$ in the vicinity of the impinging wall as H/d is increased.

Fig.5.54 shows the development of the velocity fluctuations at the jet centreline. Firstly, it shows that, near the nozzle exit, for $H/d = 2$, the velocity fluctuations are the largest, which could be a consequence of the relative short distance between the nozzle exit and the target wall, also for $H/d = 2$, the fluctuating levels remain relatively constant for $0.3 < x/d < 0.7$, however, they decrease sharply at $x/d > 0.8$, probably due to streamwise fluid deceleration. As H/d is further increased, the centreline velocity fluctuations near the nozzle exit decrease, probably an indication that the target wall no longer affects the fluctuations. Particularly, since the values of u'_{rms}/U_e for $H/d = 4$ rise in comparison to $H/d = 3$, this time as a result of increasing levels of u'_{rms}/U_e within the shear layer of the jet which affect the jet centreline velocity fluctuations (Fig.5.52). Also, $H/d = 4$ shows a marked increase in u'_{rms}/U_e at approximately $0.6 < x/d < 0.8$ due to the mixing layer having penetrated the jet axis (Fig.5.52 and Fig.5.53). In addition, in comparison to steady jets, the mixing layer penetrates the jet axis at smaller H/d distances. This is due to the general widening of the mixing layer as a consequence of the pulsating frequency as seen in previous sections.

Fig.5.55 shows the effect of the nozzle-to-plate spacing on the radial velocity fluctuations near the impinging wall. It shows that the effect of H/d near the stagnation point is to increase the value of v'_{rms}/U_e as it is increased. It also shows that for $H/d = 2$ and $H/d = 3$, the radial profiles of v'_{rms}/U_e are relatively similar. They both present two distinct local maximum located at approximately $r/d = 0.7$ and $r/d = 1.4$. The magnitude of the first local maximum is similar for both values of H/d, however, the magnitude of the second maximum is greater for $H/d = 2$. As the nozzle-to-plate spacing is increased to $H/d = 4$, the location of the first maximum shifts slightly away from the stagnation point. Interestingly, whereas lower values of H/d exhibit a second maximum, for $H/d = 4$ a minimum is present instead. Finally, in comparison to steady jets, the pulsed regime leads to relatively similar values of the radial velocity fluctuations, at least for the

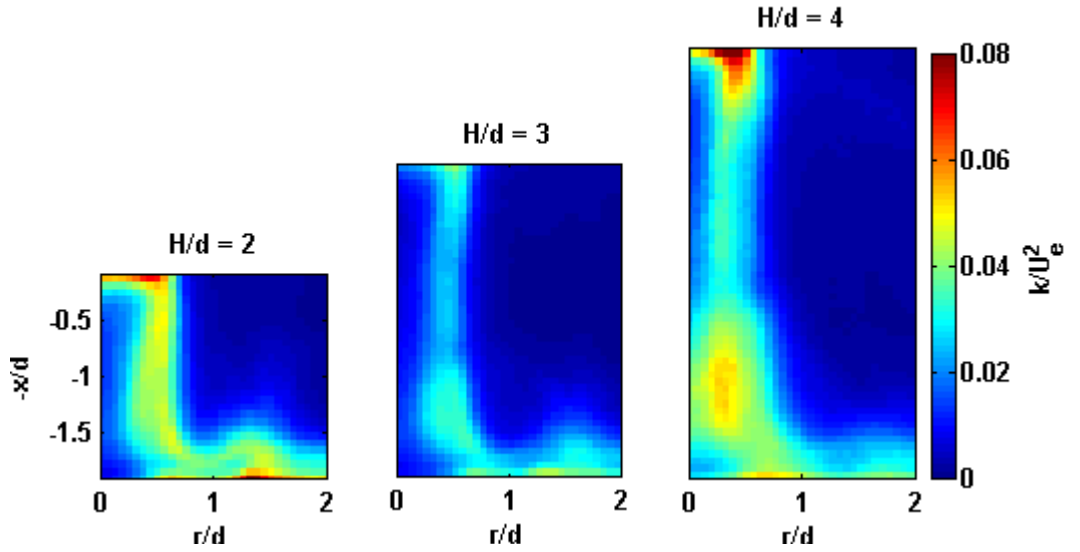

Figure 5.56: Effect of the nozzle-to-plate spacing on the mean turbulent kinetic energy ($Re \approx 4200$, $St = 0.50$)

non-dimensional spacings tested.

5.5.4 Turbulent Kinetic Energy

Fig.5.56 shows that the non-dimensional spacing significantly affects the mean turbulent kinetic energy, in particular within the shear layer of the jet. Firstly, the jet situated at $H/d = 2$ shows the largest values of the mean TKE in the shear layer, probably as a consequence of the vortices being distorted by the impinging wall. However, for $H/d = 3$, the values of k/U_e^2 exhibit a reduction, followed by an increase when $H/d = 4$, as a result of the increase of both the axial and radial velocity fluctuations for such spacing. It is also evident that for $H/d = 4$ the mixing layer has penetrated the jet axis, which is not the case for steady jets. In steady jets, there is a direct relationship between H/d and k/U_e^2 within the shear layer, that is as H/d increases, k/U_e^2 also increases. However, for pulsed jets, the effect of H/d is closely linked to the pulsating frequency. Usually, lower values of k/U_e^2 are desired so that mixing is a minimum within the shear layer in order to better preserve the initial thermal characteristics of the jet. In pulsed jets, in order to achieve the lowest possible values of the mean TKE, both the Strouhal number and the nozzle-to-plate spacing must be considered.

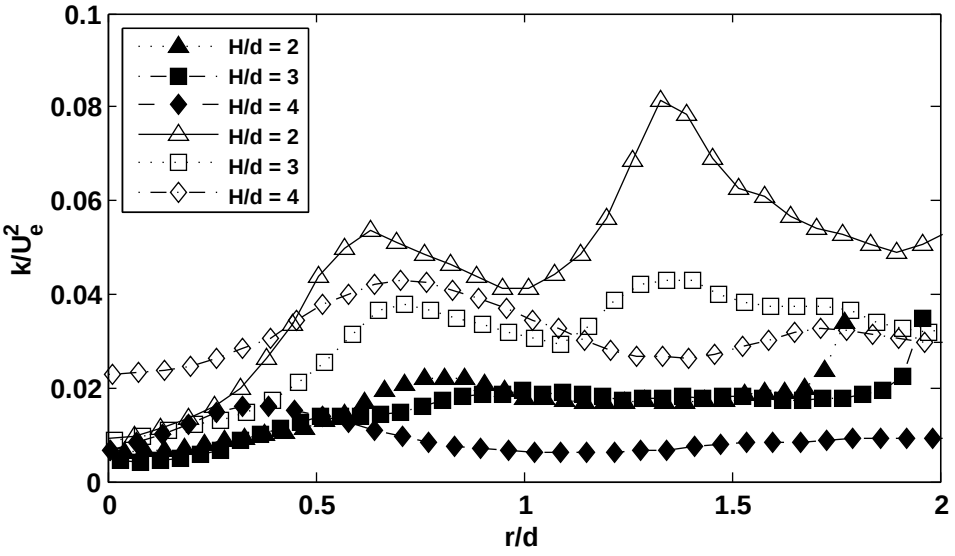

Figure 5.57: Effect of the nozzle-to-plate spacing on the mean turbulent kinetic energy near the impinging wall; closed symbols - steady jet, open symbols pulsed jet ($Re \approx 4200$, $St = 0.50$, x/H = 0.95)

Fig.5.57 shows radial profiles of the mean turbulent kinetic energy near the impinging wall. It shows that the profiles for $H/d = 2$ and $H/d = 3$ follow a similar trend, with the difference that the profiles for $H/d = 2$ exhibit larger values. Interestingly, for $H/d = 2$ and $H/d = 3$, there is a second peak at $r/d \approx 1.4$, however, as H/d is increased to 4 nozzle diameters, there is a minimum present instead. The elimination of this second peak for $H/d = 4$ could be due to the similarity between increasing H/d to reducing the pulsating frequency. This implies that, when H/d is increased, vortices are less likely to interact with each other, which could be the probable cause for the presence of a second peak when $H/d = 2$ and $H/d = 3$, making the peak for $H/d = 2$ higher, probably due to a more marked interaction between vortices.

5.5.5 Skewness Factor

Fig.5.58 shows that the axial skewness factor for $H/d = 2$ shows lower values than the jet at $H/d = 3$ near the nozzle exit, this indicates that the wall induces turbulent deceleration with an upwards tendency. As H/d is increased to $H/d = 3$, the negative values of u'^3/U_e^3 increase, indicating that the wall has a weaker

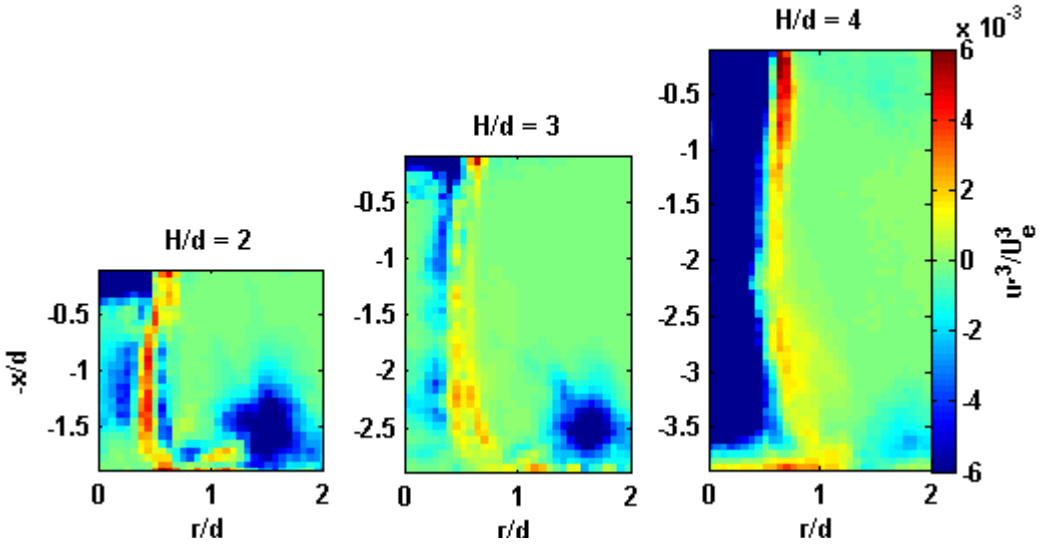

Figure 5.58: Effect of the nozzle-to-plate spacing on the skewness factor in the axial direction ($Re \approx 4200$, $St = 0.50$)

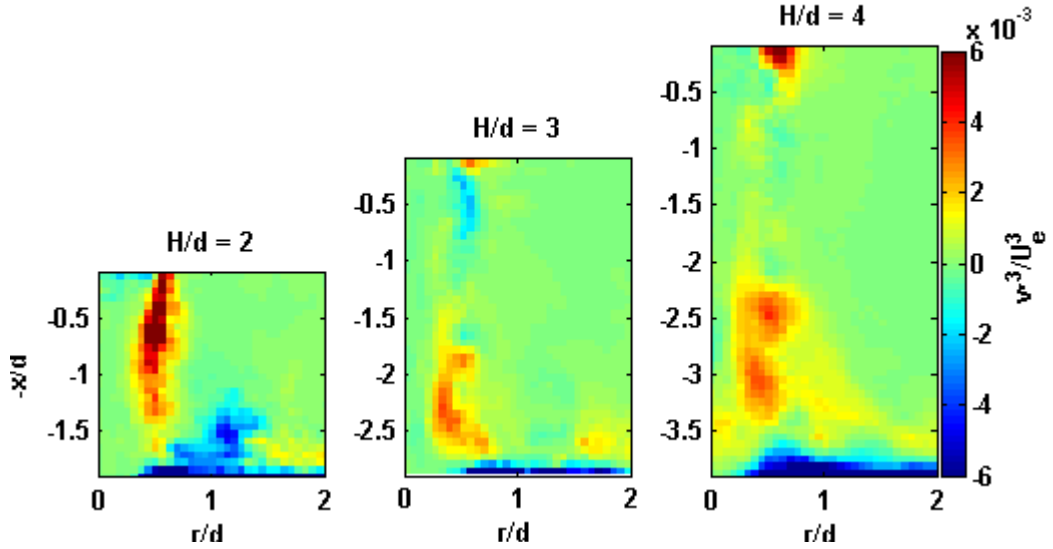

Figure 5.59: Effect of the nozzle-to-plate spacing on the skewness factor in the radial direction ($Re \approx 4200$, $St = 0.50$)

influence on the skewness factor near the nozzle exit. Interestingly, for $H/d = 4$, the values of u'^3/U_e^3 significantly decrease again, however, this decrease can not be attributed to the wall, instead it could be attributed to a natural generation of turbulent deceleration due to the longer distance that the pulse must travel as a result of the larger nozzle-to-plate spacing. Fig.5.58 also shows that the distribution of the axial skewness factor within the shear layer is most balanced when $H/d = 3$, indicating that for the given frequency, $H/d = 3$ corresponds to the non-dimensional spacing for which vortex rings reach the wall more effectively, i.e. with the least distortion. Finally, Fig.5.58 also shows that for $1 < r/d < 2$ there is a region of significant negative values of u'^3/U_e^3, which is not present for steady jets. Furthermore, the effect of H/d within this region is to increase u'^3/U_e^3 as it increases. This region of turbulent axial deceleration could be present for pulsed jets as a result of the vortices forcing fluid upwards (negative direction), which explains the reason for the increase on the values of u'^3/U_e^3 as H/d is increased, that is, the vortex is less strong near the impinging wall as H/d is increased, therefore, less capable of inducing turbulent deceleration.

Fig.5.59 shows the distribution of the radial triple correlations. Firstly, this figure shows that H/d affects the shear layer differently. For instance, for the lower non-dimensional spacing, the shear layer exhibits considerable radial turbulent acceleration, whereas, for $H/d = 3$ and $H/d = 4$, the shear layer is virtually unaffected by H/d for $0 < H/d < 0.55$, however, for the steady jet, v'^3/U_e^3 within the shear layer increases as H/d is increased. The presence of radial turbulent acceleration for $H/d = 2$ could be a result of the vortex rings being forced away from the jet axis as a consequence of the stronger radial acceleration present for such spacing (see Fig.5.50c). Fig.5.59 also shows that as H/d is increased, there is an increase in the values of v'^3/U_e^3 for approximately $x/d > 0.55$ within the shear layer. This increase could be a result of differences on the interaction between vortices and the wall as H/d is changed. For instance, the vortices, near the wall, become weaker as H/d is increased. This could explain the presence of negative values of v'^3/U_e^3 for $H/d = 2$, that is, the vortex, as it reaches the wall, is relatively stronger than for the other nozzle-to-plate spacings, therefore, experiencing stronger "resistance" as it forces fluid radially, generating turbulent

deceleration.

5.5.6 Reynolds Stress

The effect of the nozzle-to-plate spacing on the Reynolds stress for pulsed jets is considerably more pronounced than for steady jets, both within the shear layer of the jet and the wall jet region, as shown in Fig.5.60. The effect of H/d within the jet shear layer is particularly evident for $H/d = 2$ where a new type of Reynolds stress is present (O)[4]. This type of Reynolds stress is generated by positive values of v'. Therefore, it is similar to the expulsion type of Reynolds stress, however, its momentum transfer is directed away from the impinging wall i.e. upwards expulsion, which has only been encountered within the shear layer of the transitional pulsating jet situated at $H/d = 2$ for $0 < x/H < 0.45$ and also for $0.65 < x/H < 0.85$. In addition, only for $H/d = 2$, there is a region of Reynolds stress linked to entrainment (en) at approximately $0.5 < x/H < 0.8$ and $0.9 < r/d < 1.5$. Finally, for $H/d = 3$ and $H/d = 4$, the distribution of the Reynolds stress adopts a behaviour similar to steady jets. That is, entrainment (en), expulsion (e) and sweeping Reynolds stress (S) increase as the non-dimensional spacing is increased. However, this increase is more marked for pulsating jets.

The nozzle-to-plate spacing also affects the distribution of the Reynolds stress closer to the impinging wall and within the wall jet, but its effects are not as drastic in comparison to the jet shear layer. For example, at $0 < r/d < 1$ the type of Reynolds stresses present are the same independently of H/d. However, their magnitudes are affected by the nozzle-to-plate spacing and, similarly to steady jets, dominated by the radial turbulent component v'. In addition, for $r/d > 1$ the type of Reynolds stresses present (ejection (E) and wallwards interaction (W))is the same for $H/d = 2$ and $H/d = 3$, however, for $H/d = 4$ there is a generation of ejection (E) Reynolds stress located at approximately $1.25 < r/d < 1.75$, as a consequence of the presence of turbulent deceleration for both u' and v' (Fig.5.58, and Fig.5.59). Finally, for $r/d > 1.5$ there is a presence of high-speed

[4]This type of Reynolds stress is only present in the shear layer of the transitional jet pulsed at $H/d = 2$. Therefore, it was denoted by (O) because it does not merit a new notation

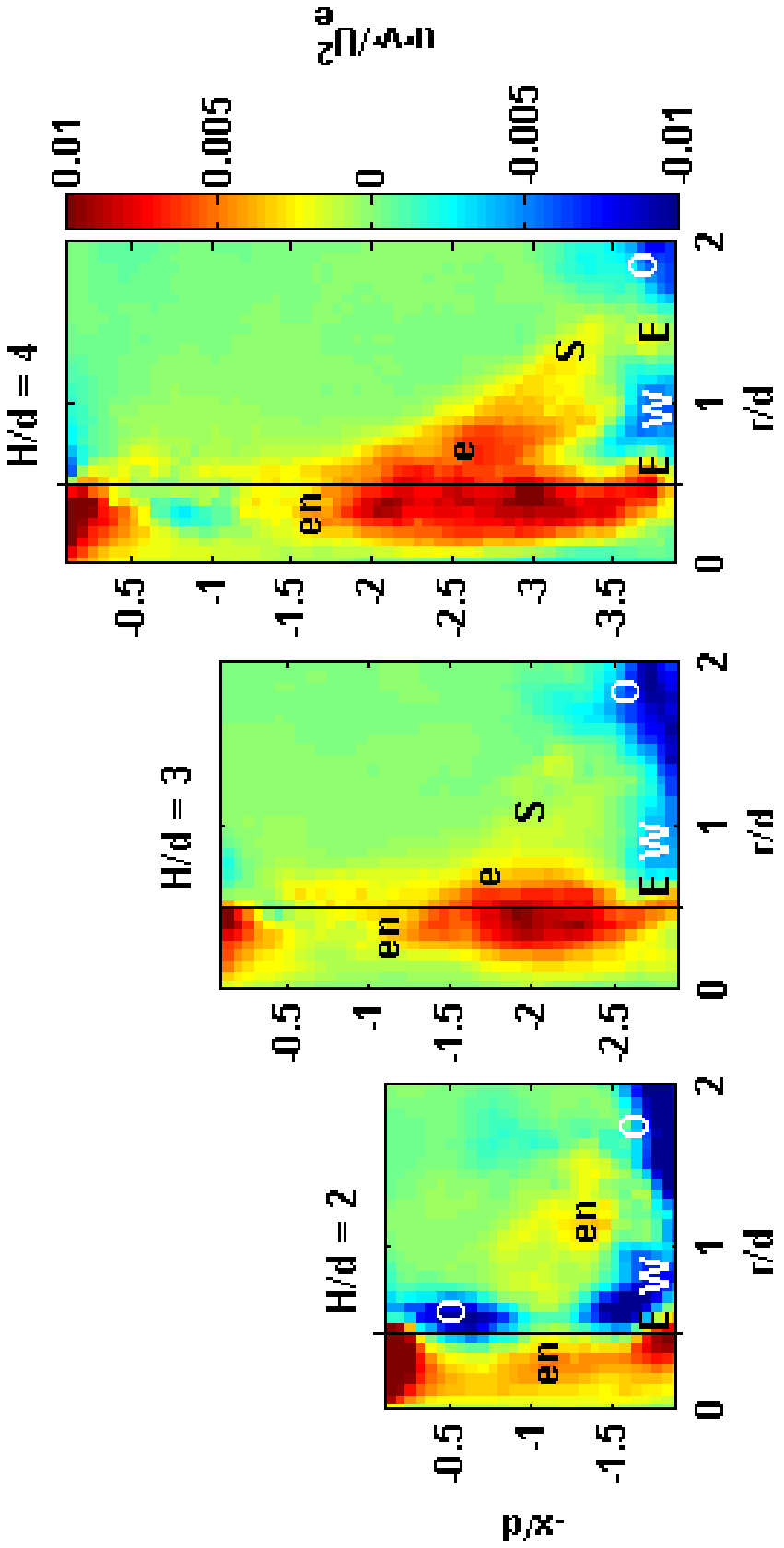

Figure 5.60: Effect of the nozzle-to-plate spacing on the Reynolds stress; entrainment (en), expulsion (e), ejection (E), sweep (S), wallward interaction (W), outward interaction (O) ($Re \approx 4200$, $St = 0.50$)

fluidic interactions away from the wall (O), which increases as H/d is increased. These type of Reynolds stress is dominated by the axial turbulent velocity, u', therefore, its increase is directly related to the increase of the axial skewness factor as H/d is increased (Fig.5.58). Consequently, the upward tendency of this type of Reynolds stress is less dominant as "O" increases, which occurs when H/d is increased. This indicates that as the nozzle-to-plate spacing is increased, which leads to weaker vortices impinging on the wall, such vortices generate less momentum transfer away from the target surface.

5.5.7 Mean Axial Momentum Balance Near the Wall

The of effect the nozzle-to-plate spacing was found to be rather straight forward, therefore, only the most significant findings will be presented in this section graphically. First of all, the distribution of the terms of the mean momentum equation are dominated by the axial convection and the radial diffusion as source terms, which are transformed into static pressure near the wall. However, the effect of the nozzle-to-plate spacing is to reduce the contribution of the radial diffusion as H/d is increased. Interestingly, the location of the local maximum of the radial diffusion is fixed at approximately $r/d = 0.65$, which is in direct relation to the location of the local maximum of the radial velocity component near the impinging wall (Fig.5.50), which is a result of the "fixing" effect of the pulsation on the local maximum of the mean radial velocity component. Also, pulsed jets exhibit a larger contribution of the radial diffusion than steady jets for $r/d > 0.6$, again, in line with the presence of larger values of the mean radial velocity component, V, indicating that it dominates the radial diffusion term.

Finally, for $H/d = 4$ a significant influence of the nozzle-to-plate spacing is observed as shown in Fig.5.61. It can be observed, that for this particular configuration, $H/d = 4$ and $St \approx 0.5$, the contribution to the mean axial momentum due to axial convection for the pulsed jet, is more pronounced than that of the steady jet. This increase in the contribution of the axial convection is directly linked to the steeper gradient, $\partial U/\partial x$, for the pulsed jet situated at $H/d = 4$ compared to its steady counterpart (Fig.5.49), this increase is evident, even though the local mean axial velocity, U, is larger for the steady jet. This indicates that

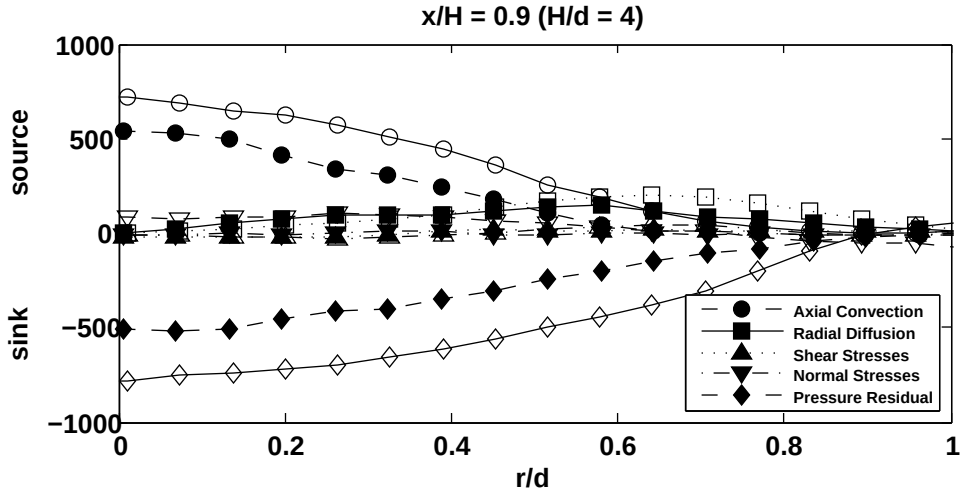

Figure 5.61: Mean axial momentum balance non-dimensionalised by d/U^2; closed symbols - steady jet, open symbols pulsed jet ($x/d = 4$, $x/H = 0.9$, $St \approx 0.50$)

the contribution to the term of the axial convection is dominated by the spacial gradient of the velocity, $\partial U/\partial x$.

Chapter 6

Flow Regime Summary and Heat Transfer Implications

6.1 Introduction

This chapter serves a dual purpose, firstly, it provides an overall summary of the major findings and differences between the steady and the pulsed flow regimes, making it easier to visualise the major differences between the two types of jet impingement flow studied. In addition, heat transfer implications are deduced from the flow field data, taking into consideration the differences between the two flow regimes, in other words, the objective of this chapter is to recognise which type of jet flow offers potential for improved heat transfer from the understanding of the flow field acquired from this study. This will facilitate the identification of the parameters which would lead to increased heat transfer and that will require further consideration, i.e. heat transfer studies.

6.2 Flow Regime Summary and Heat Transfer Implications

EFFECT OF Re	**Steady Jets**	**Pulsed Jets**	**Implications**
Time-average flow field	The jet core widens as the Reynolds number is increased. Centreline velocity decay is unaffected by Reynolds number.	The centreline velocity decays more rapidly as the Reynolds number is increased and decays more rapidly than steady jets. There is no evidence of the jet core widening with the Reynolds number. The maximum radial velocity near the wall is fixed by the presence of a pulsating frequency independently of the Reynolds number.	The pulsed jets developed larger values of the mean radial velocity near the wall, this could be translated into increased heat transfer for the pulsed jet, although not necessarily
Velocity fluctuations	Axial velocity fluctuations exhibit insignificant response to Re. However, radial velocity fluctuations near the impinging wall reduce with increasing Re. Centreline axial velocity fluctuations also decrease with increasing Re.	There is a decrease in both the axial and radial velocity fluctuations as the Reynolds number is increased. The centreline axial fluctuations fall within similar levels. Finally, the radial velocity fluctuations even though larger than the steady jet, also decrease with increasing Re.	The lower values of the centreline axial velocity fluctuation for pulsed jets could indicate that, due to lower mixing, the initial thermal conditions are better preserved in pulsed jets. However, near the stagnation point, steady jets exhibit lower values of the axial velocity fluctuations which is linked to increased hear transfer, implying better heat transfer characteristics of steady jets at the stagnation point
Turbulent kinetic energy	TKE within the shear layer is not directly linked to Re, with $Re = 6250$ leading to largest values of TKE within the shear layer. In contrast, as Re is increased, the TKE near the impinging wall decreases, in particular for $0.6 < r/d < 1.75$.	Following from the velocity fluctuations, the TKE within both the jet shear layer and near the impinging wall decrease as Re is increased.	The reduction of the TKE within the jet shear layer for pulsed jets as Re is increased points to the benefit of using pulsed jets with higher Reynolds numbers in order to reduce mixing within the shear layer, therefore, better preserving the initial thermal condition of the jet

Skewness factor	Distribution of axial skewness factor within the shear layer is balanced only for $Re = 4000$. For the jet with the largest Reynolds number, the axial skewness factor within the shear layer becomes predominantly negative. The values of the radial skewness factor near the impinging wall decrease with increasing Re.	The effect of the Reynolds number on the skewness factor is similar to that of the velocity fluctuations, that is, they decrease with increasing the Reynolds number.	-
Reynolds stress	The Reynolds stress $u'v'$ within the shear layer increases with increasing Re. There is a significant change in the type and magnitude of the Reynolds stress near the impinging wall as the Reynolds number is increased. It is interesting to notice that the wall-wards type (W) establishes as the dominant type of Reynolds stress as the Re is increased, especially, since this type of Reynolds Stress is associated with slow-speed fluidic interactions towards the wall.	The Reynolds stresses related to entrainment and expulsion decrease as the Reynolds number is increased. In addition, there is no significant change on the distribution of the Reynolds stress near the wall. However, wall-wards and outwards (away from the wall) type Reynolds stresses become more dominant as Re is increased.	Similar deductions can be make by observing the Reynolds stress distribution as the velocity fluctuations. For pulsed jets it would be beneficial to use as high a value of the Reynolds number as possible, due to the reduction observed in the entrainment and expulsion Reynolds stress present as Re is increased
Axial momentum balance	There is no significant effect of the Reynolds number on the distribution of the mean axial momentum balance. Also, as expected, the axial convection and radial diffusion terms are source terms which are balanced by being transformed into pressure momentum.	There is a considerable change in the distribution and profile shape of the various terms of the mean axial momentum balance. In particular, it can be noticed that the normal stress term appears as a sink term for $Re = 4800$ and $Re = 7990$. However, in all cases the momentum balance equation is dominated by the axial convection term.	-

Power spectrum analysis	The dominating frequencies that correspond to small vortex formation within the shear layer are $St = 0.25$, $St = 0.175$ and $St = 0.75$.	Those jets pulsated near any fundamental frequency of vortex shedding, and in the case of the turbulent jet the 8^{th} subharmonic, exhibit a behaviour similar to that of steady jets. However, in the case of the turbulent jets the jet also exhibits a marked reduction in the Reynolds stress ($u'v$) within the shear layer.	Not sufficient data for educated deductions
EFFECT OF H/d	**Steady Jets**	**Pulsed Jets**	**Implications**
Time-average flow field	Increasing H/d allows the jet to develop for longer. This leads to a relative widening of the jet core when the axial length scale is non-dimensionalised with respect to H. Also, the maximum radial velocity near the wall decreases with increasing H/d.	The centreline velocity decays more rapidly in pulsed jets. Also, similarly to steady jets, the maximum radial velocity near the wall increases as H/d is decreased. However, for $H/d = 3$ the radial velocity near the wall is larger than for $H/d = 2$ for the pulsed jet. This contrasting effect is attributed to the interaction between the different vortex rings and the impinging wall, which is significantly affected by the nozzle-to-plate spacing.	The sustained increase of the radial velocity near the impinging wall could be translated into improved heat transfer for pulsed jets for $r/d > 1.0$. However, in order for this observation to be validated a proper heat transfer study must be carried out.
Velocity fluctuations	Both the axial and radial velocity fluctuations develop larger values due to the larger space available to the jet before impingement. Also, the radial velocity fluctuations near the impinging wall decrease with increasing H/d.	There is no obvious direct link between the velocity fluctuations and H/d. Nonetheless, H/d significantly changes the turbulence intensity levels. In addition, and in line with previous findings, the fluctuation levels for the pulsed jet are larger than that of the steady jet.	The increase in the axial velocity fluctuations near the stagnation point for the pulsed jet located at $H/d = 4$ indicate a deterioration of the stagnation heat transfer. In addition, this increase is only significant for $H/d > 3$ indicating that for $H/d < 3$ the heat transfer characteristics for both pulsed and steady jets at the stagnation point would be similar

Turbulent kinetic energy	The TKE within the shear layer increases with increasing H/d. The TKE near the wall tend to decrease with increasing H/d.	In line with the velocity fluctuations, the TKE within the shear layer is significantly affected by the choice of H/d. In all cases, there is an increase in the TKE within the shear layer and near the impinging wall for $0.6 < x/H < 1$.	The jet situated at $H/d = 3$ exhibits the lesser amount of mixing within the shear layer, therefore, this would be the value of H/d which can potentially result into the best heat transfer to the wall.
Skewness factor	The axial skewness factor within the shear layer is only balance when $H/d = 3$. Also, the magnitude of the radial skewness factor decreases with increasing H/d.	H/d has a pronounced effect on both the axial and radial skewness factor. Interesting, there is a region of where there are negative values of the axial skewness factor for $0.6 < x/H < 0.9$ and $1.0 < r/d < 2.0$ which increases in magnitude as H/d is also increased.	-
Reynolds stress	Due to the longer distance that the fluid must travel before impingement, the Reynolds stress associated with entrainment and expulsion increase with H/d. However, the distribution of the Reynolds stress near the wall is less sensitive to H/d than Re and remained almost unchanged for the values of H/d tested.	The distribution of the Reynolds stress for the various values of H/d tested highlights the influence of the nozzle-to-plate spacing on the distribution of such stress. In accordance to the results on steady jets, H/d can be singled out as the most influential parameter affecting the distribution of this Reynolds stress ($u'v'$).	The presence of combined wall-wards and outwards type Reynolds stresses for $H/d = 3$ confirm that $H/d = 3$ has the potential for enhanced heat transfer in comparison to other spacings. However, the choice of H/d is also linked to the pulsating frequency
Axial momentum balance	The distribution of the mean axial momentum is significantly affected by H/d. The profiles of the both the source and sink terms become flatter as H/d is increased, in particular, the profiles of the radial diffusion term.	It is only for $H/d = 4$ that the pulsating jet ($St = 0.50$) exhibit larger values for the dominating terms of the mean axial momentum balance near the impinging wall in comparison to the steady jet. However, the shape of the different profiles is rather similar.	-

EFFECT OF St	**Transitional Jets**	**Turbulent Jets**	**Implications**
Time-average flow field	The jet centreline velocity decays more rapidly as St is increase. The jet core widens as St increases. The mean radial velocity component increases with St to values larger than that of an equivalent steady jet.	Similarly to transitional jets, the centreline velocity decays more rapidly as St is increased. However, there is no evident widening of the jet core with increasing St. Also, the radial velocity near the wall increases with St	-
Velocity fluctuations	Both the axial and radial velocity fluctuations increase with St and exhibit wider profiles than the steady jet. For the lower pulsating frequencies, the centreline axial fluctuations fall below those of the steady jet. However, the axial fluctuations within the shear layer and the radial fluctuations near the wall are larger than those of the steady jet.	The width of the axial and radial velocity fluctuations within the shear layer is similar to the steady jet. There is a decrease of the axial fluctuations when St is increased. Centreline and radial fluctuations near the wall increase with St	There is less mixing at the jet centreline for transitional jets when pulsed at the lower frequencies. Also, the values of the axial velocity fluctuations near the stagnation point are lower for the transitional jet, indicating that the transitional pulsed jets would exhibit better heat transfer characteristics at the centreline
Turbulent kinetic energy	In a similar line as the velocity fluctuations, the TKE energy experiences an overall increase with increasing St. Only near the wall for $St = 0.10$ the TKE falls below that of the steady jet.	TKE within the shear layer and near the wall decrease with increasing St. However, their magnitude is larger than that of the steady jet.	Turbulent pulsed jets exhibit a reduction of TKE within the shear layer as St is increased which is not the case for transitional pulsed jets. This implies that there is less mixing present within the shear layer of turbulent and pulsating jets, especially, as the Strouhal number is increased.
Skewness factor	The axial skewness factor shows no significant change due to St. However, the radial skewness factor increases with St.	Axial skewness factor decreases with increasing St. The radial skewness factor remains unaffected within the shear layer, with a moderate decrease near the wall with increasing St	-

Reynolds stress	The Reynolds stress within the shear layer are wider and exhibit larger values than the steady jet, which increase with St. There is a significant change to the distribution of the Reynolds stress near the wall with increasing St. Interestingly, the effect is similar to increasing the Reynolds number since wall-wards fluidic interactions become dominant as St increases, but also the appearance of an outwards Reynolds stress as St is increased further.	The Reynolds stresses associated with entrainment and expulsion decrease with increasing St. On the other hand, the distribution of the Reynolds stress near the wall exhibit no significant response to the pulsating frequency. However, their magnitude decreases with increasing St.	The turbulent jet pulsed at the highest frequency exhibits less entrainment and expulsion than the steady jet. In addition, both entrainment and expulsion increase in transitional and pulsating jets. Therefore, turbulent pulsed jets at high pulsating frequencies could lead to improved heat transfer in comparison to both steady and transition pulsed jets
Axial momentum balance	The axial momentum distribution fall below that of the steady jet, apart for the radial diffusion term which remains a source term for longer when $St = 0.50$. Also, the normal shear stress is a sink term for the lower values of St tested.	The normal stress becomes a source term for the lower pulsating frequency.	-

Chapter 7

Conclusion

The effects of the Reynolds number, the nozzle-to-plate spacing, and the Strouhal number have been systematically examined. To conclude this investigation, the major findings will be presented. They include:

In relation to new knowledge

- It was found that the shear layer can be considered as transitional for Reynolds numbers which are higher than that for which transition occurs at the centreline ($Re \approx 4000$). This transition refers to the break up of the shear layer into turbulent eddies that travel separately towards the impinging wall, which are also larger than those of "fully" turbulent jets ($Re = 10000$). This transitional behaviour is characterised by an increase in both the velocity fluctuations and the Reynolds stresses within the jet shear layer, which is followed by a decrease in these quantities as the Reynolds number is further increased. The presence of this transitional behaviour was observed at $Re = 6250$.

- The concept of a critical Strouhal number is introduced, which helps predict the effect of the strouhal number. It was defined as $St_c = d/U_e$ based on a steady jet with similar Reynolds number. It was found, for instance, that near the impinging wall the local maxima of the profile of the mean radial velocity component of steady jets is similar is magnitude to that of pulsed jets when pulsed at $St \approx St_c$. Similarly, when a jet is pulsed at $St \gtrapprox St_c$ reductions in both the turbulent kinetic energy and the Reynolds stresses

within the jet shear layer can be expected.

Influence of the experimental variables to the flow field

- It was found that the Reynolds number affects both steady and pulsed jets differently. Increasing the Reynolds number leads to an increase in the spreading of a steady jet, which is not as pronounced for pulsed jets. However, for pulsed jets increasing the Reynolds number has an effect similar to increasing the Strouhal number, that is, it leads to an increase in the vorticity field. Therefore, the effects of the Reynolds number and the Strouhal number are analogous in this respect. This explains the decrease in both the mean TKE and the Reynolds stresses for pulsed jets as the Reynolds number is increased. That is, the vortex pairs become stronger and mixing is contained within the vorticity field more effectively. For steady jets, mixing increases as the Reynolds number is increased.

- The nozzle-to-plate spacing has a more pronounced effect on pulsed jets than steady jets. For pulsed jets, the effect of H/d is a combination of its effects on steady jets, as well as the effects of the Strouhal number. Since it was found that, to some extent, increasing H/d is analogous to reducing the Strouhal number. In addition, for low values of H/d the impinging wall affects the flow field significantly, especially, for pulsed jets. This is particularly evident in the distribution of the Reynolds stresses, since for $H/d = 2$, a new type of Reynolds stress was found, which has an influence away from both the jet axis (positive v') and the impinging wall (negative u'). Also, it was found that for $H/d = 4$ the contribution to momentum transport due to axial convection was larger for the pulsed jet as a consequence of a larger spatial gradient of the axial velocity component near the wall.

- The strouhal number also affects the flow field of turbulent and transitional jets differently. For instance, the spread rate of the transitional jet is more responsive to St, which increases as St is increased. However, for both jets, vorticity increases as St is increased. Most interesting of all, is the different effects of the Strouhal number on the velocity fluctuations and the

Reynolds stresses. For turbulent jets, both of these quantities decrease as St is increased. However, this decrease is only present for the transitional jet when $St > 0.25$.

Deductions related to heat transfer

- Mixing is contained more efficiently within the shear layer of pulsed jets, therefore, the initial thermal characteristics of the jet at exit could be better preserved.

- The transitional jet at $H/d = 4$ and $St \approx 0.5$ leads to enhanced momentum transport compared to the steady jet, suggesting that this jet could lead to higher rates of heat transfer.

- The use of turbulent pulsating jets instead of transitional pulsating jets in heat transfer applications could be advantageous since mixing within the shear layer is reduced for turbulent jets as the Strouhal number is increased. Therefore mixing is reduced preserving the initial thermal characteristics of the jet.

- It was also found that near the impinging wall, the velocity field indicates that steady jets exhibit conditions that indicate better heat transfer characteristics. However, for $r/d > 1.5$ the changes in the distribution of the Reynolds stresses indicate that pulsed jets can exhibit enhanced heat transfer due to the presence of wallward directed Reynolds stresses (W). This could explain contradictions in the literature on the enhancement effects of the pulsation. For instance, if stagnation or local heat transfer coefficients are extracted, steady jets could present higher rates of heat transfer, as demonstrated by Mladin [4]. However, if averaged heat transfer coefficients are calculated, then pulsed jets could exhibit enhanced heat transfer as demonstrated by the results of Sailor [19]. Also, scatter in the data for pulsed jet heat transfer can be attributed to different combinations of the Strouhal number, the Reynolds number and the nozzle-to-plate spacing, in addition to other parameters that were not examined in this work, for instance, the effect of the nozzle type.

In relation to practical applications

- Pulsating jets could be used for flow control applications that require the presence of a local maximum of the mean radial velocity component at a fixed location (near the impinging wall). This is possible because the position of the local maxima of the mean radial velocity component is fixed by the presence of a pulsation, at least for the nozzle-to-plate spacings tested.

Suggested Areas for Further Research

This investigation also found areas that deserve further study, or that can complement this work. Some suggestions include:

- Further studying the development of the shear layer in smaller increments of the Reynolds number, in order to assess the point at which the shear layer becomes transitional i.e, separate turbulent eddies are formed, and also, increasing the resolution near the impinging wall so that the evolution of the vortex dynamics at smaller Reynolds number increments can be observed

- Expanding the study to larger radial distances from the stagnation point since pulsed jets, for $r/d > 0.6$, exhibit larger values of the mean radial velocity component near the wall, therefore, this is where heat transfer enhancement from pulsed jets can be expected [19]

- A study of the development of the thermal field would be complementary. It would define clear links between the thermal field and the velocity field

- A heat transfer study would be beneficial in order to help understand the forced convection mechanisms at the wall, with a clear link to the velocity field

References

[1] C. Carcasci. An experimental investigation on air impinging jets using visualisation methods. *International journal of thermal science*, 38:808–818, 1999.

[2] J. San and M. Lai. Optimum jet to jet spacing of heat transfer for staggered arrays of impinging air jets. *International journal of heat and mass transfer*, 44:3997–4007, 2001.

[3] E. C. Mladin and D. A. Zumbrunnen. Alterations to coherent flow structures and heat transfer due to pulsations in an impinging air-jet. *Int. j. therm. sci.*, 39:236–248, 2000.

[4] E. C. Mladin and D. A. Zumbrunnen. Local convective heat transfer to submerged pulsating jets. *International journal of heat and mass trasfer*, 40(14):3305–3321, 1997.

[5] J. Vejrazka. *Experimental study of a pulsating round impinging jet (Etude experimentale d'un jet circulaire impactant pulsant)*. PhD thesis, Laboratoire des ecoulements geophysiques et industriels, Grenoble, December 2002.

[6] K. Jamabunathan, E. Lai, M. A. Moss, and B. L. Button. A review of heat transfer data for single circular jet impingement. *International Journal of heat and fluid flow*, 13(2):106–115, June 1992.

[7] LaVision. *Tools for Davis: Highspeedstar*. LaVision, 2005. Germany.

[8] LaVision. *Tools for Davis:Davis FlowMaster software for Davis 7.0*. LaVision, November 2005. Germany.

[9] Janice A. Fitzgerald and Suresh V. Garimella. A study of the flow field of a confined and submerged impinging jet. *International journal of heat and mass transfer*, 41(8–9):1025–1034, 1998.

[10] K. Nishino, M. Samada, K. Kasuya, and K. Torii. Turbulence statistics in the stagnation region of an axisymmetric impinging jet flow. *International journal of heat and fluid flow*, 17:193–201, 1996.

[11] E. Baydar and Y. Ozmen. An experimental and numerical investigation on a confined impinging air jet at high reynolds numbers. *Applied therman engineering*, 25:409–421, 2005.

[12] T. S. O'Donovan and D. B. Murray. Jet impingement heat transfer - part i: mean and root-meant-square heat transfer and velocity distributions. *International journal of heat and mass transfer*, 50:3291–3301, 2007.

[13] D. Cooper, D. C Jackson, B. E. Launder, and G. X. Liao. Impinging jet studies for turbulence model assessment - i. flow-field experiments. *International journal of heat and mass transfer*, 36(10):2675–2684, 1993.

[14] J. Brown. *Heat transfer between a staggered array of hot air jets and a jet engine nacelle lipskin*. PhD thesis, School of Aeronatical Engineering, The Queen's University of Belfast, September 1999.

[15] A. A. Kendoush. Theory of stagnation region heat and mass transfer to fluid jets impinging normally on solid surfaces. *Chemical engineering and processing*, 37:223–228, 1998.

[16] M. Angioletti, R. M. Tommaso, E. Nino, and G. Ruocco. Simultaneous visualization of flow field and evaluation of local heat transfer by transitional impinging jets. *International journal of heat and mass transfer*, 46:1703–1713, 2003.

[17] C. F. Ma, Q. Zheng, S. C. Lee, and T. Gomi. Impingement heat transfer and recovery effect with submerged jets of large prandtl number liquid - i. unconfined circular jets. *International journal of heat and mass transfer*, 40(6):1481–1490, 1997.

[18] O. A. Moreno, R. H. Katyl, J. D. Jones, and P. A. Moschak. Mass transfer of an impinging jet confined between parallel plates. *IBM J. RES. Develop.*, 37(2):143–155, March 1993.

[19] D. J. Sailor, D. J. Rohli, and Q. Fu. Effect of variable duty cycle flow pulsations on the heat transfer enhancement for an impinging air jet. *International journal of heat and fluid flow*, 20:574–580, 1999.

[20] Y. Zvirin. Heat transfer between a pulsating impinging jet and a flat surface. *Israel journal of technology*, 5(1–2):152–169, 1967.

[21] H. J. Poh, K. Kumar, and A. S. Mujumdar. Heat transfer from a pulsed laminar impinging jet. *International communications in heat and mass transfer*, 32:1317–1324, 2005.

[22] J. F. Tomich and E. Patterson. Some new results on momentum and heat transfer in compressible turbulent free jets. *AIChE Jounal*, pages 948–954, September 1967.

[23] G. N. Abramovich. *The theory of turbulent jets*. The Massachusetts Intitute of Technology, first edition, 1963.

[24] I. Wygnanski and H. Fiedler. Some measurements in the self-preserving jet. *J. fluid mech.*, 38(3):577–612, 1969.

[25] R. Chevray and N. K. Tutu. Intermittency and preferential transport of heat in a round jet. *J. fluid mech.*, 88(1):133–160, 1978.

[26] A. J. Yule. Large-scale structure in the mixing layer of a round jet. *J. fluid mech.*, 89(3):413–432, 1978.

[27] M. R. Davis and P. O. A. L. Davies. Shear fluctuations in a turbulent jet shear layer. *J. fluid mech.*, 93(2):281–303, 1979.

[28] J. C. Lau, P. J. Morris, and M. J. Fisher. Measurements in subsonic and supersonic and free jets using a laser velocimeter. *J. fluid mech.*, 93(1):1–27, 1979.

[29] A. K. M. F. Hussain and K. B. Q. Zaman. The 'preferred mode' of the axisymmetric jet. *J. fluid mech.*, 110:39–71, 1981.

[30] A. K. M. F. Hussain and A. R. Clark. On the coherent structure of the axisymmetric mixing layer: a flow-visualization study. *J. fluid mech.*, 104:263–294, 1981.

[31] R. A. Antonia, B. R. Satyaprakash, and A. K. M. F. Hussain. Statistics of fine-scale velocity in turbulent plane and circular jets. *J. fluid mech.*, 119:55–89, 1982.

[32] M. A. Z. Hasan and A. K. M. F. Hussain. The self-excited axisymmetric jet. *J. fluid mech.*, 115:59–89, 1982.

[33] D. Liepmann and M. Gharib. The role of streamwise vorticity in the near-field entrainment of round jets. *J. fluid mech.*, 245:643–668, 1992.

[34] M. D. Fox, M. Kurosaka, L. Hedges, and K. Hirano. The influence of vortical structures on the thermal fields of jets. *J. fuid mech.*, 255:447–472, 1993.

[35] F. Lemoine, Y. Antoine, M. Wolff, and M. Lebouche. Simultaneous temperature and 2d velocity measurements in a turbulent heated jet using combined laser-induced fluorescence and lda. *Experiments in fluids*, 26:315–323, 1999.

[36] L. Pietri, M. Amielh, and F. Anselmet. Simultaneous measurements of temperature and velocity fluctuations in a slightly heated jet combining a cold wire and laser doppler anenometry. *International journal of heat and fluid flow*, 21:22–36, 2000.

[37] N. J. Lawson and M. R Davidson. Self-sustained oscillation of a submerged jet in a thin rectangular cavity. *Journal of fluids and structures*, 15:59–81, 2001.

[38] P. O'Neill, J. Soria, and D. Honnery. The stability of low reynolds number round jets. *Experiments in fluids*, 36:473–483, 2004.

[39] S. M. Anderson and K. Bremhorst. Investigation of the flow field of a high heated jet of air. *International journal of heat and fluid flow*, 23:205–219, 2002.

[40] S. Z. Shuja, B. S. Yilbas, and M. Rashid. Confined swirling jet impingement onto an adiabatic wall. *International journal of heat and mass transfer*, 46:2947–2955, 2003.

[41] Y. M. Chung, K. H. Luo, and N. D. Sandham. Numerical study of momentum and heat transfer in unsteady impinging jets. *International journal of heat and fluid flow*, 23:592–600, 2002.

[42] T. J Craft, L. J. W. Graham, and B. E. Launder. Impinging jet studies for turbulence model assessment - ii. an examination of the performance of four turbulence models. *International journal of heat and mass transfer*, 36(10):2685–2697, 1993.

[43] D. Khummongkol and P. Khummongkol. Heat transfer between an impinging air jet and an impinged water surface. *Energy*, 23(3):239–245, 1998.

[44] S. Ashfirth-Frost, K. Jambunathan, and C. F. Whitney. Velocity and turbulence characteristics of a semiconfined orthogonally impinging slot jet. *Experimental thermal and fluid science*, 14:60–67, 1997.

[45] K. Kataoko, Y. Kamiyama, S. Hashimoto, and T Komai. Mass transfer between a plane surface and an impinging turbulent jet: the influence of surface-pressure fluctuations. *Journal of fluid Mechanics*, 119:91–105, 1982.

[46] S. Aydore and P. J. Disimile. Natural coherent structure dynamics in near field of fully turbulent axisymmetric jet. *AIAA Journal*, 35(7), July 1997.

[47] E. Baydar. Confined impinging air jet at low reynolds numbers. *Experimental thermal and fluid science*, 19:27–33, 1999.

[48] M. Fairweather and G. K. Hargrave. Experimental investigation of an axisymmetric impinging turbulent jet: 1 - velocity field. *Experiment in fluids*, 33:464–471, 2002.

[49] I. Bedii Ozdemir and J. H. Whitelaw. Impingement of an axisymmetric jet on unheated and heated flat plates. *Journal of fluid mechanics*, 240:503–532, 1992.

[50] J. Lee and S. Lee. The effect of nozzle aspect ratio on stagnation region heat transfer characteristics of elliptic impinging jet. *International journal of heat and mass transfer*, 43:555–575, 2000.

[51] M. D. Deshpande and R. N. Vaishnav. Submerged laminar jet impingement on a plane. *Journal of fluid mechanics*, 114:213–236, 1982.

[52] L. Huang and M. S. El-Genk. Heat transfer of an impinging jet on a flat surface. *International journal of heat and mass transfer*, 37(13):1915–1923, 1994.

[53] Jung-Yang San, Chih-Hao Huang, and Ming-Hong Shu. Impingement cooling of a confined circular air jet. *International journal of heat and mass transfer*, 40(6):1355–1364, 1997.

[54] S. V. Garimella and B. Nenaydykh. Nozzle-geometry effects in liquid jet impingement heat transfer. *International journal of heat and mass transfer*, 39(14):2915–2923, 1996.

[55] J. Lee and S. Lee. The effect of nozzle aspect ratio on stagnation region heat transfer characteristics of axisymmetric impinging jet. *International journal of heat and mass transfer*, 43:3497–3509, 2000.

[56] S. Ashforth-Frost, K. Jambunathan, C. F Whitney, and S. J. Ball. Heat transfer from a flat plate to a turbulent axisymmetric impinging jet. *Proc. instn. mech. engrs.*, 211:167–172, 1997.

[57] F. Sarghini and G. Ruocco. Enhancement and reversal heat transfer by competing modes in jet impingement. *International journal of heat and mass transfer*, 47:1711–1718, 2004.

[58] V. Tesar and Z. Travnicek. Increasing heat and/of mass transfer rates in iminging jets. *Jounal of visualization*, 8(2):91–98, 2005.

[59] Z. Q. Lou, A. S. Mujumdar, and C. Yap. Effects of geometric parameters on confined impingment heat transfer. *Applied thermal engineering*, 25:2687–2697, 2005.

[60] A. A. Kendoush. Theory of convective heat and mass transfer to fluids flowing normal to a plane. *Int. comm. heat and mass transfer*, 23(2):249–262, 1996.

[61] L. Song and J. Abraham. The structure of wall-impinging jets: computed bersus theoretical and measured results. *Journal of fluids engineering*, 125:997–1005, November 2003.

[62] P. Brevet, C. Dejeu, E. Dorignac, M. Jolly, and J. J. Vullierme. Heat transfer to a row of impinging jets in consideration of optimisation. *International journal of heat and mass transfer*, 45:4191–4200, 2002.

[63] C. T. Chang, G. Kojasoy, and F. Landis. Confined single and multiple jet impingement heat transfer i. turbulent submerged liquid jets. *International journal of heat and mass transfer*, 38(5):833–842, 1995.

[64] W. G. Hill and P. R. Greene. Increased turbulent jet mixing rates obtained by self-excited acoustic oscillations. pages 520–525. Joint applied mechanics, fluids engineering and bioengineering conference, Transactions of the ASME, September 1977.

[65] K. B. M. Q. Zaman and A. K. M. F. Hussain. Vortex pairing in a circular jet under controlled excitation. part 1. general jet response. *Journal of fluid mechanics*, 101(3):449–491, 1980.

[66] A. K. M. F. Hussain and K. B. M. Q. Zaman. Vortex pairing in circular jet under controlled excitation. part 2. coherent structure dynamics. *Journal of fluid mechanics*, 101(3):493–544, 1980.

[67] L. J. W. Graham and K. Bremhorst. Application of the $\kappa - -\epsilon$ turbulence model to the simulation of a fully pulsed free air jet. *Journal of fluids engineering*, 115:70–74, March 1993.

[68] K. Bremhorst and P. G. Hollis. Velocity field of an axisymmetric pulsed, subsonic air jet. *AAIA Journal*, 28(12):2043–2049, December 1990.

[69] M. Tsubokura, T. Kobayshi, N. Taniguchi, and W. P. Jones. A numerical study on the eddy structures of impinging jet excited at the inlet. *International journal of heat and fluid flow*, 24:500–511, 2003.

[70] S. Marzouk, H. Mhiri, S. El-Golli, G. Le-Palec, and P. Bournot. Numberical study of momentum and heat transfer in a pulsed plane laminar jet. *International journal of heat and mass transfer*, 46:4319–4334, 2003.

[71] J. Mi, D. S. Nobes, and G. Nathan. Influence of jet exit conditions on the passive scalar field of an axisymmetric free jet. *J. fluid mech.*, 432:91–125, 2001.

[72] H. Lai, J. W. Naughton, and W. R. Lindberg. An experimental investigation of starting impinging jets. *Journal of fluids engineering*, 125:275–282, March 2003.

[73] N. Y. Obot, A. S. Mujumbar, and W. J. M. Douglas. Effect of semiconfinement on impingement heat transfer. *Proc. 7th int. heat transfer conf.*, (3):395–400, September 1982.

[74] P. Harkness. The effect of reynolds number on heat transfer from an impinging jet to a flat plate and the enhancement of such heat transfer by means of pulsatile jet flow. Master's thesis, School of Aeronautical Engineering, The Queen's University of Belfast, May 2003.

[75] R. B. Wicker and J. K. Eaton. Near field of a coaxial jet with and without axial excitation. *AIAA Journal*, 32(3):542–546, March 1994.

[76] M. Raffel, C. E. Willert, and J. Kompoenhans. *Particle image velocimetry: A practical guide*. Springer, 1997.

[77] K. Bremhorst and P. J. Gehrke. Measured reynolds stress distributions and energy budgets of a fully pulsed round air jet. *Experiments in fluids*, 28:519–531, 2000.

[78] S. V. Garimella C. Li. Prandtl-number effects and generalized correlations for confined and submerged jet impingement. *International journal of heat and mass transfer*, 44:3471–3480, 2001.

[79] R. Gardon and J. C. Akfirat. The role of turbulence in determining the heat transfer characteristics of impinging jets. *International journal of heat and mass transfer*, 8:1261–1272, 1965.

[80] J. M. Wallace, H. Eckelmann, and R. S. Brodkey. The wall region in turbulent shear flow. *Journal of fluid mechanics*, 54(1):39–48, 1972.

[81] L. Cheng and T. Wu. Confined and submerged turbulent jet impingment cooling heat transfer. Technical report, Purdue University, Deparment of Nuclear Engineering, 2003.

Appendix A

Background

General Features of Impinging Jets

Due to their highly localised heat and mass transfer rates, impinging jets are widely used in many industrial applications, whether cooling or heating of a surface is required. Examples include, drying of clothes, cooling turbine blades, cooling of electronic equipment, aircraft anti-icing systems, etc. As a consequence, the study of impinging jets continuous to be present in many prestigious universities and research centres, in order to develop better and improved correlations describing impinging jet flow.

Firstly, let us consider the flow of a jet impinging orthogonally on a plane surface. This type of flow is normally divided into four zones or regions (adapted from [81] and [14]): (See Fig.A.1)

1. A transition zone of flow establishment (zone I)
2. A zone of established flow in the original direction of the jet (zone II)
3. A deflection zone (zone III)
4. A zone of established flow in the radial direction (zone IV)

The potential core is present in zone I. It extends, by definition, to the point at which the jet velocity on the jet centreline falls below the original exit velocity of the jet. With increasing distance from the exit the potential core narrows,

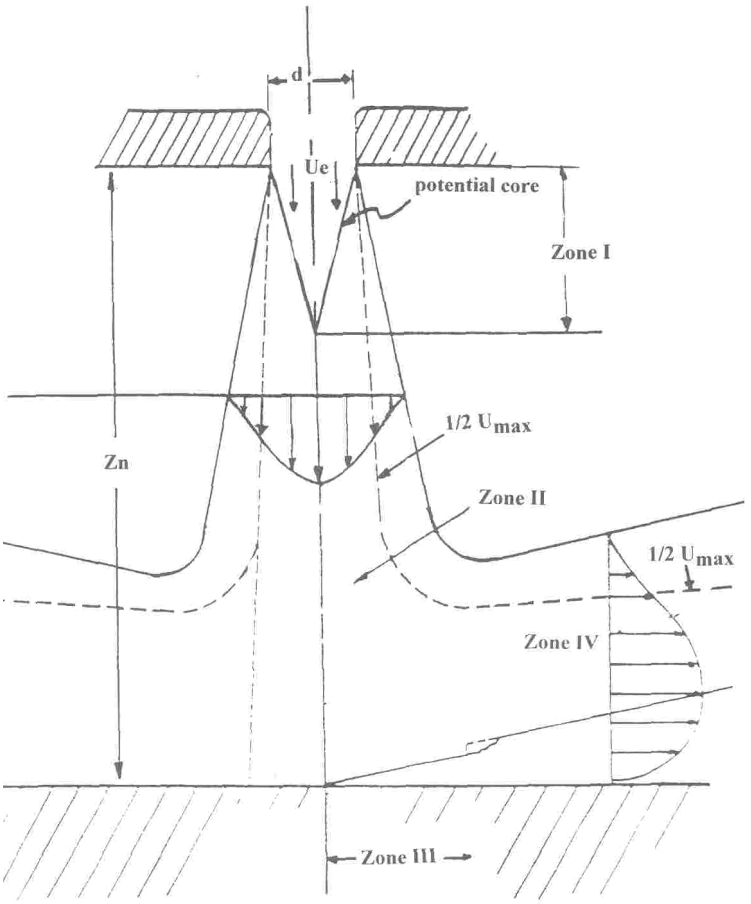

Figure A.1: Impinging jet main regions (from [14])

while the free boundary layer of the jet widens, due to the mixing and inherent momentum exchange between the jet and the ambient fluid.

In zone II, the velocity profile across a cross-section of the jet is non-uniform. At greater nozzle-to-plate spacings the axial velocities reduce with increasing the distance from the nozzle exit. In contrast, in zone I there is always a zone in the centre of the jet where the velocity profile is similar to that at the exit of the jet. This indicates that if the impingement surface is close enough to the jet exit, zone II will not have an opportunity to develop.

Zone III, the deflection zone, which is sometime referred to as the stagnation, or impingement zone. Due to the presence of the impingement surface, It is characterised by a rapid decrease in axial velocity and a corresponding increase in static pressure and, an acceleration in all directions perpendicular to the original flow. This accelerating flow continuous to entrain ambient fluid at its free boundary, while the friction present at the boundary with the impingement surface affects the inner region, resulting in the generation of the decelerating wall jet of zone IV. It is precisely in zones III and IV that the mass and heat transfer process between the fluid and the surface occurs.

Type of Jet Flow

Jets can be divided into several categories depending on the type of jet. It is important, at any given time, to be aware of the type of jet being studied, specially, since both their dynamic and thermodynamic characteristics can differ. They can be classified as follows:

Relative to Impingement Jets can be thought of as *impinging* jets (i.e. at some point their trajectory is altered by the presence of a surface) and *non-impinging*[1] jets (i.e. they are free to develop for the majority[2] of their trajectory).

Relative to Confinement Confinement refers to jets which are discharged between two surfaces, one being the impinging wall, the second, usually par-

[1] Also known as free jets or free-surface jets

[2] In theory their trajectory extents to infinite this is not possible in practice

allel to the target wall and aligned with the nozzle exit. Depending on the level of confinement, jets can be *confined, unconfined or semi-confined.*

Relative to the Surrounding Medium Depending on the medium where the jet is discharged. They can be classified as *submerged* and *un-submerged.* Submerged jets are those jets discharged on the same medium or surrounding fluid as the jet. On the other hand, un-submerged jets are discharged on a different medium or fluid.

Relative to Discharge Symmetry In relation to the way on which the jet propagates through the medium. They are mainly divided into two types: *Axisymmetric and Planar jets.* An axisymmetric jet is symmetrical to an axis in the streamwise direction. These jets normally originate on point sources (orifice, nozzle, pipe, etc). A planar jet has a plane of symmetry. They typically originate when the source is a slot, as a result, they are also known as slot jets.

Jet Configuration

This section will introduce the parameters used to define the configuration of the jet. These include: jet diameter, jet-to-plate spacing, jet-to-jet spacing and others. See Fig.A.2 for a typical example of the geometrical parameters used to define the configuration of a jet. It is important to remember that the symbols used to refer to a given parameter or distance vary throughout the literature, depending on the axis selection or otherwise. In this work the notation used is that which appear to be the most common among researchers. In this section the different notations will be introduced, but the preferred nomenclature will be clearly identified. The parameters needed to define the jet configuration are:

Jet Diameter It defines the diameter of the jet in units of length. It is typically denoted by d (preferred), D or w . In the study of jet flows it is normally used as the base distance to which other parameters are related, such as the Reynolds number (Re), which is also used to generate non-dimensional parameters.

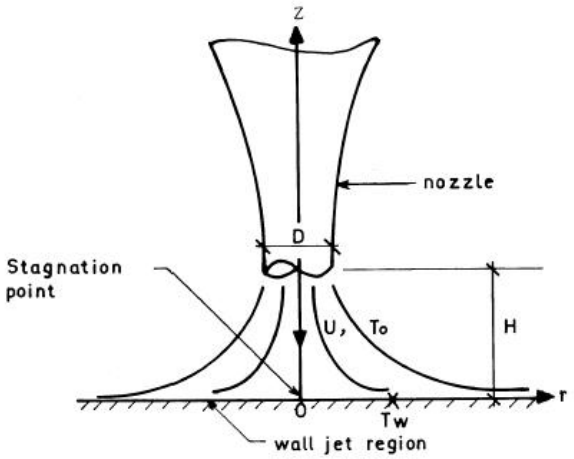

Figure A.2: Figure showing main geometry of impinging jet [15]

Distance from Nozzle There are two distances to consider relative to the nozzle. In one hand, when dealing with impinging jets in particular, the nozzle-to-plate distance H/d, which is the non-dimensional distance between the plate and the nozzle in relation to the diameter, i.e. $H = z/d$. On the other hand, it is also important to know the distance from the nozzle to a given point along its axis. This distance could be denoted by x (preferred), y or z, depending on the chosen reference axes. This distance is normally also non-dimensionalised with respect of the nozzle diameter, i.e. x/d.

Radial Distance from Jet Centreline It is the distance between the jet axis or centreline to a given point. It is the non-dimensional distance in radial coordinates. Depending on the reference axes chosen, it could be x/d, y/d or r/d (preferred). For free-surface jets, it is normally non-dimensionalised with respect to the jet half radius ($r_{1/2}$) at the streamwise coordinate being considered . In the case of impinging jets it is normally the non-dimensional radial[3] distance with respect to the jet diameter (r/d).

Nozzle-to-Nozzle Distance/Spacing This is the non-dimensional distance between adjacent nozzles[4]. It is represented by h/d or p/d (preferred). This distance is most significant when dealing with multiple-jet systems.

[3] r represents the cross-stream coordinate from the axis of symmetry

[4] Nozzle in this context refers to all types of nozzles: orifice, smooth contraction, pipe nozzle, etc.

Jet Characterisation

Jet Half Radius

This is a parameter used mainly when describing free-surface jets. It is defined as the radial distance from the jet axis at which the velocity component is half of that at the centerline. It can be denoted as b, y_b, b' , and $r_{1/2}$.

Jet Rate of Decay (B_u)

The term B_U relates to the slowing down of the centreline velocity as the jet is discharged. It is known that U_C (centreline velocity) is inversely proportional to the streamwise distance from the nozzle exit (x). This parameter is sometimes used as a means to generate non-dimensional velocities. The general form of the jet rate of decay can be express as follows:

$$B_u = \frac{U_c}{U_e} = K\frac{d}{x} \tag{A.1}$$

Where U_c and U_e are the centreline and the exit velocities, respectively, d is the jet exit diameter, z is the streamwise distance from the nozzle exit, and finally, K is a constant obtained experimentally.

Jet Spread Rate (c)

The jet spread rate is a quantity describing the development of the jet. It defines the jet width as it develops. As the jet is discharge, the jet widens, this widening is described by the spread rate. It is defined as:

$$c = \frac{db}{dx} \tag{A.2}$$

Where b is the jet width and x is the distance from the jet nozzle.

Secondary Flow Structures

Coherent Structures

These structures are observed in many types of flows, in particular, those where shear layers develop. They are also present in jet flows. They have been observed to have a pronounced influence on the characteristics of jets, especially, on their heat transfer. The natural appearance of coherent structures in a jet is know as the *natural roll-up frequency*. This natural frequency can be altered by means of an external forcing frequency or pulse.

Although there are various ways to define a coherent structure, and there is sometimes disagreement into exactly what they are. The most basic definition of such a phenomenon is one in which there is an element of repetition. These structures tend to follow a pattern and appear within a flow at regular time intervals. For example, the plume of smoke emerging from a chimney tend to resemble each other. While the existence of these structures is clear from visual observations, their mathematical description is far more difficult. Several instantaneous physical quantities have been proposed and used to describe coherent structures, all yielding different answers. For example, coherent structures are sometimes defined as regions of high vorticity. There is increasing evidence that coherent eddies (such as thermal, plumes, or rolled-up vortices) carry most of the turbulent fluxes of momentum, heat, and scalars. This fact led to many recent investigations on coherent structures [46][3]. Figure A.3 is a typical example of the formation of coherent structures in a jet.

Boundary Layer

After a jet impinges on a surface, the flow is deflected radially along the surface. This region of the jet is known as the wall-jet region. This type of flow has the general characteristics of a flow over a flat plate where a boundary layer forms. The characteristics of the BL closely correspond to the heat and mass transfer behaviour within this region.

When a fluid flows over a body, near the body's surface, a region where viscous effects are noticeable exits, this region is called the boundary layer. The thickness

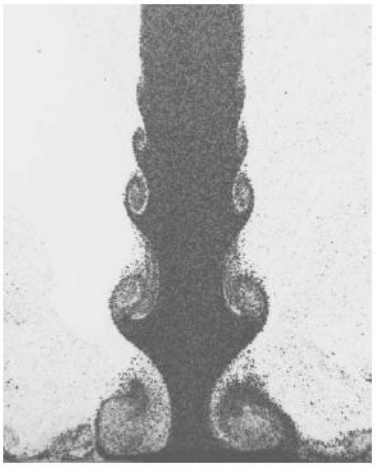

Figure A.3: Typical formation of coherent structures visualised with PIV system (from [16])

of the boundary layer (BL) is denoted by δ. It is defined as the distance from the body's surface at which $u = 0.99u_o$. Where u_o is the free stream velocity. In order to understand the dynamics of a fluid, it is important to understand the behaviour of the BL since its development affects the fundamental characteristics of the flow (particularly those that relate to the surface e.g. mass or heat transfer). There are two types of BL's, namely, laminar BL and turbulent BL. Laminar BL's are characterised by an orderly structure within it, where there is no mixing of its streamlines. In the other hand, a turbulent BL is characterised by increased levels of interaction between streamlines i.e. turbulence (therefore the name). They are also associated with a more pronounced effect of viscosity.

Dimensionless Numbers

This section introduces those dimensionless numbers that are commonly used when studying the fluid mechanics and heat transfer characteristics of jets. They are included in this chapter in order to provide those readers from other engineering backgrounds with a basic understanding of these parameters.

Reynolds Number (Re)

This is a non-dimensional number which indicates the influence of velocity effects in relation to viscous effects. It is also used to classify jets as laminar or turbulent. For a typical application (jet) the system is said to be transitional when Re is approximately 4000. For jets, it is defined as:

$$Re = \frac{U_e d}{\nu} \tag{A.3}$$

Where U_e is the mean velocity at the nozzle exit, d is the nozzle exit diameter and ν is the kinematic viscosity of the fluid.

Prandtl Number (Pr)

The Prandtl is a non-dimensional parameter used in a convecting system which characterises the regime of convection. It is given as the ratio of thermal to kinematic diffusivity. It serves as a measure of the efficiency of a fluid to transfer heat to a surface. It can also be regarded as a measure of the relative effectiveness of momentum and energy transport, by diffusion, in the velocity and thermal boundary layers. For most fluids, the Prandtl number is a function of the temperature. A high Prandtl number indicates a thin thermal boundary layer with respect to the momentum effects. This implies an efficient transport of thermal energy.

$$Pr = \frac{\nu}{\alpha} \tag{A.4}$$

Where α is the thermal diffusivity and ν is the kinematic viscosity (a momentum diffusivity).

Strouhal Number (St)

The Strouhal number is regarded as a dimensionless frequency. It can help describe the frequency at which a given event occurs e.g. the generation of vortices in a system, the systematically drop or rise of a particular parameter, etc. It is

written as:

$$St = \frac{fd}{U_e} \tag{A.5}$$

Where f is the frequency, d is the nozzle exit diameter and U_e is the mean velocity at the nozzle exit.

Appendix B

Detailed Drawings of the Experimental Rig

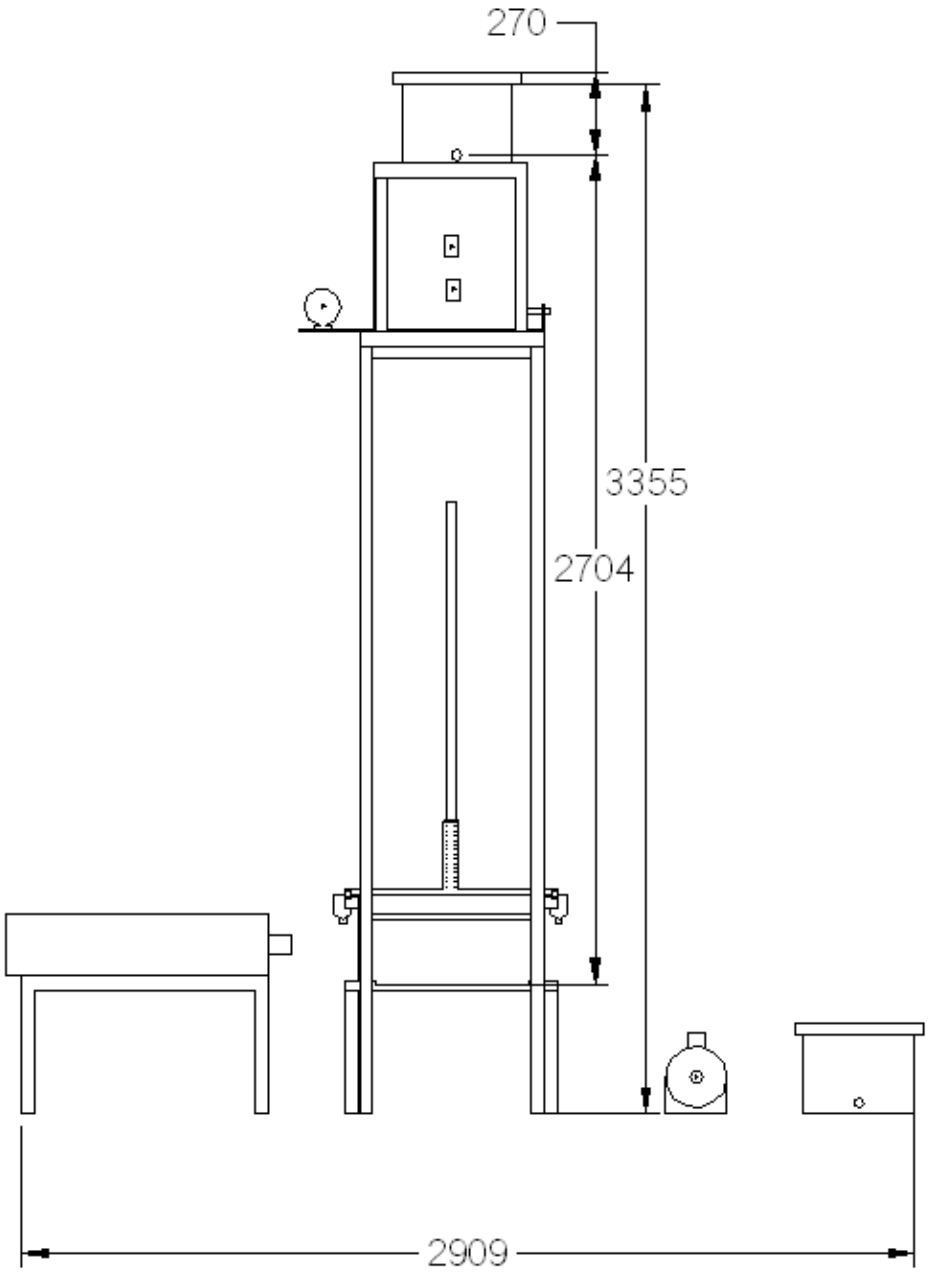

Figure B.1: Experimental rig overall dimensions

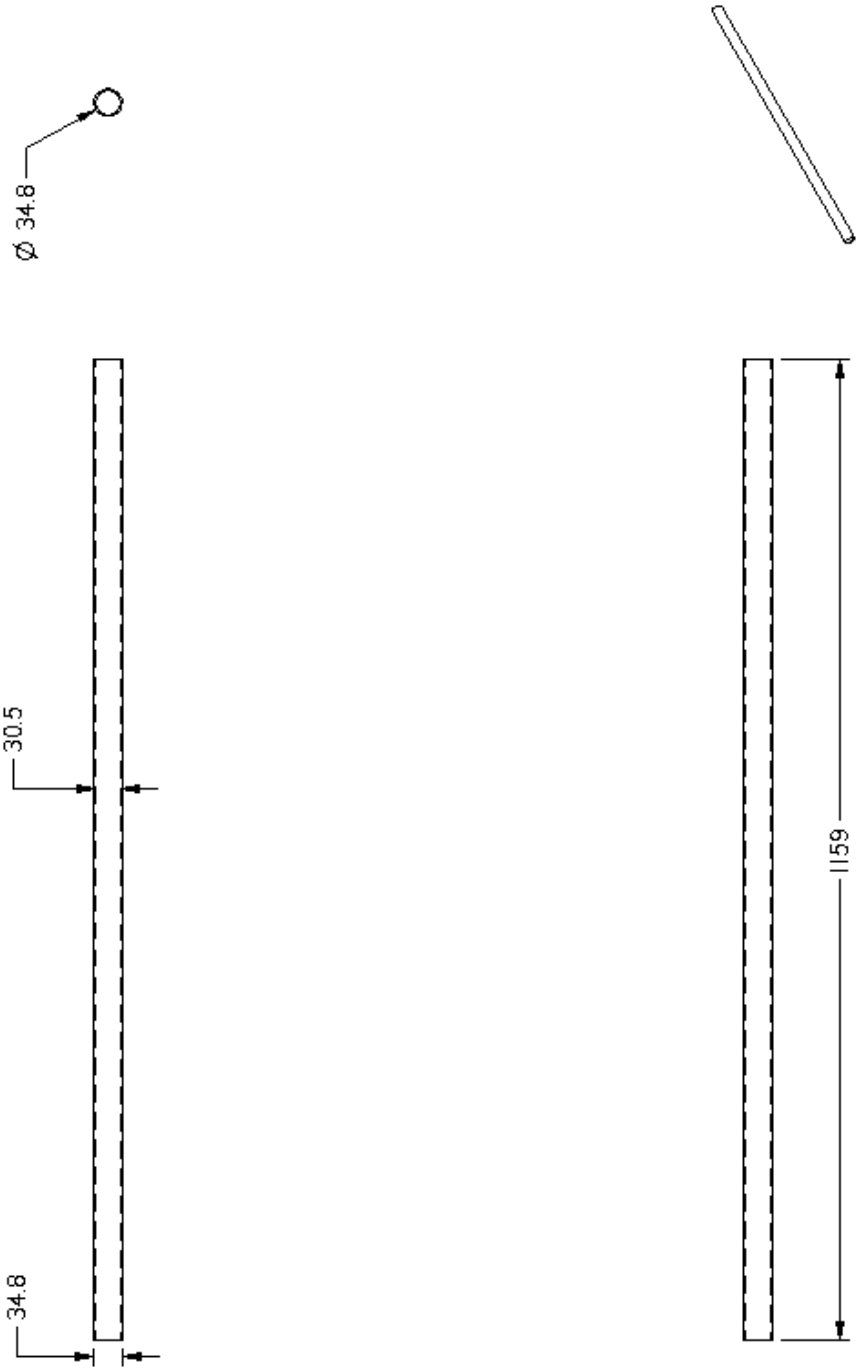

Figure B.2: Nozzle

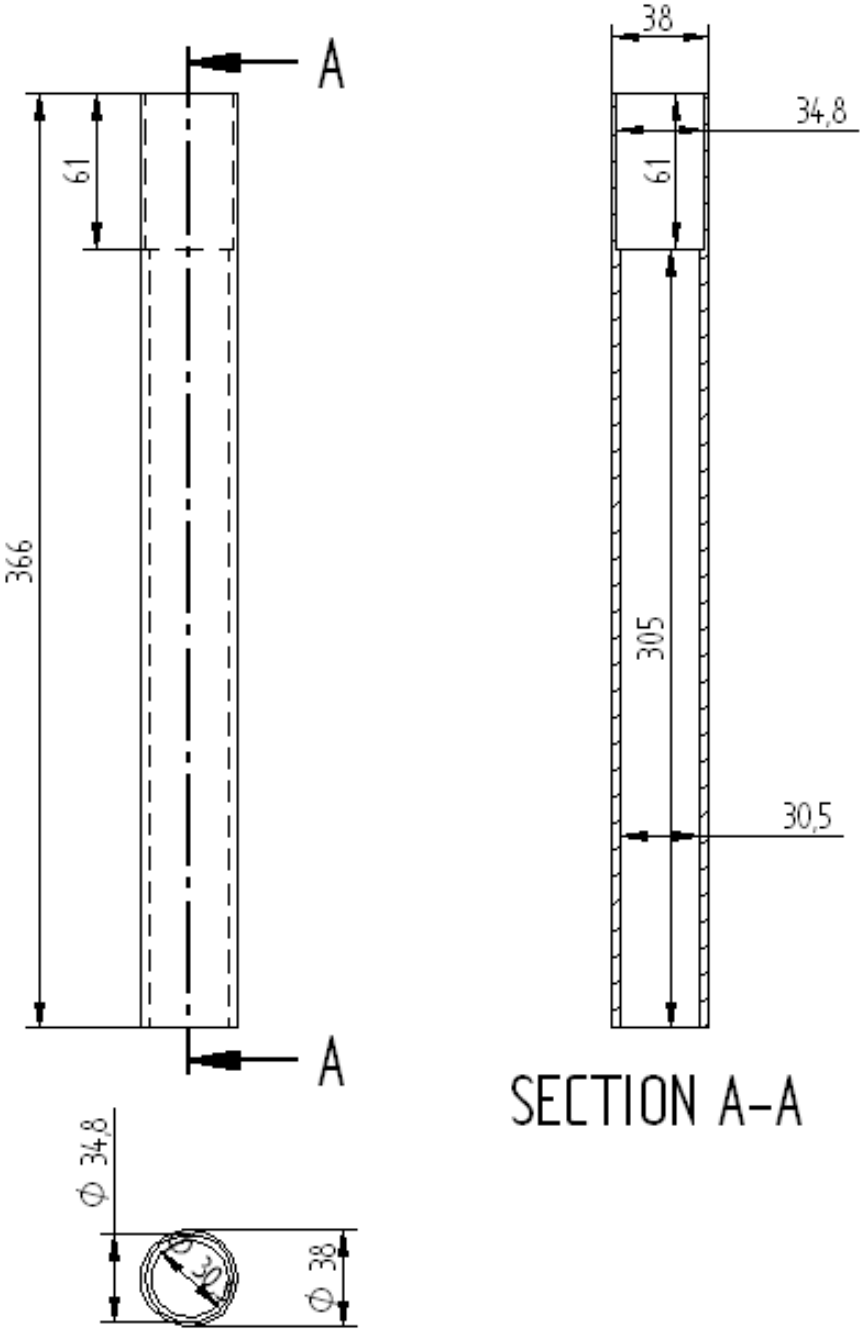

Figure B.3: Nozzle sleeve

FEATURES

- Brass body.
- Full bore.
- Quarter turn operation.
- Blow-out vandal-proof assembly.
- ½" to 2" sizes
- PTFE ball seals.
- Nitrile 'O' ring seals.
- BS 21 Taper Thread.
- ISO 228 (BS 2779) Parallel Thread.
- ANSI (NPT) American Thread.
- Chrome plated finish.
- PN25 rated.

RANGE

Patt. No.	Sizes ½"	¾"	1"	1¼"	1½"	2"
PB100	•	•	•	•	•	•
PB100PT	•	•	•	•	•	•
PB100AT	•	•	•	•	•	•

DIMENSIONS (MM)

Description	Sizes ½"	¾"	1"	1¼"	1½"	2"
A Face to Face	50	58	69	81	88.5	110
B Centre Line to Lever	46	50	52	70	76	83
C Lever Length	100	100	110	135	135	165
D Port Bore	14.5	19	25	30	38	47.5
Weight kg	0.176	0.25	0.38	0.624	0.84	1.45

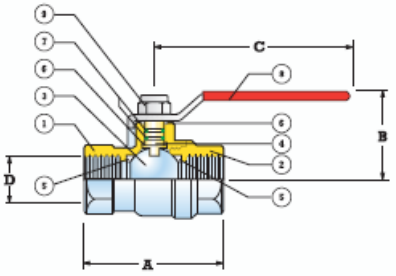

Figure B.4: Rotating valve (from Pegler catalogue)

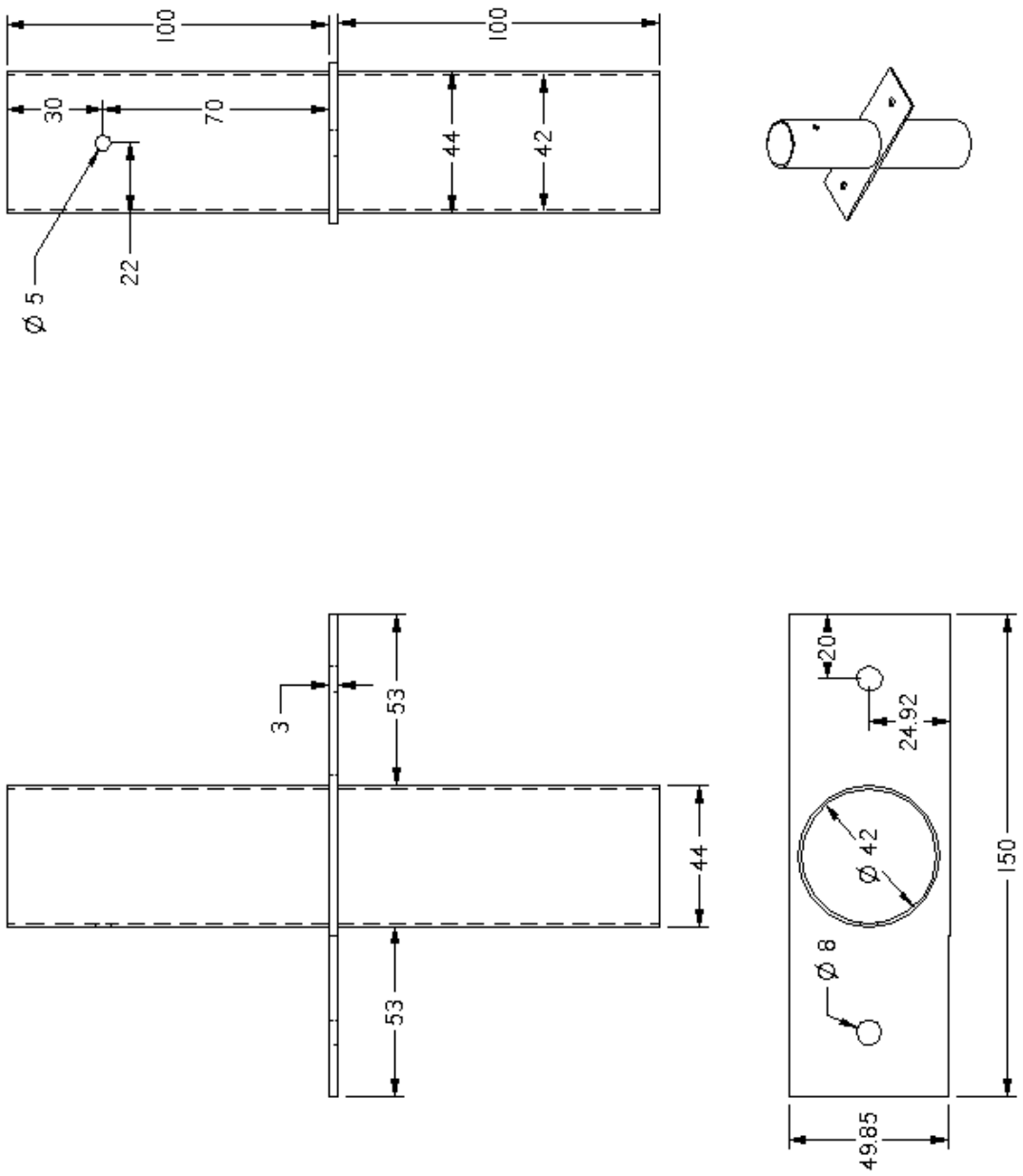

Figure B.5: Nozzle fixture (sleeve)

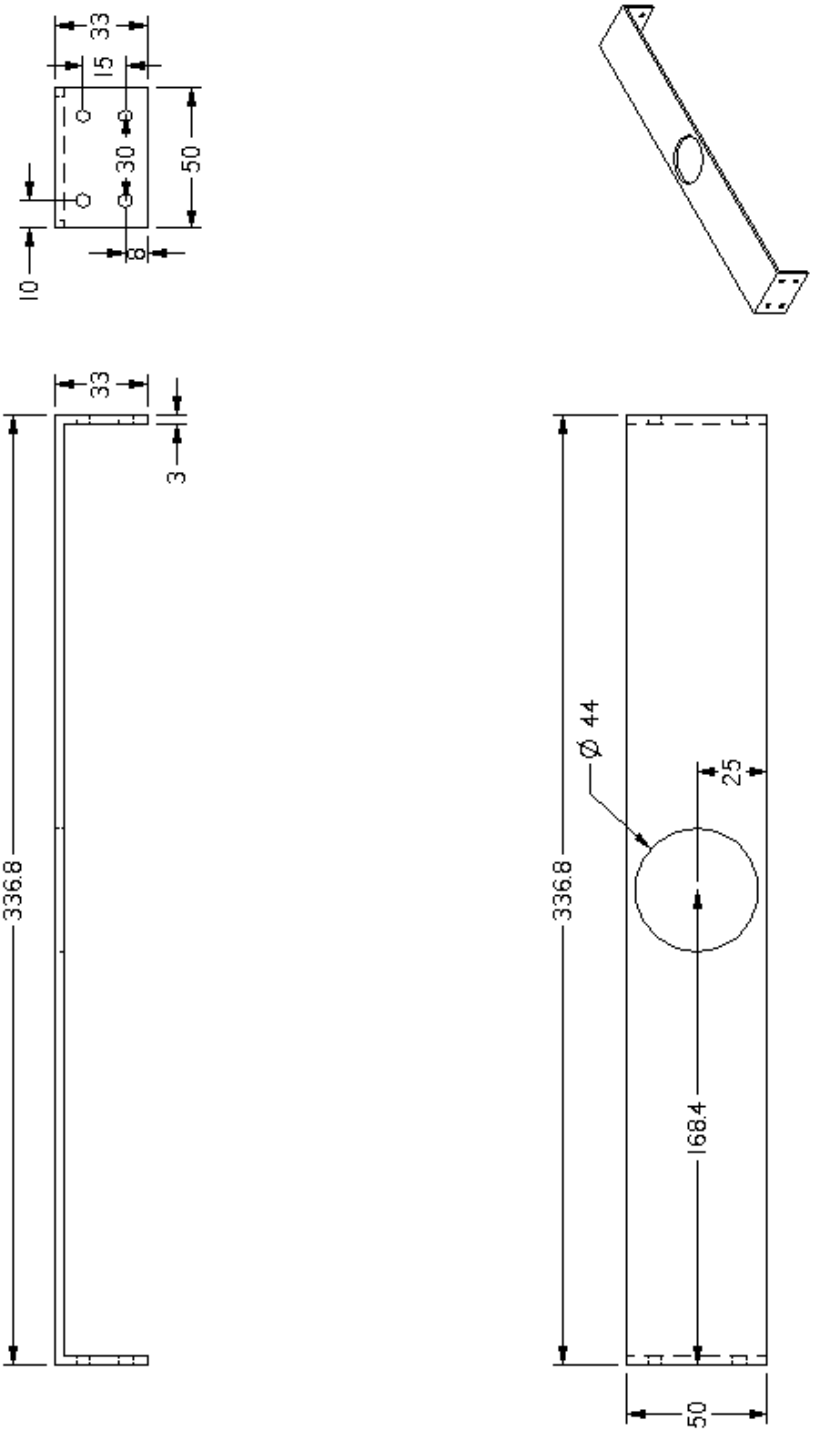

Figure B.6: Nozzle fixture (horizontal)

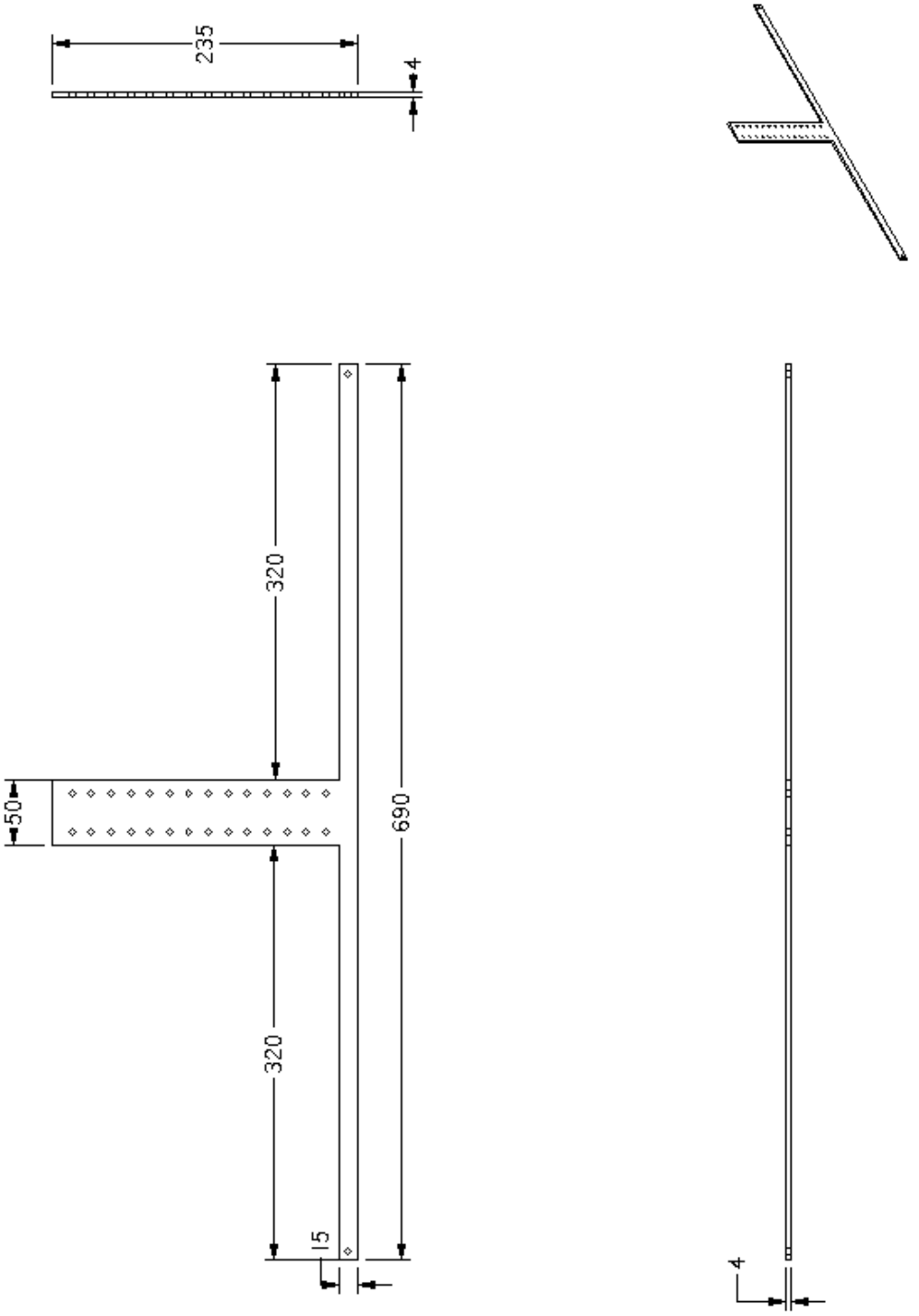

Figure B.7: Nozzle fixture (vertical)

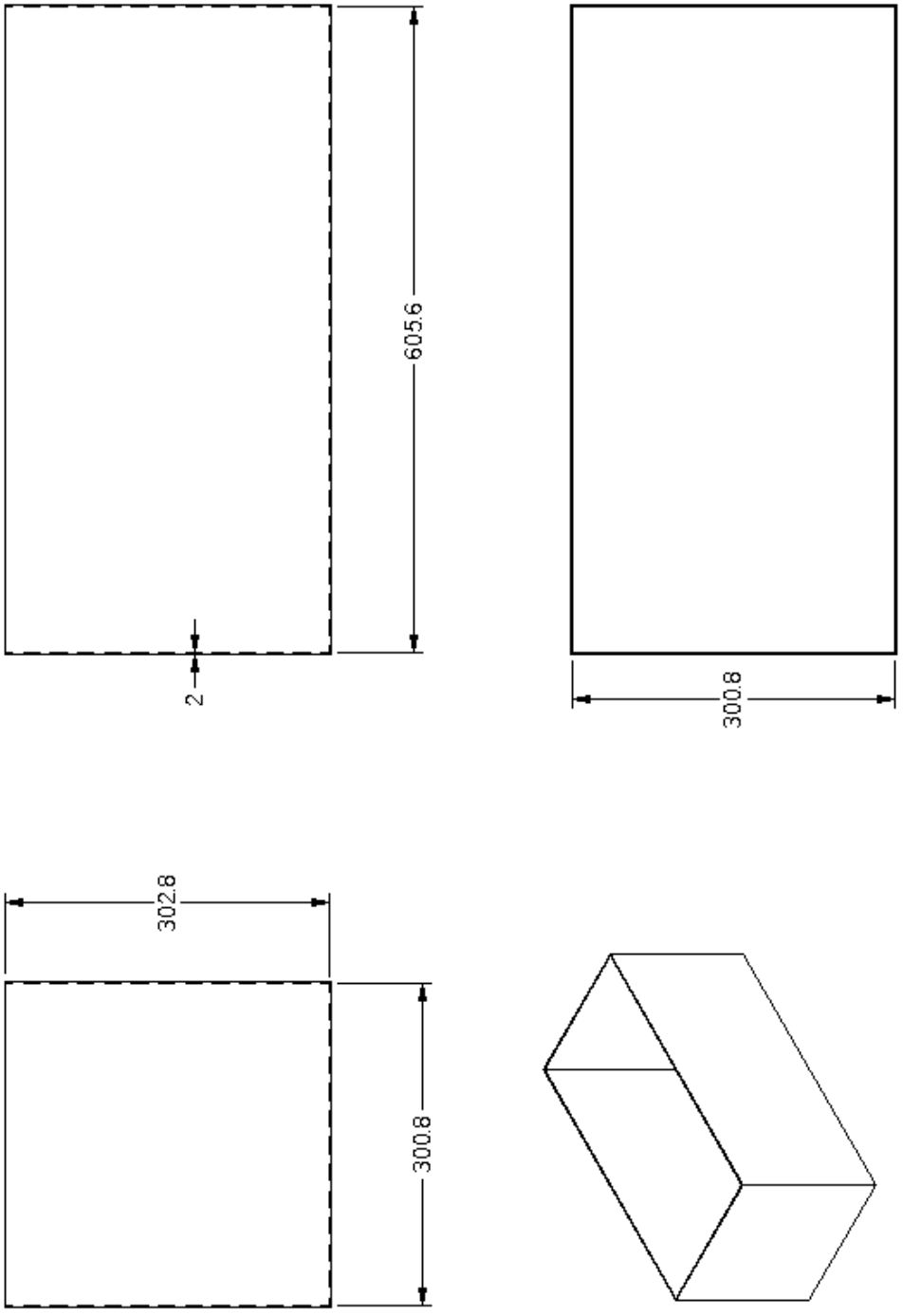

Figure B.8: Water tank

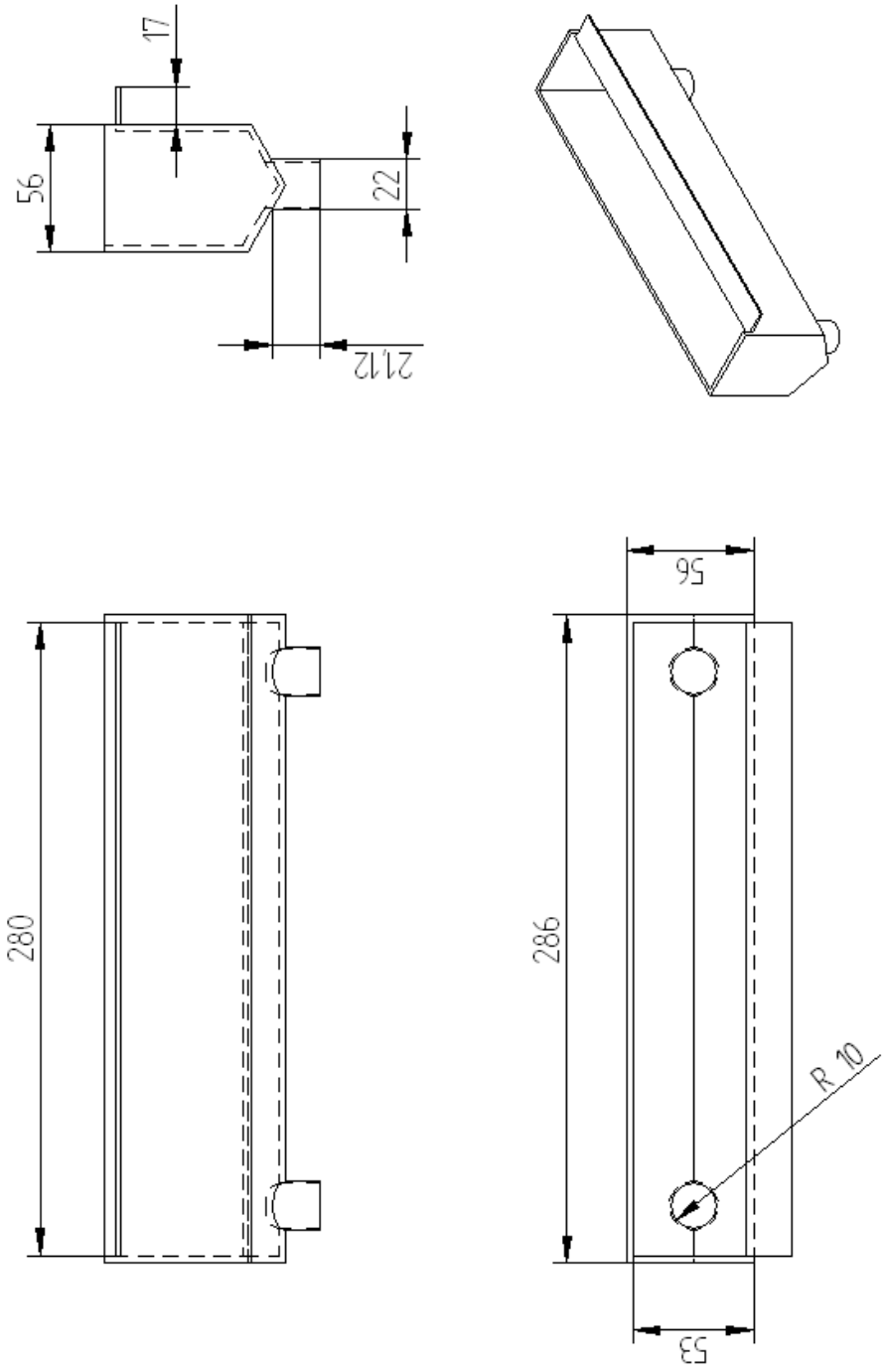

Figure B.9: Water tank overflow collector (small)

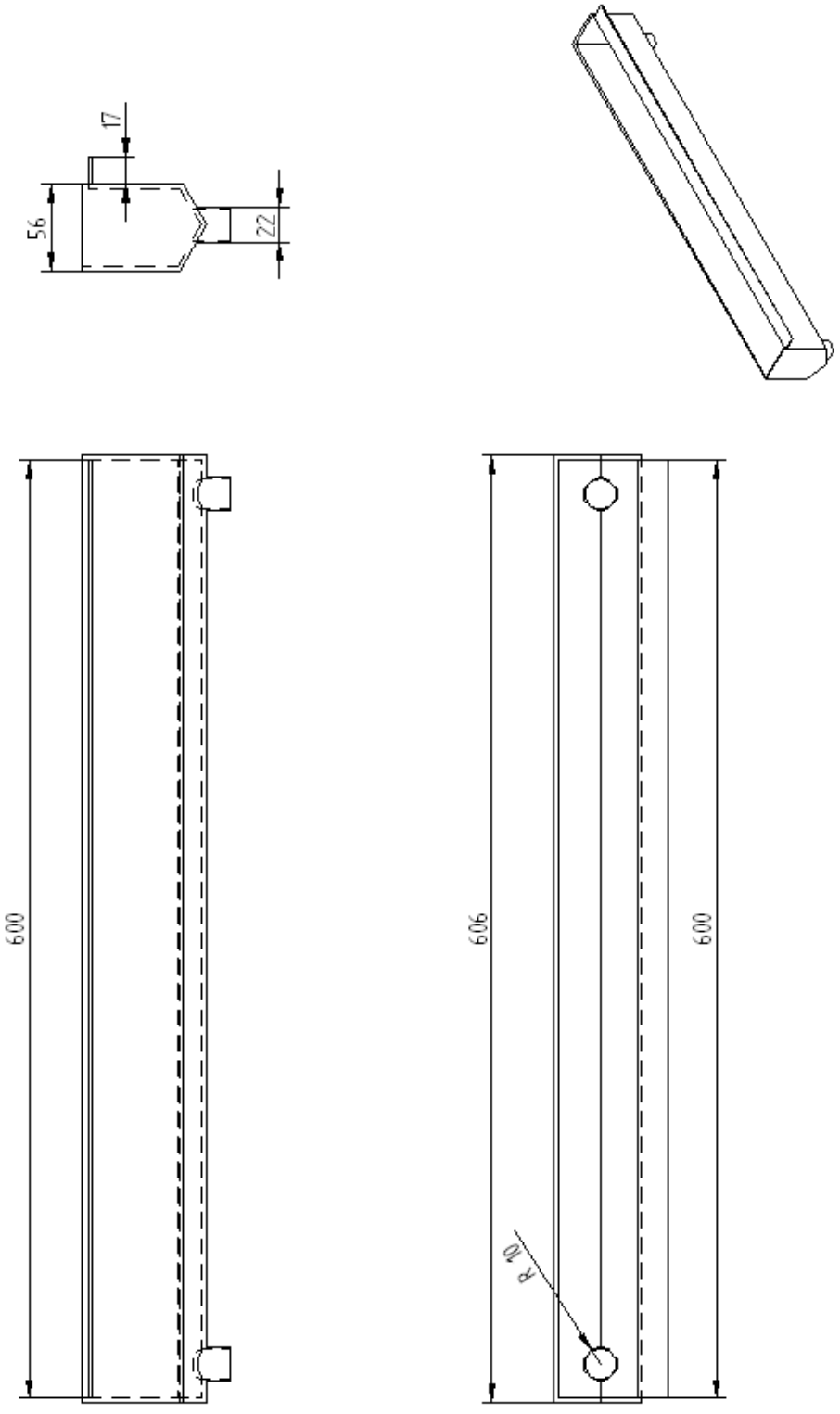

Figure B.10: Water tank overflow collector (large)

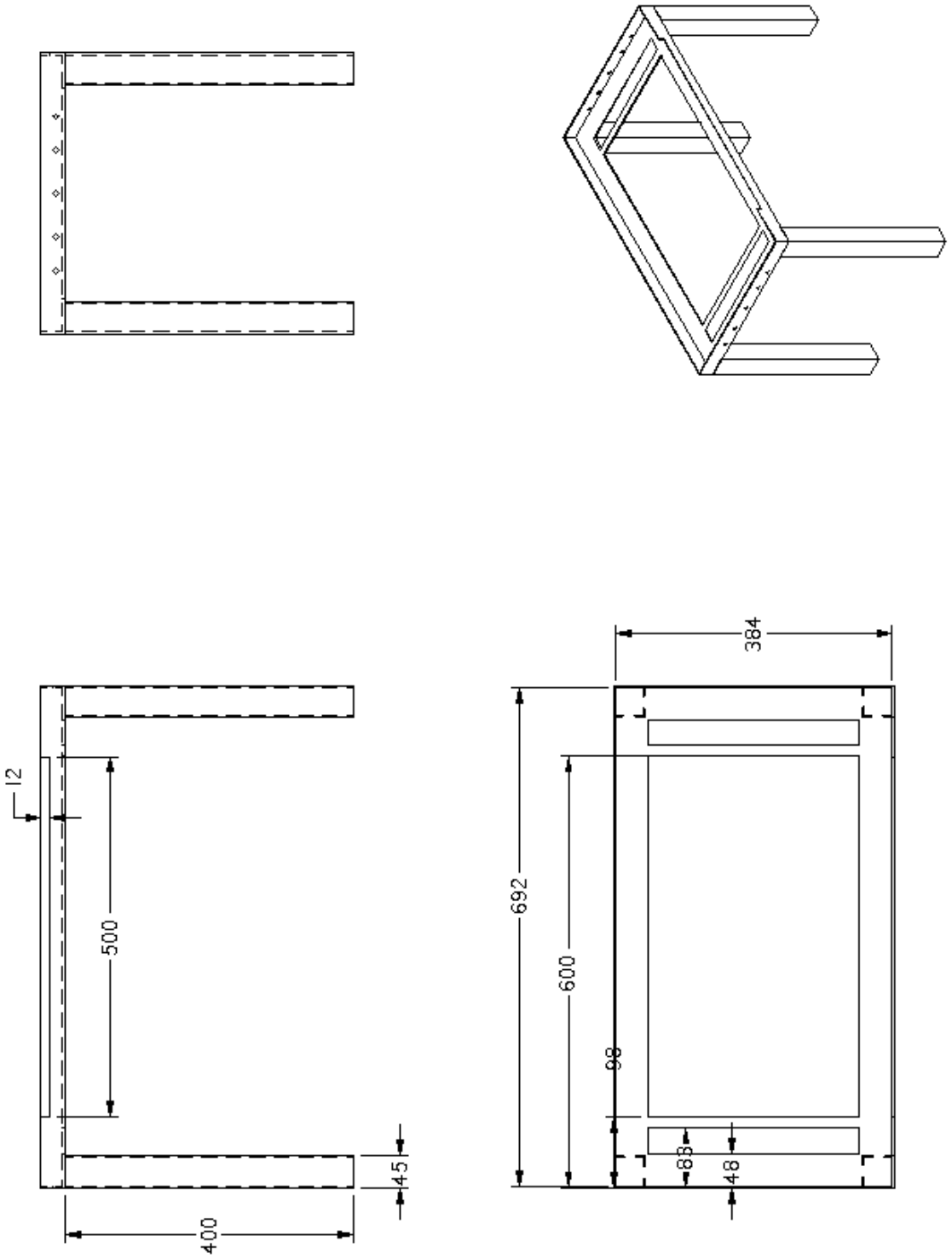

Figure B.11: Water tank support frame

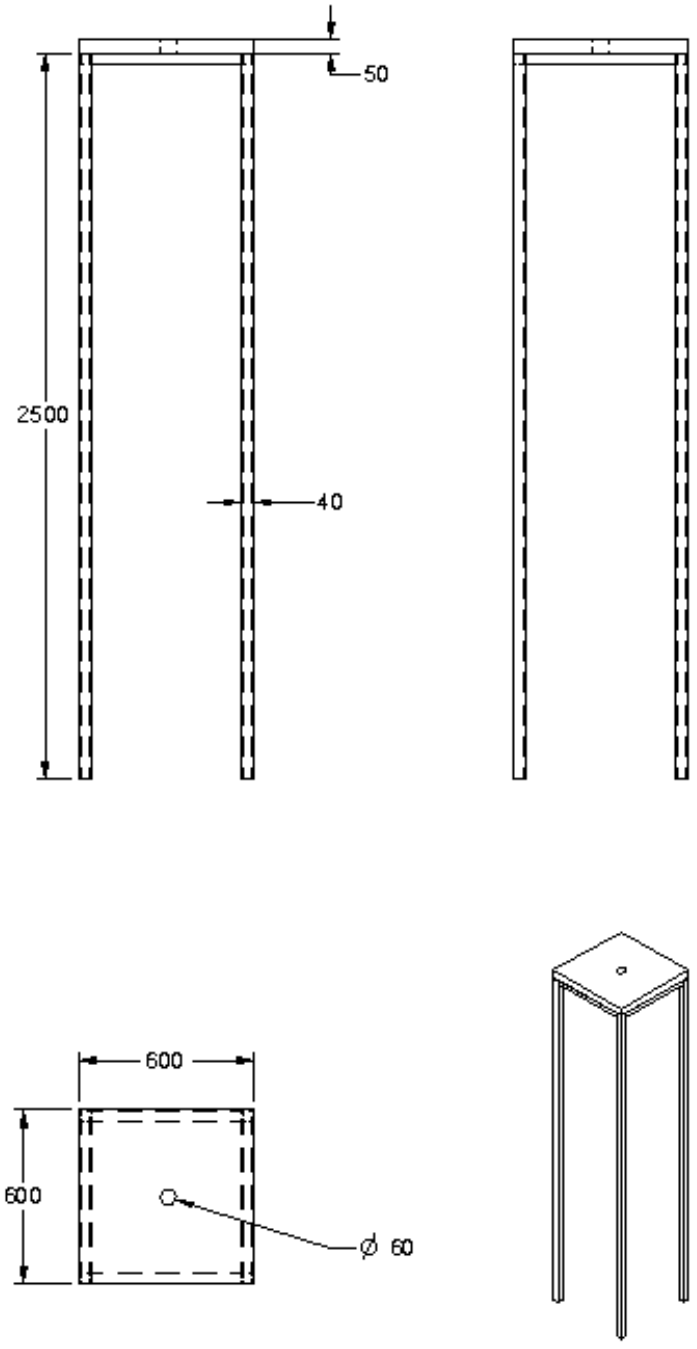

Figure B.12: Overhead tank support frame

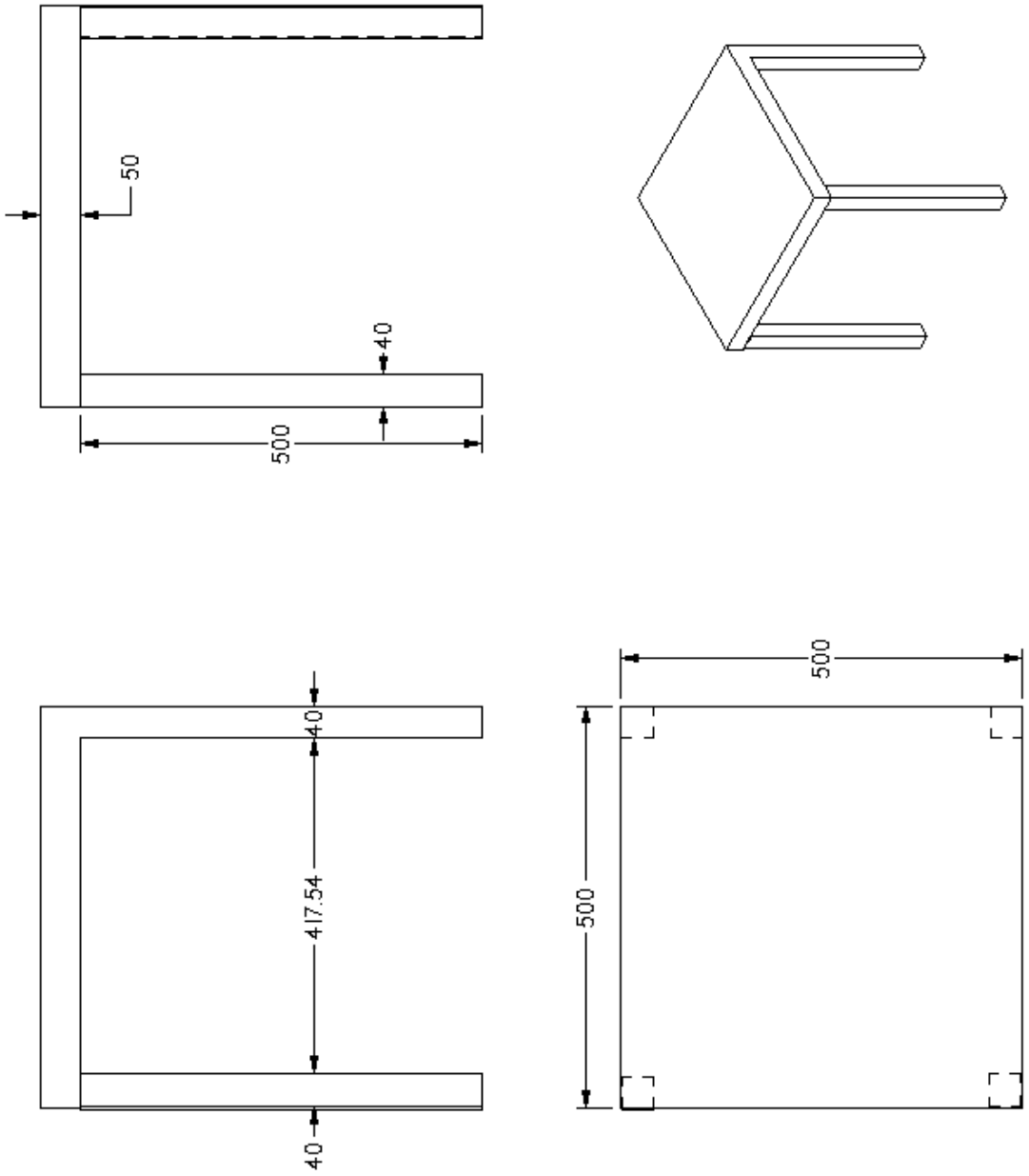

Figure B.13: Overhead tank table

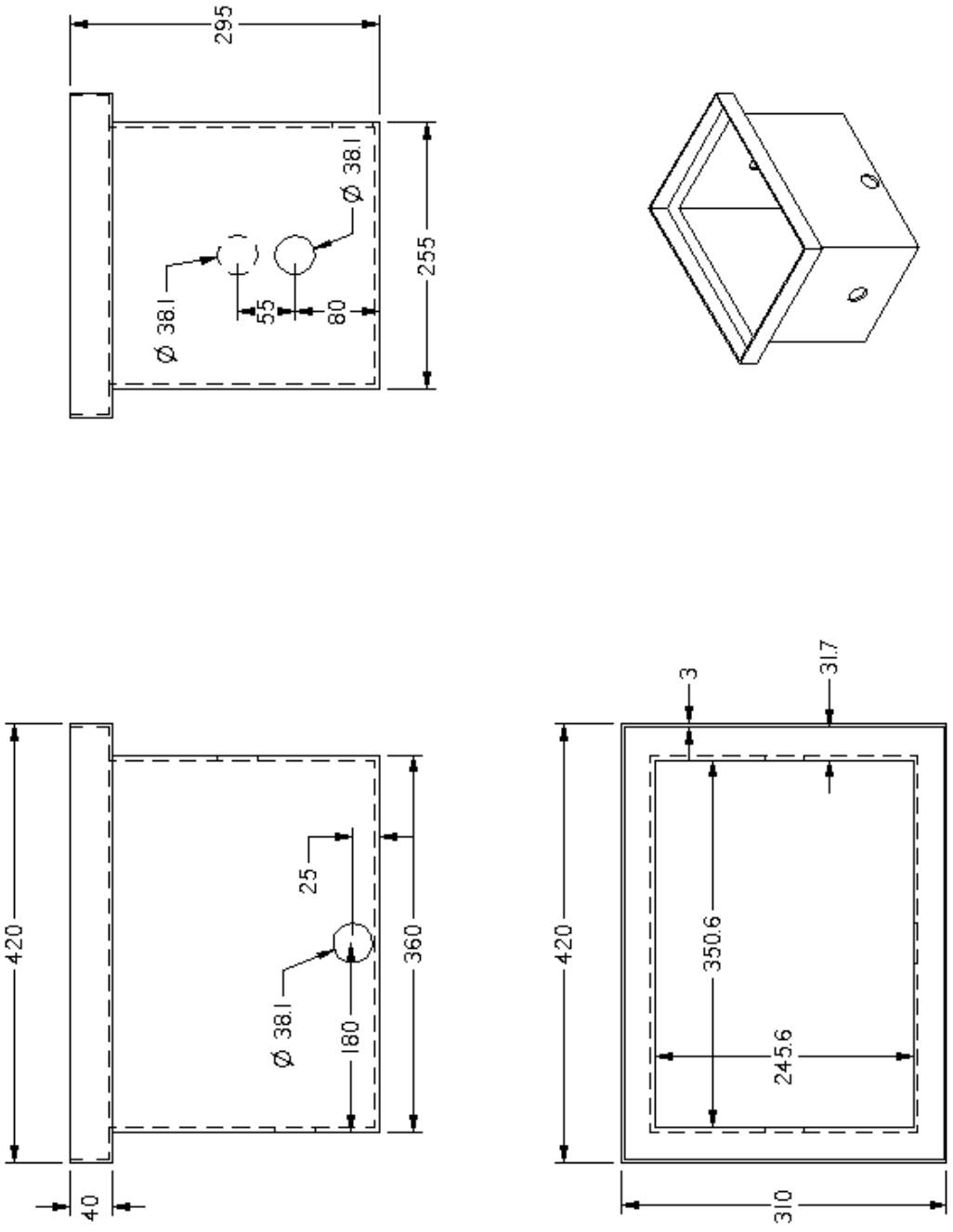

Figure B.14: Overhead tank

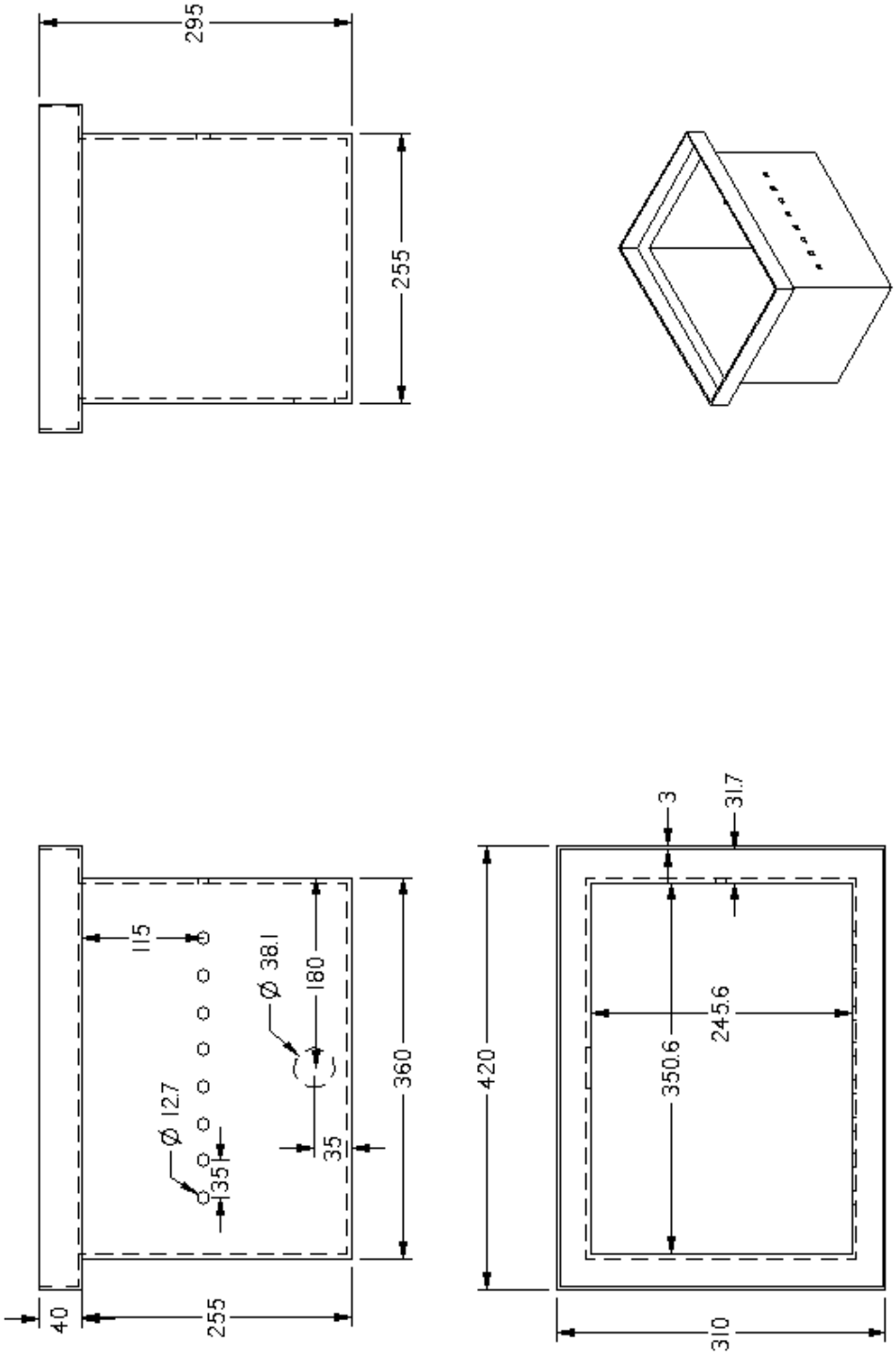

Figure B.15: Reservoir

Appendix C

Design Process

C.1 Water Pulsator

The design process of pulsator is included in order to aid researchers wanting to study pulsatile water flows. Some design considerations that can easily overlooked will be highlighted. Generating a water pulse is a delicate process, one fundamental requirement for the pulsating mechanism (whichever it may be) is for the component to be completely water tight (to avoid water leakage), but more importantly, and easily overlooked, the components must be air tight. If the components is not air tight, air can enter the water flow leading to bubble formation. As a result, extreme consideration must be given to the incorporation of appropriate seals in the design stage. The need for air tightness can be reduced by a simple consideration when designing an experimental rig. For instance, in the experimental setup used in this work, the nozzle is perpendicular to the ground and above the impinging plate, due to the force created by the weight of the water within the nozzle, suction within the nozzle is present (particularly noticeable when the rotating valve is closed). If this setup is reversed, that is, the nozzle impinges the target plate from underneath (i.e. vertically up), the suction within the nozzle will not be present, or not as strongly (this was not put to practice). This simple rearrangement minimises the need for air tightness.

It was also observed that higher pulsating frequencies could be achieved for water flows. In order to reach them, the design of the sealing, use of bearing, or other components must be considered carefully, in particular, their resistance

to water and the life expectancy of the component, for instance, the bearings. As a consequence, it is of paramount importance to allow for maintenance of the component in the preliminary design stage. Seals and other components have a surprisingly short life span when exposed to tough requirements, for example air tightness.

From a physical point of view, two factor must be considered; cavitation and water hammer. Cavitation must be particulary considered when high frequencies are used. It can be minimised by being included in the preliminary design stage, when this is not possible, the water can be treated to remove its air content. Now, the effect of water hammer must not be underestimated since it adds significant stress on the tubes or pipes in the system. Therefore, pressure relief valves or other pressure control devices must by utilised.

When these design considerations are kept in mind throughout the design process of a water pulsator, the overall design process should run smoothly.

C.2 Experimental Rig

Design Requirements

This project is concerned with the study of impinging jets, both steady and pulsating. An experimental facility had to be custom built for this purpose. It was decided to have an orthogonal axis-symmetric jet impinging on a flat surface with a fully developed boundary layer at the exit. Another requirement imposed on the facility was that it should be suitable for Particle Image Velocimetry (PIV). A list of the design requirements will be shown below so that their design implementation can be clearly explained subsequently. There were:

- To provide structural support for the various components and minimise vibrations
- To provide a flat surface as the impinging wall
- To provide an orthogonal and axis-symmetric jet
- To generate a fully developed velocity profile at the exit

- In the steady case to produce a smooth steady jet with minimal vibrations
- To generate a fully pulsed jet
- To be visually accessible (PIV requirement)

Design Implementation

In order to fulfil all the requirements for the experimental rig. A water tank was designed and the following steps were taken:

- An aluminium frame was designed to support the water tank and to provide the stability and strength required. As a safety precaution all metal components were painted black to minimise unwanted reflections from the laser
- To generate a fully developed velocity profile at the exit a round pipe was used as nozzle. It had a length to diameter ratio of 50, in order to ensure that the velocity profile was fully developed at the nozzle exit
- Particle Image Velocimetry (PIV) was the method chosen for data acquisition. It offers many advantages, including a complete flow field vision of the process being studied, as well as, providing an non-intrusive method for data acquisition. Excellent PIV measurements can be taken in various types of fluids. When water is used excellent results can be obtained. As a results, water was chosen as the working fluid. One of the main advantages of using water for PIV usage is that it can be easily seeded (PIV requirement). As a consequence of using water as the working fluid another requirement emerged, namely, a need to maintain a constant water pressure at the test section. This was achieved by using an elevated water reservoir which became the supply source for the water used in the test section
- In order to minimise the vibrations in the test section, the same elevated water reservoir was used, but with no artificial means to propel the fluid. In other words, a gravity fed mechanism was put in place

- The target plate (impinging surface) was a Perspex sheet ($30x300x600mm$) located at the bottom of the water tank

- To ensure visual access to the test section (PIV requirement), a water tank was designed. The tank was made of glass, which ensures both a clear surface for visual access and structural support to carry the weight of water

- To ensure that the jet impinges orthogonally to the surface, a fixing mechanism was devised. It holds the length of the nozzle in place and perpendicularly to the water tank structure. To ensure that the jet is axis-symmetric a round nozzle was used and a PVC adaptor was designed to cover the last 10 diameters of the nozzle in order to ensure that the nozzle exit is round. Finally, in order to prevent gravitational effects to distort the development of the wall jet, the supporting legs of the water tank can be adjusted to ensure that the target surface is parallel to the floor. Also, to further ensure axis-symmetry, the excess water originating from the nozzle is extracted from all sides of the water tank

- To produced a pulsed jet a pulsator was devised. It consists of a rotating ball valve and a driving motor. This pulsator can reach frequencies of up to 2.8 Hz. The design of this pulsator was one of the driving factors of this project. In order to assist researchers willing to undertake similar research.

Appendix D

PIV Principles

Introduction

Particle Image Velocimetry (PIV) is a technique that provides quantitative measurements of complex instantaneous velocity fields from a qualitative visualisation of the flow. The origin of this technique as it is known today can be traced back as far as the early 30's [76]. In the last 20 years PIV has developed dramatically thanks to various key technological advancements, for instance, the change from analogue recording and evaluations techniques to digital techniques. The continuous development of PIV can be largely attributed to the inherent advantages it offers. For example, it offers fast, non-intrusive and whole field velocity measurements. This section will provide an overview of the principles behind Particle Image Velocimetry.

PIV Principles

The basic elements needed for Particle Image Velocimetry are; a light source, a recording device and tracer particles. Tracer particles are needed in most applications. These particles have to be illuminated at least twice within a very small time interval, therefore, the need for a potent light source (typically a laser is used). The light reflected or scattered by these particles is recorded, then evaluated at a later stage. They are recorded on a single frame or on a sequence of frames. Since there are at least two frames recorded in a known time interval, the displacement of the particles during this time has to be evaluated using very

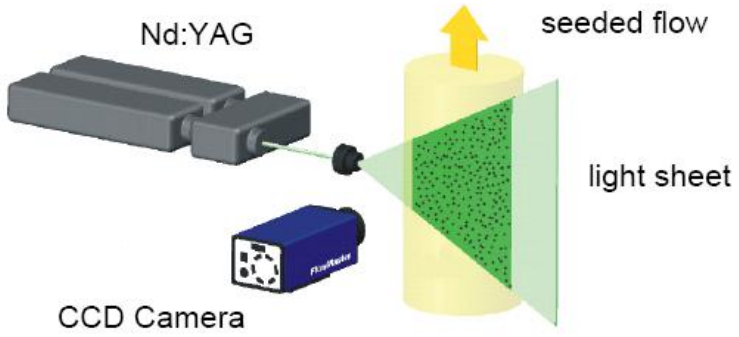

Figure D.1: Typical Particle Image Velocimetry Setup (figure from Davis software manual)

sophisticated post processing which enables the extraction of velocity information. The light scattered by the particles when illuminated by a laser is normally captured by a CCD camera and stored in a PC in real time. At this point the images stored in the computer are only raw images. They only reflect a change or displacement of particles. Every one of these images is now divided into small subareas, called interrogation areas, or windows. The local displacement vector of the tracer particles shift between two consecutive images is now extracted using statistical methods (auto and cross correlation). A homogeneous displacement of the tracer particles between the two exposures is a basic assumption of the PIV technique . Once the local displacement vectors (one per interrogation window) have been computed, the local velocity vectors are calculated by taking into account the time delay between exposures and the image magnification. Since image magnification also plays role in extracting the velocity vectors, calibration of the raw image is a fundamental requirement in order to minimise error. A typical set-up for PIV recording is shown in Figure D.1.

The fundamental elements needed for PIV measurement will now be described. They will be introduced briefly, although providing enough detail for the basics behind PIV to be clearly understood[1]. The assumptions behind Particle Image Velocimetry will also be introduced.

[1]There are many sources available for detailed information on PIV, for instance, the book by M. Raffel [76]

PIV Assumptions

The inherent assumptions in the PIV method are: (1) the tracer particles or seeding particles must follow the fluid motion. This implies that they must be small enough so that they do not have an influence on the flow being studied, normally this is avoided by having particles with a density similar to the fluid being used; (2) The tracer particles must be homogeneously distributed, this facilitates the image analysis process and reduces the number of erroneous and/or missing vectors; and finally; (3) The particles must have uniform displacement within the interrogation window.

Tracer Particles

The selection of appropriate tracing particles is of paramount importance. In PIV the velocity of the fluid is directly extracted from the particle displacement, therefore, the particle must follow the flow accurately. The primary source of error in PIV measurements is the influence of gravitational forces if the density of the seeding particles and the fluid do not match. As a consequence, particles with density similar to that of the fluid must be used. However, small particle density sometimes implies smaller particles and less light being scattered to expose the camera frame. As the size of the particle increases so does the light scattered, it now becomes evident that in some practical applications a trade-off is compulsory. The seeding particles used in the experiments were Sphericel 110P8 provided by LaVision Gmbh and are specifically manufactured for PIV applications in water.

Light Source

In most PIV applications, lasers are used as the light source, this is mainly due to their ability to emit monochromatic light with high energy density, which can be easily converted in to a 2-D light sheet. This light sheet can be used to illuminate and record the tracer particle without chromatic aberrations.

PIV Recording

In order to carry out the recording of a PIV experiment. A recording devise is required. This is normally a digital camera, with solid state imagers, such

as: charge injection devices (CID), CMOS imagers to convert light into electonic signal, and charge coupled devices (CCD) which are the most commonly used. Digital recording converts light into an electronic signal, this leads to images that are readily available for inspection. The benefits from using digital photography are; (1) feedback during recording and; (2) avoidance of chemical processing, therefore, reducing the time needed to post-process and evaluate the images.

Image Evaluation

The final step is then the evaluation of the different images obtained during the recording. Very complex algorithms, based on auto and cross-correlation analysis of the images, need to be used in order to extract the velocity information from the images for each interrogation window. This process involves numerous calculations which makes the post-processing of the images a time consuming process. With increasing developments of computer processing speeds, the time required for post-processing is being reduced.

Appendix E

Experimental Procedure

This section describes the series of steps that were carried out in order to complete each experiment. This are included so that repeatability of the presented data can be easily attained. They include:

1. The first step when starting an experiment was to ensure that the water within the water tank was clean and free of alien particles. The presence of such particles could affect the results obtained with the PIV system. Furthermore, they could reflect the laser light reducing the efficiency of the system and therefore, affecting the quality of the data

2. The geometric parameters involved in a given experiments were adjusted. They include: setting the nozzle to plate spacing, checking that the nozzle was perpendicular to the target plate, finally, checking that the target plate was parallel to the floor. A bubble level was used

3. The doors to the laboratory were closed and the laboratory's interlock was activated

4. The laser was switched on at the minimum possible power setting needed to visualise the laser light sheet (protective goggles were used every time the laser was on)

5. The laser head is then allowed to warm up. According to the manufacturer's instructions it takes 20 minutes to warm up from cold, and 10 minutes from standby

6. The laser light sheet was adjusted. This involved alignment of the light sheet, as well as, focusing the light sheet. The light sheet was aligned in such a way that it was perpendicular to the target plate, parallel to the nozzle, and located at the centre of the nozzle

7. Once the light sheet was aligned, the calibration plate was put in place. It was placed within the test section so that it would be collinear with the light sheet (already adjusted in previous step). The field of view of the camera was adjusted in such a way that it would cover as much as the calibration plate as possible. The camera was then calibrated using Davis software developed by LaVision

8. Once the whole system is calibrated, and the nozzle in place, the seeding particles were added. The pumps were switched on and the PIV system was set to continually grab images of the test section. Then the particles were added slowly into the water tank. This was necessary in order to avoid over seeding the flow. Seeding of flow is critical for good PIV measurements

9. Before starting any experiment, the temperature of the water was measured and recorded. The room temperature is also measured and recorded

10. Once the temperature is measure and recorded. The required nozzle exit velocity is set and the recording of the raw images is started. In the experiments for the steady jet, the recording was manually triggered at any given time. The recordings for the pulsed experiments was triggered by means of a TTL signal produced by the tachometer. This was to ensure that the start of the recording was the same for every single recording

11. After the recording of the images the final temperature of the water is measure and recorded. Finally, the room temperature is also measured and recorded

12. This procedure is then repeated for every experiment

Appendix F

Normal Probability Plots

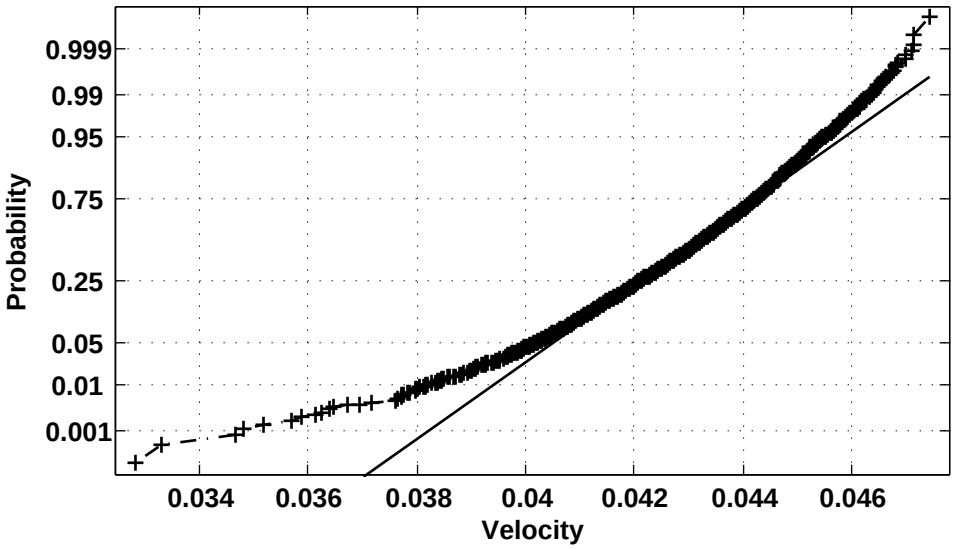

Figure F.1: Normal probability plot at $r/d = 0$ and $x/d = 1$ (H3/1500)

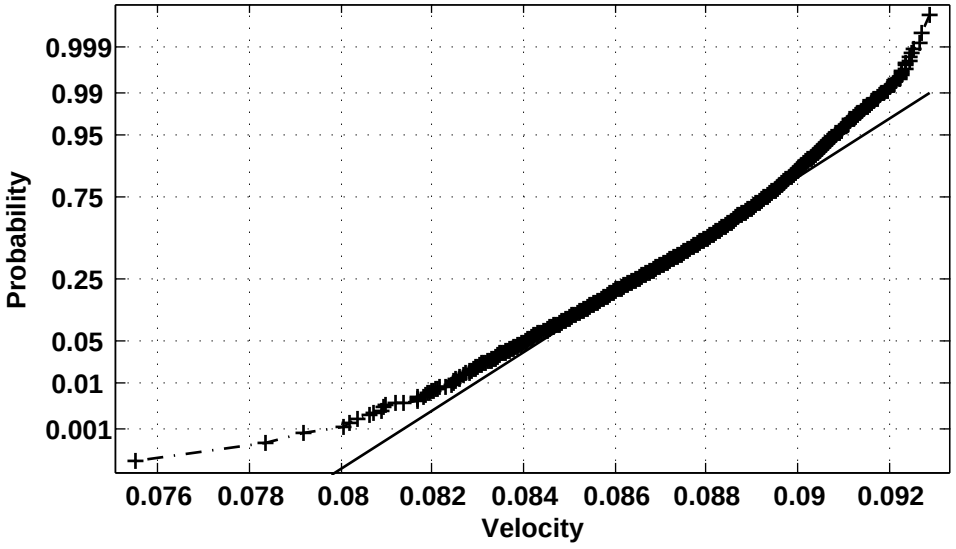

Figure F.2: Normal probability plot at $r/d = 0$ and $x/d = 1$ (H3/2500)

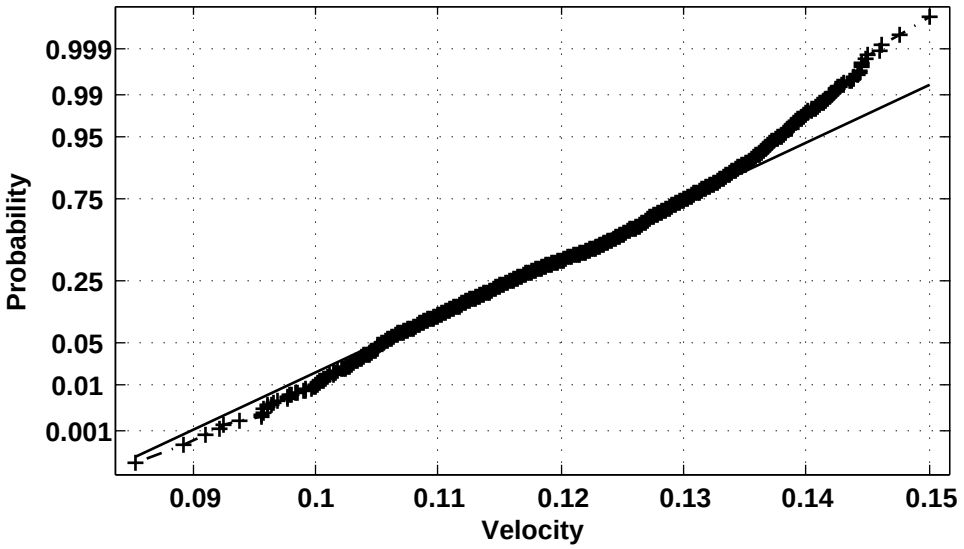

Figure F.3: Normal probability plot at $r/d = 0$ and $x/d = 1$ (H2/4000)

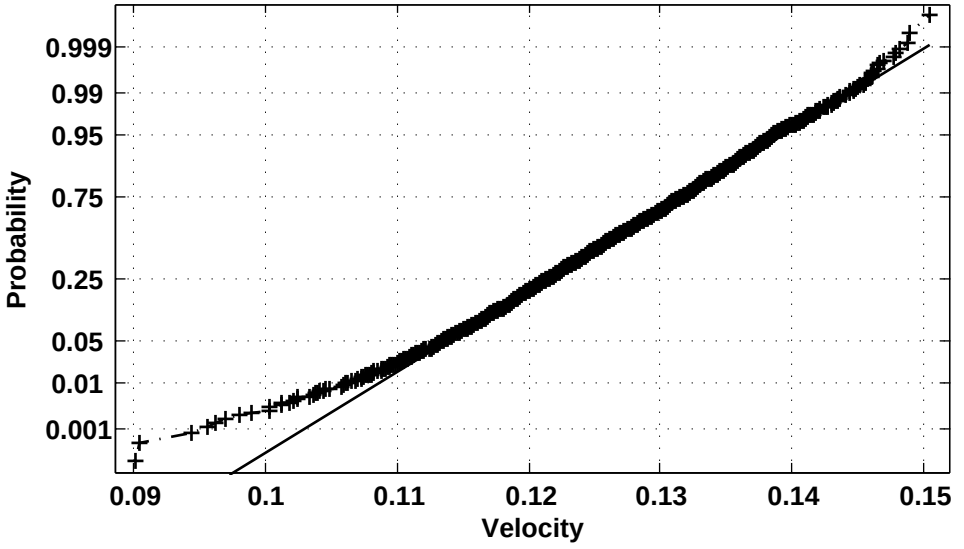

Figure F.4: Normal probability plot at $r/d = 0$ and $x/d = 1$ (H3/4000)

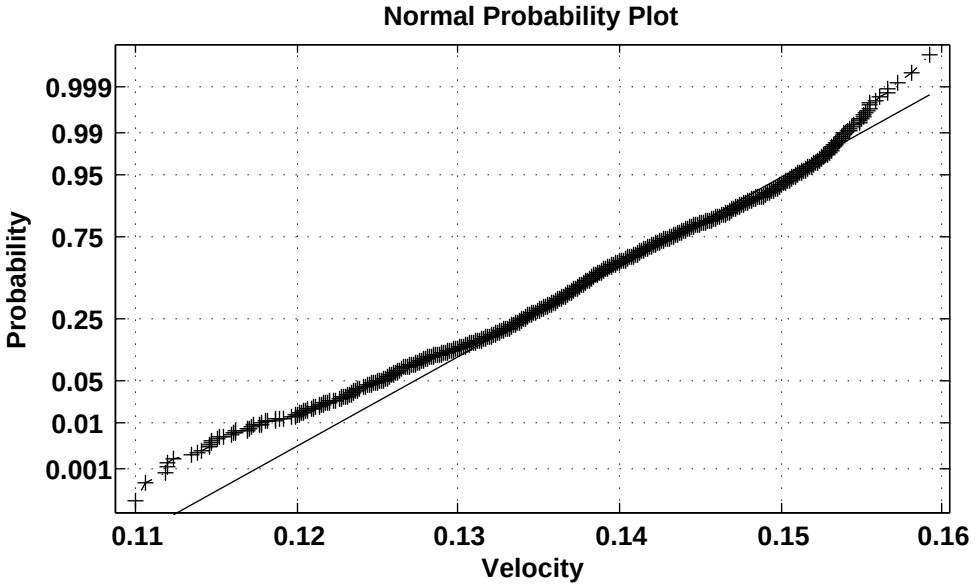

Figure F.5: Normal probability plot at $r/d = 0$ and $x/d = 1$ (H4/4000)

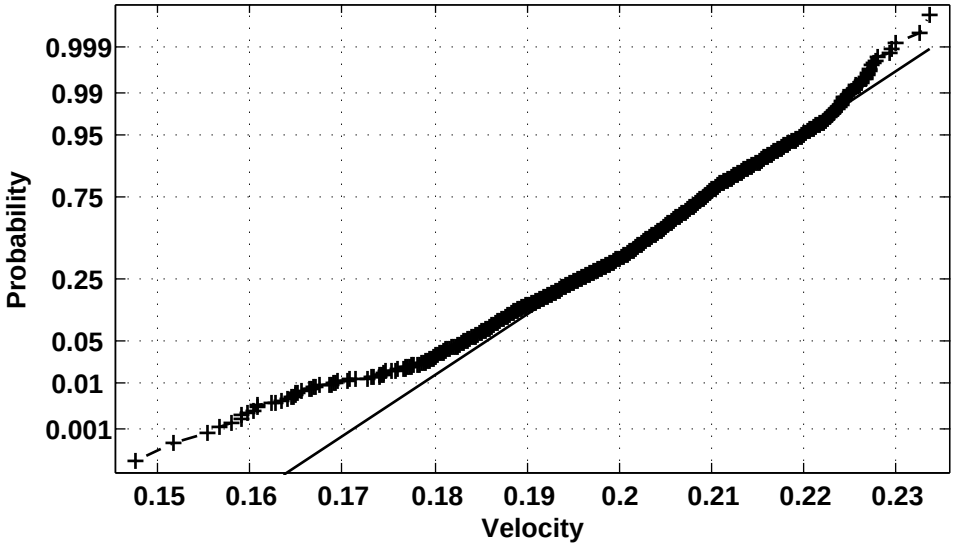

Figure F.6: Normal probability plot at $r/d = 0$ and $x/d = 1$ (H3/7000)

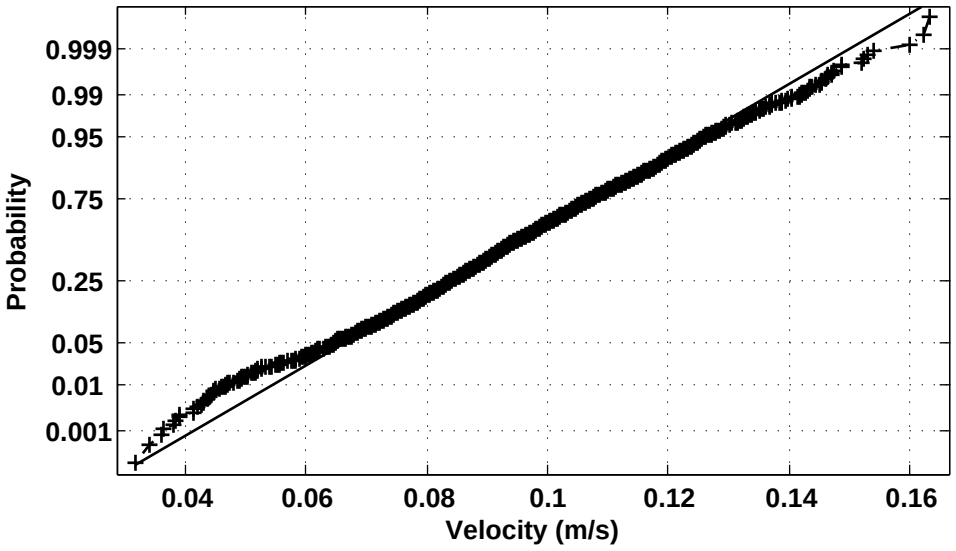

Figure F.7: Normal probability plot at $r/d = 0$ and $x/d = 1$ (H3/10000)

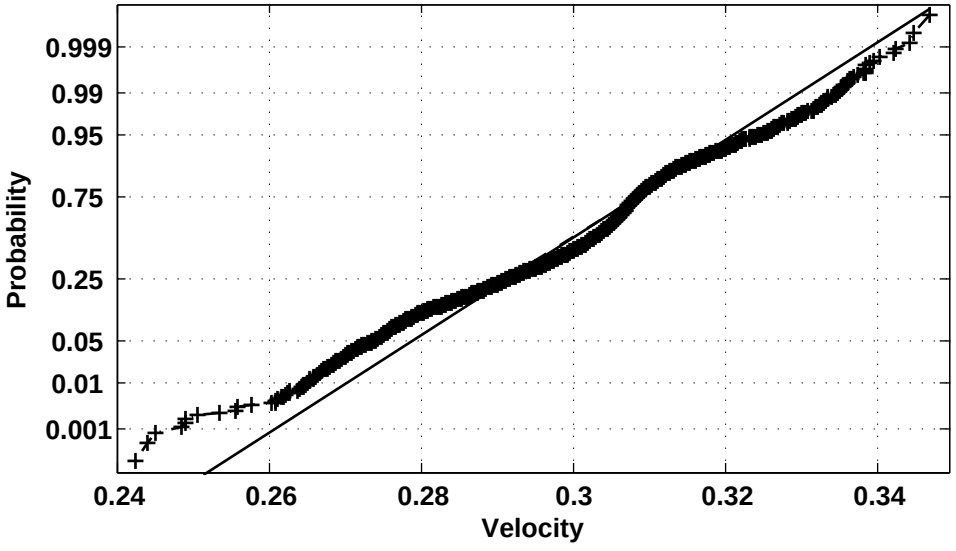

Figure F.8: Normal probability plot at $r/d = 0$ and $x/d = 1$ (H4/8000)

Appendix G

Phased-averaged velocity plots

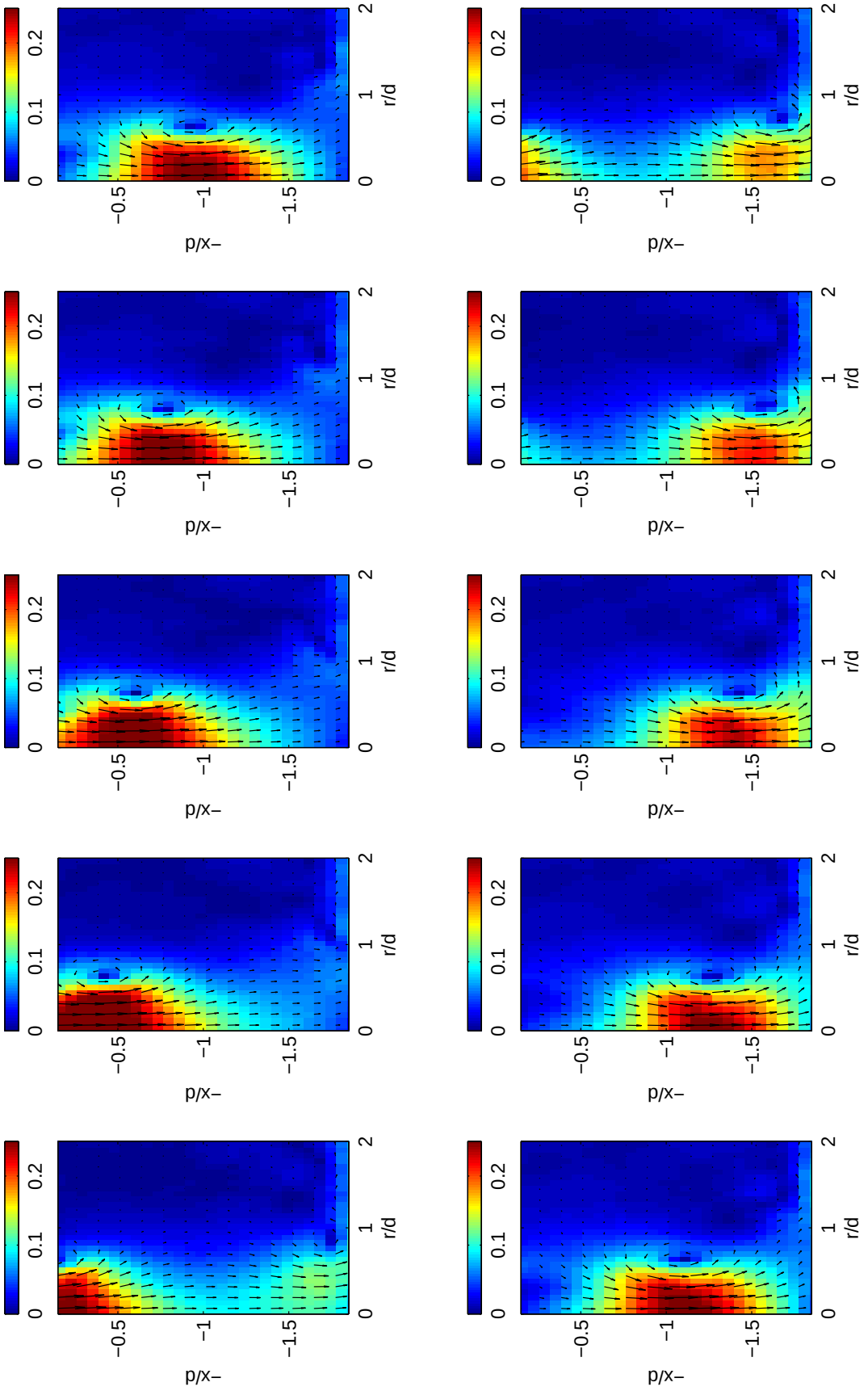

Figure G.1: Phase-averaged cycle for $Re = 4420$, $H/d = 2$ and $St = 0.50$; figures taken at 35 degree intervals

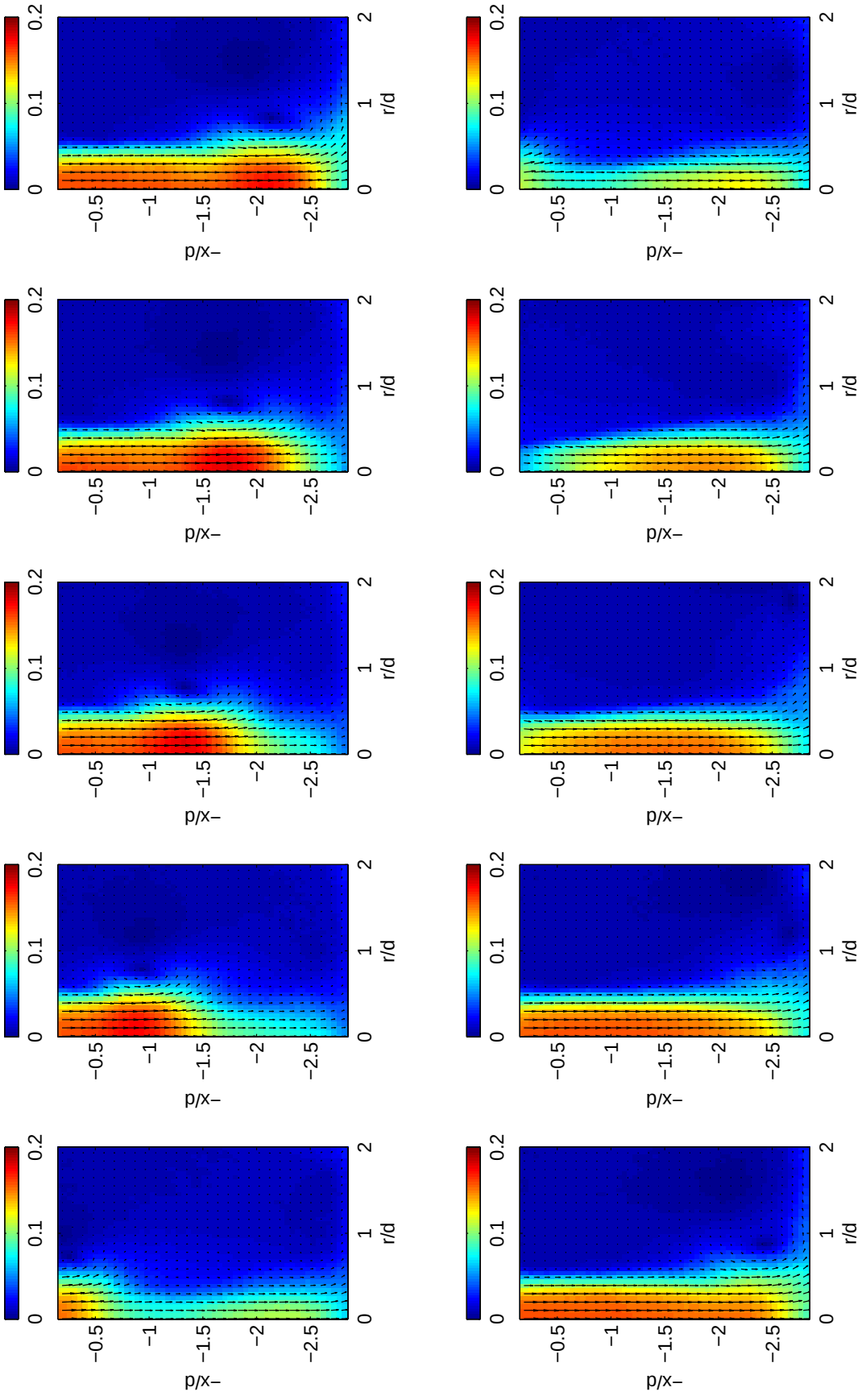

Figure G.2: Phase-averaged cycle for $Re = 3800$, $H/d = 3$ and $St = 0.10$; figures taken at 35 degree intervals

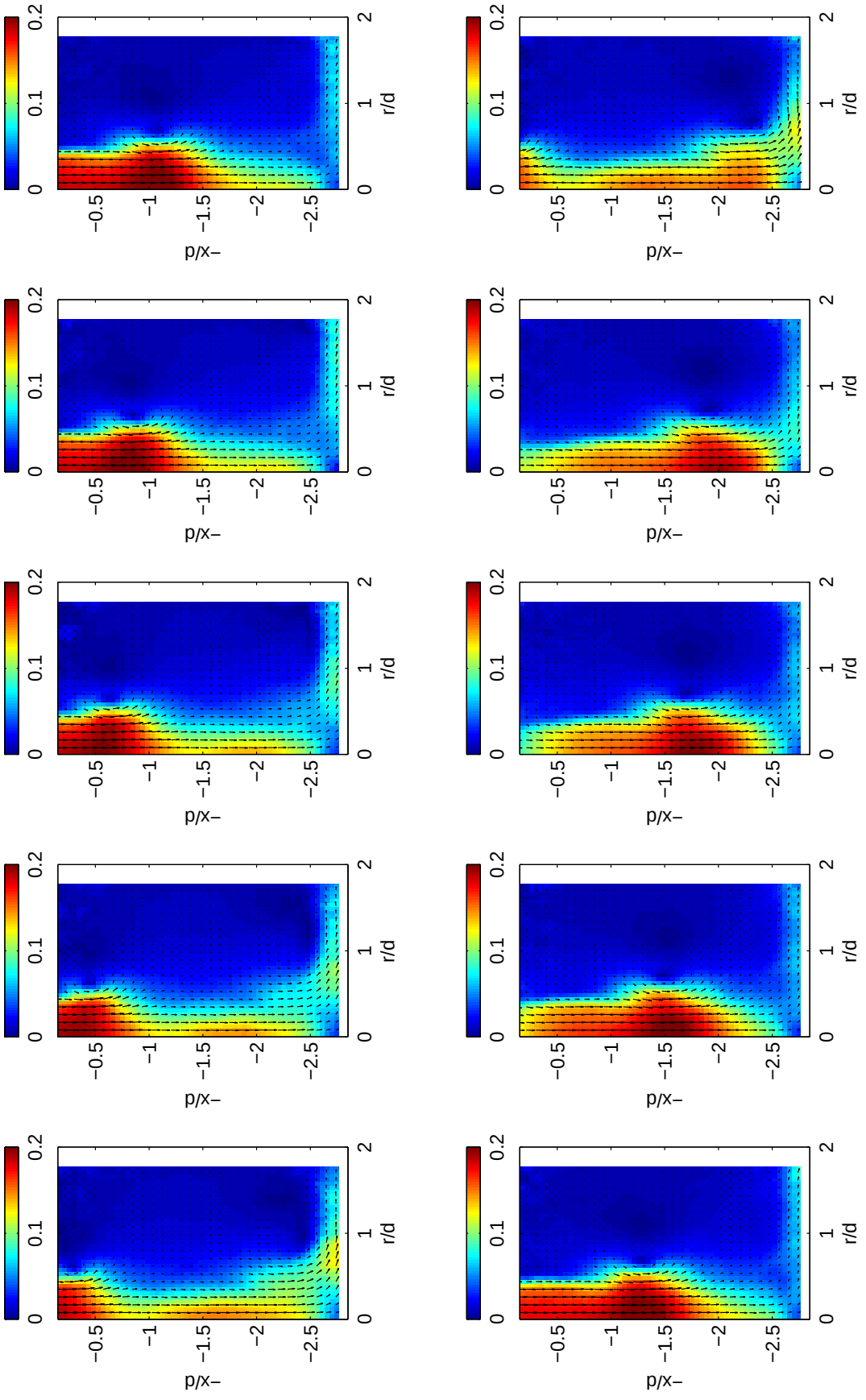

Figure G.3: Phase-averaged cycle for $Re = 4800$, $H/d = 3$ and $St = 0.25$; figures taken at 35 degree intervals

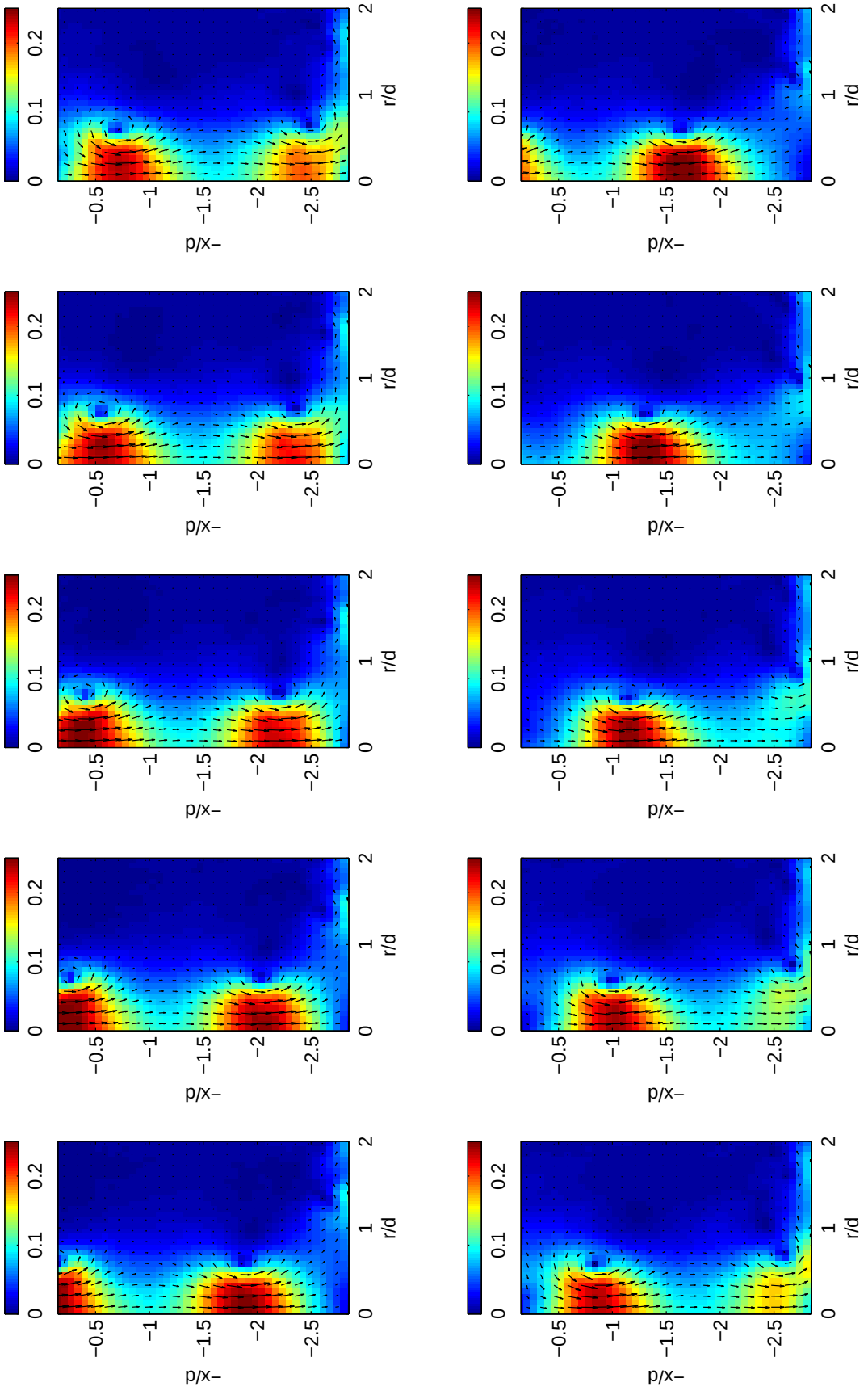

Figure G.4: Phase-averaged cycle for $Re = 4315$, $H/d = 3$ and $St = 0.50$; figures taken at 35 degree intervals

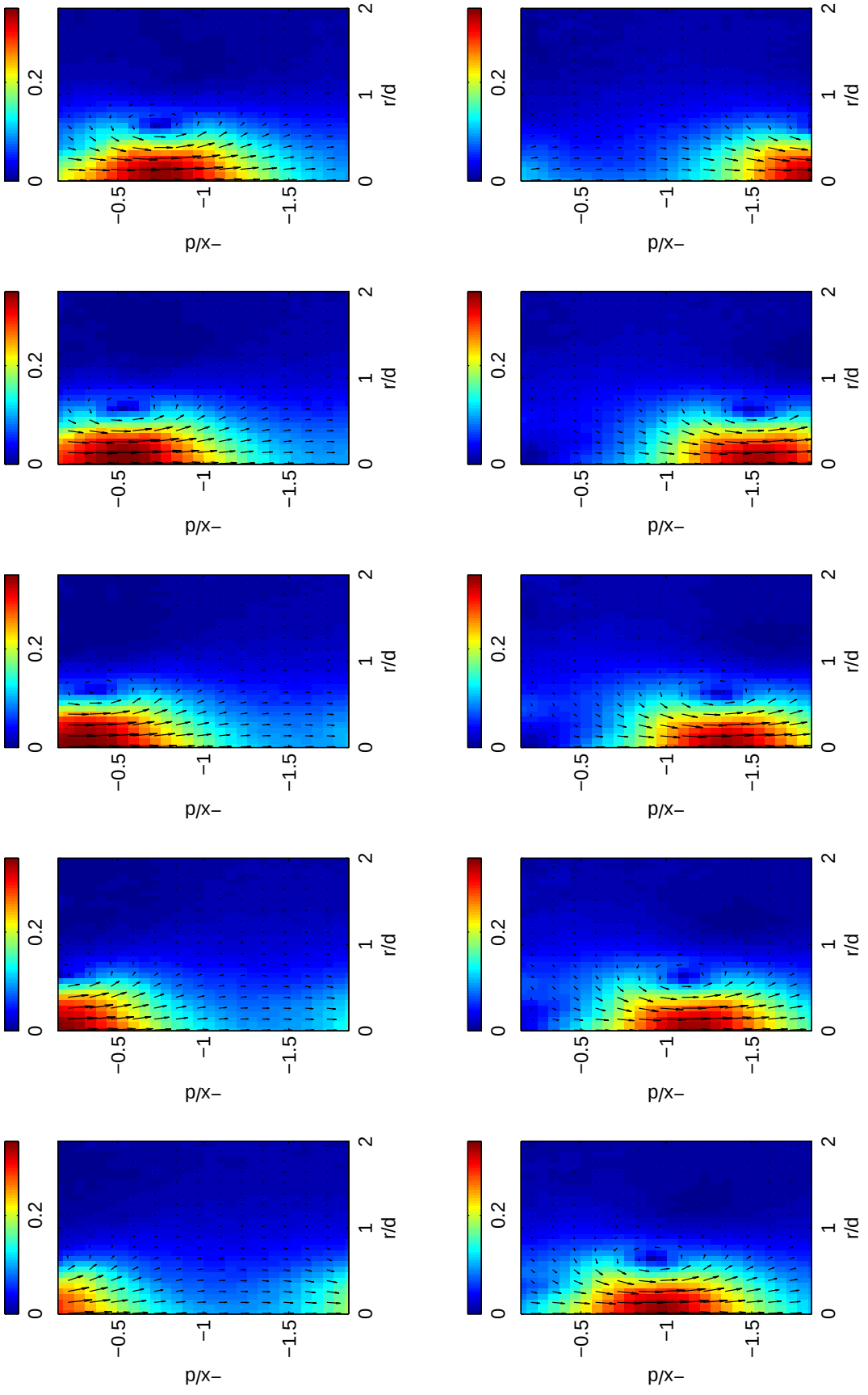

Figure G.5: Phase-averaged cycle for $Re = 5250$, $H/d = 4$ and $St = 0.50$; figures taken at 35 degree intervals

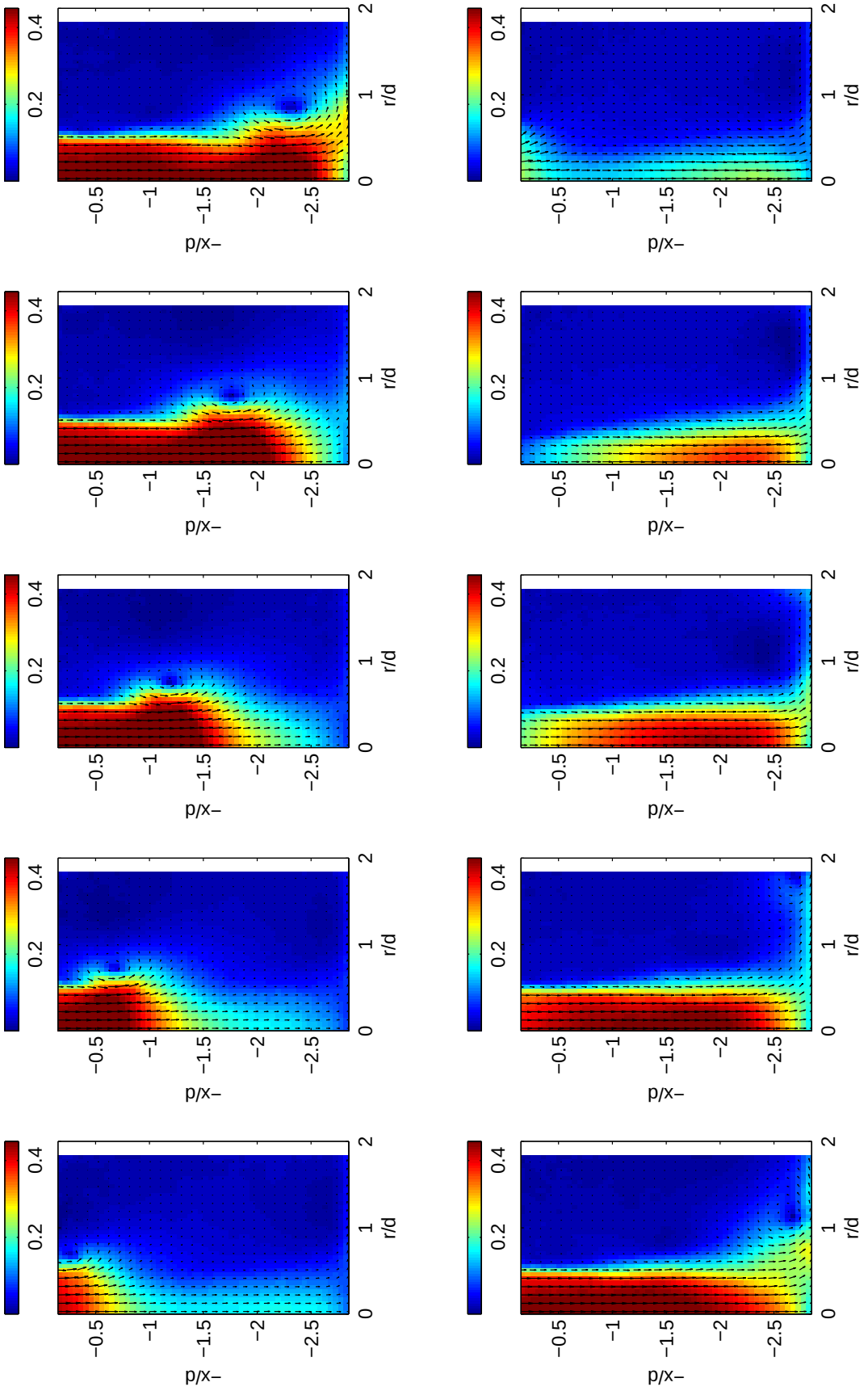

Figure G.6: Phase-averaged cycle for $Re = 10560$, $H/d = 3$ and $St = 0.10$; figures taken at 35 degree intervals

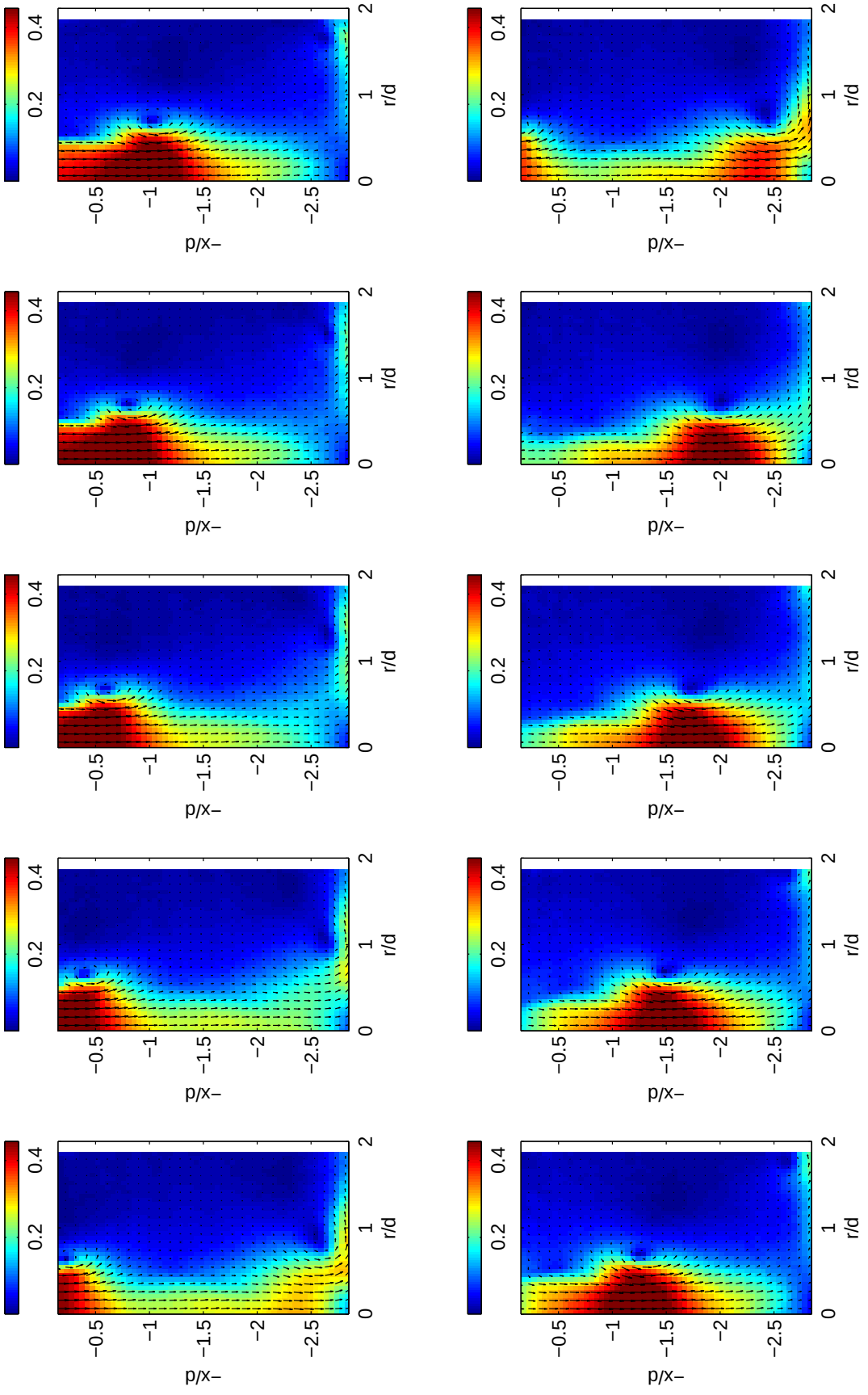

Figure G.7: Phase-averaged cycle for $Re = 10240$, $H/d = 3$ and $St = 0.25$; figures taken at 35 degree intervals

Appendix H

Phased-averaged vorticity plots

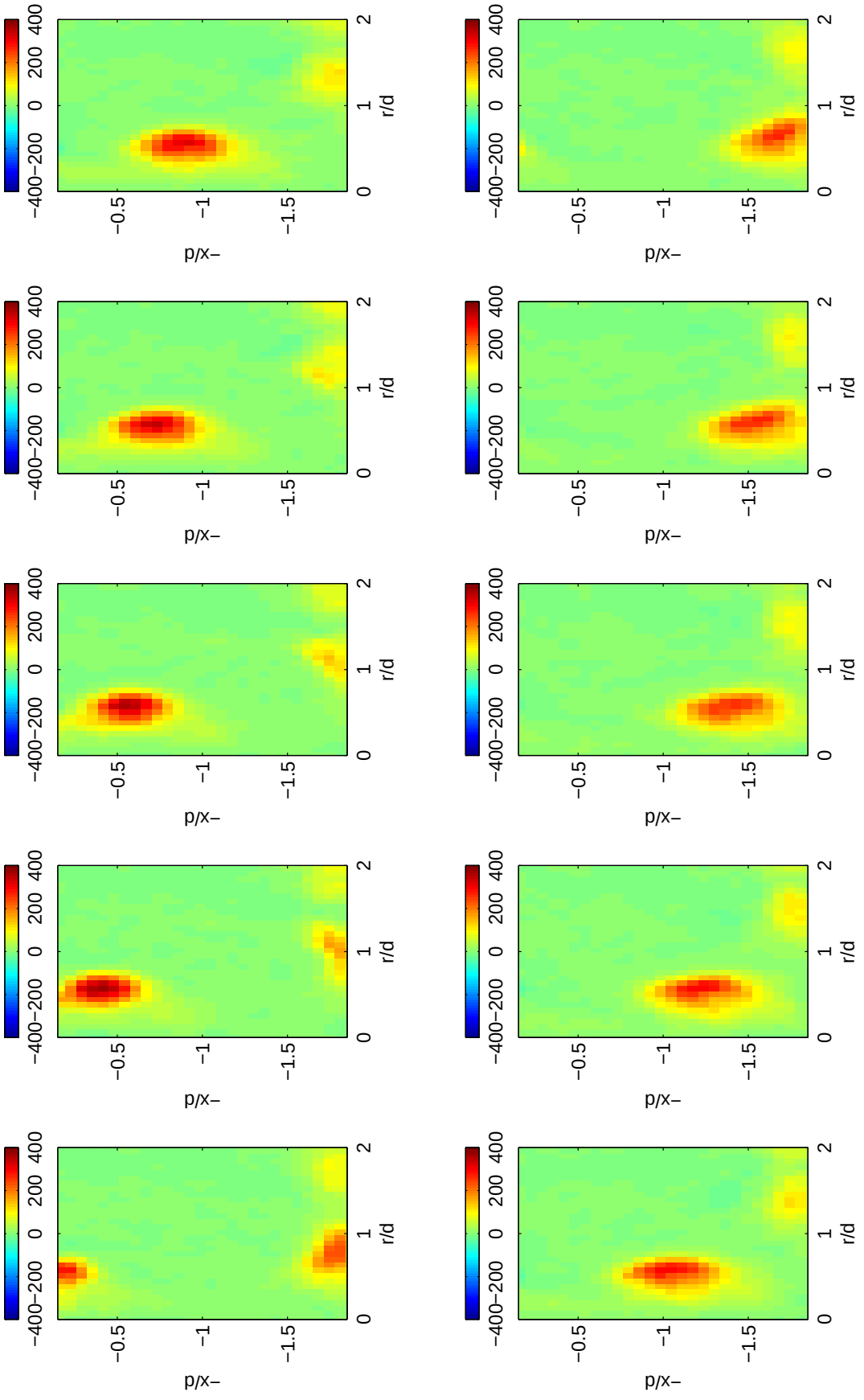

Figure H.1: Phase-averaged vorticity plots for $Re = 4420$, $H/d = 2$ and $St = 0.50$; figures taken at 35 degree intervals

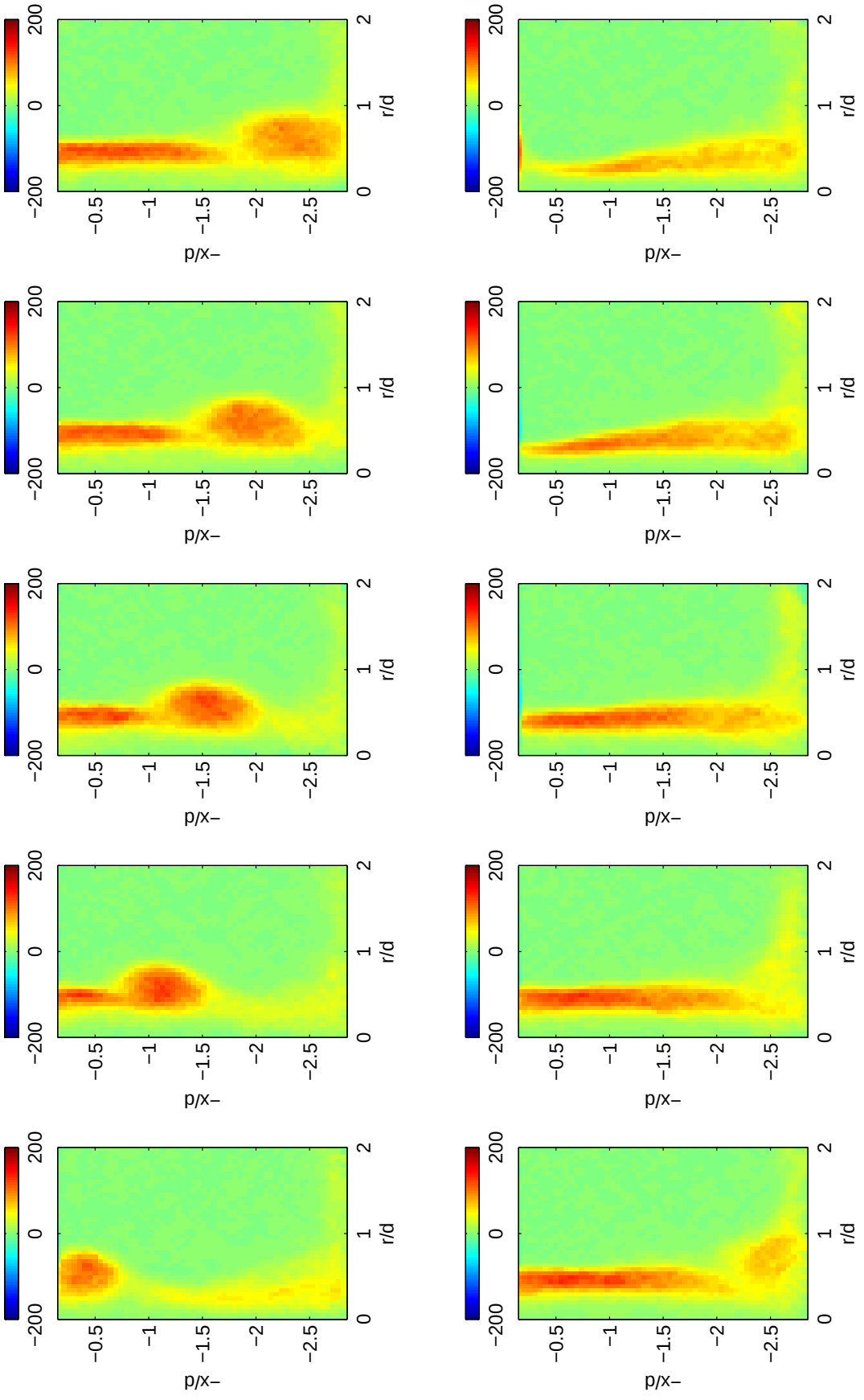

Figure H.2: Phase-averaged vorticity plots for $Re = 3800$, $H/d = 3$ and $St = 0.10$; figures taken at 35 degree intervals

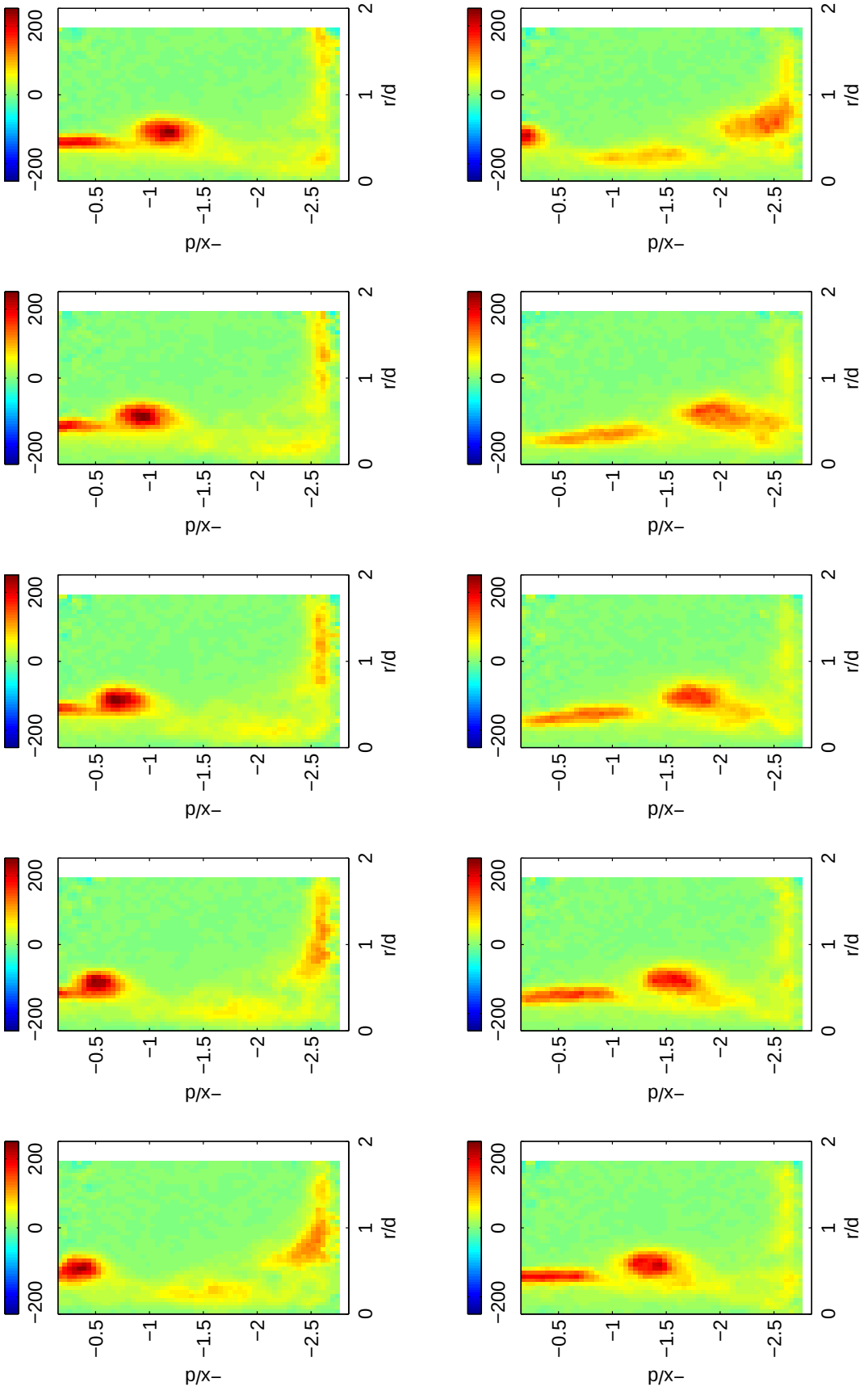

Figure H.3: Phase-averaged vorticity plots for $Re = 4800$, $H/d = 3$ and $St = 0.25$; figures taken at 35 degree intervals

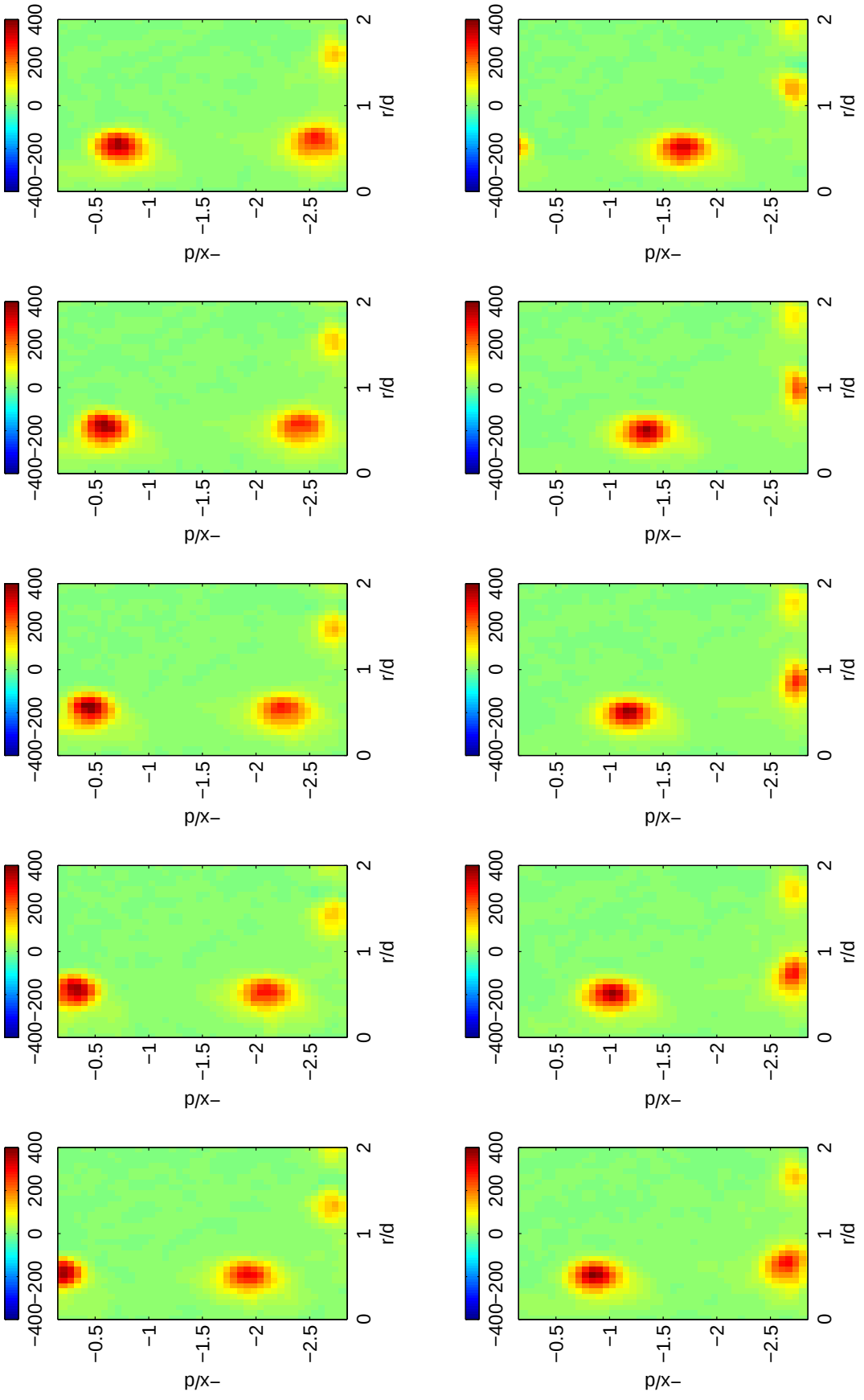

Figure H.4: Phase-averaged vorticity plots for $Re = 4315$, $H/d = 3$ and $St = 0.50$; figures taken at 35 degree intervals

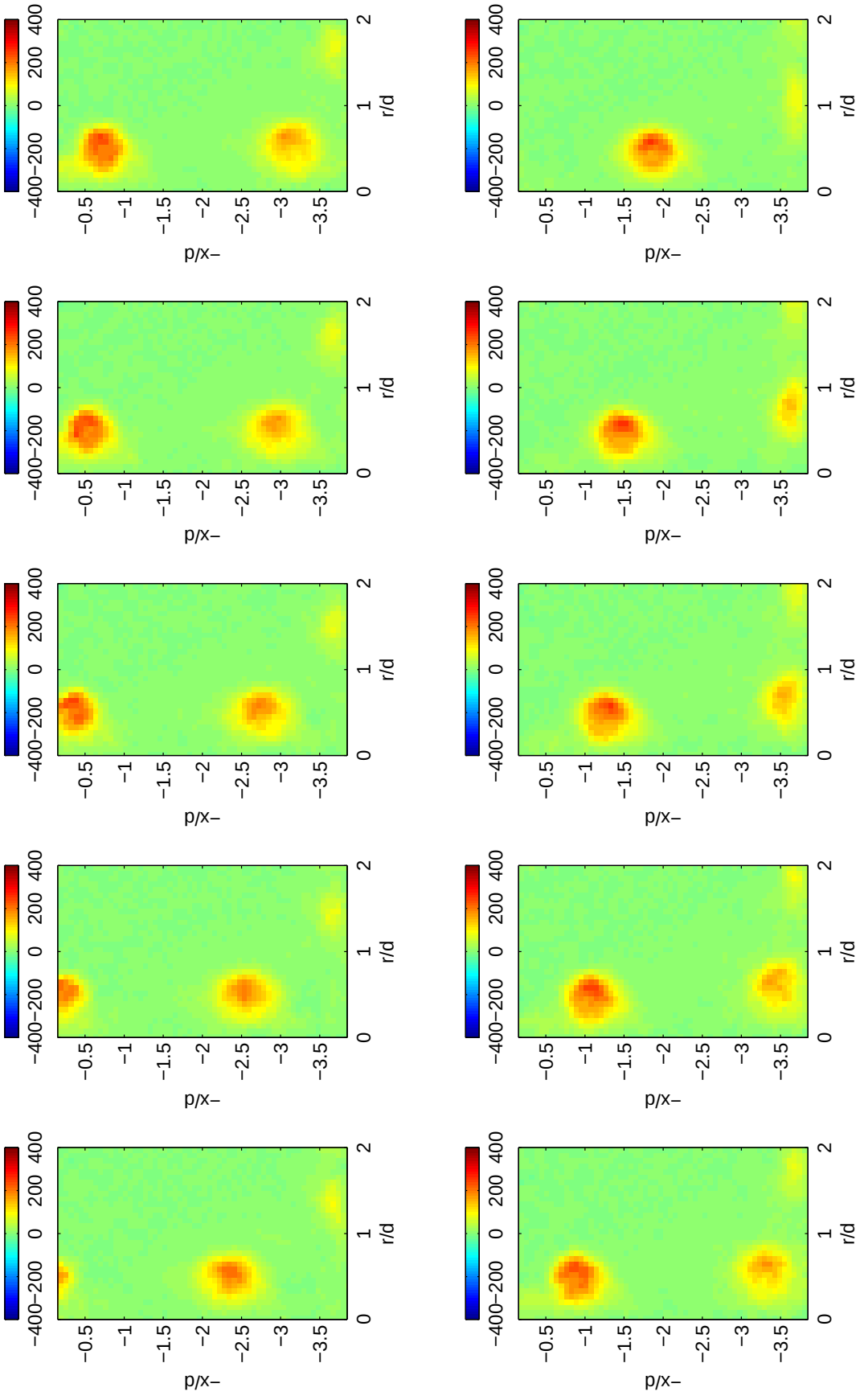

Figure H.5: Phase-averaged vorticity plots for $Re = 5250$, $H/d = 4$ and $St = 0.50$; figures taken at 35 degree intervals

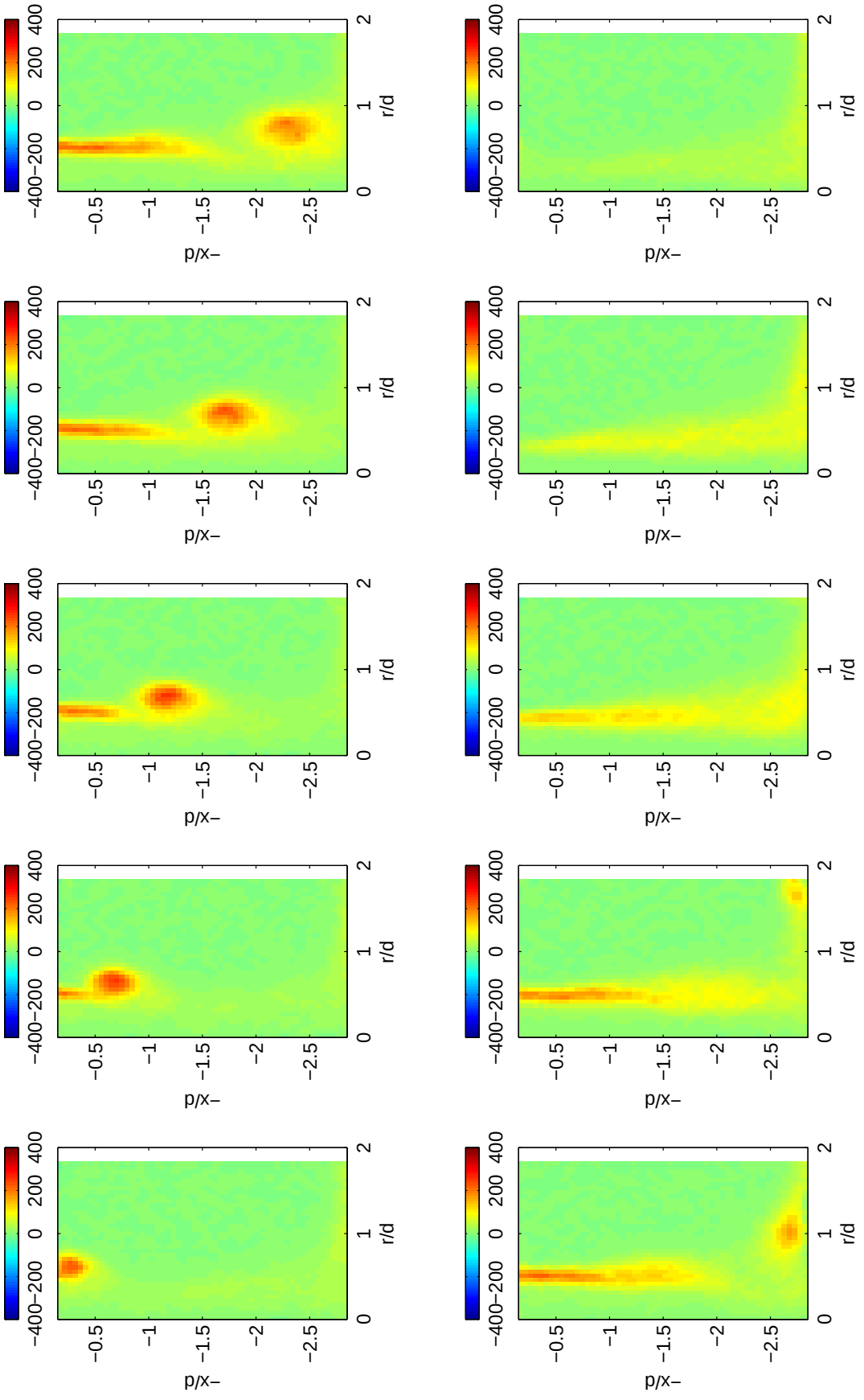

Figure H.6: Phase-averaged vorticity plots for $Re = 10560$, $H/d = 3$ and $St = 0.10$; figures taken at 35 degree intervals

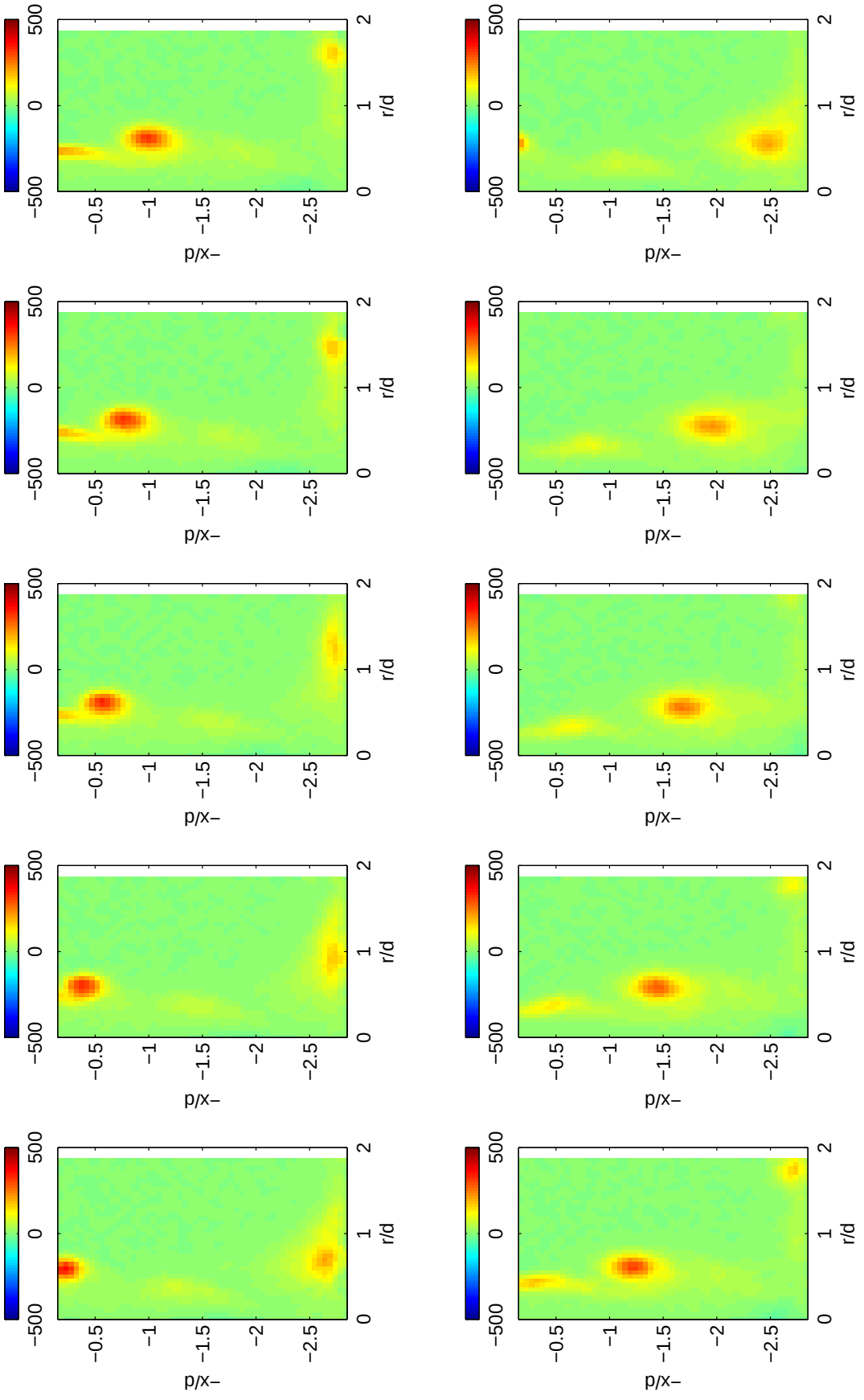

Figure H.7: Phase-averaged vorticity plots for $Re = 10240$, $H/d = 3$ and $St = 0.25$; figures taken at 35 degree intervals